

m⁶A mRNA METHYLATION IN DEVELOPMENT AND DISEASE

by
Caroline Alexandra Beecher Vissers

A dissertation submitted to Johns Hopkins University in conformity with the requirements for
The degree of Doctor of Philosophy

Baltimore, Maryland
December 2019

Abstract

Chemical modifications on mRNA have recently garnered attention as major regulators of cell behavior in embryonic development and many types of disease. In particular, *N*⁶-adenosine (m⁶A), is an abundant mRNA modification that mediates mRNA fate. Through distinct reader protein binding, m⁶A promotes various processing events such as mRNA degradation, alternative splicing, nuclear export, and translation initiation. While we have known of the existence of m⁶A for many years, the recent discovery of m⁶A demethylases has spurred interest in this dynamic modification as a regulatory system. In vitro work showed that m⁶A appears to be especially important in stem cell biology, where knockout of the m⁶A methyltransferase complex components causes major impairments in stem cell self-renewal and differentiation. In vivo work has been severely limited by the fact that full knockout of *Mettl3* or *Mettl14*, which are central parts of the m⁶A methyltransferase complex, is embryonic lethal. We therefore used conditional knockout mice in which *Mettl14* is knocked out in neural stem cells. My thesis has focused on the role of m⁶A in in vivo brain development, with studies on m⁶A in mammalian development and Fragile X Syndrome. We showed that m⁶A promotes mRNA degradation of transcripts that regulate the balance between stem cell self-renewal and neurogenesis. Loss of m⁶A slows the tempo of neurogenesis and also revealed that neural stem cells are normally pre-patterned with transcription of neural genes prior to differentiation. In parallel, I studied the role of m⁶A in hypoxic breast cancer cells because hypoxia induces the m⁶A demethylase, ALKBH5, to drive global changes in m⁶A methylation patterns. In this system, m⁶A promotes translation of modified transcripts to promote global translation, cell division, and oxidative metabolism. The study of m⁶A in multiple systems reveals the incredible cell-type specificity and dynamic nature of m⁶A.

Primary Reader and Advisor: Hongjun Song

Secondary Reader: Shigeki Watanabe

Preface & Acknowledgements

My initial interests in stem cell biology and epigenetics drove me to join Hongjun Song's lab in the Department of Neuroscience at Johns Hopkins. At the time, the field of epitranscriptomics was starting to unfold, and Hongjun suggested that my interest in epigenetics may extend to epitranscriptomics. I will be forever grateful for the opportunity he gave me to work on a brand-new project in the lab studying m⁶A in mouse and human brain development. In collaboration with two other lab members, Kijun Yoon and Francisca Rojas Ringeling, we fervently pursued this project and were regularly surprised by the impact that a single methylation on mRNA has on brain development. I later continued this study first as a Grass Fellow at the MBL and then through a collaboration with Dr. Ryoichiro Kageyama at Kyoto University, where I studied how m⁶A regulates the oscillatory expression pattern of fate-determining genes in neural stem cells.

We next collaborated with Yongchao Ma's Lab at Northwestern, who reached out to us after finding that *Fmr1* knockout mice, which model Fragile X Syndrome, phenocopy *Mettl14* conditional knockout mice. We worked with Yongchao and his graduate student, Brittany Edens, to show that m⁶A and FMRP interact to promote nuclear export of m⁶A-modified FMRP target gene transcripts and thereby regulate neural stem cell behavior.

At the beginning of my third year, the Song Lab moved to the University of Pennsylvania, yet I elected to stay at Johns Hopkins. I established a collaboration with Dr. Gregg Semenza, who graciously supported me in a new study of m⁶A in hypoxic breast cancer cells. I appreciate the level of independence allotted to me and was especially inspired by Dr. Semenza's commitment to translational research that could improve cancer patient outcomes. His winning the Nobel Prize during my time in his lab was the cherry on top of my wonderful experience working with him.

This scientific journey was exciting yet arduous, and my successes would not have been possible without the support of family and friends. I'd first like to thank my parents, Laurel Beecher and Kees Vissers, for their continuous support of my work and encouragement to always do my

best. I'd also like to thank my sister, Elizabeth Vissers, who inspires me with her tenacity and passion to make the world a better place.

My time in Baltimore was truly special because of the lifetime friendships that formed. My life was changed by Jessica Joseph, Jessica Cassin, and Allison Daitch, who all helped me grow into a more open and understanding person. There are countless more people who added spice and joy to the adventures of graduate school. Many thanks to Francisca Rojas Ringeling, Emily Cook, Jaclyn Smith, Tessa Montague, Alex Schnell, and Daniel Berman. I also learned some important life lessons from Erik Maroney, in particular that I have more luck in science than in dice.

Dedication

I would like to dedicate this thesis to the family member who has been by my side through thick and thin. To Watson Vissers, for unconditional love and patience.



Contents

Abstract	ii
Preface & Acknowledgements	iii
Dedication	iv
List of Tables	vii
List of Figures	viii
1. Introduction: the Epitranscriptome in Stem Cell Biology and Neural Development	1
1.1 Modifications of Particular Interest.....	3
1.2 Detection of Epitranscriptomic Modifications.....	7
1.3 Epitranscriptomics in Stem Cell Biology.....	12
1.4 Epitranscriptomics in Neural Development.....	17
1.5 Epitranscriptomics in Neurodevelopmental Disease.....	23
1.6 Concluding Remarks and Future Outlook.....	25
1.7 Figures.....	27
2. Temporal Control of Mammalian Cortical Neurogenesis by m⁶A Methylation	30
2.1 Summary & Highlights.....	32
2.2 Introduction.....	33
2.3 Results.....	34
2.4 Discussion.....	43
2.5 Star Methods.....	47
2.6 Figures.....	62
2.7 Supplemental Figures.....	75
3. m⁶A Methylation Alters the Oscillatory Period of Ascl1 to Regulate Neurogenesis	95
3.1 Introduction.....	96

3.2 Results.....	97
3.3 Future Work.....	100
3.4 Discussion.....	100
3.5 Methods.....	102
3.6 Figures.....	106
4. m⁶A in Neurodevelopmental Disorders: Fragile X Syndrome	110
4.1 Summary.....	111
4.2 Introduction.....	112
4.3 Results.....	113
4.4 Discussion.....	115
4.5 Star Methods.....	117
4.6 Figures.....	123
4.7 Supplemental Figures.....	127
5. Hypoxia-inducible Factors Repress Translation via ALKBH5-mediated m⁶A	130
Demethylation in Hypoxic Breast Cancer Cells	
5.1 Summary.....	131
5.2 Introduction.....	133
5.3 Results.....	134
5.4 Discussion.....	142
5.5 Methods.....	144
5.6 Figures.....	150
5.7 Supplemental Figures.....	160
6. Concluding Remarks	172
7. Bibliography	174
8. Curriculum Vitae	199

List of Tables

2.1	List of Primers Used in the Current Study	86
2.2	Dataset from m ⁶ A-Seq of E13.5 Mouse Forebrain, Day 47 Human Forebrain Organoids, and PCW11 Fetal Human Cortex.....	87
2.3	GO Analysis of m ⁶ A-Tagged Genes in E13.5 Mouse Forebrain	88
2.4	Dataset from RNA Decay Assay of WT and Mettl14 cKO NPCs.....	89
2.5	Gene and Disease Ontology Analysis of m ⁶ A-Tagged Genes in Mouse and Human.	90

List of Figures

1.1	Summary of the most-studied epitranscriptomic modifications	27
1.2	Summary of epitranscriptomic marks in embryonic stem cell biology	28
1.3	m ⁶ A in neural development	29
2.1	Nervous system <i>Mettl14</i> deletion results in residual radial glia cells and ongoing neurogenesis in the postnatal mouse cortex.....	62
2.2	<i>Mettl14</i> ^{-/-} RGCs and NPCs exhibit prolonged cell cycle progression.....	64
2.3	<i>Mettl3</i> regulates cell cycle progression of NPCs and maintenance of embryonic cortical RGCs.....	66
2.4	m ⁶ A tags transcripts related to transcription factors, cell cycle, and neuronal differentiation in the embryonic mouse brain, and promotes their decay.....	68
2.5	Post-transcriptional regulation of pre-patterning gene levels and protein production by m ⁶ A signaling in cortical neural stem cells.....	70
2.6	METTL14 regulates cell cycle progression of human NPCs.....	72
2.7	Conserved and unique features of m ⁶ A mRNA methylation in human forebrain organoids, human fetal brain and embryonic mouse forebrain.....	73
2.S1	Nervous system <i>Mettl14</i> deletion in mice results in postnatal lethality and deficits in timely production of cortical neuron subtypes.....	75
2.S2	Flow cytometry analysis reveals delayed cell-cycle progression of <i>Mettl14</i> cKO NPCs.....	77
2.S3	<i>Mettl3</i> is essential for m ⁶ A mRNA methylation and proper cell-cycle progression of mouse NPCs.....	79
2.S4	m ⁶ A-Seq analysis of mouse embryonic forebrain.....	81
2.S5	Expression of neuronal genes in RGCs of embryonic cortex in vivo.....	83
2.S6	<i>Mettl14</i> regulates cell-cycle progression of hNPCs.....	85
2.S7	Comparison of m ⁶ A mRNA Landscaped among human forebrain organoids, fetal brain, and mouse embryonic forebrain.....	87
2.M1	Movie time-lapse imaging of WT NPCs using a dual-fluorescence reporter system.....	94
2.M2	Movie time-lapse imaging of <i>Mettl14</i> cKO NPCs using a dual-fluorescence reporter system.....	94
3.1	<i>Ascl1</i> mRNA is regulated by m ⁶ A.....	106
3.2	m ⁶ A regulates the oscillatory period of <i>Ascl1</i> in NSCs.....	107
3.3	YTHDF2-mediated degradation of m ⁶ A-modified mRNA regulates <i>Ascl1</i> oscillations.....	108
3.4	Elongated <i>Ascl1</i> oscillation impairs the timing of neurogenesis	109
4.1	Genetic knockout of <i>Fmr1</i> leads to delayed neural progenitor cell cycle progression.....	123
4.2	FMRP preferentially binds m ⁶ A-modified RNAs to promote their nuclear export in regulating neural differentiation.....	125
4.S1	EdU incorporation does not differ between WT and <i>Fmr1</i> KO NPCs.....	127
4.S2	Binding and gene expression analysis.....	128

5.1	HIF regulation of transcriptional changes in response to hypoxia largely occurs through a shared pathway with ALKBH5.....	150
5.2	Dynamic changes in m ⁶ A transcript coverage depend on HIF and ALKBH5 expression.....	152
5.3	HIF and ALKBH5 mediate m ⁶ A methylation patterns across the epitranscriptome..	154
5.4	HIF regulates global translation via ALKBH5 and m ⁶ A.....	156
5.5	HIFs and ALKBH5 regulate protein expression via increased translation of m ⁶ A-modified mRNA.....	158
5.S1	Confirmation of knockdown efficiency and mRNA expression.....	160
5.S2	Differential mRNA expression in MCF-7 NTC subclone exposed to 1% or 20% O ₂ for 24 h.....	161
5.S3	Differential mRNA expression between MCF-7 NTC and HIF-DKD subclones exposed to 1% O ₂ for 24 h.....	162
5.S4	Differential mRNA expression between MCF-7 NTC and ALK-KD subclones exposed to 1% O ₂ for 24 h.....	163
5.S5	Gene ontology analysis of HIF- and ALKBH5-dependent mRNAs.....	164
5.S6	Comparison of FTO and ALKBH5 mRNA expression levels in cells exposed to 20% or 1% O ₂ for 48 h.....	165
5.S7	Gene ontology of mRNAs that are methylated in NTC cells after exposure to 1% O ₂ for 24 h.....	166
5.S8	Potential m ⁶ A functions mediated by known YTH domain-containing reader proteins.....	167
5.S9	Analysis of differentially expressed proteins in MCF-7 cells.....	169
5.S10	HIF and ALKBH5 prevent aberrant translation under hypoxic conditions.....	170
6.1	Differential expression of m ⁶ A machinery.....	173

Chapter 1

Introduction: the epitranscriptome in stem cell biology and neural development

Foreword: This work was written as part of a review *Neurobiology of Disease* – Special Issue: Frontiers in Neuroepigenetics, which will be published in 2020. The text in this thesis introduction includes some additional information beyond the review work. This represents the development of the field of epitranscriptomics up to its current status in December 2019.

The epitranscriptome in stem cell biology and neural development

Caroline Vissers^{1,2}, Guo-li Ming^{2,3}, Hongjun Song^{2,3}

¹ Biochemistry, Cellular, and Molecular Biology Graduate Program, Johns Hopkins University School of Medicine, Baltimore, Maryland 21205, USA

² Institute for Cell Engineering, Johns Hopkins University School of Medicine, Baltimore, Maryland 21205, USA

³ Department of Neuroscience and Mahoney Institute for Neuroscience, Department of Cell and Developmental Biology, Institute for Regeneration, University of Pennsylvania, Philadelphia, PA 19104, USA

Abstract:

The blossoming field of epitranscriptomics has recently garnered attention across many fields by showing that chemical modifications on RNA have immense biological consequences. Methylation of bases in RNA, including N6-methyladenosine (m⁶A), 2-O-dimethyladenosine (m⁶A_m), N1-methyladenosine (m¹A), and 5-methylcytosine (m⁵C) and isomerization of uracil to make pseudouridine (Ψ), dynamically regulate gene expression, are critical for developmental processes, and contribute to disease states. The role of the epitranscriptome is especially relevant in stem cell biology and neurobiology. In particular, m⁶A occurs at the highest levels in the brain compared to any other tissue and plays major roles in embryonic stem cell differentiation, brain development, and neurodevelopmental disorders. However, studies in these areas have published conflicting results on epitranscriptomic regulation of stem cell pluripotency and mechanisms in neural development. In this review we will provide an overview of the current understanding of several RNA modifications and disentangle the various findings on epitranscriptomic regulation of stem cell biology and neural development.

I. Introduction / Modifications of Particular Interest (Figure 1):

N6-methyladenosine: m⁶A

Epitranscriptomic detection technologies have been focused on m⁶A, making it one of the best-studied modifications to date. m⁶A occurs in various types of RNA, including tRNA, rRNA, non-coding RNA (ncRNA), and mRNA. In 2012, two groups independently published m⁶A RIP-Seq (MeRIP-Seq) techniques [1, 2]. Subsequent mapping of m⁶A in the transcriptome showed that it is most commonly added at a defined consensus sequence of DRACH (D=A,U or G; R=G or C; H=A, U, or C). m⁶A can occur in the coding region, but is especially enriched in the 3'UTR and 5'UTR [1, 2]. While m⁶A does not alter Watson-Crick-Franklin base pairing, it can modify protein binding and affect mRNA secondary structure [3, 4]. Numerous m⁶A binding proteins, or readers, have been identified. Individual readers confer unique downstream fates on m⁶A-modified mRNA, including altered mRNA stability, translation, localization, and splicing. m⁶A methylation patterns in the transcriptome appear to be tissue-specific and species-specific [5]. On a global level, 0.2 to 0.5% of all adenines are m⁶A modified [6]. The highest levels occur in the brain, where up to 30% of all transcripts are modified [7]. Since m⁶A is the focus of most epitranscriptomics studies described in this review, we will briefly review the proteins involved in m⁶A dynamics.

m⁶A Methyltransferase Complex

An increasing list of proteins form the methyltransferase complex that adds m⁶A onto mRNA. This complex includes a core heterodimer unit of METTL3 and METTL14, both of which are necessary for successful m⁶A addition to RNA [8]. Additional proteins in the mammalian complex include WTAP [8, 9], KIAA1429 [10], and RBM15/B [11]. These accessory proteins contribute to RNA binding, target specificity, and nuclear localization of the complex. The complex acts co-transcriptionally, meaning that the dynamics of m⁶A are likely due to demethylase activity

and changes in initial transcript methylation, but not new methylation of mature transcripts [12, 13]. Notably, knockout of either METTL3 or METTL14 is embryonic lethal [14-17].

m⁶A Demethylases

There are two known m⁶A demethylases, ALKBH5 and FTO [18, 19]. ALKBH5 co-localizes with nuclear speckles, indicating that both methylation and demethylation occur in the nucleus. On the other hand, FTO can act in the nucleus and cytoplasm. However, the in vivo activity of FTO as an m⁶A demethylase has recently been questioned, with the suggestion that it may instead act on m⁶A_m [10, 20-22]. Still, one recent study reported that FTO can demethylate m⁶A, m⁶A_m, and m¹A. The specificity of FTO remains a major hurdle in the field of m⁶A; confirming its target is critically important so as not to mis-attribute a phenotype or biological function to the wrong epitranscriptomic mark. Finally, full knockouts of either ALKBH5 or FTO are not lethal, though they appear to be especially important in the cellular stress response [20, 23, 24].

m⁶A Reader Proteins

The highly variable functions of m⁶A can be attributed to its many distinct reader proteins. The central group of readers is the YTH-domain-containing family of proteins, which bind directly to m⁶A. These readers have recently been reviewed elsewhere [25, 26]. Briefly, YTHDC1 is found in the nucleus and regulates splicing, while YTHDF1, YTHDF2, YTHDF3, and YTHDC2 are cytoplasmic with various functions. YTHDF1 promotes translation, YTHDF2 promotes mRNA degradation, and YTHDF3 seems to promote either translation or degradation in a context-specific manner. Finally, the binding specificity and function of YTHDC2 remain unclear and may only be functional under special cellular conditions [26].

N6,2-O-dimethyladenosine: m⁶A_m

Unlike the internal m⁶A modification, N⁶,2'-O-dimethyladenosine (m⁶A_m) occurs in the mRNA terminus at the first nucleotide following the N⁷-methylguanosine (m⁷G) cap. Approximately 0.0036% to 0.0169% of all adenines are m⁶A_m modified when averaged across multiple human tissue types, corresponding to 526 to 1,028 unique transcripts, depending on the tissue type [5]. The number of m⁶A_m-modified transcripts were previously thought to be much higher, but improved detection sensitivity has led to the viewpoint that m⁶A_m is only moderately abundant [27]. FTO can remove m⁶A_m from mRNA, though it also acts on other modifications like m⁶A. In contrast, three independent studies in 2019 confirmed that the cap-specific m⁶A_m methyltransferase is phosphorylated C-terminal domain (CTD)-interacting factor 1 (PCIF1), which is thought to be unique to m⁶A_m and targets newly transcribed mRNA by associating with RNA Polymerase II [28-30]. By knocking out PCIF1 in various cell lines, Boulias et al. found that m⁶A_m most strongly correlates with high expression and increased transcript stability [30]. However, this was not universally true for all m⁶A_m-modified transcripts, leaving the regulatory capacity of m⁶A_m up for debate.

Liu et al. analyzed the m⁶A_m profile across tissues in both mice and humans and found that the m⁶A_m methylome pattern is more clearly resolved in the brain than any other tissue. Furthermore, different brain regions (cerebellum, hypothalamus, and brainstem) are distinguishable from one another based on their m⁶A_m patterns. Next, Liu et al. found a negative correlation between m⁶A_m-modified mRNA and protein levels [5], which seemingly conflicts with the previous result that m⁶A_m promotes mRNA stability [30]. Nonetheless, the highly specific m⁶A_m pattern in brain tissue suggests it may play a regulatory role in neural mRNA processing. Finally, Sendinc et al. found that m⁶A_m decreases cap-dependent translation but does not affect mRNA stability [31]. The field would greatly benefit from identification of m⁶A_m reader proteins that could help disentangle its potential downstream functions.

N1-methyladenosine: m¹A

m¹A is steadily gaining attention as sequencing becomes easier, yet the abundance of m¹A remains under debate. Some studies found that 0.015% to 0.16% of adenines are m¹A modified, corresponding with over 4,000 mRNA transcripts (about 20% of the transcriptome) [32, 33]. Others claim that only about 400 total m¹A sites exist in mRNA [34, 35]. m¹A also occurs in tRNA, which may be functionally distinct from m¹A in mRNA. Though our understanding of the modification is limited, major progress was made through identification of putative m¹A methyltransferases. Namely, TRMT6 and TRMT61A form a complex in the cytosol, and TRMT10C and TRMT61B complex in the mitochondria [36]. Currently, ALKBH3 is the only known m¹A mRNA demethylase, though it also acts on DNA and m³C in RNA [37-39]. However, ALKBH1 can demethylate m¹A in tRNA to impair translation initiation and elongation [40]. In mRNA, m¹A is also thought to promote translation: it primarily exists in the 5'UTR near the translation initiation site (TIS), and its positive charge can induce changes in secondary mRNA structure [32, 36]. To our knowledge, no studies of m¹A in the brain have been performed, leaving a major gap in knowledge that will undoubtedly be explored in the coming years.

5-methylcytosine: m⁵C

m⁵C is added to tRNA, rRNA, and mRNA by a variety of methyltransferases with specific RNA targets [41]. DNMT2 and especially NSUN2 are the most well-characterized m⁵C methyltransferases that act on both tRNA and mRNA [42-44]. NSUN2-mediated m⁵C mRNA methylation promotes mRNA nuclear export through ALYREF, a nuclear m⁵C reader protein [43]. Additionally, m⁵C may cooperate with m⁶A to enhance translation of particular transcripts like p21 [42]. Finally, m⁵C addition to a subset of ncRNAs called vault RNAs (vtRNAs) reduces downstream miRNA production [45]. Though no m⁵C direct demethylases has been identified, ten-eleven translocation (Tet) enzymes can oxidize m⁵C to 5-hydroxymethylcytosine (hm⁵C) and then unmodified cytosine [46]. The frequency of hm⁵C is about one hm⁵C per 5000 m⁵C [47]. This is slightly enriched in mRNA, with hm⁵C occurring on $\sim 7 \times 10^{-6}$ of the total cytosines [48]. In

Drosophila, hm⁵C was shown to preferentially mark mRNAs in coding regions and promote their translation [47, 49]. However, no RNA hm⁵C reader proteins have been identified and its downstream function in mammals remains unclear.

7-methylguanosine: m⁷G

In addition to m⁷G modification of the cap in mRNA, which promotes translation and protects mRNA from degradation [50], two independent studies identified m⁷G internally in miRNAs [51] and mRNA [52]. These 2019 studies by Pandolfini et al. and Zhang et al., respectively, show that m⁷G disrupts secondary structures of G-quadruplexes to mediate miRNA processing and promotes translation of modified mRNA. Both groups showed that a complex between METTL1 and WDR4 catalyzes m⁷G addition to RNA in mammals [51, 52]. This is the same enzymatic complex that adds m⁷G to tRNA to regulate translation [53], while WBSR22 regulates m⁷G addition to rRNA [54]. To date, no m⁷G demethylases have been identified.

Pseudouridine: Ψ

While pseudouridine (Ψ) is one of the most abundant modifications in ncRNA, its existence in mRNA is a recent finding [55, 56]. PUS1 and PUS7 enzymes isomerize uridine to pseudouridine [57] in an mRNA structure-dependent manner [58]. Other PUS-family proteins add Ψ to other types of RNA. On the other hand, no direct readers or removal enzymes have been identified, indicating Ψ may be irreversible. Some downstream effects of Ψ include weakening interactions between mRNA and Pumilio family proteins (PUFs) [59] and stabilizing RNA structure by improved base stacking and increased hydrogen bonding [55, 60, 61]. Ψ has also been hypothesized to promote translation efficiency, though this remains to be proven [55].

II. Detection of epitranscriptomic modifications:

m⁶A sequencing

The ability to detect epitranscriptomics marks is necessary to understand the biology. Development of sensitive and accurate sequencing techniques is an ongoing process that is central to progression of the field as a whole. Due to this importance, we will provide a brief overview of the current technologies available for detection of m⁶A and highlight the rapid progress made in the past two years.

RIP and CLIP-seq

The first method developed to detect m⁶A was methylated RNA immunoprecipitation (IP) and sequencing (MeRIP-seq, m⁶A-seq) using an antibody against m⁶A. This method calculates enrichment of mRNA fragments after m⁶A IP relative to total input mRNA using peak-calling methods like MACS. However, peaks represent an accumulation of aligned sequencing reads and do not provide single-base resolution. Furthermore, current m⁶A antibodies cannot distinguish between m⁶A and m⁶A_m, meaning m⁶A sites identified by meRIP-seq likely contain significant false positives or inaccuracies. Nonetheless, as the first method developed, meRIP-seq was fundamental in establishing the field of epitranscriptomics and revolutionized our understanding of m⁶A biology. MeRIP-seq was further improved by UV-induced RNA-antibody crosslinking that allows for single base resolution. A number of methods using UV crosslinking have been developed, including photoactivatable ribonucleoside-enhanced crosslinking and immunoprecipitation (PAR-CLIP), UV crosslinking and immunoprecipitation (UV CLIP), and m⁶A individual-nucleotide-resolution crosslinking and immunoprecipitation (miCLIP). These and other antibody-based methods have been reviewed in-depth elsewhere [62].

Enzymatic Detection of m⁶A

In 2019, two antibody-free methods for global m⁶A detection were published. These techniques overcome the limitations of antibody specificity and the large quantities of RNA necessary for successful RIP-Seq methods and reduce the difficulty of library preparation. First, Garcia-Campos*, Edelheit* et al. developed a technique for RNA digestion via m⁶A sensitive RNase (MAZTER-seq), which uses the bacterial RNase MazF to detect m⁶A. MazF cleaves RNA upstream of “ACA” sites, but not “m⁶A-CA” sites. Therefore, by fragmenting mRNA with MazF, ligating adapters and reverse transcribing, and finally amplifying and sequencing, MAZTER-seq can identify m⁶A sites as read-through ACA sites that are not at the terminal end of a read. In contrast, unmodified ACA sites occur at either end of every read. However, MAZTER-seq is limited by the fact that it can only detect m⁶A in ACA sites, which represents a mere 16% of all m⁶A sites in mammals. Furthermore, MazF digestion led to only 50-60% of reads beginning and ending with ACA, suggesting that MazF cleavage of ACA sites is fairly limited. Still, for the sites that are quantifiable by MAZTER-seq, the method provides high sensitivity, single nucleotide resolution, and rough quantification of the percent of a particular gene transcript that is m⁶A modified [63].

The second enzymatic technique developed in 2019 entails deamination adjacent to RNA modification targets (DART-seq). This method utilizes APOBEC1, a cytosine deaminase that induces cytosine-to-uracil (C-to-U) editing in both DNA and RNA. By fusing APOBEC to the YTH domain of m⁶A-binding proteins, K. Meyer targeted the base editing system to m⁶A sites. This in turn allows for transcriptome-wide mapping of m⁶A with only 10 ng of input mRNA and comparable sensitivity to antibody-based approaches. More specifically, APOBEC1 deaminates the cytidine immediately following m⁶A in the DRACH motif. C-to-U editing analysis of DART-seq reads detected m⁶A sites with 64% overlap with m⁶A sites identified by MeRIP-seq. This percentage could be interpreted as the sensitivity of DART-seq, or as the promiscuity of MeRIP-seq in identifying marks besides m⁶A. Furthermore, 91.4% of C-to-U editing sites are preceded by an A, confirming the specificity of APOBEC1-YTH for cytidines directly adjacent to m⁶A. DART-

seq has several major advantages over other available techniques: it can be used as an indicator of m⁶A abundance on individual RNAs, it distinguishes between m⁶A and m⁶A_m, and it can be combined with long-read PacBio sequencing to identify isoform-specific methylation patterns [64]. Overall, DART-seq provides an exciting platform to improve the ease and accuracy of transcriptome-wide identification of m⁶A and holds great potential for pushing the field of epitranscriptomics forward.

Nanopore Direct RNA Sequencing

Direct RNA sequencing is one of the most recently developed methods for detection of mRNA modifications. Using Oxford Nanopore Technology (ONT) sequencing, Lorenz et al. developed a software to identify m⁶A sites from in vitro HEK293T RNA. This m⁶A Identification using Nanopore Sequencing (MINES) was able to use nanopore electric current data to predict previously reported m⁶A sites from CLIP-seq data with about 80% accuracy, though this only represented about 35% of the total reported CLIP sites and requires the m⁶A site to be in the DRACH consensus motif. However, MINES still depends on averaging signal deviations at every predicted m⁶A site, meaning it currently cannot be used for single molecule detection that would determine the percentage of reads methylated at a particular site [65]. In an independent study, Liu et al. also used current intensity changes in ONT sequencing to create an algorithm that can detect m⁶A methylation with up to 88-91% accuracy by combining information on base quality, mismatch, and deletion frequency. However, this algorithm also depends on averaging of reads for one site and therefore cannot predict the modification status of individual transcripts [66]. Current ONT sequencing also cannot differentiate between m⁶A and m¹A, which hinders its utility as the field of epitranscriptomics moves toward more in-depth analysis of distinct modifications. Still, direct RNA m⁶A nanopore sequencing provides an exciting avenue for future detection strategies, particularly because the software tools can be applied to any nanopore RNA sequencing and does not require additional processing to detect m⁶A.

Detection of other mRNA modifications

Pseudouridine can be identified through chemo-selective alteration of the modified base followed by sequencing. Specifically, Ψ can be selectively modified by N-cyclohexyl-N'- β -(4-methylmorpholinium)ethylcarbodiimide (CMC) to form a covalent adduct that arrests reverse transcription. Therefore, recurrent reverse transcription termination sites have been used to map Ψ at single-nucleotide resolution [55-57, 67]. This method was further improved by using N₃-CMC, a derivative of CMC that contains an azide, which allows for biotinylation of Ψ -N₃-CMC adducts and streptavidin enrichment (CeU-seq). This increased the sensitivity of Ψ detection nearly 10-fold, with 2,084 Ψ sites identified in HEK293T cells [68].

m¹A mapping has been a major challenge due to its extremely low stoichiometries, with estimates ranging from only about 50 modified mRNA transcripts [35] up to about a thousand [33]. However, m¹A can also occur on tRNA, lncRNA, and rRNA, and total stoichiometry does not necessarily correlate with functional power. Transcriptome-wide mapping of m¹A was first performed using an antibody pull-down method (m¹A-seq) [32, 33]. More recently, multiple independent studies generated single base-resolution methods that use misincorporation patterns upon reverse transcription of m¹A-containing RNA, which depends on m¹A disrupting Watson-Crick-Franklin base pairing [34, 36, 69]. Most recently, Khoddami et al. published a method that can detect m⁵C, Ψ , and m¹A at single-base resolution in a modified RNA bisulfite sequencing method named RBS-Seq [44]. However, this study found significantly different epitranscriptomics patterns than previous work; it remains difficult to tell if new methods are more specific or less sensitive than previous methods. In upcoming years, we expect rapid progression in single experiment combined mapping of multiple modifications, in particular those that disrupt base pairing (m¹A, m¹G, m²G, m³C).

III. Epitranscriptomics in stem cell biology:

Epitranscriptomics appears to be especially important in stem cell biology, as it contributes to self-renewal and differentiation capacity. m⁶A is by far the most studied RNA modification in stem cells, particularly in embryonic stem cells (ESCs) and induced pluripotent stem cells (iPSCs).

Embryonic Stem Cells (ESCs)

Early reports of m⁶A in ESCs were somewhat conflicting. In 2014, Wang et al. found that knockdown of Mettl3 and Mettl14 reduces m⁶A abundance and impairs stem cell self-renewal [15]. In contrast, Batista et al. then reported that Mettl3 knockout in mESCs improves self-renewal but blocks differentiation [16]. However, both of these studies examined mESC in vitro, which muddies our understanding of the exact stage the ESCs are in and what m⁶A might do to drive embryonic development in vivo. This gap was addressed by Geula et al., who performed one of the first major studies of m⁶A in naïve pluripotent mouse ESCs. Naïve mESCs exist in a distinct molecular state compared to more advanced, “primed” epiblast stem cells (EpiSC). By knocking out Mettl3, they identified m⁶A as a key driver of termination of the naïve state and entry into the primed state, which is necessary for proper lineage differentiation at the post-implantation embryonic stage. The effects of impaired differentiation are so drastic that loss of m⁶A causes early embryonic lethality [6]. Importantly, this study further clarified that m⁶A regulates the genes governing both naïve and primed states, and that loss of m⁶A causes upregulation of whichever genes are modified in that particular stem cell state. So, naïve mESCs show enhanced pluripotency upon Mettl3 knockdown, whereas primed EpiSC show increased stability of lineage-commitment genes upon loss of m⁶A [6, 70]. Mechanistically, this study and others determined that m⁶A primarily functions in development by reducing mRNA stability, which allows for the rapid clearance of key naïve pluripotency-promoting transcripts or pro-differentiation transcripts, depending on the stem cell stage [6, 15, 16, 71].

In addition to the traditional Mettl3/Mettl14-mediated addition of m⁶A to mRNA, several other m⁶A methyltransferases were thought to exist. In particular, METTL16 was identified in human cells as an m⁶A methyltransferase that primarily targets small nuclear RNA (snRNA), specifically U6 snRNA, and other non-coding RNAs [72]. Additionally, METTL16 regulates expression of the SAM synthetase MAT2A [73], which is highly consequential for all modifications that use SAM as a methyl donor. To this end, Mendel et al. found that METTL16-mediated modification of Mat2a mRNA is necessary for proper embryonic development of mouse blastocysts, and homozygous knockout of Mettl16 is embryonic lethal. Analysis of E2.5 Mettl16 KO mouse blastocysts showed that only 20 genes are differentially expressed relative to the WT, with Mat2a showing the most significant downregulation. However, by E3.5 the global transcriptome was massively dysregulated [74]. The role of this non-canonical m⁶A pathway in embryonic development suggests that m⁶A in snRNA is uniquely regulated and has distinct functions at different stages of development. While the more common Mettl3/Mettl14-mediated pathway has garnered the most attention, understanding the complexities of the epitranscriptome as it changes during development will be necessary to accurately characterize the many roles of m⁶A.

m⁵C in mESCs

The overwhelming focus of research in ESCs has been centered around m⁶A, but there is also one published study on m⁵C in mESCs. In 2017, Amort*, Rieder* et al. identified 12,492 m⁵C sites in nuclear mESC mRNA. Modified mRNAs were enriched for gene ontologies corresponding to cell cycle, RNA processing, chromatin modification, and developmental processes. Though the functionality of m⁵C in mESCs was not shown, a correlation between m⁵C sites and RNA binding protein (RBP) sites was identified. Approximately 29% of m⁵C sites in mESCs overlap with known RBP sites. More specifically, the largest overlaps correspond to UPF1 binding, which regulates nonsense-mediated RNA decay. Additionally, SRSF3 and SRSF3 splicing factors and the PRC2

subunit EZH2 have binding sites that significantly overlap with m⁵C sites. This led to the hypothesis that m⁵C may contribute to RBP binding and functionality, though this requires further validation [75]. As detection of diverse mRNA modifications continues to improve and orphan methyltransferase targets are identified, we expect our understanding of epitranscriptomics regulation of stem cells to grow rapidly. Notably, the low stoichiometry of some modifications relative to m⁶A should not decrease their perceived importance, as the power of the modification is derived from the strength of its downstream effects, which vary widely among reader proteins.

tRNA epitranscriptomic regulation of ESCs

Finally, modification of ncRNA, especially tRNA, also regulates ESC self-renewal and differentiation. For example, m⁷G on tRNA in mESCs promotes translation of mRNAs crucial for cell cycle progression and neural differentiation [50]. Similarly, NSUN3-mediated addition of m⁵C to mitochondrial tRNA promotes mESC proliferation and balances differentiation into mesoderm, endoderm, and neuroectoderm [76].

Induced Pluripotent Stem Cells (iPSCs)

The understanding that m⁶A contributes to pluripotency and differentiation drove studies of its regulatory capacity in iPSCs. In 2015, Chen et al. showed that high abundance of m⁶A increases the reprogramming efficiency of mouse embryonic fibroblasts (MEFs) to pluripotent stem cells, in part by altering expression of key pluripotency factors like Oct4, Sox2, and Nanog. This study further found an interplay between microRNA (miRNA) binding to mRNA and enhanced METTL3 binding to mRNA to promote de novo addition of m⁶A [17]. This concept of m⁶A interplay with noncoding RNAs has been explored with contrasting conclusions, and has been reviewed in-depth elsewhere. [77]. Furthermore, Chen et al. found that Mettl3 knockdown reduces iPSC colony formation [17]. However, Geula et al. found that Mettl3 knockdown does not impair reprogramming efficiency, but rather slows proliferation of iPSCs in early reprogramming [6].

Finally, in 2019, Wu et al. found that *Mettl3* knockdown decreases the proliferation rate of porcine iPSCs (piPSCs) and impairs expression of key pluripotency genes, though they did not test for reprogramming efficiency. This study further identified that m⁶A promotes YTHDF1-mediated translation of JAK2 in piPSCs, while promoting degradation of SOCS3 via YTHDF2 [78]. Both of these mechanisms lead to upregulation of the JAK2-STAT3 signaling pathway, which is known to promote stem cell self-renewal by increasing expression of the core pluripotency genes *Klf4* and *Sox2* [78, 79].

Overall, m⁶A clearly regulates the pluripotency of iPSCs, but its role in reprogramming likely depends on the cellular context of the starting material or the stage of reprogramming. As was the case in ESCs, m⁶A may alter expression of the gene transcripts already present. Still, further investigation is needed to identify the fate of m⁶A-modified transcripts. While m⁶A-mediated mRNA degradation appears to be a major mechanism, expression of other reader proteins suggests a more complex system. Understanding how m⁶A reader proteins selectively bind particular mRNA targets will be a major step forward in further elucidating the mechanisms of m⁶A action in iPSCs.

Regulation of Stem Cell Epitranscriptomes

Upstream regulation of m⁶A deposition or differential expression of the writers, readers, and erasers contributes to the function of m⁶A in stem cells. For example, in 2015 Aguiló et al. showed that zinc finger protein 217 (*ZFP217*) coordinates epigenetic regulation with m⁶A deposition. More specifically, *ZFP217* is a transcription factor that directly activates transcription of several key pluripotency genes, then blocks m⁶A modification of these genes by sequestering *METTL3* in mESCs and iPSCs. *ZFP217* knockdown causes global increases in m⁶A levels, which correlates with a decreased half-life of *Nanog*, *Sox2*, *c-Myc*, and *Klf4* mRNA transcripts. This in turn impairs pluripotency and reprogramming [80].

Next, in 2018 Wen et al. found that another zinc-finger protein, *Zc3h13*, is critical for m⁶A deposition, and *Zc3h13* knockdown significantly impairs self-renewal and maintenance of

pluripotency in mESCs [81]. This study was based on the finding that Zc3h13 can form a complex with WTAP, Virilizer (Kiaa1429), and Hakai, which also contribute to the METTL3-METTL14 m⁶A methylation complex [82, 83]. Wen et al. then showed that Zc3h13 knockdown in mESCs decreases global m⁶A levels to about 30-40% of m⁶A levels in the control, and confirmed m⁶A dependency on Zc3h13 through MeRIP-seq. More specifically, Zc3h13 promotes m⁶A deposition by localizing the Zc3h13-WTAP-Virilizer-Hakai complex to nuclear speckles; loss of Zc3h13 causes these complex components, as well as Mettl3/Mettl14, to significantly shift to localization in the cytoplasm. Functionally, Zc3h13 knockdown impairs mESC self-renewal, decreases expression of pluripotency genes, and increases expression of differentiation markers in correlation with differential m⁶A modification of these gene transcripts [81]. The conclusion that m⁶A promotes self-renewal is consistent with previous studies [15], and the consequences on pluripotency correspond to studies performed under similar conditions in mESCs [6]. The two studies described here on zinc finger proteins are important examples of how m⁶A may be regulated or targeted to individual transcripts in stem cells. This connection between transcription factors and epitranscriptomic regulation remains an interesting avenue for further research.

In addition to individual transcription factors, Bertero et al. showed in 2018 that the TGF β signaling pathway contributes to m⁶A-mediated regulation of pluripotency in human pluripotent stem cells (hPSCs). Activin and NODAL are members of the TGF β signaling pathway that regulate cell fate decisions via downstream transcription factors SMAD2 and SMAD3 (SMAD2/3). Bertero et al. showed that SMAD2/3 interacts with the METTL3-METTL14-WTAP complex in hESCs and hiPSCs to increase methylation of SMAD2/3 target genes, and that this interaction is dependent on phosphorylation of SMAD2/3, which requires activin-NODAL signaling. Inhibition of activin-NODAL signaling decreases m⁶A levels, particularly in genes that are bound by SMAD2/3 and regulate stem cell exit from pluripotency (especially NANOG). In this study, m⁶A was found to promote degradation of modified transcripts to allow for rapid degradation of pluripotency genes, meaning it promotes the ability of hPSCs to rapidly differentiate upon receiving extracellular cues

[84]. This contrasts with the finding from Geula et al. that m⁶A promotes pluripotency in mESCs [6], but may also be caused by differences in human and mouse stem cells. Nonetheless, Bertero et al. provide the first example of how extracellular signaling can induce dynamic changes in m⁶A to regulate cell fate through the epitranscriptome.

Finally, a single study has found a direct connection between histone methylation and sites of m⁶A deposition. This 2019 study by Huang et al. showed that histone H3 trimethylation at lysine-36 (H3K36me3) drives m⁶A methylation by recruiting and promoting interactions between the m⁶A methyltransferase complex and its target mRNA. More specifically, METTL14 binds to H3K36Me3, chromatin, and RNA, thereby promoting co-transcriptional addition of m⁶A to genes with H3K36Me3 epigenetic marks. Knockdown of the H3K36Me3 methyltransferase, SETD2, impairs binding of the m⁶A methyltransferase complex to sites that lose H3K36Me3 and globally reduces m⁶A levels. In mESCs, SETD2 knockdown induces higher expression of pluripotency factors (OCT4, SOX2, NANOG) and prevents increased m⁶A methylation during differentiation. This suggests that H3K36Me3 drives m⁶A modification to destabilize pluripotency genes and promote differentiation, and loss of either H3K36Me3 or METTL14 promotes pluripotency over differentiation [85]. This corresponds with previous reports that m⁶A is necessary for proper differentiation of mESCs [6, 16], and provides the first evidence that m⁶A addition may be directed by epigenetic marks.

While a few studies have identified how the epitranscriptome may be regulated, over 100 putative METTL3 or METTL14 binding proteins have been identified, suggesting there is much left to be learned about upstream regulation of m⁶A [86]. Both a better understanding of how the methyltransferase complex and demethylases target specific gene transcripts and an understanding of how writer, reader, and eraser expression are regulated will drive the field forward.

IV. Epitranscriptomics in Neural Development:

Recent work has shown that the epitranscriptome, in particular m⁶A, is especially important for neural development and brain function. Lence et al. performed one of the first breakthrough studies of m⁶A in the brain, using *Drosophila melanogaster* as a model organism. This study showed that m⁶A is enriched in the nervous system and that knockout of the methyltransferase components causes reduced lifespan, severe behavioral defects, and global changes in neural gene expression [87]. While this work was important for understanding m⁶A in vivo, it contrasted with mammalian studies in that loss of m⁶A methyltransferases is not embryonic lethal in flies. The next major breakthrough came by conditional knockout of the m⁶A methyltransferase complex, which allowed for the study of the epitranscriptome in mammalian brain development. Below we provide an in-depth overview of the epitranscriptome in mammalian neural development.

Cortical Development

In 2017, our lab showed that conditional knockdown (cKO) of *Mettl14* in mice and subsequent loss of m⁶A in neural progenitor cells (NPCs) drastically impairs brain development in vivo. Loss of m⁶A impairs NPC differentiation, slows cell cycle progression, and elongates the timing of cortical neurogenesis into postnatal stages. Mechanistically, m⁶A-modified genes are significantly enriched for gene ontologies that correlate with regulation of transcription, neuron differentiation, cell cycle, and stem cell differentiation. These modified transcripts have a shorter half-life than their corresponding unmodified transcripts in *Mettl14* cKO mouse forebrains, suggesting that m⁶A normally destabilizes mRNA in the developing brain. By modifying both pluripotency and differentiation promoting transcripts, the m⁶A system allows for rapid changes in gene expression that are necessary for the harmonious progression of NPCs through the distinct phases of embryonic cortical neurogenesis. To this end, we found that *Mettl14* cKO NPCs co-express stem cell and neural markers, and that rapid degradation of neural markers in WT NPCs allow for pre-patterning of differentiation by allowing transcription of pro-neural genes but

preventing significant protein production. Finally, we used iPSC-derived human brain organoids to confirm that m⁶A also regulates NPC proliferation and differentiation in humans. We then compared m⁶A-seq analysis between human post-conception week 11 embryonic brain tissue and E13.5 mice. While many gene transcripts were m⁶A-modified in both species, the human-specific modifications correlated strongly with disease ontologies for human-specific mental disorders like autism and schizophrenia [88]. This work provided the first in vivo analysis of m⁶A in mammalian brain development and highlighted the possibility that m⁶A may contribute to psychiatric or neurodevelopmental disorders in humans.

Shortly thereafter, an independent study by Wang et al. knocked out *Mettl14* in the developing forebrain, and also found that loss of m⁶A slows NPC cell cycle progression. In vitro analysis of *Mettl14* cKO NPCs showed that loss of m⁶A can cause premature differentiation, and in vivo analysis showed that *Mettl14* cKO mice had reduced numbers of Pax6⁺ NPCs and reduced numbers of Satb2⁺ late-born neurons. This led the authors to suggest that depletion of the NPC pool causes a reduction in neurogenesis [89]. This contrasted with our study, which showed an increase in Pax6⁺ cells in *Mettl14* cKO forebrains, but a similar decrease in late-born neurons; we therefore proposed that m⁶A is necessary for the timely differentiation of NPCs, and loss of m⁶A causes a build-up of Pax6⁺ NPCs [88]. These differences may stem from different methodologies or antibodies. Nonetheless, the studies agree that m⁶A regulates mRNA stability to alter gene expression and NPC fate. Next, Wang et al. identified genome-wide changes in histone modifications upon *Mettl14* knockout. Specifically, cKO NPCs show increases in histone H3 acetylation at lysine 27 (H3K27ac), histone H3 trimethylation at lysine 4 (H3K4me3), and histone H3 trimethylation at lysine 27 (H3K27me3). Chemically blocking these epigenetic marks partially rescues cKO NPC proliferation defects. The changes in histone modification were partially attributed to m⁶A-mediated stability of CBP and p300 transcripts, which are stabilized upon loss of m⁶A. However, this did not apply to transcripts in the PRC2 complex, suggesting there are also other mechanisms at play [89]. Overall, the connection between the epitranscriptome and

epigenetics in the developing brain is highly intriguing. As single transcript m⁶A editing techniques are developed, it would be pertinent to edit only CBP and p300 mRNA to quantify the degree to which their methylation contributes to the Mettl14 cKO phenotype, as opposed to the sum of many modified transcripts.

Finally, a third study conditionally knocked out Ythdf2 in the developing forebrain to show that m⁶A largely functions through YTHDF2-mediated mRNA degradation during cortical development. In this study, Li et al. showed that Ythdf2 KO mice have a very similar phenotype to Mettl14 cKO mice. In particular, loss of Ythdf2 impairs NPC proliferation and differentiation, and causes delays in cortical neurogenesis. They also found that Ythdf2^{-/-} NPCs create fewer primary neurites per neuron and shorter neurites overall when differentiated in vitro, suggesting that m⁶A also regulates neuron maturation during the differentiation process [90]. This study was necessary to confirm that m⁶A regulation of cortical development functions primarily through YTHDF2-mediated mRNA degradation and that m⁶A promotes NPC proliferation and differentiation.

Cerebellar Development

The complexity of the brain suggests that epitranscriptomic regulatory systems may have distinct functions in different parts of the brain. Indeed, Chang et al. showed that m⁶A levels are increased in the adult mouse cerebellum compared to the cerebral cortex, and that there are region-specific methylation patterns [7]. Even within the cerebellum, methylation patterns change over developmental time. In 2018, Ma et al. showed that methylation targets change across postnatal day 7 (P7), P14, P21, and P60 mouse cerebella. There are 12,452 m⁶A peaks that are turned “ON” (emerge at a later stage) over time, and 11,192 that are turned “OFF” (disappear in later stages). The groups of transcripts methylated at each timepoint correspond with the developmental processes happening at that time. For example, gene transcripts in which m⁶A is turned OFF from P7 to P14 have gene ontologies enriched for cell cycle. On the other hand, gene transcripts in which m⁶A is turned ON at P14, P21, or P60 have gene ontologies enriched for signal transduction, cell

adhesion, learning, and synaptic plasticity. Overall, m⁶A modification patterns strongly correlate with the progression from proliferating cells at P7 to mature neuronal activities at P60. This study also examined changes in expression of METTL3, METTL14, WTAP, FTO, AND ALKBH5. Though cerebellar expression of all of these genes decreased on average over time, there was a specific reduction in internal granular layers but elevated expression in Purkinje cells. Lentiviral Mettl3 knockdown at P7 lowers the number of Purkinje cells and impairs their organization along the outer surface of the inner granule cell layer. On the other hand, Alkbh5-KO mice had no observable phenotype in the cerebellum under normal conditions, which may be due to redundant action by FTO. After stressing the developing brain with hypobaric hypoxia, Alkbh5-KO mice had significantly smaller cerebella and fewer mature neurons, yet significantly more proliferating cells. This suggests that ALKBH5 is critical for promoting cerebellar neurogenesis under stress. Finally, this study showed that several important gene transcripts are differentially localized in the cytoplasm over nucleus in Alkbh5-KO cerebella, indicating that m⁶A promotes nuclear export in this tissue [24].

In contrast, Wang et al. used a Mettl3 cKO mouse model to show that m⁶A promotes mRNA degradation and alternative splicing in the cerebellum. Mettl3 cKO mice have drastically smaller cerebella, significantly fewer cerebellar granule cells (CGCs) in the internal granular layer (IGL), and disordered Purkinje cell organization relative to WT controls. Furthermore, loss of m⁶A causes significantly increased levels of apoptosis of newborn granule cells, which explains the depletion of CGCs. Again, loss of m⁶A increases mRNA stability; m⁶A modification on apoptosis-associated gene transcripts normally restricts their expression. Notably, m⁶A-mediated regulation of apoptosis appears to be specific to the cerebellum, as these transcripts are not stabilized in the cortex of Mettl3 cKO mice. Finally, Wang et al. identified an additional mechanism of m⁶A-mediated alternative splicing in the cerebellum. Exon exclusion occurs more frequently upon m⁶A depletion, especially in transcripts that are normally methylated in the WT. These alternatively spliced transcripts are enriched for gene ontologies in synapse-associated pathways and

neurotransmitter receptors. Further analysis showed that increases in intracellular calcium concentration in *Mettl3* cKO CGCs contributes to their increased apoptosis [91]. This work highlights the fact that epitranscriptomics regulation is highly cell-type specific with unique roles in different parts of the brain. How this specificity is regulated will be an interesting avenue of future research.

Adult neurogenesis

The m⁶A demethylase FTO has been implicated in numerous pathways in the mature brain, from cancer [92] to psychiatric and neurodegenerative diseases [93-97] to regulation of adult neural stem cells [98, 99]. However, understanding the role of FTO remains difficult due to its multiple functions in DNA and RNA demethylation. In fact, the first study on FTO in neurogenesis was published in 2010, before FTO was even identified as an m⁶A demethylase [18, 98]. In 2010, Gao et al. generated whole-body and neural-specific *Fto* KO mice, and found that the two have very similar phenotypes, indicating that the majority of FTO function occurs in the nervous system [98]. In 2017, Li*, Zang*, Zhang* et al. showed that FTO is expressed in adult NSCs (aNSCs) and in mature neurons and increases over postnatal time. *Fto* KO mice show reduced proliferation and aNSC differentiation, which functionally impairs learning and memory. Furthermore, loss of FTO results in slightly higher (~15%) levels of m⁶A, though only 363 genes are both m⁶A modified and differentially expressed upon loss of FTO (out of 5635 m⁶A-modified genes and 1862 FTO-dependent genes) [99]. While FTO does seem to regulate adult neurogenesis, the degree to which this is enacted through m⁶A remains in question, especially considering FTO can act on multiple targets in vivo.

Next, Chen et al. found that *Mettl3* knockdown impairs both proliferation and differentiation of aNSCs cultured in vitro. m⁶A sequencing showed that the m⁶A landscape is dynamic between proliferating and differentiating cultured aNSCs; transcripts modified only in proliferating aNSCs correlate with cell cycle, while transcripts modified only in differentiating

aNSCs are enriched for protein localization, signaling, and synapse organization [100]. This study is slightly more direct in studying m⁶A in adult neurogenesis by knocking down *Mettl3*, but the use of cultured aNSCs limits the conclusions that can be drawn; aNSCs exist in highly specialized niches in vivo that are difficult to recapitulate in vitro [101, 102].

Finally, a 2019 study by Cao*, Zhuang* et al. found that *Fto* cKO in aNSCs decreases aNSC proliferation and differentiation into NeuN⁺ neurons at 4 weeks after FTO knockout. While the fate of m⁶A-modified transcripts was not tested, individual mRNA transcripts in the Stat3 signaling pathway, *Socs5* and *Pdgfra*, were shown to play important roles in FTO-mediated regulation of aNSCs. However, *Socs5* mRNA and protein decrease in *Fto* cKO aNSCs, while *Pdgfra* mRNA and protein increase [23]. Therefore, the involvement of m⁶A and mechanisms of m⁶A-mediated regulation in aNSC remain unclear. In multiple studies, effects of *Fto* or *Mettl3* KD appear stronger in in vitro cultured cells than in vivo aNSCs. The highly dynamic nature of m⁶A in response to signaling and stress stimuli suggest that culturing systems need to be incredibly carefully controlled to maintain an accurate representation of the epitranscriptome in in vivo aNSCs.

V. Epitranscriptomics in Neurodevelopmental Disease:

In accordance with its powerful role in neural development, m⁶A has been linked to neurodevelopmental defects as well. To date, m⁶A in Fragile X Syndrome is the best-characterized interaction. Additionally, emerging genome-wide association studies and human genetics studies have linked mutations in epitranscriptomic enzymes with intellectual disability.

Fragile X Syndrome

Fragile X mental retardation protein (FMRP), encoded by *FMR1*, is an RNA-binding protein that is best known for negatively regulating the translation of its target mRNAs [103, 104]

and trafficking mRNA granules [105]. Loss-of-function mutations in FMR1 cause Fragile X Syndrome, which is marked by intellectual disability and delayed development. In 2017, Arguello et al. identified FMRP as an m⁶A binding protein in vitro [106]. Zhang et al. then showed that FMRP target genes are enriched for m⁶A marks in the mouse cerebral cortex, and that FMRP binding to m⁶A-modified mRNAs followed by interaction with YTHDF2 promotes degradation of FMRP target genes [107]. Next, Edens et al. showed that FMRP promotes nuclear export of m⁶A-modified mRNA by interaction with the CRM1 nuclear export protein. Additionally, Fmr1 KO mice phenocopy Mettl14 cKO mice in terms of delayed neurogenesis and impaired NPC proliferation. In both of these mouse models, FMRP target mRNAs are retained in the nucleus [108]. The binding affinity of FMRP for m⁶A-modified mRNA and role in nuclear export was recently confirmed by Hsu et al [109].

Intellectual Disability

Four recent studies identified correlations between epitranscriptomic modifications and intellectual disability. First, Shaheen et al. found that mutations in human PUS3, a pseudouridylation enzyme, correlates with intellectual disability and microcephaly in three affected siblings. The affected individuals also have a significant reduction in Ψ-modified tRNA relative to healthy controls in purified lymphoblastoid cells. The PUS3 deficiency phenotype in humans is largely brain-specific, suggesting that PUS3-mediated tRNA Ψ modification is especially important for cognitive function [110].

Next, both de Brouwer et al. and Shaheen et al. identified mutations in PUS7, a tRNA and mRNA pseudouridylation enzyme, that cause intellectual disability, microcephaly, speech delay, and aggressive behavior [111, 112]. Ψ at position 13 in tRNA and PUS7 target mRNAs were significantly reduced in affected individuals compared to healthy controls. Additionally, Pus7 knockout in *Drosophila* recapitulates the cognitive impairment phenotype and the molecular loss of Ψ at particular target sites [111]. This provides exciting evidence that Ψ modification of mRNA

and tRNA is not only highly conserved across species, but is critical in neural development. Additional studies using mouse models to disseminate the exact mechanism of Ψ in neural development will be an exciting next step.

Finally, Richard et al. identified frameshift mutations in METTL5, which putatively adds m⁶A to 18S rRNA [113], that cause autosomal-recessive intellectual disability and microcephaly. METTL5 is expressed in the human brain from early development and into adulthood, particularly in the cerebellar cortex, hippocampus, and striatum. Analysis in rodents confirmed ubiquitous METTL5 expression in the brain, with increased staining in neural soma and nuclei, as well as in pre- and post-synaptic regions. Finally, mettl5 knockout in zebrafish recapitulates the microcephaly phenotype and specifically causes decreases in forebrain and midbrain size [114]. While METTL5 methyltransferase action and specificity are not well characterized, this genetic evidence suggests that it is yet another epitranscriptomics modifier that is crucial for proper brain development.

VI. Concluding Remarks and Future Outlook:

The field of epitranscriptomics has reached a point where the power of various mRNA modifications has become widely accepted, but the specific mechanisms of their action remain under debate. It is becoming increasingly important to perform extremely careful experiments to detect and validate epitranscriptomics marks to prevent further confusion regarding their downstream functions. Furthermore, expression of multiple reader proteins and multiple published functions of m⁶A in a single cell type suggest that m⁶A may differentially regulate various gene transcripts within a single cell. Several important strategies to further elucidate the regulatory capacities of m⁶A in stem cells and neural development include (1) improved detection techniques for higher sensitivity and accuracy, (2) studies on how reader proteins selectively bind a subset of m⁶A-modified mRNAs, and (3) considerate analysis of data to prevent over-drawing conclusions that will hinder future studies.

In addition to clarifying studies on m⁶A, we are especially excited by the prospects of other epitranscriptomics marks in neural development and disease. Careful mapping of m¹A, m⁵C, m⁷G, m⁶A_m, and Ψ in the brain alongside generating animal knockouts of their respective modifying enzymes will greatly expand the breadth of knowledge in the field of epitranscriptomics. With an increasing number of scientists working in this field, we expect the next five years to be full of new discoveries with profound impacts in basic and translational science.

VII. FIGURES

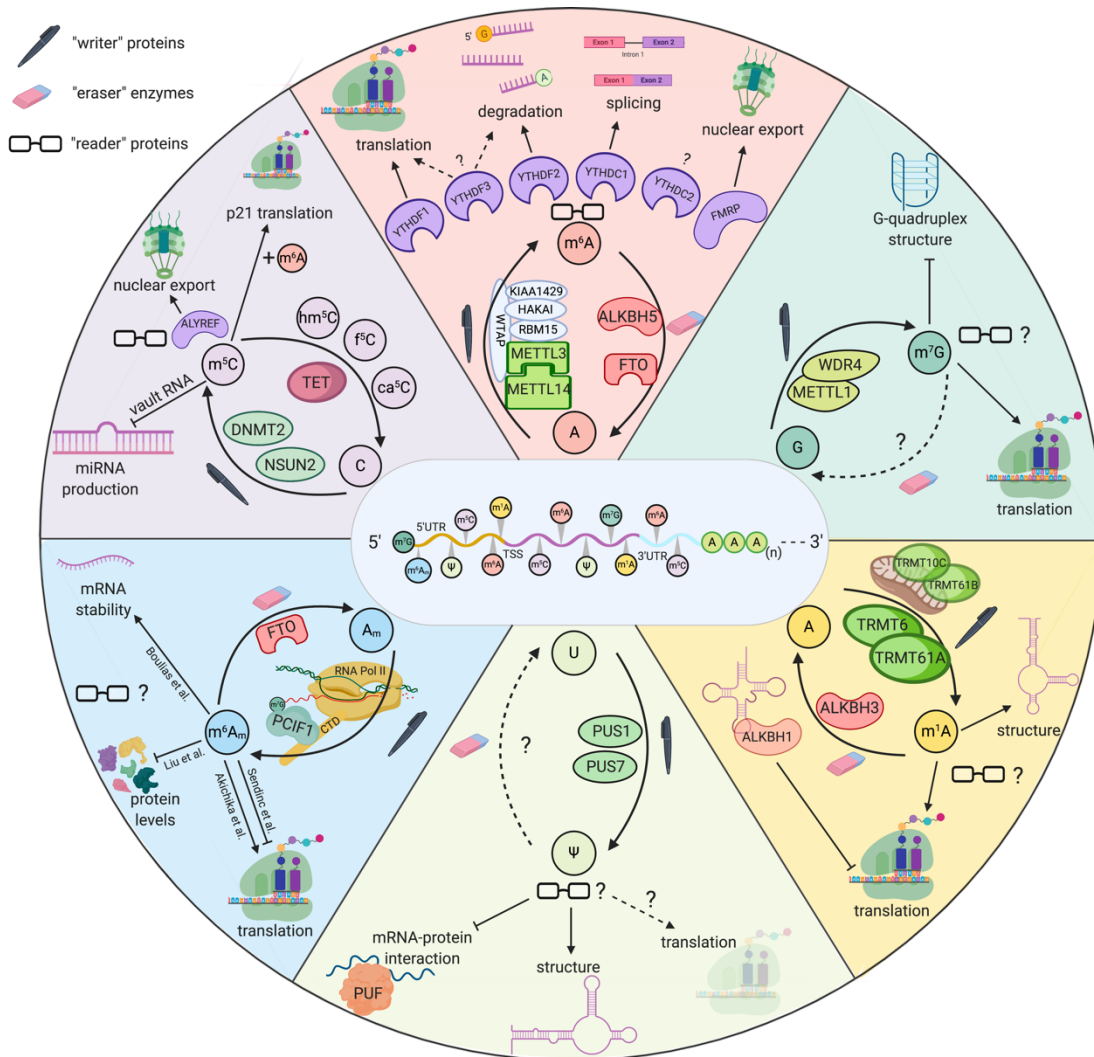


Figure 1: Summary of the most-studied epitranscriptomic modifications. This includes m⁶A (top center, pink), m⁷G (top right, green), m¹A (bottom right, yellow), Ψ (bottom center, lime), m⁶A_m (bottom left, blue), and m⁵C (top left, purple). Each panel shows the known methyltransferase components and demethylases, as well as any known reader proteins and functions of the epitranscriptomic mark.

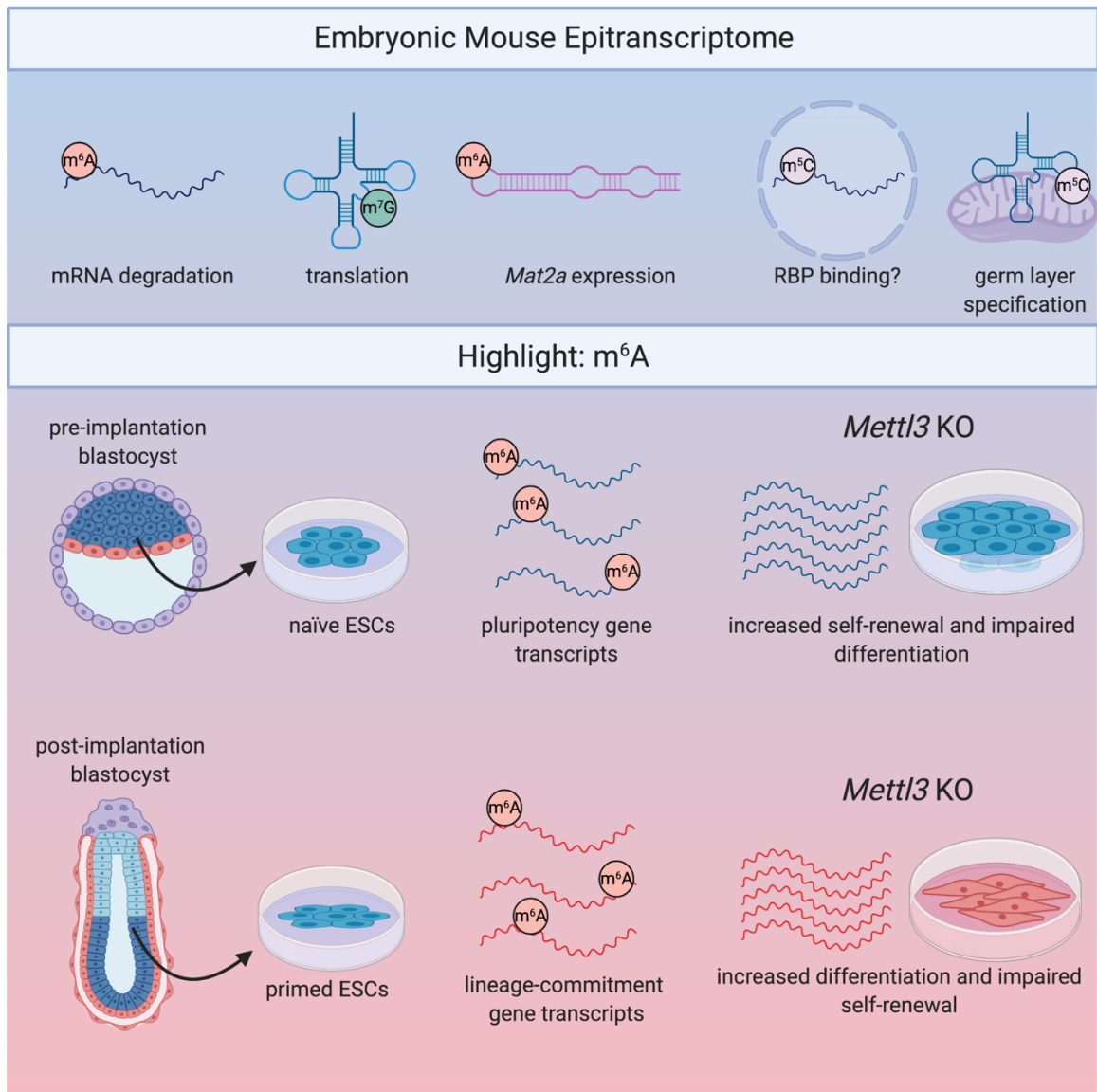


Figure 2: Summary of epitranscriptomic marks in embryonic stem cell biology. Top: known modifications identified in mouse embryonic stem cells (ESCs) include m⁶A on mRNA, m⁷G on tRNA, m⁶A on snRNA, m⁵C on nuclear mRNA, and m⁵C on mitochondrial tRNA. Bottom: Multiple studies showed that m⁶A promotes mRNA degradation in ESCs. In naïve ESCs, pluripotency-promoting gene transcripts are m⁶A modified. In primed ESCs, lineage-commitment gene transcripts are modified. Knocking out *Mettl3* stabilizes these different sets of gene transcripts at different developmental timepoints, causing opposite effects on naïve vs primed ESCs fate.

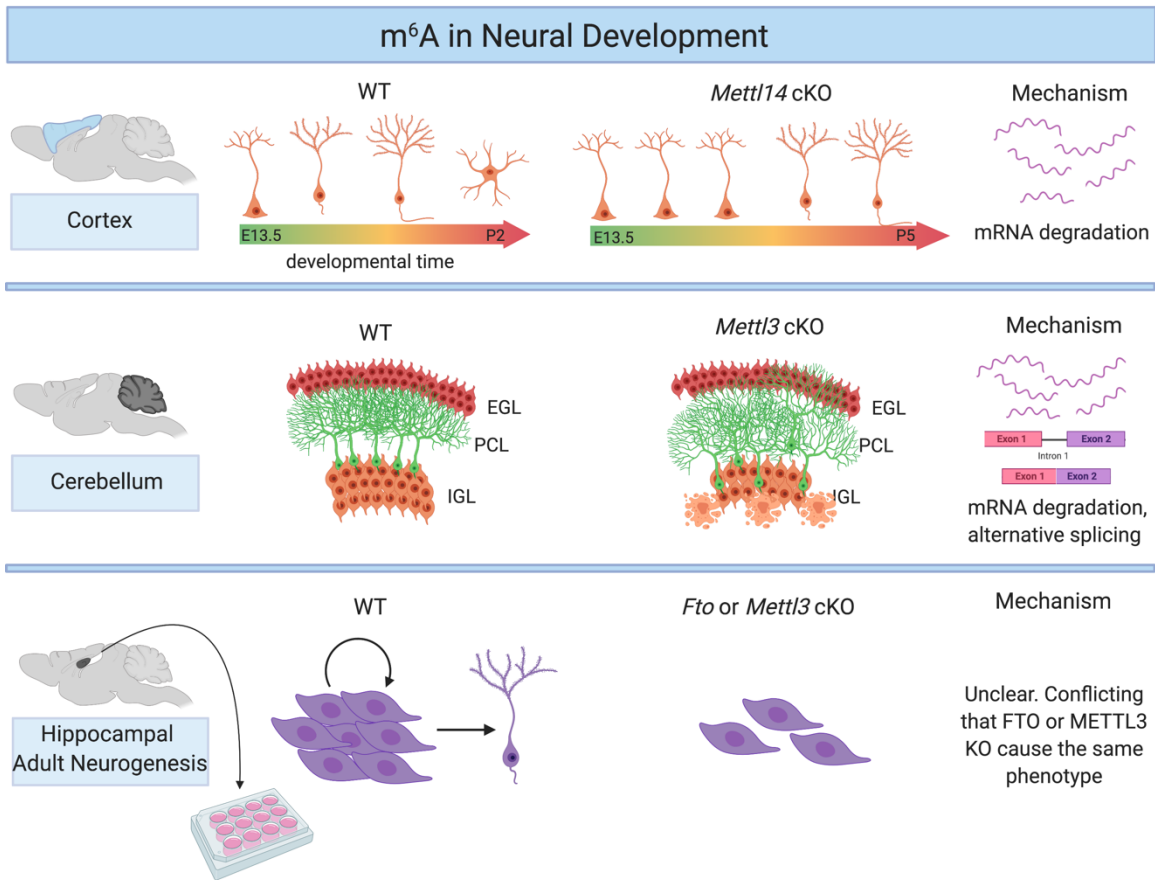


Figure 3: m⁶A in neural development. Top: m⁶A in cortical development regulates the progression of neurogenesis over developmental time by promoting mRNA degradation of key gene transcripts. Middle: m⁶A in cerebellar development regulates inner granule layer (IGL) neuron organization and apoptosis and Purkinje cell layer (PCL) organization, but does not seem to effect external granule layer (ECL) organization. m⁶A promotes mRNA degradation and alternative splicing. Bottom: in vitro adult neurogenesis studies show that knockdown of either the demethylase *Fto* or the methyltransferase *Mettl3* impairs adult neural stem cell proliferation and differentiation.

Chapter 2

Temporal Control of Mammalian Cortical Neurogenesis by m⁶A Methylation

Foreword: This work stemmed from my first two years of graduate school and was performed entirely in the lab of Hongjun Song. We initially tried to generate brain-specific *Mettl14* conditional knockout mice in order to study adult neurogenesis, but found that even conditional knockout mice died before reaching adulthood. We therefore shifted our focus to the role of m⁶A in the developing brain and were excited by the drastic phenotype of *Mettl14* cKO mice. This work was published in *Cell* (PMCID: PMC5679435) and I am a co-first author.

Temporal Control of Mammalian Cortical Neurogenesis by m⁶A Methylation

Ki-Jun Yoon^{1,2,3*}, Francisca Rojas Ringeling^{4*}, Caroline Vissers^{5*}, Fadi Jacob⁶, Michael Pokrass⁷,
Dennisse Jimenez-Cyrus⁸, Yijing Su¹, Nam-Shik Kim^{1,2}, Yunhua Zhu², Lily Zheng⁴, Sunghan
Kim², Xinyuan Wang¹, Peng Jin⁹, Xiaoxi Zhuang¹⁰, Sergi Regot⁷, Stefan Canzar¹¹, Chuan He¹²,
Guo-li Ming^{1,2,3,5,6,7,10,13#}, and Hongjun Song^{1,2,3,4,5,6,7,8,13,14#}

¹Department of Neuroscience and Mahoney Institute for Neurosciences,

²Institute for Cell Engineering, ³Department of Neurology, ⁴The Pre-doctoral Human Genetic Training Program, ⁵The Biochemistry, Cellular and Molecular Biology Graduate Program, ⁶The Solomon H. Snyder Department of Neuroscience, ⁷Department of Molecular Biology and Genomics, ⁸The Cellular and Molecular Medicine Graduate Program, ⁹Department of Human Genetics, School of Medicine, Emory University, Atlanta, GA 30322, USA, ¹⁰Department of Psychiatry and Behavioral Sciences, Johns Hopkins University School of Medicine, Baltimore, MD 21205, USA, ¹¹Gene Center, Ludwig-Maximilians-Universität München, 81377 Munich, Germany, ¹²Department of Chemistry, Institute for Biophysical Dynamics, Howard Hughes Medical Institute, University of Chicago, Chicago, IL 60637, USA, ¹³The Institute for Regenerative Medicine, ¹⁴The Epigenetics Institute, Perelman School for Medicine, University of Pennsylvania, Philadelphia, PA 19104, USA.

*These authors contributed equally to this work.

#co-corresponding authors

Lead contact: Hongjun Song (shongjun@mail.med.upenn.edu)

I. SUMMARY

N⁶-methyladenosine (m⁶A), installed by the Mettl3/Mettl14 methyltransferase complex, is the most prevalent internal mRNA modification. Whether m⁶A regulates mammalian brain development is unknown. Here we show that *Mettl14* deletion in the embryonic mouse brain diminishes m⁶A content, prolongs cell cycle progression of radial glia cells, and extends cortical neurogenesis into postnatal stages. *Mettl3* knockdown also prolongs neural progenitor cell cycle and promotes radial glia cell maintenance. m⁶A-sequencing of the embryonic mouse cortex reveals enrichment of mRNAs related to transcription factors, neurogenesis, cell cycle and neuronal differentiation, and m⁶A-tagging promotes their decay. Notably, *Mettl14*^{-/-} radial glia cells precociously express neuronal proteins. Further analysis uncovers previously unappreciated transcriptional pre-patterning in cortical neural stem cells. Comparison of m⁶A-mRNA landscapes between mouse and human cortical neurogenesis reveals enrichment of human-specific m⁶A-tagging of transcripts related to brain disorder risk genes. Our study identifies an epitranscriptomic mechanism in heightened transcriptional coordination during mammalian cortical neurogenesis.

HIGHLIGHTS

- m⁶A depletion leads to prolonged cell cycle progression of cortical neural progenitors
- m⁶A promotes decay of transcripts related to cell cycle, neurogenesis, and neuronal differentiation in neural progenitors
- *Mettl14* deletion uncovers transcriptional pre-patterning for normal cortical neurogenesis
- m⁶A-seq reveals conserved and unique m⁶A mRNA methylation landscapes in mouse and human cortical neurogenesis.

II. INTRODUCTION

Proper development of the nervous system is critical for its function, and deficits in neural development have been implicated in many brain disorders, such as microcephaly, autistic spectrum disorders, and schizophrenia [115-117]. In the embryonic mouse cortex, radial glia cells (RGCs) function as neural stem cells, sequentially giving rise to neurons residing in different cortical layers and then switching to glial production before their depletion during early postnatal stages [116, 118]. Such a precise and predictable developmental schedule requires a highly coordinated genetic program [119]. Indeed, previous studies have revealed transcriptional cascades that orchestrate the dynamics of mammalian cortical neurogenesis [120-127]. Recent discoveries of widespread mRNA chemical modifications [128, 129] raise the question of whether this mechanism plays any regulatory role in cortical neurogenesis.

Modified nucleotides in mRNAs were initially discovered over 40 years ago, but little was known about the extent, transcript identities, and potential functions of various reversible chemical modifications until very recently [128, 129]. High-throughput sequencing approaches have revealed a dynamic “epitranscriptome” landscape for many mRNA modifications in various organisms, including N⁶-methyladenosine (m⁶A), N¹-methyladenosine (m¹A), 5-methylcytosine (m⁵C), 5-hydroxymethylcytosine (hm⁵C), pseudouridine (Ψ), and 2'-O-methylnucleotides [62]. Among these modifications, m⁶A is the most abundant internal modification in mRNAs of eukaryotic cells [130]. m⁶A profiling has so far mostly been performed with cell lines and bulk tissues due to the need for a substantial amount of input mRNAs. These studies revealed m⁶A sites in over 25% of human transcripts, with enrichment in long exons, and near transcription start sites and stop codons [1, 2, 131, 132]. In mammals, m⁶A is installed by the methyltransferase complex consisting of Mettl3 (methyltransferase-like 3), Mettl14, Wtap (Wilms tumor 1-associated protein), KIAA1429, RBM15 (RNA-binding motif protein 15) and its paralogue (RBM15B) [11], whereas its removal is mediated by demethylases Fto (fat mass and obesity-associated) and Alkbh5 (alkB homolog 5) [129, 133]. Recent in vitro studies have identified multiple functions of m⁶A in mRNA

metabolism, from processing in the nucleus to translation and decay in the cytoplasm [129]. The field has just started to investigate physiological functions of m⁶A. For example, *Mettl3* or *Mettl14* knockdown reduces m⁶A levels and decreases self-renewal of primed mouse embryonic stem cells (mESCs) [15], whereas *Mettl3* knockout naïve mESCs exhibit improved self-renewal and impaired differentiation, due to dysregulated decay of m⁶A-tagged transcripts, such as *Nanog* [6, 16].

Identification of the molecular machinery mediating m⁶A mRNA methylation provides an entry point to explore physiological functions of this pathway in vivo. Studies of *Drosophila* development showed that m⁶A methylation regulates sex determination and neuronal functions by modulating mRNA splicing [134, 135]. In Zebrafish embryos, m⁶A-tagging promotes clearance of maternal mRNAs and maternal-to-zygotic transition [136]. In mice, germline *Mettl3* deletion results in early embryonic lethality [6]. The function of m⁶A methylation in the intact mammalian system remains elusive; almost nothing is known about its role in mammalian embryonic brain development. Here we used the *Mettl14* conditional knockout mouse as a model to examine m⁶A function in embryonic cortical neurogenesis in vivo. We further investigated underlying cellular and molecular mechanisms of how m⁶A tagged transcripts are processed. Finally, we extended our analysis to human embryonic cortical neurogenesis using induced pluripotent stem cell (iPSC)-derived forebrain organoids and compared m⁶A-mRNA landscapes between mouse and human cortical neurogenesis. Together, our results reveal critical epitranscriptomic control of mammalian cortical neurogenesis and provide novel insight into mechanisms underlying this highly coordinated developmental program.

III. RESULTS

Nervous system *Mettl14* deletion extends cortical neurogenesis into postnatal stages

We first investigated the expression pattern of molecular players mediating m⁶A signaling during mouse embryonic cortical neurogenesis. Mining the recently published single-cell RNA-seq dataset of RGCs and their progeny [127] revealed that *Mettl14* exhibits the highest expression in RGCs,

whereas other m⁶A methyltransferase components (Mettl3, Wtap), demethylases (Fto, Alkbh5) and m⁶A readers (Ythdf2, Ythdf3) exhibited relatively constant levels during neurogenesis (Figure S1A). To examine the functional role of m⁶A methylation during cortical development in vivo, we conditionally deleted Mettl14 in the developing mouse nervous system using the Nestin-Cre;Mettl14^{fl/fl} conditional knockout (cKO) model (Figure S1B). We confirmed Mettl14 deletion at the protein level with Western blot analysis of E17.5 brains (Figure S1B). The cKO animals were smaller in size by P5 compared to wildtype (WT) littermates, and all cKO animals died before P25 (Figure S1C-D). Thus, the function of m⁶A molecular machinery in the nervous system is indispensable for life in the mammalian system.

We next examined cortical structures at P5. cKO mice exhibited enlarged ventricles with an adjacent dense layer of cells that resembled the embryonic germinal zone (Figure 1A). Immunohistological analysis showed the presence of Pax6⁺ and Nestin⁺ cells with radial fibers along the ventricle in cKO mice, but not in WT mice (Figure 1A-B). During mouse cortical development, Pax6⁺ RGCs are largely depleted by P5 [137]. In contrast, a substantial number of Pax6⁺ cells were present in cKO mice at P5 (Figure 1C). Neurogenic Pax6⁺ RGCs give rise to intermediate progenitor cells (IPCs) expressing Tbr2/Eomes [138]. The presence of Pax6⁺ cells in cKO mice was accompanied by Tbr2⁺ IPCs, which were absent in WT mice by P5 (Figure 1D-E). To confirm that cortical neurogenesis continued postnatally, we pulsed animals with EdU at P5 and analyzed 2 days later. Significant numbers of EdU⁺Pax6⁺ proliferating RGCs, EdU⁺Tbr2⁺ IPCs, and EdU⁺Tbr2⁺TuJ1⁺ neuroblasts were present in cKO mice, but very few in WT littermates (Figure 1F-G). These results indicate that cKO mice maintain neurogenic RGCs with extended cortical neurogenesis into postnatal stages.

To further characterize the impact of Mettl14 deletion on cortical development, we examined neuronal subtype and glia production. We pulsed animals with EdU at E15.5 and examined them at P5. Compared to WT littermates, cKO mice exhibited a significantly decreased

number of EdU⁺Satb2⁺ neurons, suggesting a deficit in producing late-born upper-layer neurons (Figure 1H-I). Direct measurement of the number of different cortical neuron subtypes also showed a reduced number of Satb2⁺ upper-layer neurons, but comparable numbers of Tbr1⁺ and Ctip2/Bcl11b⁺ lower-layer early-born neurons in P5 cKO mice (Figure S1E-F). On the other hand, analysis of Ctip2⁺ neurons at E17.5 showed reduced numbers in cKO mice, suggesting a delay in the production of neuron subtypes of different cortical layers, rather than differentiation deficits (Figure S1G-H). In addition, we observed a significant decrease in the number of s100 β ⁺ astrocytes in cKO mice at P5 (Figure 1J-K). Together, these results indicate that Mettl14 function is critical for proper temporal progression of neurogenesis and gliogenesis during mouse cortical development in vivo.

Mettl14 deletion in neural progenitor cells leads to protracted cell cycle progression

Given the well-defined temporal progression of cortical neurogenesis from RGCs [119], we suspected that there could be RGC deficits during embryonic stages in cKO mice. Interkinetic nuclear migration (INM), the periodic movement of the cell nucleus in phase with cell-cycle progression, is a common feature of developing neuroepithelia [116, 139]. We pulsed animals with EdU at E17.5 to label cells in S-phase and followed positions of nuclei in EdU⁺Pax6⁺ RGCs (Figure 2A). While there was no difference at 0.5 hr after EdU labeling, nuclei of labeled RGCs were positioned further away from the ventricular surface at 6 hr in cKO mice compared to WT (Figure 2B), suggesting delayed INM and potential cell cycle deficits. To directly examine the S to M phase transition of the cell cycle, we analyzed expression of phospho-Histone 3 (pH3), an M phase marker, 2 hr after EdU labeling (Figure 2C). We found a significant decrease in the percentage of EdU⁺pH3⁺Pax6⁺ cells among all pH3⁺Pax6⁺ cells in cKO mice, suggesting a prolonged S to M phase transition of RGCs (Figure 2D). To examine cell cycle exit of proliferating neural progenitors, we analyzed expression of Ki67, a proliferation marker, 24 hr after EdU labeling

(Figure 2E). We found a significant decrease in the percentage of Ki67 negative cells among EdU⁺ cells in cKO mice, indicating a delay in cell cycle exit (Figure 2F).

To address the cell intrinsic effect of Mettl14 deletion on cell cycle progression, we performed time-lapse imaging of individual cortical neural progenitor cells (NPCs) cultured from E13.5 mouse cortex. We used a dual reporter system with nuclear localized H2B-mCherry and a GFP-tagged Cdk2 substrate, DNA Helicase B (DHB) [140]. Cdk2 becomes active during the G₁-S transition and phosphorylates DHB-GFP, which is then translocated from nucleus to cytoplasm. Therefore, the presence of GFP in the mCherry⁺ nucleus indicates cells in G₁ phase, whereas translocation to the cytoplasm indicates S phase initiation, and continual buildup of cytoplasmic GFP occurs until mitosis (Figure S2A). Quantification of the length between sequential mitoses showed an increase of the total cell cycle length in Mettl14 cKO NPCs (Figure 2G-H; Movie S1 and S2). Further analysis of different cell cycle phases revealed a specific increase of the S-G₂-M phases in the absence of Mettl14, but no difference in the G₁ phase (Figure 2I-J).

To quantify cell cycle characteristics at the population level, we pulsed NPCs with EdU for 30 min and performed flow cytometry analysis 0 or 5 hr later (Figure S2B). We found a significant decrease in the percentage of EdU⁺ cells that divided in Mettl14 cKO NPCs compared to WT at 5 hr, confirming a delay in cell cycle progression (Figure S2C-D).

Mettl3 regulates embryonic cortical neurogenesis

Consistent with the finding that Mettl14 is a critical component of the m⁶A methyltransferase complex [141], Mettl14 deletion led to a significant reduction of m⁶A levels in mRNAs from both embryonic mouse cortex in vivo and cultured cortical NPCs (Figure 3A-B). To further assess our model that m⁶A methylation regulates cortical neurogenesis, we compared the phenotype of Mettl14 cKO to knockdown of Mettl3, another critical component of the m⁶A methyltransferase complex [141].

We first confirmed effective Mettl3 knockdown (KD) with Q-PCR and diminished m⁶A content in mRNAs from Mettl3 KD cells with dot blot analysis (Figure S3A-C and Table S1). We next performed population cell cycle analysis with EdU pulse-chase and flow cytometer quantification (Figure S3D). We found a significant reduction in the percentage of GFP⁺EdU⁺ NPCs that divided upon Mettl3 KD (Figure 3C-D), similar to the effect of Mettl14 cKO (Figure S2C-D).

To examine the impact of Mettl3 KD on RGC behavior in vivo, we electroporated plasmids co-expressing GFP and the shRNA against mouse Mettl3, or the control shRNA, in utero at E13.5 and analyzed GFP⁺ cells at E17.5. Newborn neurons normally migrate toward the cortical plate (CP) through the intermediate zone (IZ), whereas self-renewing RGCs remain in the ventricular zone (VZ) and subventricular zone (SVZ) [116]. Compared to the control group, GFP⁺ cells with Mettl3 KD were more abundant in the VZ and SVZ and less abundant in the CP (Figure 3E-F), similar to the result from EdU fate mapping in Mettl14 cKO mice (Figure 1H). There was also a significant increase in the percentage of GFP⁺Pax6⁺ cells among all GFP⁺ cells with Mettl3 KD compared to the control group (Figure 3G).

Together, these results indicate that decreasing m⁶A levels by either Mettl14 cKO or Mettl3 KD leads to consistent phenotypes of protracted cell cycle progression of cortical NPCs and reduced differentiation of RGCs during mouse embryonic cortical neurogenesis.

m⁶A tags transcripts related to transcription factors, cell cycle, and neurogenesis, and promotes their decay

To gain insight into the molecular mechanism underlying m⁶A regulation of cortical neurogenesis, we performed m⁶A-seq of mouse forebrain at E13.5, a stage enriched for neural stem cells. We identified 4,055 high confidence m⁶A peaks corresponding to 2,059 gene transcripts (Figure S4A and Table S2). Similar to previous findings from cell lines [1, 2, 131, 132], our in vivo analysis showed enriched distribution of m⁶A sites near stop codons (Figure S4B). We found no correlation

between transcript levels and m⁶A-tagging (Figure S4C). Notably, many transcripts encoding transcription factors were m⁶A-tagged, such as Pax6, Sox1, Sox2, Emx2, and Neurog2/ Neurogenin 2 (Figure 4A-B). Gene ontology (GO) and Wikipathways analyses of m⁶A-tagged transcripts revealed enrichment of genes related to cell cycle, stem cell, and neuronal differentiation (Figure 4A-C and Table S3). We observed similar m⁶A-tagging for a group of transcripts in cortical NPCs derived from E13.5 mouse cortex (Figure S4D and Table S1).

To determine the functional consequence of m⁶A-tagging on mRNAs, we explored whether Mettl14 deletion affects decay of m⁶A-tagged transcripts with an RNA stability assay [6, 71]. Cortical NPCs derived from E13.5 WT and Mettl14 cKO mice were treated with Actinomycin D to halt de novo transcription, and RNA-seq was performed 0 and 5 hr later to obtain the ratio of mRNA levels for each gene in order to measure their stability (Figure S4E). Across the transcriptomes, m⁶A-tagged transcripts exhibited significantly lower stability compared to non m⁶A-tagged transcripts in the WT NPCs, and this difference was reduced in cKO NPCs (Figure 4D and Table S4). Direct comparison of WT and Mettl14 cKO NPCs showed that m⁶A-tagged transcripts exhibited a larger increase in their stability compared to non-tagged transcripts upon Mettl14 deletion; one m⁶A tag per transcript was sufficient to increase stability and there was a minimal additional effect of more tagging sites (Figure 4E). It should be noted that our m⁶A-seq method could not determine whether multiple sites are simultaneously methylated in the same transcript. We confirmed our result with the direct measurement of the half-life of a selected group of transcripts (Figure 4F and S4F; Table S1).

All together, these results support a model that m⁶A methylation of mRNAs related to cell cycle and neurogenesis confers their rapid turnover during the dynamic progress of cortical neurogenesis; a lack of m⁶A-tagging attenuates the decay of these mRNAs, resulting in deficits in temporal specification and cell cycle progression of NPCs.

Mettl14 deletion uncovers transcriptional pre-patterning for normal cortical neurogenesis

Among the 2,059 m⁶A-tagged genes in the E13.5 mouse cortex, two major GO terms were generation of neurons and neuronal differentiation (Figure 4C). For example, IPC marker *Tbr2* and *Neurog2*, and neuronal markers *Neurod1* and *Neurod2* [142], were m⁶A-tagged in E13.5 forebrain in vivo (Figure 5A) and in cultured cortical NPCs (Figure S4D). Q-PCR analysis of total mRNA showed increased levels of *Tbr2*, *Neurog2*, *Neurod1*, and *Neurod2*, but not non tagged *Rad17*, in *Mettl14* cKO NPCs compared to WT NPCs (Figure 5B and Table S1). This result raised the possibility that neuronal lineage genes are already expressed in neural stem cells and their levels are actively suppressed post-transcriptionally by m⁶A-dependent decay; alternatively, *Mettl14* deletion may transcriptionally upregulate these neuronal genes.

To differentiate between these two possibilities, we quantified the levels of nascent mRNA using the metabolic labeling approach with 4-thiouridine (4sU) [143, 144]. We found comparable and even lower levels of nascent mRNA of neuronal lineage genes, such as *Tbr2*, *Neurog2*, and *Neurod2*, in *Mettl14*^{-/-} NPCs in comparison to WT NPCs (Figure 5B and Table S1). The lower levels of nascent mRNA observed for some neuronal lineage genes in *Mettl14* cKO NPCs could be explained by a negative feedback loop at the level of transcription, originating from elevated expression of stem cell genes, such as *Emx2* and *Sox1* (Figure 5B). Similarly, we found comparable levels of pre-mRNA for neuronal lineage genes in *Mettl14* cKO compared to WT NPCs (Figure S5A and Table S1), suggesting that the increase in the total mRNA of neuronal lineage genes in *Mettl14* cKO NPCs is not due to transcriptional upregulation. Together, these results support that neuronal lineage genes are already expressed in neural stem cells under normal cortical neurogenesis. Consistent with our result, mining the published single-cell RNA-seq dataset [127] revealed expression of neuronal lineage genes, such as *Tbr2*, *Neurog2*, *Neurod6* and *Tubb3/Tuj1*, in individual RGCs in the embryonic mouse cortex in vivo (Figure S5B).

We next examined *Tbr2* and *Neurod1* protein levels in RGCs in vivo. *Pax6*⁺*Tbr2*⁺ cells were localized in the SVZ in WT at E17.5, but extended into the VZ in *Mettl14* cKO mice (Figure 5C-D). *Pax6*⁺*Neurod1*⁺ cells were rare, but detectable just above the SVZ in WT cortices. In

contrast, cKO mice exhibited a significantly increased number of Pax6⁺Neurod1⁺ cells with a much broader distribution, including in the SVZ and VZ (Figure 5E-F). To specifically examine expression in RGCs, we pulse-labeled juxtaventricular newborn cells by FlashTag (FT) [127]. We found a significantly increased number of FT⁺Pax6⁺Tbr2⁺ and FT⁺Pax6⁺Neurod1⁺ cells in Mettl14 cKO cortex compared to those in WT 3 hr after labeling (Figure S5C-D). Given that FT⁺ cells at 3 hr upon labeling are exclusively undifferentiated RGCs [127], these results suggest that Mettl14 regulates neuronal lineage gene expression directly in RGCs.

To further assess our model that mRNA decay regulates neuronal lineage gene expression in RGCs, we performed in vivo knockdown experiments for the components of CCR4-NOT complex (Cnot7 and Cnot1), a major cytoplasmic mRNA deadenylase complex responsible for mRNA decay [145, 146]. Both Cnot7 KD and Cnot1 KD led to increased numbers of Tbr2⁺Pax6⁺ and Neurod1⁺Pax6⁺ cells and location closer to the ventricular surface compared to the control shRNA (Figure S5E-F), phenotypes resembling Mettl14 cKO (Figure 5C-F).

Taken together, our results suggest heightened transcriptional coordination and a previously unappreciated transcriptional pre-patterning mechanism for mammalian cortical neurogenesis, in which late IPC and neuronal genes are already transcribed in cortical neural stem cells and these transcripts are down regulated post-transcriptionally by m⁶A-dependent decay.

METTL14 regulates cell cycle progression of human cortical NPCs

We next examined whether m⁶A function is conserved in human cortical neurogenesis. Using a previously developed protocol [147], we differentiated human iPSCs into a highly pure population of NESTIN⁺SOX2⁺ NPCs (hNPCs; 96.4 ± 1% among all cells; n = 5; Figure S6A). We co-expressed GFP and the validated shRNA against human METTL14 in these hNPCs (Figure S6B). After 4 days, we labeled cells with EdU for 30 min and performed cell cycle analysis with flow cytometer quantification 14 hr later (Figure S6C). Similar to results from mouse Mettl14 cKO NPCs

(Figure S2C-D), we found a significant decrease in the percentage of GFP⁺EdU⁺ hNPCs that divided with METTL14 KD, indicating a delayed cell cycle progression (Figure 6A-B).

We recently developed a human iPSC-derived forebrain organoid model, which exhibits transcriptome profiles similar to fetal human cortex during development up to the second trimester [148]. Around day 47, these forebrain organoids resemble mouse cortical neurogenesis at E13.5 (Figure S6D). We microinjected plasmids co-expressing GFP and the shRNA against human METTL14, or the control shRNA, into the lumen of forebrain organoids and performed electroporation to transfect RGCs (Figure S6E). After 7 days, we pulsed organoids with EdU for 1 hr and performed cell cycle analysis of GFP⁺ cells 14 hr later (Figure S6F). Similar to findings from monolayer hNPC cultures, we observed a significant decrease in the percentage of GFP⁺EdU⁺ cells that divided with METTL14 KD (Figure 6C-D). Together, these results indicate that m⁶A mRNA methylation plays a conserved role in regulating cortical NPC cell cycle progression in both mouse and human.

m⁶A-seq of human forebrain brain organoids and fetal brain reveals conserved and unique m⁶A landscape features compared to embryonic mouse forebrain

Finally, we performed m⁶A-seq of day 47 human forebrain organoids. We detected 11,994 high confidence m⁶A peaks associated with 4,702 transcripts (Figure S7A and Table S5). Our previous systematic RNA-seq analyses of human forebrain organoids at different stages revealed that transcriptomes of organoids around day 47 were similar to human fetal cortex at 8-12 post-conception weeks (PCW) [148]. We further performed m⁶A-seq of PCW11 fetal human brain and identified 10,980 high confidence peaks associated with 5,049 transcripts (Figure S7B and Table S6). m⁶A sites were enriched near transcription start sites and stop codons for both human samples (Figure S7C-D). Furthermore, m⁶A profiles from both samples showed significant overlap (Figure 7B). GO analysis of m⁶A-tagged transcripts shared in both samples showed enrichment of genes related to neurogenesis, neuronal differentiation and development (Figure 7C and Table S7). Many

recently identified risk genes for schizophrenia and autistic spectrum disorders have been shown to be dynamically expressed and play critical roles during mammalian embryonic brain development [149, 150]. Interestingly, disease ontology analysis of these m⁶A-tagged genes shared in both human samples showed enrichment related to mental disorders, mental retardation, schizophrenia and bipolar disorder (Figure 7C and Table S7).

We further performed comparison among m⁶A landscapes during mouse and human cortical neurogenesis. About 19.3%, 34.7% and 31.4% of detected transcripts exhibited m⁶A-tagging in E13.5 mouse brain, day 47 human forebrain organoids, and PCW11 human fetal brain, respectively (Figure S7E). Therefore, m⁶A mRNA methylation appears to be more prevalent in human. Among transcripts expressed in all three samples, 856 genes were commonly m⁶A-tagged (Figure 7D). These commonly m⁶A-tagged transcripts are enriched for genes related to neurogenesis and neuronal differentiation (Figure S7F and Table S7). Notably, 1,173 transcripts were expressed in both species, but only m⁶A-tagged in both human samples (Figure 7D). Ontology analysis of these human-specific m⁶A-tagged transcripts showed enrichment of genes related to mental disorders and mental retardation (Figure 7E-F and Table S7). In contrast, analysis of the gene set of m⁶A-tagged transcripts shared between mouse and human showed enrichment for oncogenic processes (Figure 7E). Notably, among genes associated with the 108 loci recently identified for genetic risk of schizophrenia [151], 60 genes were m⁶A-tagged in human and 21 genes were uniquely tagged in both human forebrain organoids and fetal brain, but not in mouse E13.5 forebrain.

IV. DISCUSSION

From flies to mammals, neurogenesis is a highly coordinated process with sequential waves of gene expression [152]. Here we revealed a critical role of m⁶A mRNA methylation in this process in the mammalian system in vivo. Our results suggest a model that m⁶A-tagging of transcripts related to neural stem cells, cell cycle, and neuronal differentiation confers their rapid turnover to control the

transcriptome composition at different phases of the dynamic cortical neurogenesis process. The observation of RGCs expressing markers thought to be expressed only in late IPCs and post-mitotic neurons in *Mettl14* cKO mice led to the discovery of transcriptional pre-patterning in normal cortical neurogenesis and identifies m⁶A mRNA methylation as a key mechanism to prevent precocious expression of genes of later lineage status at the protein level in stem cells. We also provide the emerging “epitranscriptomic” field with databases of m⁶A mRNA landscapes of mouse and human cortical neurogenesis and identify intriguing human-specific features.

Transcriptional pre-patterning for cortical neurogenesis

The concept of pre-patterning initially came from analysis of chromatin states within multipotent progenitors to regulate the fate choice for liver and pancreas [153]. Recent genome-wide mapping studies have suggested that epigenetic pre-patterning is important for spatio-temporal regulation of gene expression and may be a widespread phenomenon in cell fate decision [154]. Our study suggests, for the first time, transcriptional pre-patterning in normal cortical neural stem cells *in vivo*. Consistent with our model, *Pax6* has been shown to bind and activate both *Tbr2* and *Neurod1* promoters [155]. We showed that pre-patterned transcripts are tagged with m⁶A and subjected to rapid decay, therefore most of them are present in low levels among the bulk mRNA preparation and little protein under normal conditions – a likely reason why such a mechanism has escaped detection in previous studies. While epigenetic mechanisms play a key role in transcriptional regulation during neurogenesis [156, 157], epitranscriptomic regulation as a post-transcriptional mechanism could provide the speed and additional specificity, while maintaining plasticity of gene expression. By working in concert, the epigenetic landscape can permit transcription of certain genes, such as genes defining late lineage states, while the epitranscriptome prevents aberrant protein production. Future studies are needed to investigate whether transcriptional pre-patterning is a general mechanism in fate specification of other stem cells during development.

Heightened transcriptional coordination of mammalian cortical neurogenesis by m⁶A

Our study provides the first in vivo evidence in the mammalian system to support the emerging notion that m⁶A methylation plays a critical role in developmental fate transition. The precise and predictable developmental schedule of cortical neurogenesis requires rapid, tightly controlled changes in gene expression [119]. Our results suggest that epitranscriptomic m⁶A-tagging, via regulation of mRNA decay, provides a key mechanism for temporal control of dynamic gene expression, which in turn regulates cell cycle progression of cortical neural stem cells in both mouse and human.

There are three major categories of m⁶A-tagged transcripts in the embryonic mouse brain. First, many classic transcription factors involved in neural stem cell maintenance and neurogenesis, such as Pax6, Sox2, Emx2, and Tbr2, are m⁶A-tagged and subject to rapid decay. Second, cell cycle-related transcripts, such as Cdk9, Ccnh/Cyclin H, and Cdkn1C/p57, are m⁶A-tagged. Functionally, the loss of m⁶A-tagging leads to prolonged cell cycle progression of cortical NPCs, resulting in delayed generation of different neuronal subtypes, extension of cortical neurogenesis into postnatal stages and deficits in astrocyte generation in vivo. Third, transcripts that were generally thought to be expressed only in later IPCs and post-mitotic neurons, such as Neurod1 and Neurod2, are m⁶A-tagged and expressed in neural stem cells. While expression of transcription factors is known to overlap during different stages of mammalian cortical neurogenesis [142], our finding suggests a greater degree of transcriptional coordination than previously thought. On the other hand, expression of detectable neuronal proteins in a significant number of RGCs located in the SVZ in the absence of Mettl14 highlights the critical role of the epitranscriptomic mechanism in preventing precocious gene expression during the normal process of mammalian cortical neurogenesis.

Conserved and unique features of human m⁶A landscape during cortical neurogenesis

Our study provides databases of m⁶A mRNA landscapes during mouse and human cortical neurogenesis. Consistent with a similar role for m⁶A mRNA methylation in regulating cell cycle progression of cultured human NPCs and mouse NPCs in vitro and in vivo, the shared m⁶A-tagged transcripts in our mouse and human samples are enriched with genes related to neural stem cells, cell cycle, and neurogenesis. Notably, many genes associated with genetic risk for mental disorders, such as schizophrenia and autistic spectrum disorders, are only m⁶A-tagged in humans, but not in mice, raising the possibility that epitranscriptomic dysregulation may contribute to these human brain disorders. So far, one association study found evidence of ALKBH5 in conferring genetic risk for major depression disorder [158], and two studies identified association of FTO mutations with growth retardation and developmental delay [159, 160].

In summary, our study identifies a critical and conserved role of an m⁶A epitranscriptomic mechanism in the temporal control of mammalian cortical neurogenesis via promotion of mRNA decay of transcripts related to transcription factors, neural stem cells, cell cycle, and neuronal differentiation. Future studies will address how this epitranscriptomic mechanism interacts with various epigenetic mechanisms to coordinate dynamic transcriptomes during brain development, and how dysregulation of epitranscriptomic mechanisms may contribute to brain disorders.

V. STAR METHODS

KEY RESOURCE TABLE

CONTACT FOR REAGENT AND RESOURCE SHARING

Further information and requests for resources and reagents should be directed to and will be fulfilled by the Lead Contact Hongjun Song (shongjun@mail.med.upenn.edu). There are no restrictions on any data or materials presented in this paper.

EXPERIMENTAL MODEL AND SUBJECT DETAILS

Animals

Exons 7, 8, and 9 of mouse *Mettl14* were targeted by inserting a single loxP site in intron 6 and an FRT-flanked neomycin resistance gene coupled with a loxP site in intron 9, with the consideration that they contain the DPWW active motif (Figure S1B). The targeting construct was electroporated into 129 mESCs, selected for neomycin resistance, screened for homologous recombination by Southern blotting, and selected mESC clones were used to generate chimeric mice by injection into C57BL/6J mouse blastocysts. Chimeric mice were bred to wild type C57BL/6J mice to test for germline transmission of the mutant allele, which was identified by PCR. The PCR-positive lines were crossed with a α -actin promoter-driven Flp recombinase to remove the neomycin resistance gene via FRT site recombination. The neomycin cassette-deleted mice were identified by PCR, and the resultant *Mettl14^{f/f}* allele and Nestin-Cre^{+Tg} mice (Jackson Laboratory stock: 003771) [161] were used to generate Nestin-Cre^{+Tg}; *Mettl14^{+/f}* mice and Nestin-Cre^{+/+}; *Mettl14^{f/f}* mice. WT and cKO mice were generated by crossing Nestin-Cre^{+Tg}; *Mettl14^{+/f}* males and Nestin-Cre^{+/+}; *Mettl14^{f/f}* females.

For in utero electroporation analysis, timed-pregnant CD1 mice (Charles River Laboratory) at E13.5 were used as previously described [147]. Timed pregnant mice were euthanized by cervical dislocation, and embryos were euthanized by decapitation before the dissection step. All

animal procedures used in this study were performed in accordance with the protocol approved by the Institutional Animal Care and Use Committee of Johns Hopkins University School of Medicine.

Primary mouse NPCs

Mouse NPCs were isolated from *Mettl14* WT and cKO mouse embryonic cortices and cultured in Neurobasal medium (Gibco BRL) containing 20 ng/ml FGF2, 20 ng/ml EGF, 5 mg/ml heparin, 2% B27 (v/v, Gibco BRL), Glutamax (Invitrogen), Penicillin/Streptomycin (Invitrogen) on culture dishes pre-coated with Matrigel matrix (2%, Corning).

Human iPSC cultures and fetal brain sample

The human iPSC line used in the current study (C1) was fully characterized [147, 162]. iPSCs were cultured in stem cell medium, consisting of DMEM:F12 (Invitrogen) supplemented with 20% Knockout Serum Replacer (Gibco), 1X Non-essential Amino Acids (Invitrogen), 1X Penicillin/Streptomycin (Invitrogen), 1X 2-Mercaptoethanol (Millipore), 1X Glutamax (Invitrogen), and 10 ng/ml FGF-2 (Peprotech). Culture medium was changed every day. Human iPSCs were passaged every week onto a new plate pre-seeded with irradiated CF1 mouse embryonic fibroblasts (Charles River Laboratory). Human iPSCs were detached from the plate by treatment of 1 mg/ml Collagenase Type IV (Invitrogen) for 1 hr. iPSC colonies were further dissociated into smaller pieces by manual pipetting. All studies were performed under approved protocols of Johns Hopkins University School of Medicine. Human iPSCs were differentiated into primitive hNPCs according to a previously published protocol (Li et al., 2011). Briefly, iPSCs were passaged onto MEF feeders, and after 3 days, induction medium containing Advanced DMEM:F12 (50%) and Neurobasal medium (50%), CHIR99201 (4 μ M, Cellagentech), SB431542 (3 μ M, Cellagentech), Bovine serum albumin (5 μ g/ml, Sigma), hLIF (10 ng/ml, Millipore), Compound E (0.1 μ M, EMD Millipore), Glutamax (Invitrogen), Pen/Strep, supplemented with N2 and B27 (Invitrogen), was added to the culture. After 6 days of differentiation, hNPCs were dissociated with

Accutase (Invitrogen) and plated, with the aid of a ROCK inhibitor (Y-27632, 3 μ M, Cellagentech), onto culture dishes pre-coated with Matrigel matrix (2%, Corning).

The PCW11 fetal human cortical tissue was used for m⁶A-seq. All procedures used in this study were performed in accordance with the protocol approved by the Institutional Stem Cell Research Oversight Committee of Johns Hopkins University School of Medicine and Lieber Institute for Brain Development.

METHOD DETAILS

DNA constructs

For knockdown experiments for mouse genes, short hairpin RNA sequences (see KEY RESOURCE TABLE) were cloned into the retroviral vector expressing GFP under the control of the EF1a promoter and a specific shRNA under the control of human U6 promoter (pUEG) as previously described [163]. For knockdown experiments for human METTL14, a short hairpin RNA sequence was cloned into the lentiviral vector expressing GFP under the control of the human ubiquitin C promoter and the specific shRNA under the control of human U6 promoter (cFUGW: Addgene plasmid 14883) as previously described [147]. The efficacy of each shRNA was confirmed in mouse B16-F10 cells (ATCC), or hNPCs derived from the C1 iPSC line.

In utero electroporation and FlashTag

In utero electroporation was performed as described previously [147]. In brief, timed-pregnant CD1 mice (Charles River Laboratory) at E13.5 or E14.5 were anesthetized and the uterine horns were exposed and approximately 1 to 2 μ l of plasmid DNA, 0.5 μ g/ μ l pCAG-GFP (Addgene plasmid: 11150) and 2.5 μ g/ μ l cFUGW plasmid with the control shRNA, or the shRNA against mouse Mettl3, Cnot1 and Cnot7, was injected manually into the lateral ventricles of embryos using a calibrated micropipette. Five pulses (40 V, 50 ms in duration with a 950 ms interval) were delivered across the uterus with two 5-mm electrode paddles (CUY650-5, Nepa Gene) positioned on either

side of the head by a square wave electroporator (CUY21SC, Nepa Gene). After electroporation, the uterus was placed back in the abdominal cavity and the wound was sutured. Mouse embryos were analyzed at E17.5. For FlashTag of RGCs, 1 μ l of 10 μ M of a carboxyfluorescein succinimidyl ester (CellTrace CFSE, ThermoFisher) was injected into the lateral ventricle of the E17.5 embryos using a calibrated micropipette. Mouse embryos were collected 3 hr later, fixed with with 4% paraformaldehyde in PBS overnight at 4°C for analysis. All animal procedures were performed in accordance with the protocol approved by the Johns Hopkins Institutional Animal Care and Use Committee.

Immunohistology and confocal imaging

For EdU labeling, timed pregnant mice were injected with EdU (150 mg/kg bodyweight, Invitrogen) at defined time points before euthanasia. For immunostaining of tissue sections, brains were fixed with 4% paraformaldehyde in PBS overnight at 4°C as previously described [147]. Samples were cryoprotected in 30% sucrose in PBS, embedded in OCT compound, and sectioned coronally (20 μ m-thickness) on a Leica CM3050S cryostat. Brain sections were blocked and permeabilized with the blocking solution (5% normal donkey serum, 3% Bovine serum albumin, and 0.1% Triton X-100 in PBS) for 1 hr at room temperature, followed by incubation with primary antibodies diluted in the blocking solution at 4°C overnight. After washing, secondary antibodies diluted in blocking solution were applied to the sections for 1 hr at room temperature. Nuclei were visualized by incubating for 10 min with 0.1 μ g/ml 4,6-diamidino-2-phenylindole (DAPI, Thermo Fisher Scientific) in PBS. For EdU labeling, Click-iT EdU Alexa Fluor 647 Imaging Kit (Thermo Fisher Scientific) was used following the manufacturer's protocol. Stained sections were mounted with ProLong Gold anti-fade reagents (Thermo Fisher Scientific) and analyzed. All the antibodies used are listed in KEY RESOURCE TABLE.

Mouse and human NPC electroporation

Approximately 1.0×10^6 mouse or human NPCs were resuspended in 100 μ L Mouse Neural Stem Cell Nucleofector Solution from the Lonza Nucleofector Kit for Mouse Neural Stem Cells (Lonza, VAPG-1004). Additionally, 10 μ g of the appropriate plasmid was added to the cell solution. The solution was then placed in a cuvette provided in the Nucleofector Kit and electroporated using a Lonza Nucleofector 2b device (LONZA). Next, the cells were resuspended in NPC media as described above with Rock Inhibitor (Y-27632, 3 μ M, Cellagentech) to reduce cell death. Cells were allowed to grow for at least 3 days before analysis.

Human forebrain organoid culture

Protocols for generation of forebrain organoids were detailed previously [148]. Briefly, human iPSCs were cultured in stem cell medium, consisting of DMEM:F12 (Invitrogen) supplemented with 20% Knockout Serum Replacer (Gibco), 1X Non-essential Amino Acids (Invitrogen), 1X Penicillin/Streptomycin (Invitrogen), 1X 2-Mercaptoethanol (Millipore), 1X Glutamax (Invitrogen), and 10 ng/ml FGF-2 (Peprotech) on irradiated CF1 mouse embryonic fibroblasts (Charles River). On day 1, iPSC colonies were detached by treatment of 1 mg/ml Collagenase Type IV (Invitrogen) for 1 hr and transferred to an Ultra-Low attachment 6-well plate (Corning Costar), containing 3 ml of stem cell medium (without FGF-2), plus 2 μ M Dorsomorphine (Sigma) and 2 μ M A83-01 (Tocris). On days 5-6, half of the medium was replaced with induction medium consisting of DMEM:F12, 1X N2 Supplement (Invitrogen), 1X Penicillin/Streptomycin, 1X Non-essential Amino Acids, 1X Glutamax, 1 μ M CHIR99021 (Cellagentech), and 1 μ M SB-431542 (Cellagentech). On day 7, organoids were embedded in Matrigel (Corning) and continued to grow in induction medium for 6 more days. On day 14, embedded organoids were mechanically dissociated from Matrigel and transferred to each well of a 12-well spinning bioreactor (Spin Ω) containing differentiation medium, consisting of DMEM:F12, 1X N2 and B27 Supplements

(Invitrogen), 1X Penicillin/Streptomycin, 1X 2-Mercaptoethanol, 1X Non-essential Amino Acids, 2.5 µg/ml Insulin (Sigma).

Forebrain organoid electroporation and analysis

Day 45 forebrain organoids were transferred into PBS solution in a 10 cm petri dish for electroporation. A mixture of 0.5 µl of plasmid DNA and 0.05% Fast green was injected into the lumen of neural tube structures in forebrain organoids using a calibrated micropipette. About 3-4 locations on one side of each forebrain organoid were targeted by the injection. The DNA-injected side of the organoid was placed toward the positive electrode in the middle of 5 mm gap of electrode paddles (CUY650-5, Nepa Gene). Five pulses (40 V, 50 ms in duration with a 950 ms interval) were delivered by a square wave electroporator (CUY21SC, Nepa Gene). After electroporation, organoids were transferred back to the SpinΩ bioreactor for further culturing.

Analysis of cell cycle progression by EdU pulse labeling

Analyses of cell cycle progression of mouse NPCs, hNPCs, and dissociated human forebrain organoids were performed as described previously [164, 165]. In brief, mouse or human NPCs were pulsed by 10 µM EdU (ThermoFisher) for 30 min and washed thoroughly with NPC media. For human forebrain organoids, 10 µM EdU directly applied to culture media and organoids were incubated in the SpinΩ bioreactor for 1 hr to ensure complete penetrance, then washed thoroughly with culture media. After defined time points, cells were dissociated by Accutase, fixed with 4% paraformaldehyde in PBS for 20 min at 4°C, stained with Click-iT EdU Alexa 647 Flow Cytometry Kits (ThermoFisher) for Flow Cytometry following manufacturer's protocol. Cells were stained with Vybrant DyeCycle Violet (ThermoFisher) or 7-AAD (ThermoFisher) for DNA content and applied to flow cytometry using BD LSR II Flow Cytometer (BD Bioscience). EdU⁺ or GFP⁺EdU⁺ cells were gated and DNA content of those cells was analyzed compared to that of whole cell population. Percentages of divided cells among EdU⁺ or GFP⁺EdU⁺ population (G₁ or G₀ phase

determined by DNA content) during defined time intervals were quantified from four independent experiments.

Time-lapse live imaging of mouse NPCs

96-well glass bottom microplates (655892, Geiner bio-one) were coated with phenol red-free Matrigel (356237, Corning). After electroporation of mNPCs with 10 μ g CDK2-sensor plasmid (pPGK-H2B-mCherry-DHB(aa994-1087)-GFP), cells were plated onto the microplates at a density of 3,000 cells per well and allowed to adhere overnight. Cells were imaged using a Nikon Eclipse Ti fluorescent microscope controlled by Metamorph microscopy automation software. Temperature (37°C), CO₂ (5%), and humidity were held constant throughout experiments. Five blank positions in a well containing Matrigel and media only were used to flat field mNPC images using custom software. ImageJ was used to merge the green and red channels. To quantify the total cell cycle length, time was measured from the first cell division to the next cell division of one or both daughters. To quantify the G₁ phase length, time was measured from one cell division to the time point of significant reduction in the ratio of green/red intensity in the nucleus of the cell. S phase entry was quantitatively defined as the time when the cytoplasmic/nuclear ratio of green/red was approximately 1, as previously described [140]. A nuclear marker, H2B-mCherry, was used in the plasmid sensor to accurately segment the cytoplasm and the nucleus. The time point from S phase entry through the second cell division was then quantified as S-G₂-M length.

RNA purification and quantitative RT-PCR analysis

For gene expression analysis, total RNA fraction was isolated from cultured NPC samples with RNeasy Mini Kit (Qiagen), treated with DNaseI and reverse-transcribed into the first-strand cDNA with SuperScript III (Invitrogen). cDNAs were used for SYBR-green based quantitative real-time PCR to measure the expression level of target genes with the T method (ABI). All the primers used for quantitative PCR were listed in Table S1.

Western blot analysis

Forebrains from E17.5 embryos were quickly dissected out and homogenized in RIPA buffer (50 mM Tris pH 7.5, 120 mM NaCl, 1% Triton X-100, 0.5% Sodium Deoxycholate, 0.1% SDS, 5 mM EDTA, Phosphatase Inhibitor Cocktail (Cell Signaling), protease inhibitor cocktail (Sigma). Lysates were incubated for 15 min on ice and centrifuged at 15,000g for 15 min at 4°C. Supernatant was collected and boiled for 5 min in Laemmli sample buffer (Biorad), resolved by SDS PAGE, transferred to PVDF membrane, and immunoblotted. Primary antibodies are listed in KEY RESOURCE TABLE. Quantification of bands was performed using ImageJ software.

m⁶A dot blot assay

mRNA was harvested from homogenized forebrains at embryonic stages E15.5 and E17.5 using Dynabeads mRNA Direct Purification Kit (61011, Ambion). Four biological replicates were pooled for each sample to ensure sufficient concentration of mRNA. Dots were applied to an Amersham Hybond-N⁺ membrane (GE Healthcare) in duplicate as 100 ng mRNA per 1 µl dot. After complete drying, the mRNA was crosslinked to the membrane using a UV Stratalinker 2400 by running the auto-crosslink program twice. The membrane was then washed in PBST three times and blocked with 5% skim milk in PBST for 2 hr. The PBST wash was repeated and the membrane was incubated with primary anti-m⁶A antibody (212B11, Synaptic Systems) at 1:1000 dilution for 2 hr at room temperature. After 3 washes in PBST, the membrane was incubated in HRP-conjugated anti-mouse IgG secondary antibody for 2 hr at room temperature, then washed again 3 times in PBST. Finally, the membrane was visualized using SuperSignal West Dura Extended Duration Substrate (34075, Thermo Scientific). To confirm equal mRNA loading, the membrane was stained with 0.02% methylene blue in 0.3 M sodium acetate (pH 5.2) and quantified m⁶A levels were normalized to amount of mRNA loaded. Four biological samples in technical duplicates for each time point were used.

m⁶A-sequencing

m⁶A profiling was performed as previously described [2]. For m⁶A profiling of mouse developing brain, forebrains from WT E13.5 embryos were dissected. For m⁶A profiling of human organoids, 25 to 30 forebrain organoids at day 47 were used. For m⁶A profiling of PCW11 fetal human brain, cortex from 2 PCW11 fetuses were dissected. The total RNA was extracted using RNeasy Mini Kit (Qiagen). mRNA was isolated using the Dynabeads mRNA Purification Kit (Invitrogen) and mRNA was fragmented via sonication to 100-200 base pairs. m⁶A pull-down was performed using a rabbit polyclonal anti-m⁶A antibody (Synaptic systems), and immunoprecipitation with protein G dynabeads (ThermoFisher). m⁶A-tagged mRNAs were competitively eluted from beads with free N⁶-methyladenosine. cDNA libraries from pulled-down RNA and input RNA were prepared using the NEBNext® Ultra™ DNA Library Prep Kit for Illumina®. The experiment was performed with three technical replicates. For m⁶A profiling of day 47 human forebrain organoids, the same procedure was followed, with the exception that the experiment was performed with two technical replicates because of the amount of samples required.

m⁶A mRNA immunoprecipitation and q-PCR

Total RNA from NPCs cultured from WT E13.5 mouse forebrain was extracted using RNeasy Mini Kit (Qiagen) and mRNA was isolated using the Dynabeads mRNA Purification Kit (Invitrogen). 1% of input mRNA was reserved for reverse transcription. Full length m⁶A tagged transcripts were pulled-down using a rabbit polyclonal anti-m⁶A antibody (Synaptic systems) and a mock pull-down was done with normal rabbit IgG (Cell Signaling Technologies). Immunoprecipitation was performed with protein G dynabeads (Thermo Fisher). m⁶A-tagged mRNAs were competitively eluted from beads with free N⁶-methyladenosine. Reverse transcription of input, m⁶A pull-down and mock pull-down mRNA was performed using the SuperScript® III First-Strand Synthesis System for RT-PCR (Thermo Fisher). cDNA was used for SYBR-green based quantitative real-

time PCR. Enrichment of m⁶A tagged genes in m⁶A pull-down over input was calculated by comparing relative concentrations using Ct values (2^{-Ct}) and dividing each concentration by the relative concentration of the input. The concentrations of the immunoprecipitated RNA were then divided by the concentration in the input RNA and multiplied by 100, to obtain the percentage of transcripts in the m⁶A immunoprecipitation relative to the input. This value was then normalized to enrichment in the mock (IgG) pull-down, which was also calculated using relative concentrations to determine a percentage of the input. Primers used are listed in Table S1.

Bioinformatic analyses of m⁶A-seq

cDNA libraries from input and m⁶A pull-down were sequenced on the Illumina Nextseq platform, using a 50-cycle single-end run. Pre-processing of reads was performed using the FASTX toolkit (http://hannonlab.cshl.edu/fastx_toolkit/), namely adapters were clipped, poor quality reads were filtered out, and identical reads were collapsed. Pre-processed reads from E13.5 mouse forebrains were aligned to the mouse genome (build GRCm38/mm10), and reads from the human organoids and fetal brain to the human genome (build GRCh37/hg19), using Tophat2 [166] with default settings. m⁶A-tagged regions were identified using the MACS2 peak calling algorithm [167], with the input library as background. For identifying high confidence m⁶A regions, peaks were intersected in a pairwise fashion among all replicates using the BedTools package [168]. Peaks that overlap in at least 50% of their length among 2 or more samples were designated as high confidence m⁶A regions.

For representative coverage plots of m⁶A and input libraries, RNA-seq read alignments in bam format were transformed to bedGraph format and normalized for library size using the genomecov function from the BedTools package [168]. Analysis of m⁶A peak enrichment was performed based on 5 non-overlapping transcript segments defined as follows: Transcription start site (TSS) segment [TSS, TSS+200bp], 5'UTR [TSS+201bp, CDS start-1bp], coding region (CDS) [CDS start, CDS stop-101bp], stop codon segment [CDS stop-100bp, CDS stop+100bp], 3' UTR

[CDS stop+101bp, TTS]. Each high confidence peak was annotated to one of these regions using the BedTools package and fold enrichment was calculated from the ratio between observed peaks per region and expected number of peaks normalized by average region size. For analysis of correlation between gene expression levels and m⁶A peak fold change, we calculated RPKMs from input RNA seq libraries, using gene counts obtained with the htseq-count function from the HTSeq python package [169] that were normalized by library size and gene length defined as the length of its longest transcript. Fold changes for m⁶A peaks were obtained from MACS2 output.

Functional annotation and disease ontology

To assess enrichment of GO terms specific to a biological process, the ToppFunn module of the ToppGene Suite [170] was used. A hypergeometric probability mass function with Benjamini Hochberg FDR correction was used to identify significant enrichment for GO terms. Analysis of enrichment for Wikipathways terms was performed using ConsensusPathDB (Herwig, 2016), which calculates enrichment p-values using the Wilcoxon's matched-pairs signed-rank test, and Benjamini Hochberg FDR correction.

Disease association analysis was performed using WebGestalt [171], which uses a hypergeometric method and Benjamini Hochberg FDR correction. Protein interaction network figures were generated using Cytoscape 3.3.0 [172], with the Reactome FI plugin.

RNA degradation assay

cDNA libraries were prepared from cultured NPCs from E13.5 WT and Mettl14 cKO cortex, at 0 and 5 hr post Actinomycin D treatment, using the NEBNext® Ultra™ DNA Library Prep Kit for Illumina®. The experiment was performed with three replicates per condition. Sequencing was performed on the Illumina Nextseq platform, using a 100-cycle single-end run. Pre-processing of reads was performed using the FASTX toolkit. Gene expression levels were quantified using the RSEM package [173], which maps reads to the transcriptome using the aligner tool Bowtie2 [174].

Expected counts per gene per sample were combined into a count matrix, and this matrix was used as input for differential expression analysis using the EBSeq package [175], which uses empirical Bayesian methods to calculate the posterior probability of a gene being differentially expressed (PPDE). Posterior fold changes per gene between cKO and WT were obtained at time 0 and 5 hr after Actinomycin D treatment. Fold changes at 5 hr were normalized by fold changes at 0 hr (no Actinomycin D treatment) to specifically identify genes that degrade at a different slower rate in the cKO compared to WT, regardless of baseline changes in gene expression between two conditions. Genes with a normalized fold change higher than 2 in cKO over WT at 5 hr were considered as to be differentially degraded (Table S4).

Half-life measurement of m⁶A-tagged transcripts

Mouse NPCs were cultured in standard 6 well culture plates to approximately 80% confluence. Actinomycin D (Sigma) was added at a concentration of 5 μ M. Cells were collected at three time points after addition (0, 3 hr, 5 hr) by washing once with PBS, then lysing the cells in Buffer RLT from the RNeasy Kit (Qiagen) with 1% β -Mercaptoethanol. A cell scraper was used to remove all cells from the well plate. Each sample was normalized for cell number by quantifying DNA content using a Quant-IT PicoGreen dsDNA Assay Kit (ThermoFisher) according to manufacturer instructions. Equal amounts of cellular contents, as measured by DNA quantity, were taken from each sample and 1 pg of luciferase control RNA (Promega) was added to each sample before RNA purification. Total RNA was then purified using an RNeasy Kit and reverse transcribed using the SuperScript II First-Strand Synthesis System (Thermo Fisher). Real time PCR was performed on a Step One Plus cycler from Applied Biosystems with Fast SYBR[®] Green Master Mix. Standard curves were generated by plotting CT values against the known initial concentration of luciferase control RNA, and then used to derive mRNA concentration of each target gene at each time point. The $\ln^{mRNA\ concentrations}$ at time point 0, 3 and 5 hr were then used to perform a linear regression as a

function of time, and identify the slope of said line as the decay rate (k) (Figure S4F). Half life was calculated with the following formula: $t_{1/2} = \ln 2 / k_{\text{decay}}$ [176].

Metabolic labeling and purification of nascent RNA

4sU labeling of nascent RNA was performed as previously described [143]. Mouse NPCs from E13.5 WT and *Mettl14* cKO forebrain were cultured in standard 6 well culture plates to approximately 80% confluence, treated with 500 μM of 4sU (Carbosynth) for 1 hr, washed with PBS, and harvested with TRIzol reagent (ThermoFisher). Samples were extracted by chloroform twice and precipitated with isopropanol. Biotinylation of 4sU-RNA were carried out in a total volume of 250 μl , containing 70 μg total RNA, 10 mM HEPES (pH 7.5), 1 mM EDTA, and 5 μg MTSEA biotin- XX (Biotium) freshly dissolved in DMF (final concentration of DMF = 20%). Reactions were incubated at RT for 30 min in the dark, and excess biotin reagents were removed by chloroform extraction twice. Purified RNA was dissolved in 50 μl RNase-free water and denatured at 65°C for 10 min, followed by rapid cooling on ice for 5 min. Biotinylated RNA was separated from non-labeled RNA by incubating with 100 μl Streptavidin Magnetic Beads (ThermoFisher) for 20 min at RT. Beads were washed twice with high-salt wash buffer (500 μl each, 100 mM Tris- HCl pH 7.4, 10 mM EDTA, 1 M NaCl, and 0.1% Tween-20). 4sU-RNA was eluted with 100 μl freshly prepared 100 mM DTT followed by a second elution with an additional 100 μl 5 min later. RNA was recovered using the MinElute Spin columns (Qiagen) according to the instructions of the manufacturer, and applied for Q-PCR analysis.

Comparison between human and mouse m⁶A-seq datasets

For comparison of m⁶A sequencing data from day 47 human forebrain organoids, PCW11 fetal human cortex, and mouse E13.5 forebrains, we restricted our analysis to expressed genes with a

one-to-one ortholog between species. For determining expressed genes, we calculated RPKMs (as stated above) from input libraries, and used a threshold of $\text{RPKM} > 1$.

QUANTIFICATION AND STATISTICAL ANALYSIS

Data in figure panels reflect several independent experiments performed on different days. An estimate of variation within each group of data is indicated using standard error of the mean (SEM). We performed unpaired Student's t-test for assessing the significance of differences between two treatments (See each figure for details).

Analyses of mouse cortical neurogenesis in vivo

For quantitative analysis of electroporated neocortices, only GFP^+ cells localized within the dorso-lateral cortex were examined. 3 x 3 tiled images were obtained to cover the electroporated region of each coronal section with a 20x or 40x objective by scanning microscope (Zeiss LSM 800) and compared with equivalent sections in littermate counterparts. Quantifications were performed using Imaris software (Bitplane). Specifically, for quantification of cell fate after in utero electroporation, GFP^+ cells were marked, and $\text{GFP}^+\text{Pax6}^+$ cells were defined and counted based on the intensity of Pax6 immunofluorescence in GFP^+ cells measured with the same criteria among different groups using Imaris software. For the distribution of GFP^+ cells in each layer, the borders between different layers were defined by Pax6 immunofluorescence (VZ/SVZ) and DAPI staining (SVZ/IZ and IZ/CP). For quantification of cell fate in WT and *Mettl14* cKO mice at E17.5, P0 and P5, the regions of the primary somatosensory cortex were identified and the numbers of Pax6^+ , Tbr2^+ , $\text{S100}\beta^+$, Ctip2^+ , Satb2^+ or Tbr1^+ cells were counted in each vertical column with 100 μm width. For distribution plots, the distances between soma of $\text{EdU}^+\text{Pax6}^+$, Pax6^+ , Tbr2^+ or Neurod1^+ cells and the ventricular surface were calculated. Only $\text{EdU}^+\text{Pax6}^+$ cells within 200 μm distance from the ventricular surface were measured, and the histogram of cell location in every 20 μm interval from the ventricular surface was plotted as a percentage. For distribution plots of $\text{Pax6}^+\text{Tbr2}^+$ or

Pax6⁺Neurod1⁺ cells, the distances between soma of cells and the ventricular surface were calculated and the numbers of cells per 100 μm^2 area in every 20 μm interval from the ventricular surface were plotted as density distribution. All quantifications were performed with 4-10 brain sections from at least 4 animals. Data are presented as the mean \pm SEM and statistical significance was assessed using unpaired Student's t-test.

DATA AND SOFTWARE AVAILABILITY

The access number for the data for m⁶A-seq reported in this study is NCBI GEO: GSE99017.

ACKNOWLEDGEMENTS

We thank Christian and J. Schnoll for comments, members of Ming and Song laboratories for discussion, L. Liu, Y. Cai, and D.G. Johnson for technical assistance, and T. M. Hyde and D. R. Weinberger for dissected fetal human brain samples. K-J.Y. was partially supported by a Young Investigator Award from Brain & Behavior Research Foundation and a postdoctoral fellowship from Maryland Stem Cell Research Found (MSCRF); C.V. was partially supported by an NSF pre-doctoral fellowship and NIH T32GM007445. The research was supported by grants from NIH (R37NS047344, U19MH106434, and P01NS097206 to H.S., RM1HG008935 to C.H.; R01MH105128, R35NS097370, and U19AI131130 to G-I.M.), MSCRF (to H.S. and G-I.M.), Simons Foundation (to H.S. and G-I.M.), and Adelson Medical Research Foundation (to G-I.M.).

VI. FIGURES:

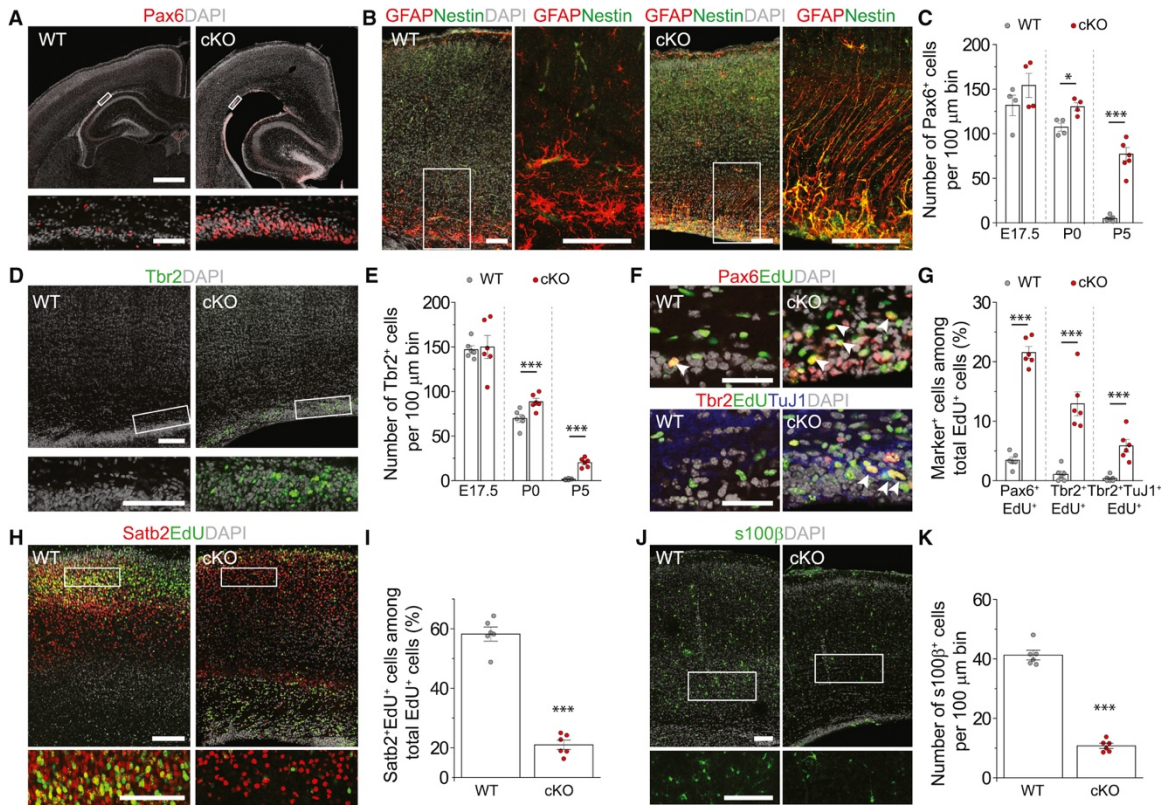


Figure 1. Nervous system *Mettl14* deletion results in residual radial glia cells and ongoing neurogenesis in the postnatal mouse cortex.

(A-C) Presence of neurogenic RGCs in P5 Nestin-Cre;*Mettl14*^{fl/fl} cKO cortices. Shown are sample confocal images (A, B) and quantifications (C). Regions in white boxes are shown at a higher magnification. Scale bars: 500 μ m (A, top panel), 50 μ m (A, bottom panel), 100 μ m (B). Values in (C) represent mean \pm SEM (n = 4-7; ***: P < 0.001; *: P < 0.05; unpaired Student's t-test).

(D-E) Preserved IPCs in P5 cKO cortices. Shown are sample confocal images (D; scale bars: 100 μ m) and quantification (E). Values represent mean \pm SEM (n = 6; ***: P < 0.001; **: P < 0.01; unpaired Student's t-test).

(F-G) Ongoing neurogenesis in P5 cKO cortices. P5 pups were injected with EdU and analyzed 48 hr later. Shown in (F) are sample confocal images of the ventricular side of the primary somatosensory cortex. Arrows indicate Pax6⁺EdU⁺ cells (top) and Tbr2⁺TuJ1⁺EdU⁺ cells (bottom).

Scale bars: 100 μm . Quantification of EdU⁺ cells with different markers is shown in (G). Values represent mean \pm SEM (n = 6; ***: P < 0.001; unpaired Student's t-test).

(H-K) Reduced production of upper-layer neurons and astrocytes in cKO cortices. Pregnant mice were injected with EdU at E15.5 and analyzed at P5. Shown are sample confocal images (H, J; scale bars: 100 μm) and quantification (I, K). Values represent mean \pm SEM (n = 6; ***: P < 0.001; unpaired Student's t-test).

See also Figure S1.

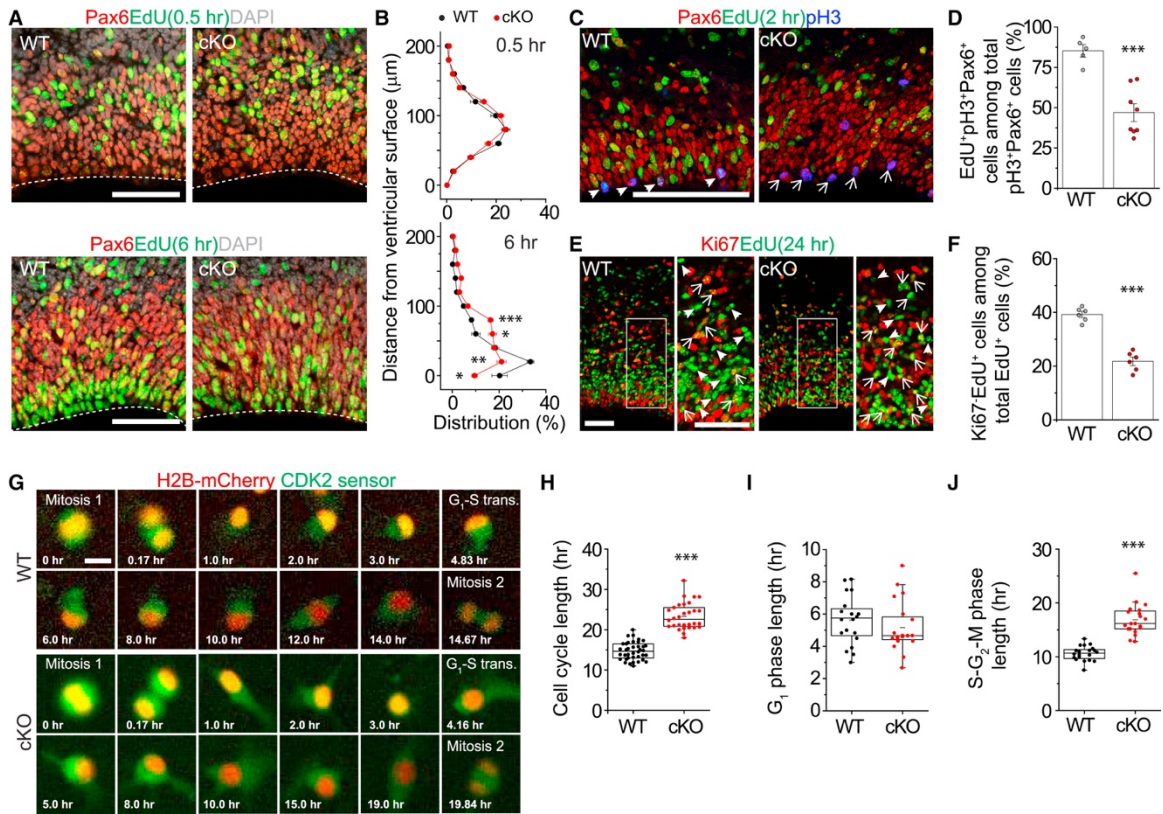


Figure 2. *Mettl14*^{-/-} RGCs and NPCs exhibit prolonged cell cycle progression.

(A-B) Abnormal INM of RGCs in *Mettl14* cKO cortices. Pregnant mice were injected with EdU at E17.5 and analyzed 0.5 or 6 hr later. Shown are sample confocal images (A; scale bars: 50 μ m) and quantification of the distance from Pax6⁺EdU⁺ nuclei to the ventricular surface (B). Values for the percentages of nuclei in each 20 μ m bin represent mean \pm SEM (n = 4; ***: P < 0.001; **: P < 0.01; *: P < 0.05; unpaired Student's t-test).

(C-D) Delayed S to M phase transition of RGCs in *Mettl14* cKO mice. Pregnant mice were injected with EdU at E17.5 and analyzed 2 hr later. Shown in (C) are sample confocal images. Arrowheads point to Pax6⁺pH3⁺EdU⁺ cells and arrows point to Pax6⁺pH3⁺EdU⁻ cells. Scale bar: 50 μ m. Shown in (D) is the quantification of the percentage of Pax6⁺pH3⁺EdU⁺ cells, representing cells proceeded from S to M phase during the 2 hr chase, among total Pax6⁺pH3⁺ cells. Values represent mean \pm SEM (n = 5 for WT and n = 8 for cKO; ***: P < 0.001; unpaired Student's t-test).

(E-F) Delayed cell cycle exit of neural progenitors in *Mettl14* cKO mice. Pregnant mice were injected with EdU at E17.5 and analyzed 24 hr later. Shown in (E) are sample confocal images. Arrowheads point to $\text{Ki67}^+\text{EdU}^+$ cells and arrows point to $\text{Ki67}^+\text{EdU}^-$ cells. Scale bar: 50 μm . Shown in (F) is the quantification of the percentage of $\text{Ki67}^+\text{EdU}^+$ cells, representing cells exited from cell cycle, among total EdU^+ cells. Values represent mean \pm SEM ($n = 6$; ***: $P < 0.001$; unpaired Student's t-test).

(G-J) Time-lapse imaging analysis of mouse NPCs showing prolonged S-G₂-M phase length in the absence of *Mettl14*. WT and cKO mouse NPCs were electroporated with plasmid co-expressing a Cdk2 sensor (green) and the H2B-mCherry nuclear marker (red), cultured for 2 days, and imaged for 48 hr. Shown in (G) are sample time-lapse images with time stamps. Scale bars: 10 μm . Also shown are box plots of quantifications for the total cell cycle length (H; $n = 38$ for WT and $n = 30$ for cKO), G₁ phase length (I; $n = 20$), and S-G₂-M phase length (J; $n = 20$). Each dot represents data from one NPC (***: $P < 0.001$; unpaired Student's t-test).

See also Figure S2.

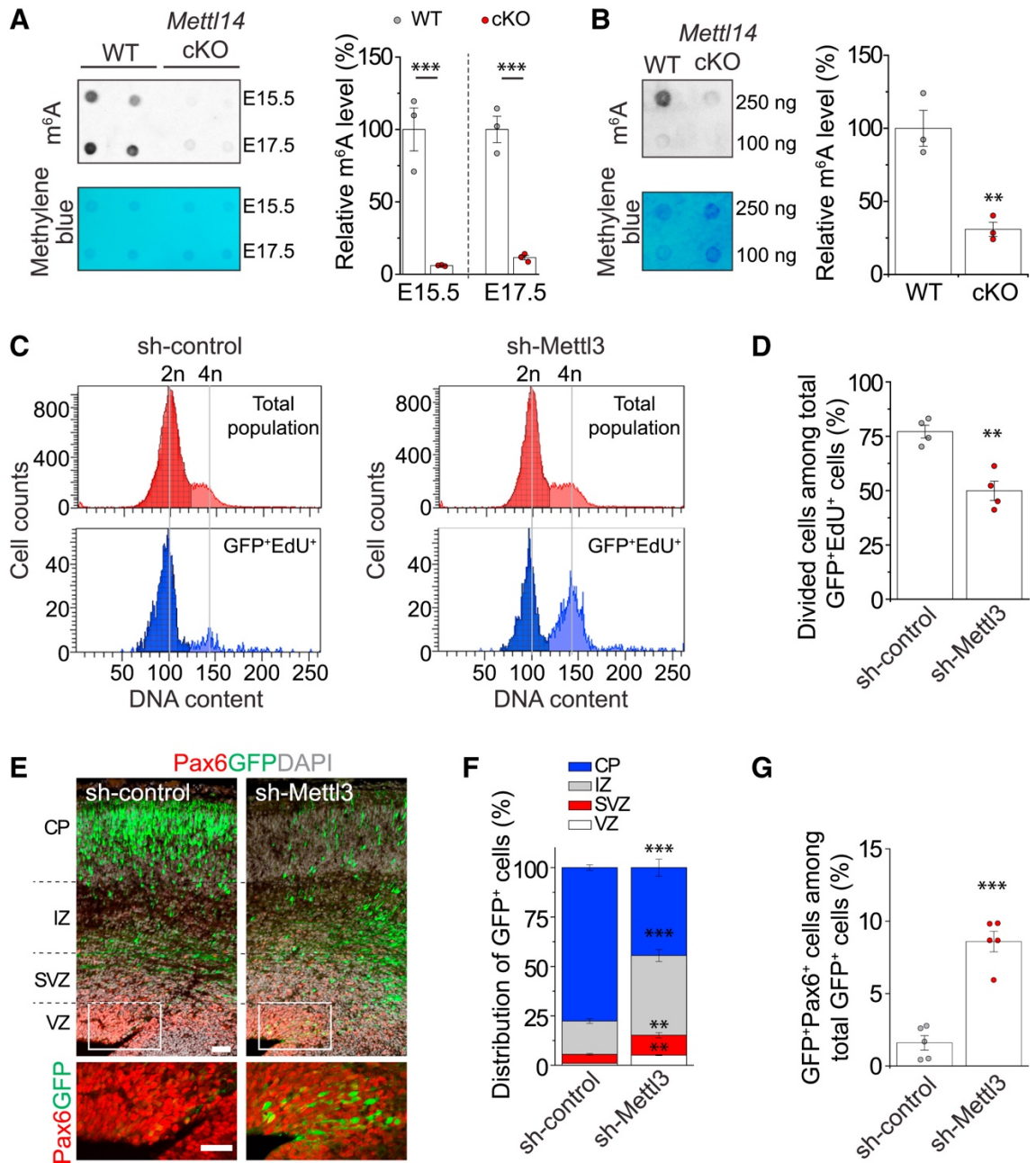


Figure 3. Mettl3 regulates cell cycle progression of NPCs and maintenance of embryonic cortical RGCs.

(A) Depletion of m⁶A-tagging on mRNAs purified from E15.5 and E17.5 *Mettl14* cKO mouse forebrain. Shown in the left panels are sample images of m⁶A dot blot and methylene blue staining (for loading controls). Data were normalized to the averaged levels of WT samples and

quantification is shown in the right panel. Values represent mean \pm SEM (n = 3; **: P < 0.01; unpaired Student's t-test).

(B) Depletion of m⁶A-tagging on mRNAs purified from Mettl14 cKO NPCs. Values represent mean \pm SEM (n = 3; **: P < 0.01; unpaired Student's t-test).

(C-D) Flow cytometry analysis of cell cycle status of mouse NPCs. NPCs were electroporated to co-express GFP and the control shRNA, or the shRNA against Mettl3. At day 4, NPCs were pulse-labeled with EdU (10 μ M) for 30 min, cultured for 9 hr, followed by EdU and DNA content (DyeCycle Violet) staining and flow cytometry analysis. Shown are sample histograms of DNA content from GFP⁺EdU⁺ cells and the total cell population (as a reference; C) and quantification (D). Values in (D) represent mean \pm SEM (n = 4; **: P < 0.01; unpaired Student's t-test).

(E-G) Embryonic mouse cortices were electroporated in utero at E13.5 to co-express GFP and shRNA-control, or GFP and shRNA-Mettl3, and analyzed at E17.5. Shown in (E) are sample confocal images. Scale bars: 50 μ m. The distribution of GFP⁺ cells in each zone (F) and the percentage of GFP⁺Pax6⁺ cells among total GFP⁺ cells (G) were quantified. VZ: ventricular zone; SVZ: subventricular zone; IZ: intermediate zone; CP: cortical plate. Values represent mean \pm SEM (n = 4; ***: P < 0.001; **: P < 0.01; unpaired Student's t-test).

See also Figure S3.

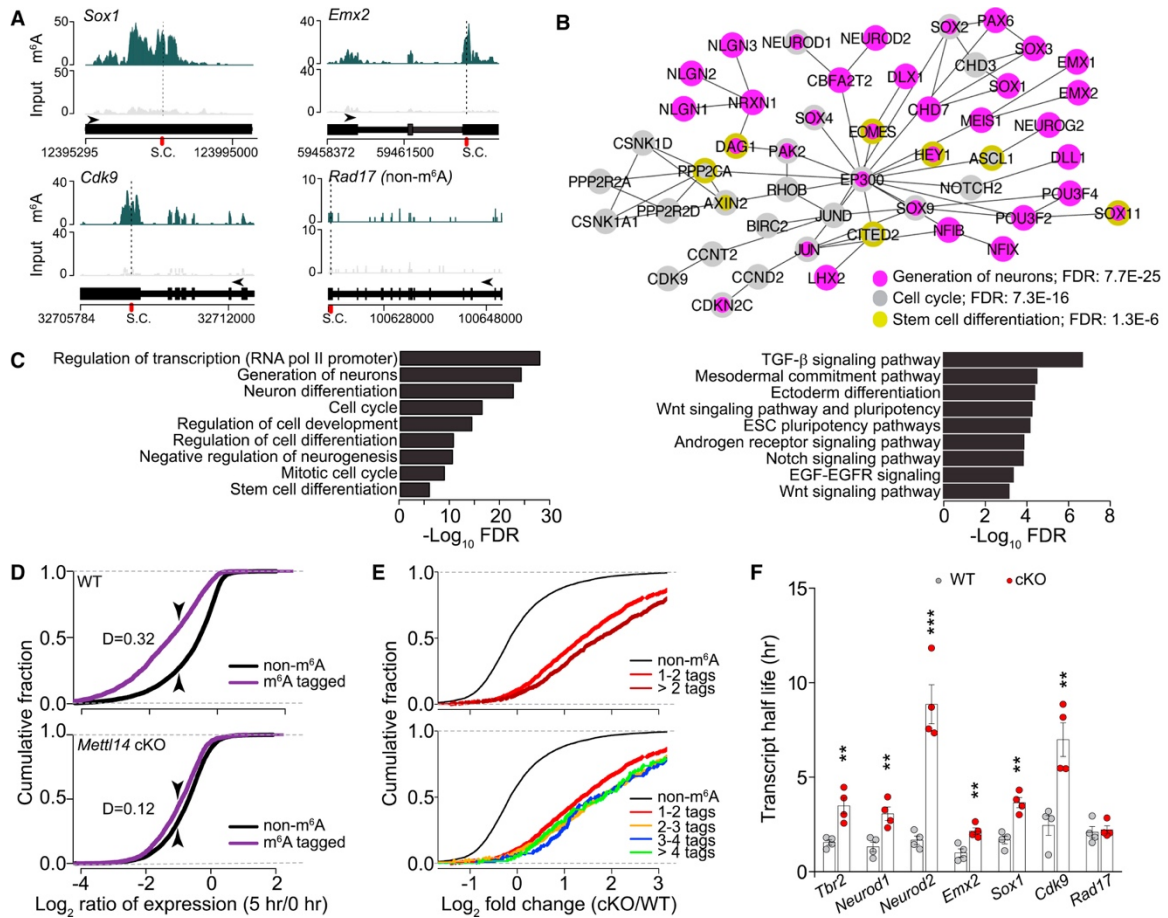


Figure 4. m⁶A tags transcripts related to transcription factors, cell cycle, and neuronal differentiation in the embryonic mouse brain, and promotes their decay.

(A) Coverage plots from m⁶A-seq of E13.5 mouse forebrains showing representative examples of m⁶A-tagged (*Sox1*, *Emx2*, and *Cdk9*) and non m⁶A-tagged (*Rad17*) transcripts. Top and middle panels show read coverages normalized by library sizes from m⁶A pulled-down and input libraries, respectively, and bottom panels show gene structures (arrows point to the direction of transcription; S.C.: stop codon).

(B-C) GO analysis of m⁶A-tagged genes reveals enrichment for biological process terms related to transcription factors, neurogenesis, cell cycle, and stem cell differentiation. Also shown is KEGG pathways gene set enrichment analysis. FDR: false discovery rate.

(D) Cumulative distribution of Log₂(gene expression ratios) at time 5 hr post ActD over time 0 hr for m⁶A tagged genes (purple line) and non-m⁶A tagged genes (black line) for WT and *Mettl14*

cKO NPCs. D = value of Kolmogorov Smirnov test statistic corresponding to maximum difference between methylated and non-methylated distributions.

(E) Cumulative distribution of \log_2 (fold change in ratios of gene expression) at 5 hr post ActD treatment over time 0 hr upon Mettl14 deletion. Top panel shows cumulative distribution for non-targets (black line) and transcripts with 1-1.9 m⁶A sites on average (bright red line), or 2 or more sites on average (dark red line). Bottom panel shows cumulative distribution for non-targets (black line) and m⁶A-tagged transcripts with 1-2, 2-3, 3-4, and 4 or more sites on average (red, yellow, blue, and green lines, respectively).

(F) Summary of half-life of a group of transcripts in WT and Mettl14 cKO NPCs. Values represent mean \pm SEM (n = 4; ***: P < 0.001; **: P < 0.01; unpaired Student's t-test

See also Figure S4, Table S2, Table S3 and Table S4.

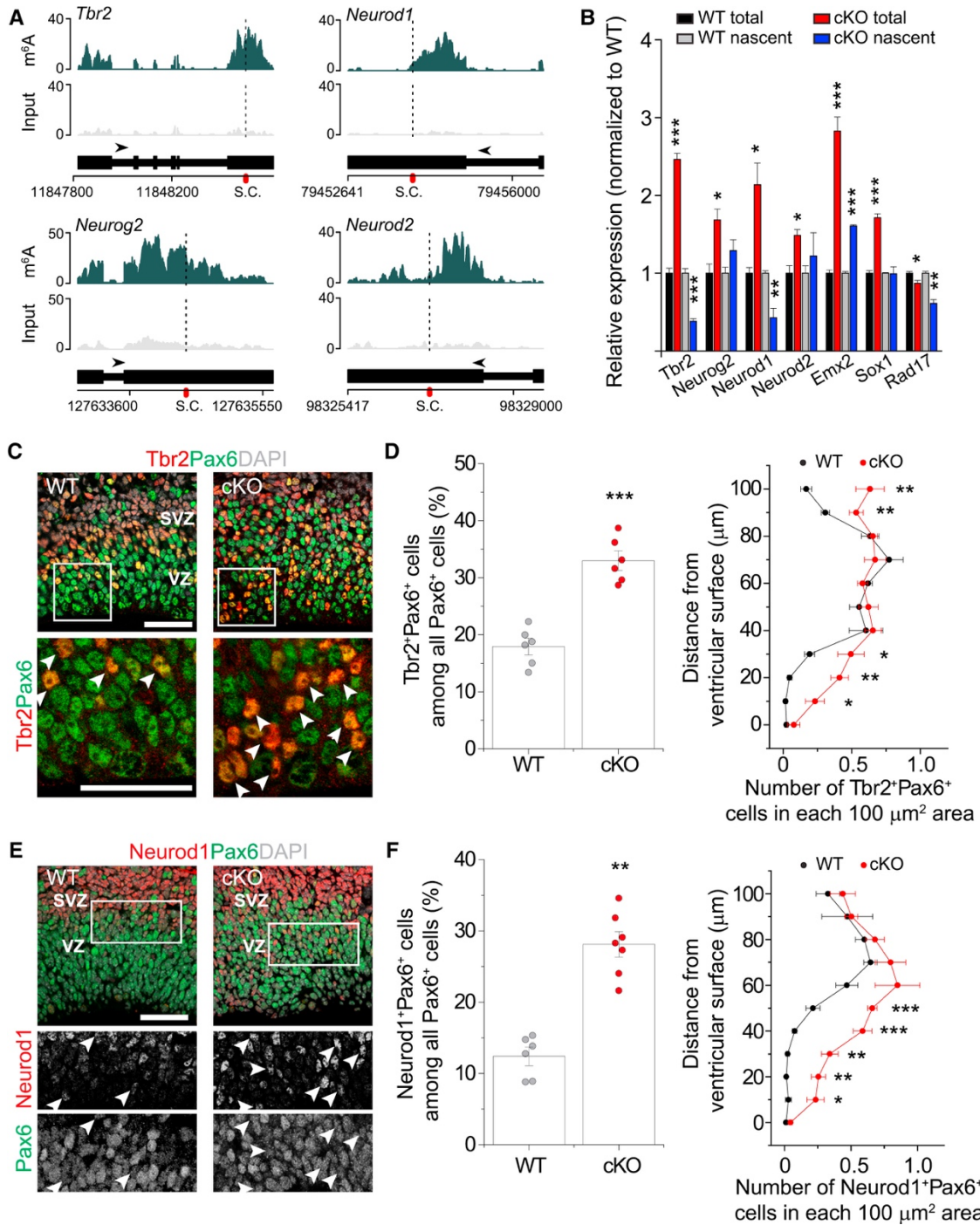


Figure 5. Post-transcriptional regulation of pre-patterning gene levels and protein production by m⁶A signaling in cortical neural stem cells.

(A) Coverage plots from m⁶A-seq of E13.5 mouse forebrains showing representative examples of m⁶A-tagged IPC (*Tbr2* and *Neurog2*) and neuronal (*Neurod1* and *Neurod2*) genes.

(B) Q-PCR analysis of total mRNA and 4sU-purified nascent mRNA from WT and Mettl14 cKO NPCs. All Ct values were first normalized to Gapdh control (not m⁶A-tagged), which were similar in both WT and cKO NPCs. The ratio (cKO over WT) was calculated for each experiment and values represent mean \pm SEM (n = 3 cultures; ***: P < 0.001; **: P < 0.01; *: P < 0.05; unpaired Student's t-test).

(C-F) Precocious expression of Tbr2 and Neurod1 proteins in RGCs in E17.5 Mettl14 cKO mice in vivo. Shown are sample confocal images (C, E; scale bars: 50 μ m) and quantifications of the percentage of Tbr2⁺Pax6⁺ cells (D), or Neurod1⁺Pax6⁺ cells (F), among total Pax6⁺ cells (top panels, n = 6) and the density distribution of Tbr2⁺Pax6⁺ (D), or Neurod1⁺Pax6⁺ cells (F), from the ventricular surface (bottom panels, n = 4). Arrows indicate Tbr2⁺Pax6⁺ (C) or Neurod1⁺Pax6⁺ cells (E). Values in (D, F) represent mean \pm SEM (***: P < 0.001; **: P < 0.01; *: P < 0.05; unpaired Student's t-test).

See also Figure S5.

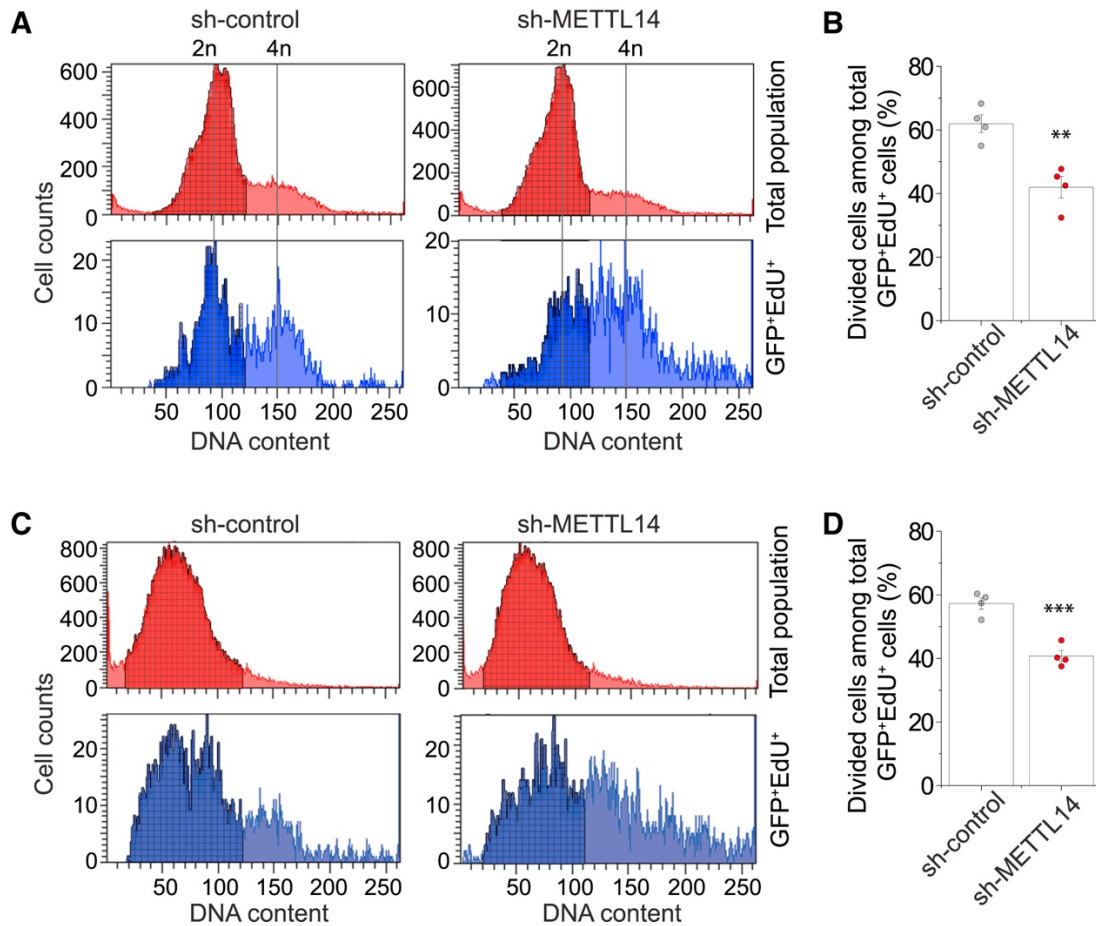


Figure 6. METTL14 regulates cell cycle progression of human NPCs.

(A-B) Flow cytometry analysis of cell cycle progression of hNPCs with METTL14 KD. Human NPCs were electroporated to co-express GFP and shRNA-control, or shRNA-METTL14. After 4 days, hNPCs were pulse-labeled with EdU (10 μ M) for 30 min, incubated for 14 hr, followed by EdU and DNA content (DyeCycle Violet) staining and flow cytometry analysis, similarly as in Figure 3C-D. Values represent mean \pm SEM (n = 4; **: P < 0.01; unpaired Student's t-test).

(C-D) Flow cytometry analysis of cell cycle progression with METTL14 KD in human forebrain organoids. Day 45 forebrain organoids were electroporated to co-express GFP and shRNA-control, or shRNA-METTL14. After 7 days, forebrain organoids were pulse-labeled with EdU (10 μ M) for 1 hr, cultured further for 14 hr, followed by dissociation and analysis similarly as in Figure 3C-D. Values represent mean \pm SEM (n = 4; ***: P < 0.001; unpaired Student's t-test).

See also Figure S6.

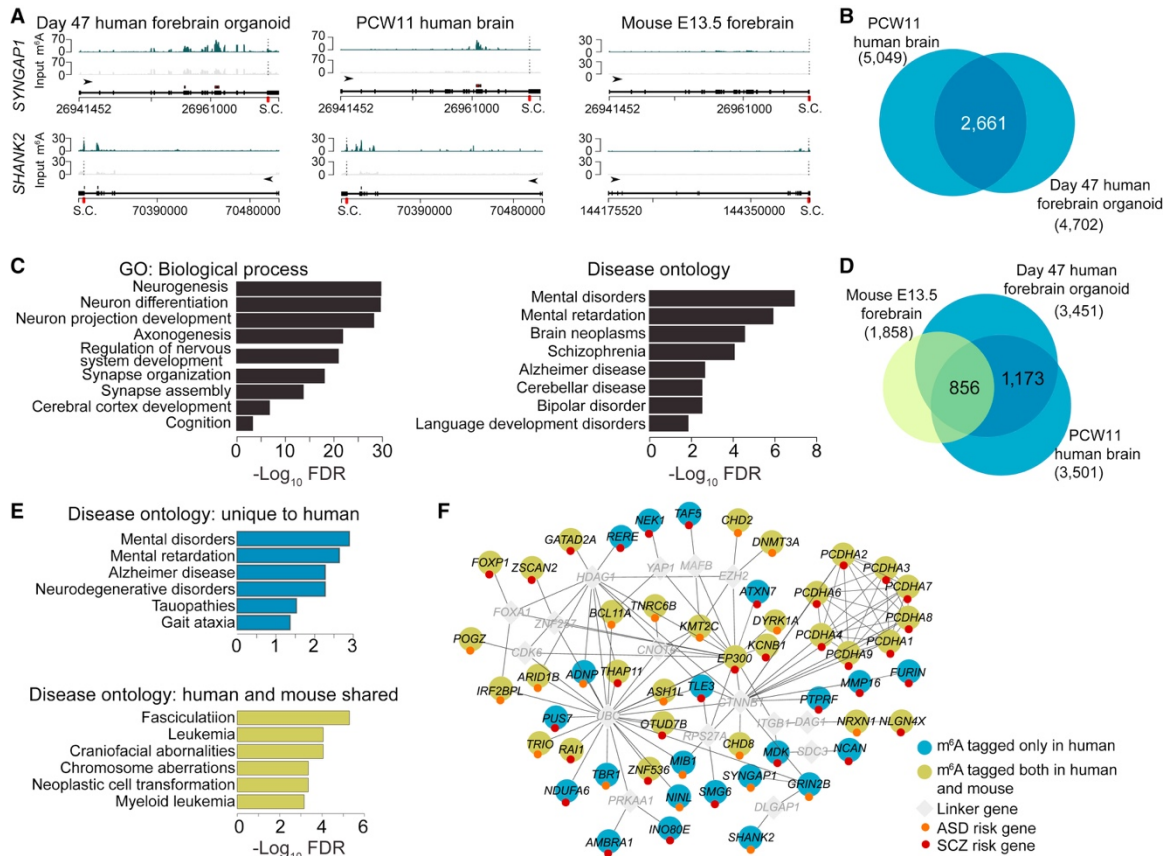


Figure 7. Conserved and unique features of m⁶A mRNA methylation in human forebrain organoids, human fetal brain and embryonic mouse forebrain.

(A) Representative plots of two m⁶A-tagged transcripts in day 47 human forebrain organoids and PCW11 human fetal brain, but not in mouse E13.5 forebrain.

(B) Venn diagram showing shared m⁶A-tagged transcripts between day 47 human forebrain organoids and PCW11 fetal human brain.

(C) GO and disease ontology analyses of shared m⁶A-tagged genes in day 47 human forebrain organoids and PCW11 human fetal brain.

(D) Venn diagram showing shared and unique m⁶A-tagged transcripts among mouse E13.5 forebrain, day 47 human forebrain cortex, and PCW11 fetal human brain. Only ortholog genes expressed in all three samples were used for analysis.

(E-F) Disease ontology analysis of transcripts uniquely m⁶A-tagged in human shows enrichment for neurodevelopmental diseases, whereas disease ontology analysis of commonly m⁶A-tagged transcripts showed enrichment for oncogenic processes.

See also Figure S7, Table S5, Table S6 and Table S7.

VII. SUPPLEMENTAL FIGURES:

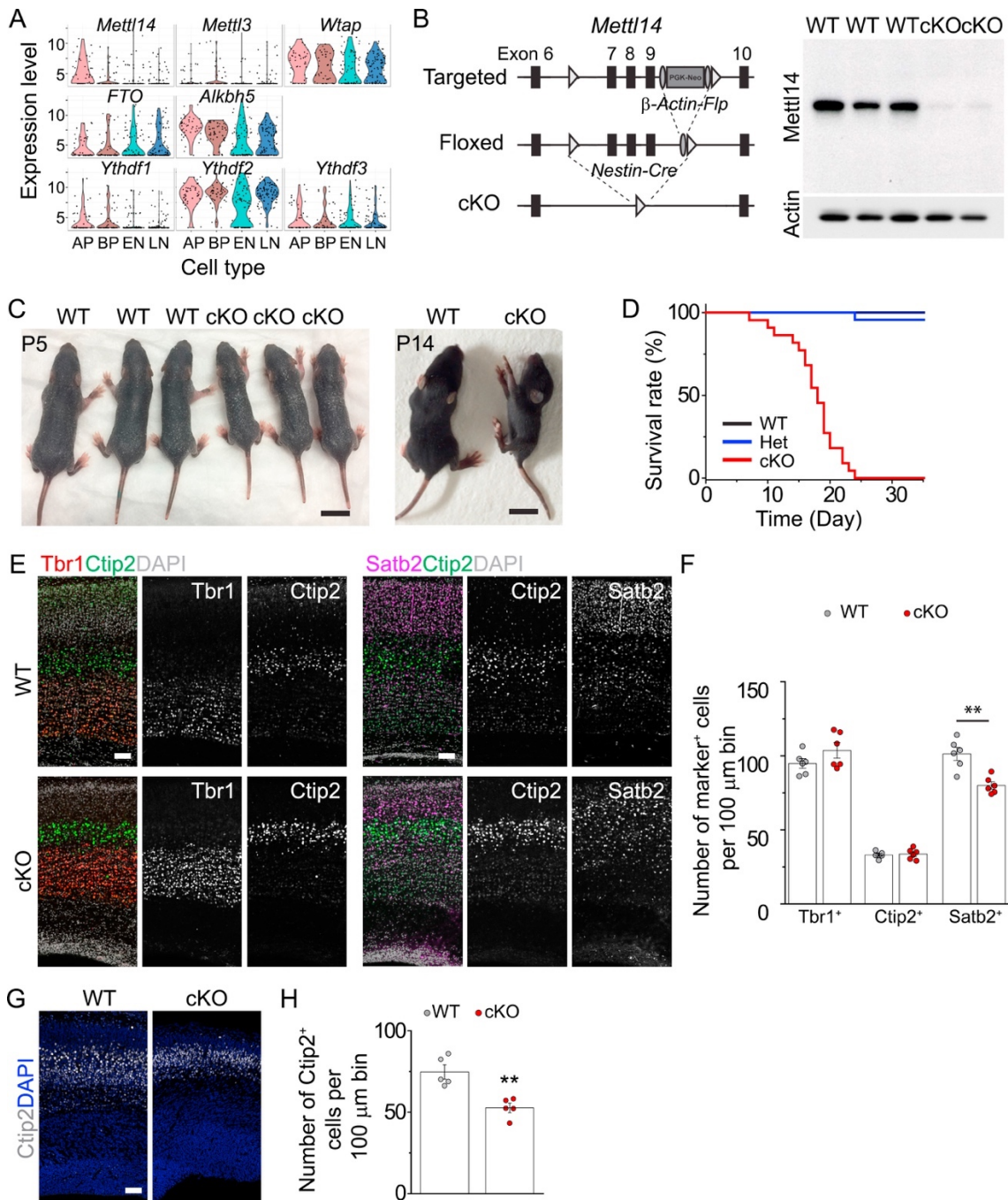


Figure S1: Nervous System *Mettl14* Deletion in Mice Results in Postnatal Lethality and Deficits in Timely Production of Cortical Neuron Subtypes, Related to Figure 1

(A) Expression of molecular mediators of m⁶A signaling based on a published single-cell RNA-seq dataset of embryonic mouse cortical neurogenesis (Telley et al., 2016). Shown are the

expression profiles of selected genes as violin plots, generated using the Seurat package of R (<http://genebrowser.unige.ch/science2016/>) (Macosko et al., 2015). AP: Apical progenitors/RGCs; BP: daughter basal progenitors/IPCs; EN: early neurons; LN: late neurons.

(B) Depletion of Mettl14 protein in the forebrain of *Nestin-Cre;Mettl14^{fl/fl}* cKO mice. Shown are the genetic deletion strategy (left) and sample western blot images from WT or cKO E17.5 forebrain lysates (right). Because *Mettl14* was only deleted in the nervous system, the minor non-neural cells contributed to the residual Mettl14 proteins (faint bands).

(C) Appearance of WT and cKO pups at P5 and P14. Note the impairment in the P14 cKO pup to maintain body balance. Scale bars, 1 cm.

(D) Survival curve of WT (n = 45), Het (n = 23) and cKO (n = 22) pups.

(E and F) Deficits in the production of upper-layer neurons in cKO cortices at P5. Shown in (E) are sample confocal images of staining for Satb2 (layer 2/3), Ctip2 (layer 5) and DAPI, or Ctip2 (layer 5), Tbr1 (layer 6) and DAPI. Scale bars, 100 μ m. Quantification is shown in (E). Values represent mean \pm SEM (n = 6; **: p < 0.01; unpaired Student's t test).

(G and H) Deficits in the production of lower-layer neurons in cKO cortices at E17.5. Shown in (E) are sample confocal images of staining for Ctip2 and DAPI. Scale bar, 100 μ m. Quantification is shown in (H). Values represent mean \pm SEM (n = 6; **: p < 0.01; unpaired Student's t test).

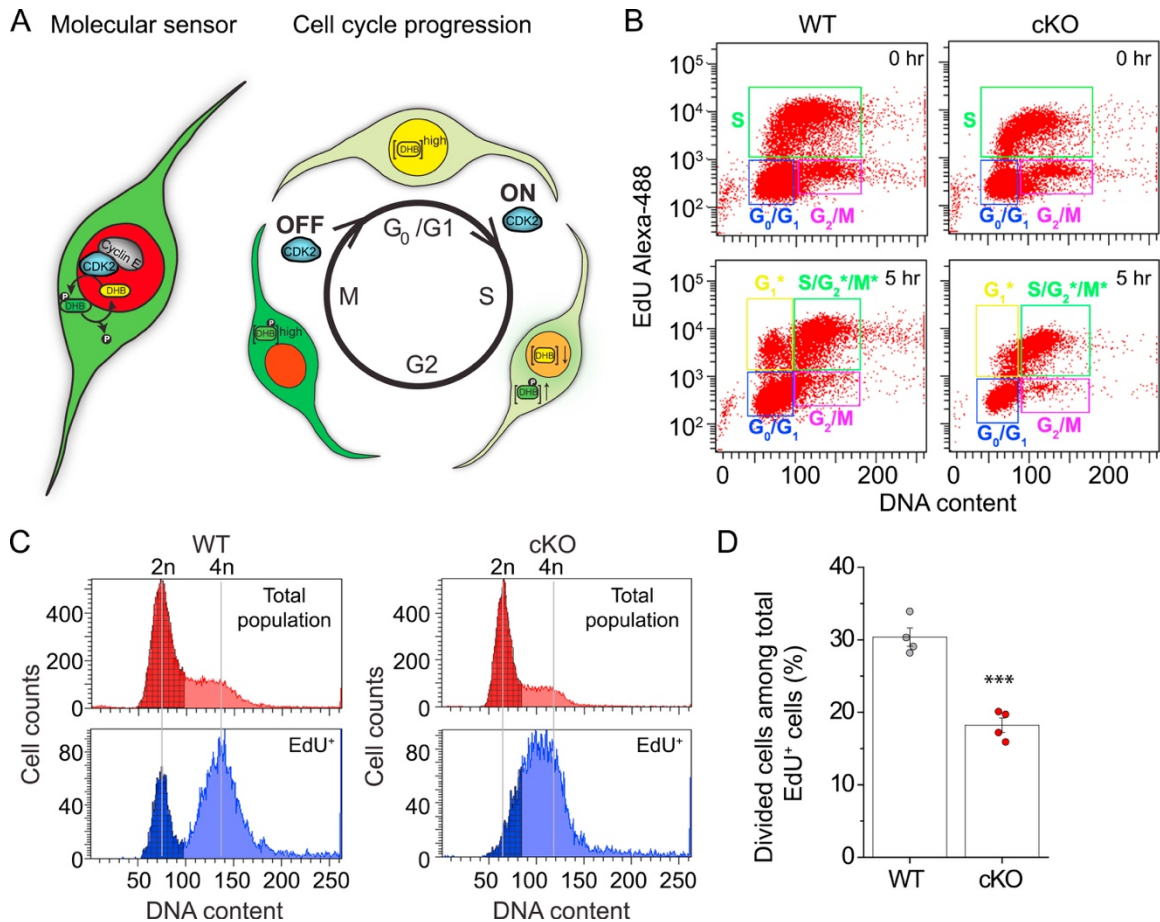


Figure S2: Flow Cytometry Analysis Reveals Delayed Cell-Cycle Progression of *Mettl14* cKO NPCs, Related to Figure 2

(A) Schematic diagrams of the dual reporter system used to track cell cycle status by time-lapse imaging. Nuclear localized H2B-mCherry and a GFP-tagged Cdk2 substrate DHB are co-expressed in the individual cell. Cdk2 becomes active during the G1-S transition and phosphorylates DHB-GFP, which is then translocated from the nucleus to the cytoplasm. The presence of GFP in the mCherry⁺ nucleus indicates cells in the G1 phase, whereas translocation to the cytoplasm indicates the initiation of the S phase, and continual buildup of cytoplasmic GFP occurs until mitosis.

(B–D) Flow cytometry analysis of cell cycle progression of WT and *Mettl14* cKO NPCs. NPCs were pulse-labeled with EdU (10 μM) for 30 min, cultured for 0 or 5 hr, followed by EdU and DNA content (7AAD) staining and flow cytometry analysis. Shown in (B) are sample dot plots at 0 and 5 hr after EdU pulsing. Cells in a specific cell cycle phase were marked in a box. Note that EdU⁺

cells (S phase at 0 hr) were segregated into divided ($G1^*$) and non-divided ($S/G2^*/M^*$) populations. Shown in (C) are sample histograms of DNA content from EdU^+ cells and the total cell population (as a reference). Quantification is shown in (D). Values represent mean \pm SEM ($n = 4$; ***: $p < 0.01$; unpaired Student's t test).

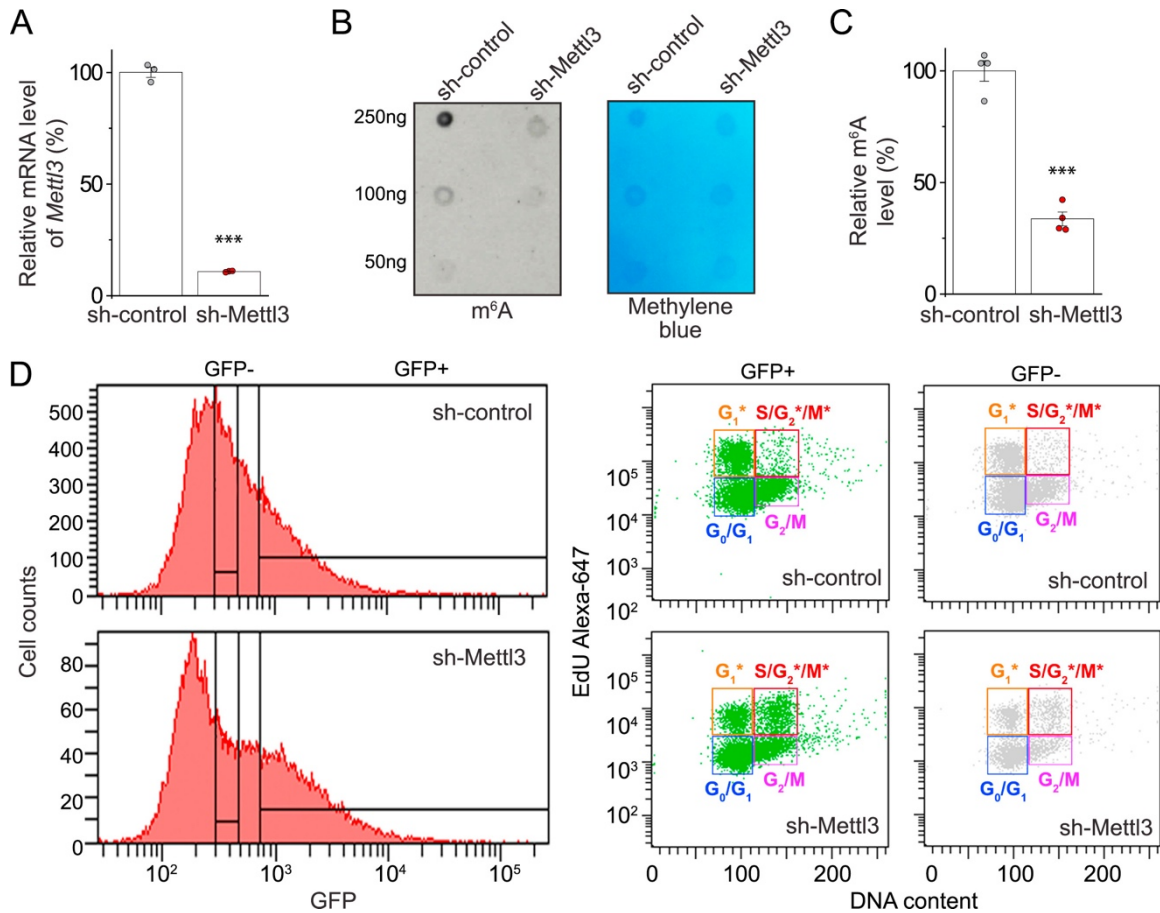


Figure S3: Mettl3 Is Essential for m⁶A mRNA Methylation and Proper Cell-Cycle Progression of Mouse NPCs, Related to Figure 3

(A) Efficacy of the shRNA against mouse *Mettl3*. Mouse B16F10 cells were transfected with shRNA-control and shRNA-*Mettl3*. The amount of *Mettl3* mRNA was assessed by Q-PCR 3 days later. Values represent mean \pm SEM (n = 3; ***: p < 0.001; unpaired Student's t test).

(B and C) Depletion of m⁶A mRNA methylation by *Mettl3* KD. Shown are sample images of m⁶A dot blot and methylene blue staining (as loading controls; B) and quantification (C). Data were normalized to the averaged levels of WT samples. Values represent mean \pm SEM (n = 3; ***: p < 0.01; unpaired Student's t test).

(D) Flow cytometry analysis of cell cycle status of mouse NPCs. Mouse NPCs were electroporated to co-express GFP and shRNA-control, or shRNA-*Mettl3*. After 4 days, NPCs were pulse-labeled with EdU (10 μ M) for 30 min, cultured for 9 hr, followed by EdU and DNA content (DyeCycle

Violet) staining and flow cytometry analysis. GFP⁺ and GFP⁻ cells were gated separately and shown as dot plots. Note that GFP⁺ cells with *Mettl3* KD showed accumulation of non-divided (S/G2*/M*) population.

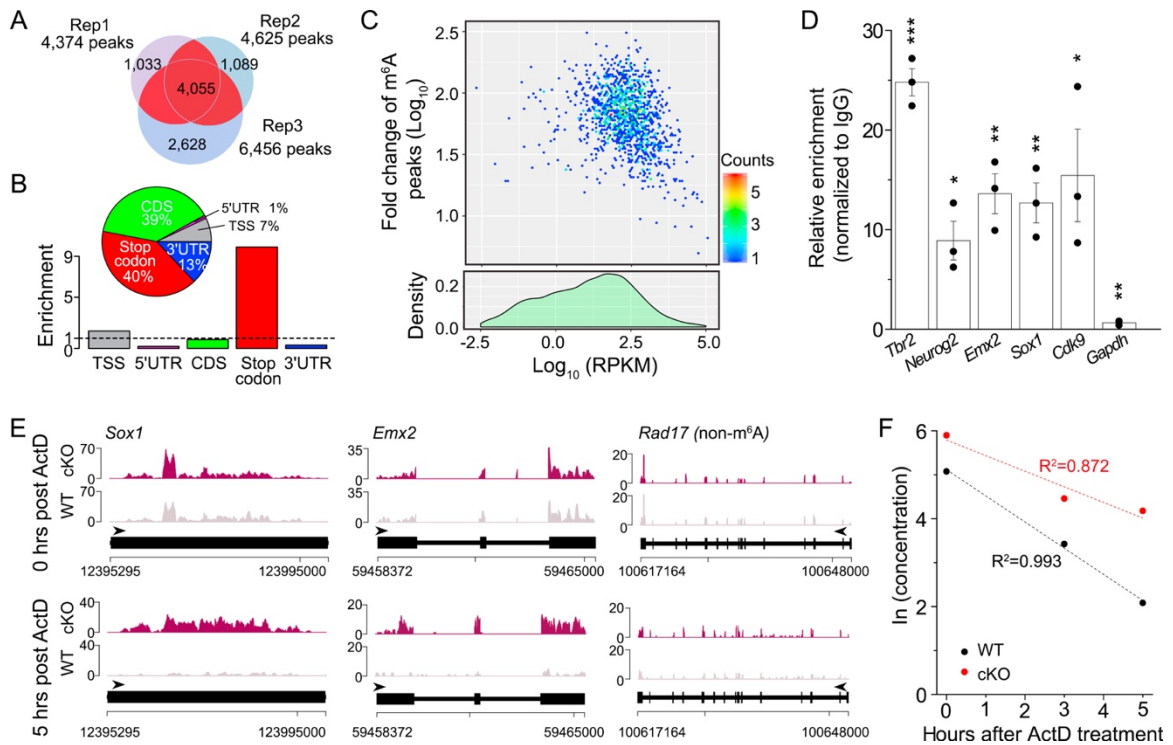


Figure S4: m⁶A-Seq Analysis of Mouse Embryonic Forebrain, Related to Figure 4

(A) Venn diagram showing intersection among m⁶A peaks identified in 3 independent m⁶A-seq experiments. 4,055 high confidence peaks shared by 2 out of 3 replicates, corresponding to 2,059 genes, were used for downstream analysis.

(B) Enrichment of m⁶A peaks in 5 non-overlapping transcript segments. Pie chart shows percentage of peaks annotated to each segment. Bar plot shows fold enrichment of peaks for each segment, normalized for the segment length.

(C) m⁶A peaks do not correlate with transcript expression levels. Scatterplot shows gene expression levels (\ln^{RPKM}) of m⁶A-tagged genes plotted against m⁶A peak $\ln^{\text{fold change}}$. Histogram shows distribution of gene expression levels (\ln^{RPKM}) for all transcripts detected in 3 RNA-seq input libraries.

(D) Validation of m⁶A-tagging in specific transcripts in cortical NPCs. The enrichment of m⁶A-tagged transcripts by IP with anti-m⁶A antibodies over IgG was quantified by Q-PCR. Values represent mean ± SEM (n = 3; ***: p < 0.01; **: p < 0.01; *: p < 0.05; unpaired Student's t test).

(E) Representative coverage plots from the RNA-seq analysis at 0 or 5 hr after treatment with ActD showing increased stability of m⁶A-tagged genes (*Sox1* and *Emx2*), but not a non m⁶A-tagged gene (*Rad17*) in *Mettl14* cKO compared to WT NPCs.

(F) Representative plot for calculating half-life of transcripts in WT and cKO NPCs. Data for *Emx2* is plotted as an example. The ln of the transcript concentration at each time point, (0, 3, and 5 hr after Actinomycin D treatment) was plotted, and a linear regression was used to determine the slope of the resultant line. The half-life was then calculated as the ln2 divided by the absolute value of the slope of the line.

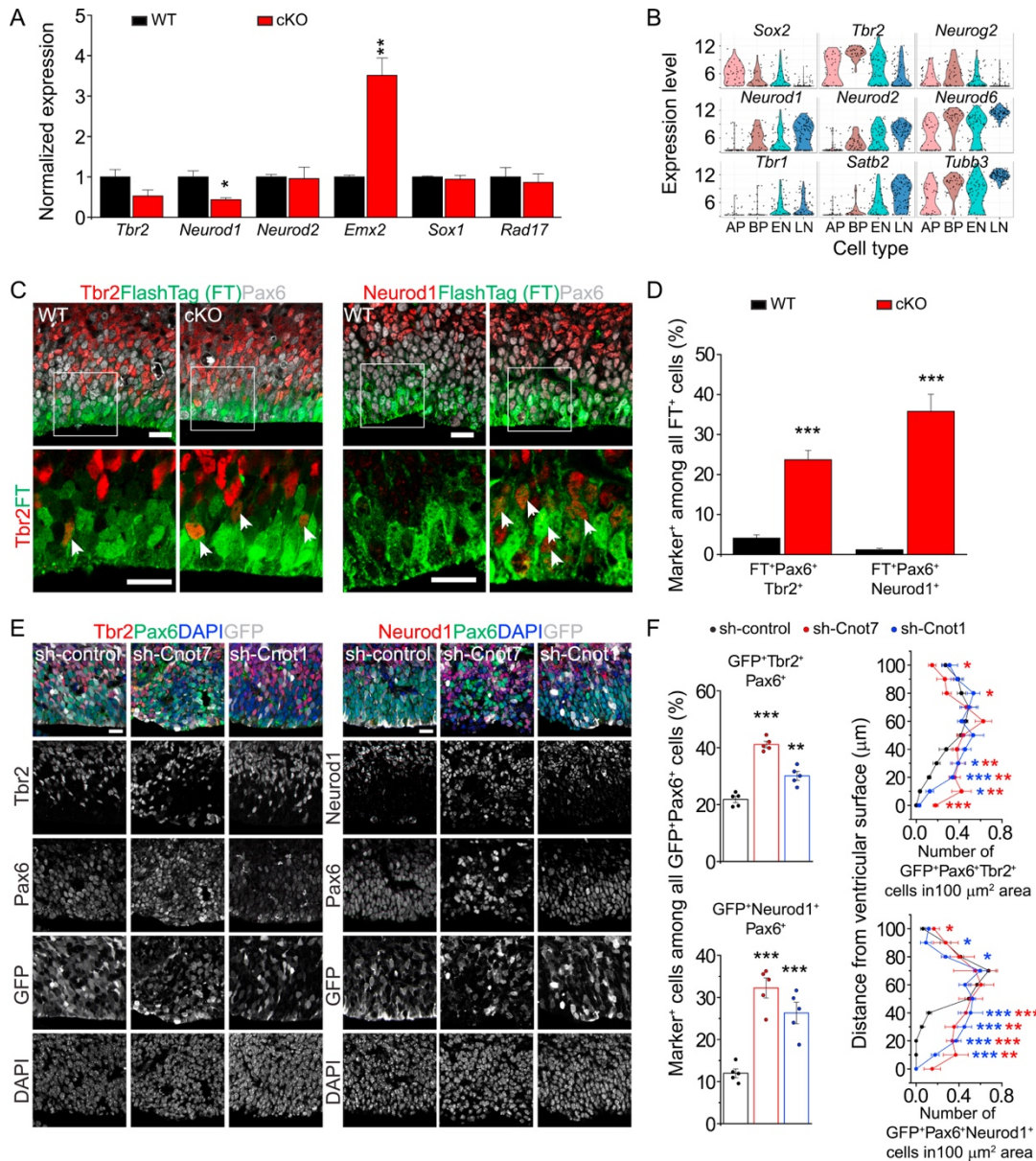


Figure S5: Expression of Neuronal Genes in RGCs of Embryonic Cortex In Vivo, Related to Figure 5

(A) Q-PCR analysis of pre-mRNA from WT and *Mettl14* cKO NPCs using pre-mRNA specific primers. All Ct values were first normalized to the *Actin* control (not m⁶A-tagged), which were similar in both WT and cKO NPCs. The ratio (cKO over WT) was calculated for each experiment and values represent mean ± SEM (n = 4 cultures; **: p < 0.01; *: p < 0.05; unpaired Student's t test).

(B) Single-cell transcriptome analysis (Telley et al., 2016) reveals the expression of neuronal lineage genes in mouse embryonic cortical RGCs in vivo. Shown are the expression profiles of neural lineage genes as violin plots, similarly as in Figure S1A.

(C and D) Increased expressions of neuronal lineage genes in FlashTag⁺ (FT⁺) RGCs 3 hr after pulse labeling. Shown are sample confocal images (C; scale bars, 20 μ m) and quantifications of the percentage of FT⁺Tbr2⁺Pax6⁺ cells, or FT⁺Neurod1⁺Pax6⁺ cells (D), among total FT⁺ cells. Values represent mean \pm SEM (n = 5 sections from 2 animals; ***: p < 0.01; unpaired Student's t test).

(E and F) Precocious expression of Tbr2 and Neurod1 proteins in RGCs upon KD of mRNA deadenylase components in vivo. Shown are sample confocal images (E; scale bars, 20 μ m) and quantifications of the percentage of GFP⁺Tbr2⁺Pax6⁺ cells, or GFP⁺Neurod1⁺Pax6⁺ cells, among total GFP⁺Pax6⁺ cells and the density distribution of GFP⁺Tbr2⁺Pax6⁺, or GFP⁺Neurod1⁺Pax6⁺ cells from the ventricular surface (F). Values represent mean \pm SEM (n = 5 sections from 3 animals; ***: p < 0.001; **: p < 0.01; *: p < 0.05; unpaired Student's t test).

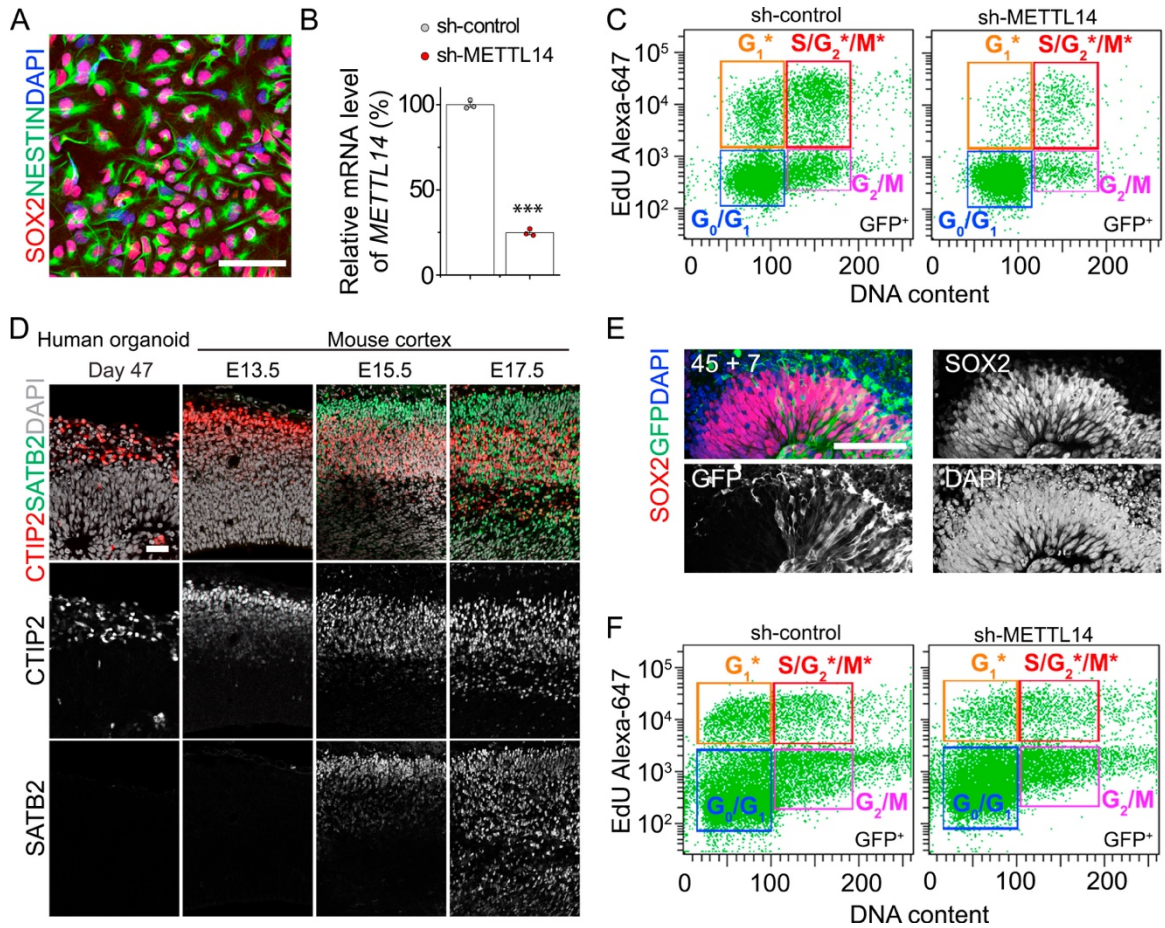


Figure S6: Mettl14 Regulates Cell-Cycle Progression of hNPCs, Related to Figure 6

(A) Validation of hNPC differentiation from human iPSCs. Shown is a sample confocal image. Scale bar, 50 μ m.

(B) Efficacy of the shRNA against *METLL14*. Human NPCs were electroporated to co-express GFP and shRNA-control, or shRNA-METLL14, and dissociated 3 days later. Amount of *METLL14* mRNA in FACS-purified GFP⁺ cells was assessed by Q-PCR. All Ct values were first normalized to the *GAPDH* control. Values represent mean \pm SEM (n = 3; ***: p < 0.01; unpaired Student's t test).

(C) Flow cytometry analysis of cell cycle progression of hNPCs with *METLL14* KD. Similar to Figure S3D.

(D) Comparison of neuronal differentiation among day 47 human forebrain organoids and embryonic mouse cortical development at E13.5, E15.5 and E17.5. Shown are confocal images of immunostaining for CTIP2 and SATB2 and DAPI. Scale bar, 50 μm . Note that day 47 human forebrain organoids exhibit a differentiation pattern most similar to E13.5 mouse cortex.

(E) Electroporation of human forebrain organoid with shRNA-expressing plasmid. Day 45 forebrain organoids were electroporated to co-express GFP and shRNA-control, or shRNA-METTL14, by microinjection into the lumen of organoids. After 7 days, organoids were pulse-labeled with EdU (10 μM) for 30 min, and cultured further for 14 hr. Shown are sample confocal images at day 52. Scale bar, 100 μm .

(F) Flow cytometry analysis of cell cycle progression with *METTL14* KD in human forebrain organoids. Shown are sample dot plots 14 hr after EdU pulse. Cells in a specific cell cycle phase were marked within a box.

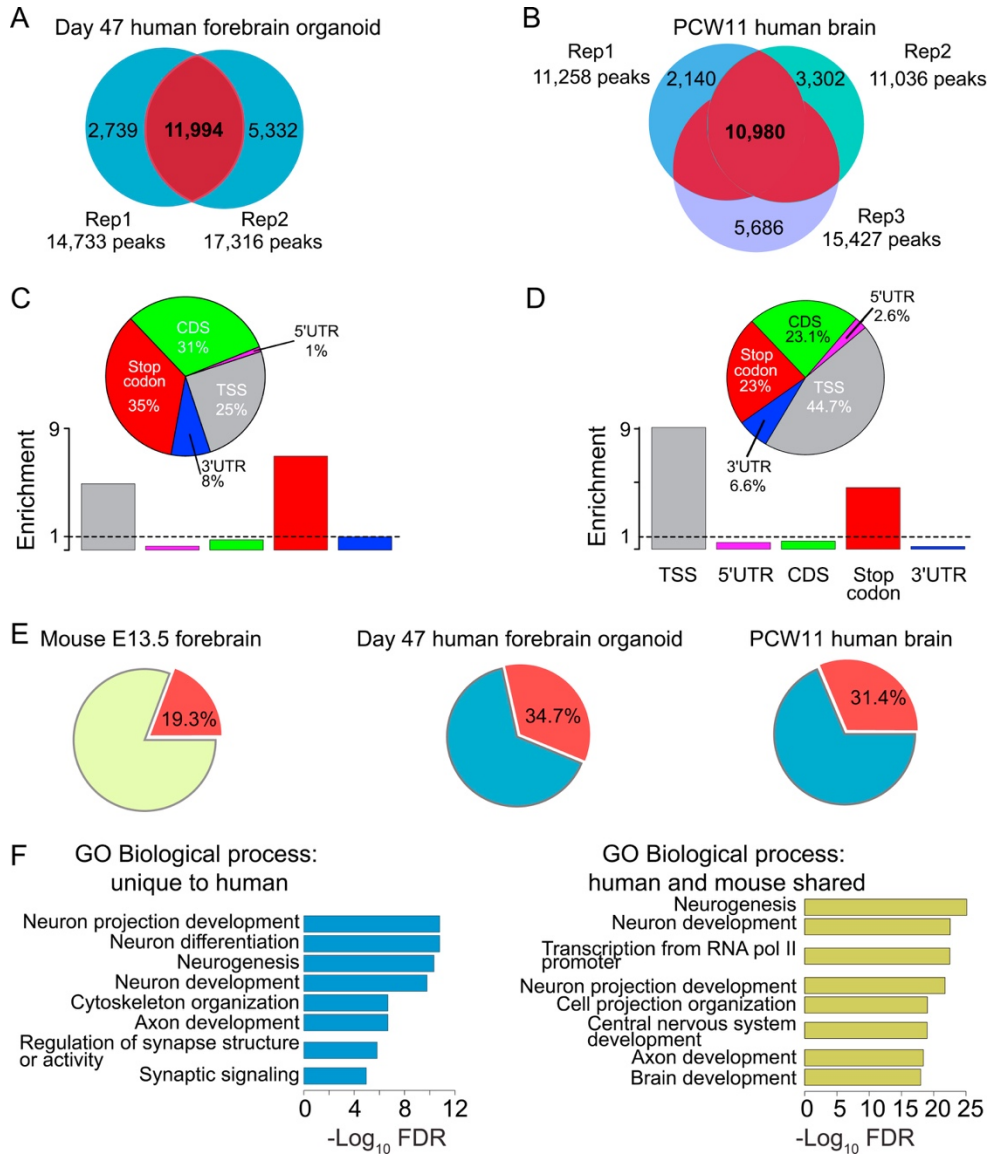


Figure S7: Comparison of m⁶A mRNA Landscaped among Human Forebrain Organoids, Fetal Brain, and Mouse Embryonic Forebrain, Related to Figure 7

(A) Venn diagram showing intersection between m⁶A peaks identified in 2 independent m⁶A-seq of day 47 human forebrain organoids. 11,994 high confidence peaks corresponding to 4,702 genes were used for downstream analysis.

(B) Venn diagram showing intersection between m⁶A peaks identified in 3 independent m⁶A-seq of PCW11 human fetal brain. 10,980 high confidence peaks corresponding to 5,049 genes were used for downstream analysis.

(C and D) Enrichment of m⁶A peaks in 5 non-overlapping transcript segments for day 47 human forebrain organoids (C) and PCW11 fetal human brain (D). Same as in Figure S4B.

(E) Pie charts showing the percentage of m⁶A-tagged genes among all expressed genes in each samples.

(F) GO analysis for m⁶A-tagged genes shared between human forebrain organoids and fetal brain, but not in mouse E13.5 forebrain (left panel), and GO analysis of m⁶A-tagged genes shared among all three samples (right panel).

	A	B	C	
1	Gene	F sequence	R sequence	Note
2	<i>Tbr2</i>	ACCAATAACAAAGGTGCAAAACAAC	TGGTATTTGTGCAGAGACTGCAA	Figure 4F, Figure 5B, Figure S4D
3	<i>Sox1</i>	GCAGCGTTCCGTGACTTTAT	GGCAGAACCACAGGAAAGAAA	Figure 4F, Figure 5B, Figure S4D
4	<i>Neurog2</i>	AGAGGTGGCCCTTGCAATC	CACACGCCATAGTCTCTTTGA	Figure 4F, Figure 5B, Figure S4D
5	<i>Neurod1</i>	ATGACCAAATCATACAGCGAGAG	TCTGCCTCGTGTCTCTCGT	Figure 4F, Figure 5B
6	<i>Neurod2</i>	AAGCCAGTGTCTCTCTGGG	GCCTTGGTCATCTTGCCTTT	Figure 4F, Figure 5B
7	<i>Emx2</i>	GTCCCAGCTTTTAAGGCTAGA	CTTTTGCCTTTTGAATTCGTTC	Figure 4F, Figure 5B, Figure S4D, Figure S4F
8	<i>Cdk9</i>	ACCAAAGCCTCACCGTATAACC	GTGAACTGACTAAGACGTTGCT	Figure 4F, Figure 5B, Figure S4D
9	<i>Rad17</i>	ACAAAGGTGACAGACTGGGTA	CGGCTCATTGTCGGACAGAC	Figure 4F, Figure 5B
10	<i>Mettl3</i>	ATCCAGGCCATAAGAAACAG	CTATCACTACGGAAGGTTGGG	Figure S3A
11	<i>human GAPDH</i>	TGATGACATCAAGAAGGTGGTGAAG	TCCTTGGAGGCCATGTGGGCCAT	Figure S6B
12	<i>human METTL14</i>	TGCAGCACCTCGATCATTTA	CCATGAGGCAGTGTTCCTTT	Figure S6B
13	<i>Actinb</i>	TGTGATGGTGGGAATGGGTCAGAA	TGTGGTGCCAGATCTTCTCCATGT	Figure S4D, Figure S5A
14	<i>Gapdh</i>	TCAACAGCAACTCCCACTTCCA	ACCCTGTTGCTGTAGCCGTATTCA	Figure 5B, Figure S4D
15	<i>pre-Tbr2</i>	AGGAAAGGGGCACCTACAAT	TCTCCGAGGGGAAGGTAAT	Figure S5A
16	<i>pre-Neurod1</i>	AGCATCAGCAACTCGGCTAT	TGACGATTCATAACCCTGGA	Figure S5A
17	<i>pre-Neurod2</i>	TGGTAGAGATGCCACACTCG	TTCATTGTCCCCATCTTC	Figure S5A
18	<i>pre-Emx2</i>	CCTCCCTCTGACGCACCTTA	CCTAATTAGTGGGGGATCA	Figure S5A
19	<i>pre-Sox1</i>	AGACTTCGAGCCGACAAGAG	TCACTCAGGGCTGAACTGTG	Figure S5A
20	<i>pre-Rad17</i>	AGCTCCCGAAAGTAAGGAC	AAGGACACAGCCAGGTATG	Figure S5A

Table S1. List of Primers Used in the Current Study, Related to Figures 4, 5, S3, S4, S5, and

S6

m6A-seq of E13.5 mouse forebrain							
Peaks identified by MACS2 in 2 or 3 replicate m6A sequencing experiments							
meanFC= mean fold change per peak							
meanPval= mean log10 of pvalue per peak							
meanQval= mean log10 of qvalue per peak							
peakID	chr	start	stop	meanFC	meanPval	meanQval	geneName
ID1	chr1	3214882	3215013	4.885505	7.144255	3.405425	Xkr4
ID2	chr1	6240085	6240331	6.51085	9.2955933	5.1929033	Rb1cc1
ID3	chr1	6248531	6248661	5.634675	8.129175	4.25045	Rb1cc1
ID4	chr1	6249794	6249894	6.327155	8.442	4.39114	Rb1cc1
ID5	chr1	6802929	6803028	4.80461	5.94877	2.32011	St18
ID6	chr1	9546255	9546398	5.292365	8.94584	4.93985	Rrs1
ID7	chr1	9546444	9546819	5.99214	10.708588	6.444145	Rrs1
ID8	chr1	9724471	9724834	7.9892433	13.681413	8.8992233	Vcpip1
ID9	chr1	9745930	9746319	5.8125425	8.6134775	4.6057125	Vcpip1
ID10	chr1	9746596	9747079	6.3882867	9.8628467	5.7024433	NR_040462
ID11	chr1	9747630	9747696	6.737455	11.317705	6.945735	NR_040462
ID12	chr1	12858937	12859343	6.4784633	8.9697333	4.9565467	Sulf1
ID13	chr1	12871905	12871987	6.43611	9.365985	5.2686	Slco5a1
ID14	chr1	13174157	13174705	8.7181	15.320307	10.337557	Ncoa2
ID15	chr1	17400649	17400786	7.7674033	13.21216	8.5102133	Intergenic
ID16	chr1	23369807	23370144	7.50186	11.301963	6.8837933	Ogfrl1
ID17	chr1	24029040	24029248	6.45373	9.63832	5.532795	Fam135a
ID18	chr1	25068028	25068219	7.2368967	10.797927	6.4428	Adgrb3
ID19	chr1	25093899	25094215	7.4681533	11.96079	7.4731333	Adgrb3
ID20	chr1	30803731	30804295	6.3815	11.735687	7.28807	Phf3
ID21	chr1	30804874	30804971	5.9861133	9.5155467	5.3768333	Phf3
ID22	chr1	30805176	30805390	5.38401	8.87386	4.8424067	Phf3
ID23	chr1	30805645	30805794	5.5632567	8.6078533	4.6190967	Phf3
ID24	chr1	30829998	30830245	5.4420333	7.5544467	3.7387033	Phf3
ID25	chr1	30830831	30831163	5.42348	8.3669167	4.4087033	Phf3
ID26	chr1	30943043	30943222	3.6231133	7.2170167	3.4469733	NR_002688
ID27	chr1	30946409	30946546	5.225235	10.83373	6.514255	NR_002688
ID28	chr1	33801390	33801610	5.746565	8.30492	4.387885	Zfp451
ID29	chr1	33801702	33802801	6.612605	11.645972	7.204995	Zfp451
ID30	chr1	33802901	33803036	5.3768867	8.6878967	4.6977133	Zfp451
ID31	chr1	34227850	34227951	5.21634	7.048465	3.31287	Dst
ID32	chr1	34589558	34589689	6.187915	8.303105	4.3928	Amer3
ID33	chr1	36103647	36104428	6.4859875	10.31531	6.0129225	Hs6st1
ID34	chr1	36335920	36336229	8.691475	15.27857	10.37783	Kansl3
ID35	chr1	36512050	36512116	6.353905	8.425765	4.513445	Cnm3
ID36	chr1	36549270	36549551	6.7809367	11.964663	7.4776767	Sema4c
ID37	chr1	36549791	36550123	5.54133	8.30883	4.3625067	Sema4c
ID38	chr1	38088169	38088610	6.2676667	9.18391	5.1259067	Rev1
ID39	chr1	38209602	38209730	7.232315	10.498825	6.24031	Aff3
ID40	chr1	38864624	38864742	6.01264	8.18334	4.284375	Chst10
ID41	chr1	38865519	38865840	6.872175	10.21248	6.026315	Chst10
ID42	chr1	42695814	42696910	5.3170667	21.51013	15.646773	Pou3f3
ID43	chr1	42697319	42697646	3.9989233	14.439783	9.5828833	Pou3f3
ID44	chr1	42697783	42699903	4.5423975	19.395915	13.81438	Pou3f3

Table S2. PAGE ONE OF: Dataset from m⁶A-Seq of E13.5 Mouse Forebrain, Day 47 Human Forebrain Organoids, and PCW11 Fetal Human Cortex, Related to Figures 4, 7, and S7

The full table can be accessed online at:

<https://www.cell.com/cms/10.1016/j.cell.2017.09.003/attachment/5f286d35-a275-46d5-b3a0-d1ae0b2d7224/mmc2.xlsx>

Gene ontology analysis: Biological Process								
m6A tagged genes expressed in mouse E13.5 forebrain								
Data from Toppgene Suite								
Category	ID	Name	p-value	q-value Bonf	q-value FDR B&H	q-value FDR	Hit Count in Quer	Hit Count in
GO: Biologic	GO:0006357	regulation of transcription from RN	5.72E-33	4.77E-29	4.77E-29	4.58E-28	369	1922
GO: Biologic	GO:0048699	generation of neurons	9.24E-29	7.71E-25	2.95E-25	2.83E-24	303	1538
GO: Biologic	GO:0030182	neuron differentiation	5.57E-27	4.65E-23	1.16E-23	1.12E-22	279	1405
GO: Biologic	GO:0007049	cell cycle	8.74E-20	7.30E-16	2.52E-17	2.42E-16	307	1771
GO: Biologic	GO:0060284	regulation of cell development	1.66E-17	1.39E-13	3.01E-15	2.90E-14	192	989
GO: Biologic	GO:0045595	regulation of cell differentiation	1.25E-13	1.05E-09	1.66E-11	1.60E-10	275	1706
GO: Biologic	GO:0050768	negative regulation of neurogenesi	1.99E-13	1.66E-09	2.52E-11	2.42E-10	74	287
GO: Biologic	GO:0000278	mitotic cell cycle	1.09E-11	9.11E-08	1.14E-09	1.09E-08	177	1019
GO: Biologic	GO:0048863	stem cell differentiation	2.03E-08	1.69E-04	1.26E-06	1.21E-05	65	303
Wikipathways analysis								
m6A tagged genes expressed in mouse E13.5 forebrain								
Data from ConsensusPathDB								
p-value	q-value	pathway	source	external_id	Hit in query list	members_in size		effective_siz
7.44E-10	9.78E-08	TGF-beta Signaling Pathway	Wikipathwa	WP366	TGFB1; PTK2; SNIP	5747; 6714;		132
1.80E-07	1.58E-05	Mesodermal Commitment Pathwa	Wikipathwa	WP2857	NOG; TCF4; ZFH4;	11190; 3717		153
2.53E-07	1.66E-05	Ectoderm Differentiation	Wikipathwa	WP2858	NUMA1; TRIM33; T	1952; 6657;		142
4.18E-07	2.20E-05	Wnt Signaling Pathway and Pluripc	Wikipathwa	WP399	PPP2R1B; PPP2R3A	6416; 5581;		101
6.02E-07	2.64E-05	ESC Pluripotency Pathways	Wikipathwa	WP3931	PDGFRB; PDGFRA;	3572; 324; 5		115
1.53E-06	5.75E-05	Androgen receptor signaling pathw	Wikipathwa	WP138	PTK2; SUMO1; SMF	9475; 5747;		89
1.78E-06	5.86E-05	Notch Signaling Pathway	Wikipathwa	WP61	EP300; RBPJ; MAPT	23462; 5295		61
6.17E-06	0.000180415	EGF-EGFR Signaling Pathway	Wikipathwa	WP437	PTK2; CRKL; LIMK2;	4303; 3717;		162
1.05E-05	0.000274906	Wnt Signaling Pathway Netpath	Wikipathwa	WP363	CSNK1G1; TCF4; SC	607; 2475; 6		51

Table S3:
GO Analysis of m⁶A-Tagged Genes in E13.5 Mouse Forebrain, Related to Figure 4

RNA-seq of cortical neural progenitors from WT and cKO mice at 0 hr after Actinomycin treatment.							
FDR<0.05							
PPEE= Posterior Probability of being Equally Expresses							
PPDE=Posterior Probability of being Differentially Expressed							
PostFC= Posterior Fold Change							
RealFC= Real Fold Change							
ensembl_gene_id	external_gene_name	PPEE	PPDE	PostFC	RealFC	Mettl14 cko	WT Mean
ENSMUSG00000069045	Ddx3y	0	1	661.3558639	33853.081	338.52081	0
ENSMUSG00000069049	Eif2s3y	0	1	353.3876231	18065.584	180.64584	0
ENSMUSG00000056673	Kdm5d	0	1	311.597793	15923.296	159.22296	0
ENSMUSG00000068457	Uty	0	1	85.18610441	137.376	111.37241	0.8007851
ENSMUSG00000026327	Serpinb11	5.24E-05	0.99994757	58.15789406	69.500337	176.02876	2.5229195
ENSMUSG00000052551	Adarb2	0.026696801	0.973303199	16.52368243	18.99762	59.907957	3.1439718
ENSMUSG00000045672	Col27a1	0.004603385	0.995396615	9.014428334	9.1614658	250.9828	27.386577
ENSMUSG00000091952	Gm17709	0.000169554	0.999830446	8.934921913	11.362691	18.656731	1.632809
ENSMUSG00000070867	Trabd2b	0.046485083	0.953514917	8.919503801	13.413006	11.872037	0.8758593
ENSMUSG00000053469	Tg	8.73E-05	0.999912707	8.811245231	12.134044	14.327506	1.1715934
ENSMUSG00000037621	Atoh8	0.000257702	0.999742298	8.568148964	10.339664	22.192558	2.1373191
ENSMUSG00000101316	Gm12663	0.006771125	0.993228875	7.971177771	9.1691678	26.808511	2.9148576
ENSMUSG00000023391	Dlx2	0.00096234	0.99903766	6.872296796	7.1297572	81.72801	11.454347
ENSMUSG00000026922	Agpat2	8.17E-12	1	6.647117931	6.8902664	80.424654	11.663664
ENSMUSG00000027971	Ndst4	0.026988506	0.973011494	6.193448558	6.4241905	72.667411	11.303085
ENSMUSG00000067276	Capn6	0.037784514	0.962215486	6.017105324	7.641535	11.852731	1.5424017
ENSMUSG00000103945	Gm38228	0.006237365	0.993762635	5.815841352	7.3459468	11.611184	1.5719859
ENSMUSG00000022297	Fzd6	5.31E-09	0.999999995	5.29855075	5.6771728	32.386648	5.6964755
ENSMUSG00000075272	Ttc30a2	0.000383808	0.999616192	5.207635347	5.9001694	18.008275	3.0438571
ENSMUSG00000022546	Gpt	0.001076145	0.998923855	4.838108343	4.988827	63.845824	12.789767
ENSMUSG00000096929	A330023F24Rik	0.042070073	0.957929927	4.831648535	5.2619523	23.540992	4.4657137
ENSMUSG00000051067	Lingo3	8.85E-05	0.999911493	4.649694531	4.6657686	532.47206	114.11526
ENSMUSG00000057886	Cbx3-ps6	0.000916068	0.999083932	4.518289442	4.7720038	33.251284	6.9600875
ENSMUSG00000038451	Spsb2	6.94E-09	0.999999993	4.474860959	4.5449339	113.27348	24.91522
ENSMUSG00000035580	Kcnh8	0.018836966	0.981163034	4.335887746	4.6783948	22.892902	4.8854615
ENSMUSG00000074811	Hps6	1.32E-07	0.999999868	4.333772398	4.3735735	184.12209	42.091063
ENSMUSG00000086043	Gm12473	9.25E-05	0.999907491	4.250686451	4.5130587	28.094768	6.2174324
ENSMUSG00000083307	AA414768	2.10E-06	0.9999979	4.200242619	4.3991146	35.571678	8.0783727
ENSMUSG00000025880	Smad7	0.005336329	0.994663671	4.128047604	4.2617552	50.103839	11.748967
ENSMUSG00000043556	Fbxl7	1.65E-05	0.999983499	4.063230768	4.1524428	71.65577	17.248701
ENSMUSG00000042510	AA986860	0.000136325	0.999863675	4.057386127	4.1735348	55.209445	13.220858
ENSMUSG00000039556	Ppp1r3f	0	1	4.015593778	4.0627951	130.45532	32.102207
ENSMUSG00000049734	Trex1	0.000601225	0.999398775	4.013245443	4.1075856	65.93418	16.044244
ENSMUSG00000106928	Gm43860	1.98E-05	0.999980202	3.993784985	4.2383705	26.065973	6.1423581
ENSMUSG00000038704	Aspdh	5.44E-06	0.999994565	3.923252186	3.9911501	86.359345	21.630215
ENSMUSG00000050830	Vwc2	0.001166433	0.998833567	3.895870618	3.9430607	121.61253	30.834702
ENSMUSG00000034463	Scara3	0.000389111	0.999610889	3.753139417	3.7694112	320.55651	85.034187
ENSMUSG00000025735	Rhbd1	0.003635341	0.996364659	3.751745891	3.9558777	26.793552	6.7656271
ENSMUSG00000060572	Mfap2	0	1	3.739919735	3.765596	201.96207	53.62615
ENSMUSG00000030862	Cpxm2	0.005579672	0.994420328	3.716664829	4.0353587	17.280052	4.2746382
ENSMUSG00000078611	Gm5901	0.003590197	0.996409803	3.600486195	3.7287388	37.991608	10.181544
ENSMUSG00000074890	Lcmt2	0	1	3.594551512	3.6099	306.71157	84.956777
ENSMUSG00000028358	Zfp618	0.001864723	0.998135277	3.545784295	3.5891737	105.83842	29.481029
ENSMUSG00000020258	Glyctk	0.000493642	0.999506358	3.489788472	3.6155432	35.970185	9.9415295
ENSMUSG00000033361	Prrg3	0.000611339	0.999388661	3.458975082	3.4707054	365.68135	105.35514
ENSMUSG00000054676	1600014C10Rik	0.000630556	0.999369444	3.432791049	3.5287763	44.944794	12.729485
ENSMUSG00000036006	Fam65b	0	1	3.416447382	3.4313916	278.87539	81.264719
ENSMUSG00000037216	Lipt1	2.03E-06	0.999997965	3.377362428	3.4234425	88.766274	25.921872
ENSMUSG00000036533	Cdc42ep3	0.001154812	0.998845188	3.312380594	3.3494035	105.1396	31.383531
ENSMUSG00000012017	Scarf2	0.001210283	0.998789717	3.292854827	3.3148754	173.47729	52.325991
ENSMUSG00000075502	Kbtbd6	8.88E-16	1	3.262617402	3.2939436	119.57344	36.294034
ENSMUSG00000030600	Lrfr1	0	1	3.252305015	3.2586385	582.46175	178.73697
ENSMUSG00000079429	Mroh2a	0	1	3.227580691	3.2415582	259.65251	80.094226
ENSMUSG00000060260	Pwwp2b	0.000523548	0.999476452	3.189369815	3.2546015	54.894803	16.859901
ENSMUSG00000043687	1190005I06Rik	0.00786559	0.99213441	3.168480303	3.3341885	21.920746	6.5675362

Table S4. PAGE ONE OF: Dataset from RNA Decay Assay of WT and Mettl14 cKO NPCs,

Related to Figure 4

The full table can be accessed online at:

[https://www.cell.com/cms/10.1016/j.cell.2017.09.003/attachment/f95a05d1-d62d-40b1-9fc2-](https://www.cell.com/cms/10.1016/j.cell.2017.09.003/attachment/f95a05d1-d62d-40b1-9fc2-82a5ab485838/mmc4.xlsx)

[82a5ab485838/mmc4.xlsx](https://www.cell.com/cms/10.1016/j.cell.2017.09.003/attachment/f95a05d1-d62d-40b1-9fc2-82a5ab485838/mmc4.xlsx)

Figure 7C						
Gene ontology analysis: Biological Process						
m6A-tagged genes shared in Day 47 human forebrain organoid and PCW11 fetal human brain						
Data from Toppgene Suite						
Category	ID	Name	p-value	q-value Bonf	q-value FDR	q-value FDR
GO: Biological Process	GO:0022008	neurogenesis	3.67E-34	3.21E-30	2.50E-30	2.41E-29
GO: Biological Process	GO:0030182	neuron differentiation	1.04E-33	9.12E-30	3.04E-30	2.94E-29
GO: Biological Process	GO:0031175	neuron projection development	3.32E-32	2.90E-28	7.25E-29	7.00E-28
GO: Biological Process	GO:0007409	axonogenesis	2.55E-25	2.23E-21	1.86E-22	1.79E-21
GO: Biological Process	GO:0051960	regulation of nervous system development	2.20E-24	1.92E-20	1.48E-21	1.43E-20
GO: Biological Process	GO:0050808	synapse organization	1.84E-21	1.61E-17	1.07E-18	1.03E-17
GO: Biological Process	GO:0007416	synapse assembly	7.54E-17	6.59E-13	2.44E-14	2.36E-13
GO: Biological Process	GO:0021987	cerebral cortex development	2.07E-09	1.81E-05	2.32E-07	2.24E-06
GO: Biological Process	GO:0050890	cognition	7.87E-08	6.88E-04	6.31E-06	6.09E-05
Disease ontology						
m6A-tagged genes shared in Day 47 human forebrain organoid and PCW11 fetal human brain						
Data from Webgestalt						
ID	Name	Size	Observed	Expected	p-value	q-value
PA447208	Mental disorders	679	62	32.04	5.79E-11	7.58E-08
PA444929	Mental retardation	494	98	52.57	6.79E-10	5.92E-07
PA443557	Brain neoplasms	253	57	26.92	2.93E-08	1.53E-05
PA447216	Schizophrenia	471	85	50.12	7.05E-07	1.54E-04
PA443319	Alzheimer disease	225	46	23.94	1.00E-05	1.46E-03
PA447199	Bipolar disorder	423	71	45.01	6.76E-05	6.10E-03
PA443660	Cerebellar diseases	162	36	17.24	1.36E-05	1.88E-03
PA444713	Language development disorders	63	17	6.70	2.27E-04	1.69E-02
Figure 7E						
Disease ontology						
m6A-tagged genes in both human organoid and fetal brain, but not in mouse E13.5 forebrain						
Data from Webgestalt						
ID	Name	Size	Observed	Expected	p-value	q-value
PA447208	Mental disorders	679	62	32.04	4.90E-07	1.28E-03
PA444929	Mental retardation	494	48	23.31	1.78E-06	2.33E-03
PA446858	Neurodegenerative diseases	473	45	22.32	6.49E-06	5.39E-03
PA443319	Alzheimer disease	225	27	10.62	8.24E-06	5.39E-03
PA447158	Tauopathies	210	24	9.91	5.71E-05	2.99E-02
PA446959	Gait ataxia	92	14	4.34	9.98E-05	0.0435667
Disease ontology						
shared m6A-tagged genes among human organoid and fetal brain, and mouse E13.5 forebrain						
Data from Webgestalt						
ID	Name	Size	Observed	Expected	p-value	q-value
PA444148	Fasciculation	61	15	2.13	1.95E-09	5.10E-06
PA446836	Craniofacial abnormalities	333	33	11.65	8.03E-08	8.76E-05
PA444750	Leukemia	492	42	17.22	1.00E-07	8.76E-05
PA443728	Chromosome aberrations	418	36	14.63	6.75E-07	4.42E-04
PA443653	Neoplastic cell transformation	284	28	9.94	8.58E-07	4.49E-04
PA444761	Myeloid leukemia	293	28	10.25	1.60E-06	6.97E-04

Figure S7F
Gene ontology analysis: Biological Process
m6A-tagged genes in both human organoid and fetal brain, but not in mouse E13.5 forebrain
Data from Toppgene Suite

Category	ID	Name	p-value	q-value Bonf	q-value FDR	q-value FDR
GO: Biological Process	GO:0030182	neuron differentiation	3.16E-15	2.13E-11	1.63E-11	1.53E-10
GO: Biological Process	GO:0031175	neuron projection development	4.85E-15	3.26E-11	1.63E-11	1.53E-10
GO: Biological Process	GO:0022008	neurogenesis	2.74E-14	1.84E-10	4.60E-11	4.32E-10
GO: Biological Process	GO:0048666	neuron development	1.46E-13	9.83E-10	1.64E-10	1.54E-09
GO: Biological Process	GO:0061564	axon development	4.90E-10	3.29E-06	2.12E-07	1.99E-06
GO: Biological Process	GO:0007010	cytoskeleton organization	5.05E-10	3.39E-06	2.12E-07	1.99E-06
GO: Biological Process	GO:0050803	regulation of synapse structure	5.16E-09	3.47E-05	1.51E-06	1.42E-05
GO: Biological Process	GO:0099536	synaptic signaling	4.22E-08	2.84E-04	1.09E-05	1.02E-04

Gene ontology analysis: Biological Process
shared m6A-tagged genes among human organoid and fetal brain, and mouse E13.5 forebrain
Data from Toppgene Suite

Category	ID	Name	p-value	q-value Bonf	q-value FDR	q-value FDR
GO: Biological Process	GO:0022008	neurogenesis	4.05E-29	2.39E-25	7.95E-26	7.36E-25
GO: Biological Process	GO:0048666	neuron development	1.90E-26	1.12E-22	2.79E-23	2.59E-22
GO: Biological Process	GO:0006357	regulation of transcription from	2.68E-26	1.58E-22	3.16E-23	2.92E-22
GO: Biological Process	GO:0031175	neuron projection development	1.80E-25	1.06E-21	1.77E-22	1.64E-21
GO: Biological Process	GO:0030030	cell projection organization	1.15E-22	6.78E-19	9.69E-20	8.97E-19
GO: Biological Process	GO:0007417	central nervous system develop	1.56E-22	9.20E-19	1.04E-19	9.65E-19
GO: Biological Process	GO:0061564	axon development	7.53E-22	4.44E-18	4.03E-19	3.73E-18
GO: Biological Process	GO:0007420	brain development	2.31E-21	1.36E-17	1.05E-18	9.69E-18

Table S5. Gene and Disease Ontology Analysis of m⁶A-Tagged Genes in Mouse and Human, Related to Figures 7 and S7

Movie S1 can be accessed online at

<https://www.cell.com/cms/10.1016/j.cell.2017.09.003/attachment/4287e8bd-c9ed-4779-aa24-a5804a21cc90/mmc6.mp4>

Movie S1. Time-Lapse Imaging of WT NPCs Using a Dual-Fluorescence Reporter System, Related to Figure 2

Movie S2 can be accessed online at

<https://www.cell.com/cms/10.1016/j.cell.2017.09.003/attachment/8659ed20-9ae2-41ff-89d9-1e45f465fa71/mmc7.mp4>

Movie S2. Time-Lapse Imaging of Mettl14 cKO NPCs Using a Dual-Fluorescence Reporter System, Related to Figure 2

Chapter 3

m⁶A methylation alters the oscillatory period of Ascl1 to regulate neurogenesis

Foreword: After establishing that m⁶A promotes mRNA degradation in neural progenitor cells to regulate neurogenesis, I was curious if mRNA degradation results primarily in simple downregulation of gene expression, or if it also functions to regulate highly dynamic patterns of gene expression. I therefore wrote a research proposal to study the role of m⁶A in oscillatory expression dynamics for fate-determining transcription factors in neural stem cells. This work was funded first by a Grass Fellowship courtesy of the Grass Foundation, which I used to start this independent research at the Marine Biological Laboratories (MBL) in Woods Hole, MA. My summer at the MBL was crucial for my development as a scientist, and gave me experience in running my own laboratory space and independent experiments. Next, I was awarded an NSF GROW award in concert with the Japanese Society for the Promotion of Science (JSPS) to continue this research in Ryoichiro Kageyama's lab at Kyoto University in Japan. Dr. Kageyama graciously accepted me into his lab for a one year visiting scholar position, during which time I learned bioluminescent live imaging techniques and gained an appreciation for oscillatory expression patterns in developmental processes.

m⁶A methylation alters the oscillatory period of Ascl1 to regulate neurogenesis

C. Vissers^{1,2,*}, H. Song³, R. Kageyama^{4,5,*}

¹ Biochemistry, Cellular, and Molecular Biology Program, Johns Hopkins University School of Medicine, Baltimore, MD 21205, USA

² Japanese Society for the Promotion of Science Strategic Fellow in collaboration with the National Science Foundation (USA)

³ Department of Neuroscience, Perelman School of Medicine, University of Pennsylvania, Philadelphia, PA, 19104, USA

⁴ Institute for Frontier Life and Medical Sciences, Kyoto University, Kyoto 606-8507, Japan

⁵ Institute for Integrated Cell-Material Sciences (iCeMS), Kyoto University, Kyoto 606-8501, Japan

* Correspondence: cvisser@jhmi.edu (C.V.), kageyama.ryoichiro.8r@kyoto-u.ac.jp (R.K.)

I. INTRODUCTION:

Regulation of gene expression has long been accepted as a major regulator of cell fate. However, gene expression does not always occur in a binary “on” or “off” pattern. In fact, dynamic patterns of gene expression often determine downstream functional effects. For example, transcription of Notch genes can occur in bursts, which produce a markedly different result than sustained transcription [177]. Similarly, several Notch pathway genes are expressed in an oscillatory pattern, and this oscillation is necessary to maintain the balance between stem cell self-renewal and differentiation [178]. Of particular interest is *Ascl1*, which oscillates with a period of approximately 3 hours and regulates neural stem cell (NSC) differentiation into neurons [179, 180]. The regulation of *Ascl1* oscillatory dynamics is important for NSC fate but remains poorly understood.

While feedback loops at the transcriptional level are important for oscillatory expression of transcription factors, mRNA processing is another major regulatory aspect [181]. Recently,

methylation at the 6th position of adenosine on mRNA, termed m⁶A, has been shown to regulate mRNA processing, including mRNA degradation in NSCs [88]. My previous work showed that many regulatory transcription factors in neural stem cells are tagged with m⁶A, including Dll1, Ascl1, Olig2, Hes1, Hes7, and Neurog2, all of which produce oscillatory patterns of protein expression [88, 178, 180, 182, 183]. Loss of m⁶A in NSCs elongates mRNA half-life and causes dysregulated transcription factor expression that impairs timely NSC differentiation [88, 89]. A short half-life of mRNA is crucial for oscillatory expression of neural transcription factors, and loss of m⁶A could disrupt this oscillation to impair neural development, as seen in mice lacking m⁶A. While previous studies of m⁶A have focused on the combined effects of m⁶A on many gene transcripts, we are specifically interested in how loss of m⁶A alters the expression patterns of individual genes. This is especially important for understanding how differential m⁶A methylation across cell types and developmental times can alter expression of individual genes that regulate cell fate. Therefore, in this study we investigated the role of m⁶A on the period of Ascl1 oscillation and its subsequent effects on neurogenesis.

We used bioluminescence live imaging techniques to visualize rapid dynamics of Ascl1 expression. Unlike fluorescence markers, which have long maturation and degradation times, luciferase is optimal for imaging the 2-3 hour period of Ascl1 with high temporal resolution [184]. We used NSCs harvested from transgenic mice that express a functional fusion of Ascl1 and firefly luciferase proteins (Ascl1-luc2) [178, 185]. Since single-transcript m⁶A editing techniques are not yet available, we used shRNA against Mettl3 (shMettl3), the m⁶A methyltransferase, to block m⁶A addition to mRNA. We then examined the effects of m⁶A loss specifically on Ascl1 expression patterns to understand how changes in mRNA dynamics regulate gene expression beyond simply increasing or decreasing mRNA abundance.

II. RESULTS:

m⁶A regulates the half-life of Ascl1 mRNA

Using published m⁶A sequencing data we identified Ascl1 as an m⁶A-modified transcript (Figure 1A). Previous work showed that m⁶A promotes degradation of modified mRNA in NSCs. To confirm that m⁶A also regulates the half-life of Ascl1-luc2 fusion mRNA, we used previously validated shRNA against Mettl3 to knockdown (KD) the methyltransferase to block m⁶A formation (Figure 2B). We then performed half-life analysis on Ascl1-luc2 in control NSCs and Mettl3-KD NSCs. Indeed, we found that the half-life of Ascl1-luc2 mRNA was significantly longer upon treatment with shMettl3 than the control (Figure 1C). In contrast, shMettl3 treatment had no effect on the half-life of a control gene transcript, Rad17, that is not m⁶A modified (Figure 1D).

m⁶A regulates the oscillatory period of Ascl1

We next examined the consequence of loss of m⁶A on the oscillatory dynamics of Ascl1-luc2. NSCs were electroporated with either scrambled control shRNA or shMettl3 and allowed to recover for 48 hours before live imaging. Cells treated with control shRNA showed a robust oscillatory expression of Ascl1 with a period of approximately 3 hours, as previously described (Figure 2A,B). Treatment with shMettl3 caused a significant elongation of the oscillatory period to approximately 9 hours (Figure 2C-E).

Ascl1 oscillation dynamics depend on m⁶A-mediated rapid mRNA degradation

To confirm that the changes in Ascl1 oscillatory period caused by shMettl3 treatment were caused by changes in mRNA degradation, we next treated NSCs with shRNA against Ythdf2 (shYthdf2). YTHDF2 is the reader protein that binds to m⁶A to promote degradation of the modified transcript. We first confirmed knockdown of Ythdf2 by qPCR (Figure 3A). Next, we electroporated Ascl1-luc2 NSCs with shYthdf2 and performed live imaging 48 hours later. Ythdf2 knockdown caused a comparable elongation of Ascl1's oscillatory period as treatment with shMettl3 (Figure 3B-D).

Loss of m⁶A impairs neurogenesis in individual cells

Previous studies have shown that *Ascl1* expression regulates differentiation of NSCs into neurons. Specifically, *Ascl1* oscillates during NSC pluripotency, then builds up to sustained expression levels, which induces expression of the differentiation marker *DCX* (Figure 4A). To study the dependency of *DCX* induction and neurogenesis on the period of *Ascl1* oscillation, we harvested NSCs from transgenic mice that express *Ascl1-luc2* and *DCX-DsRed* and performed live imaging analysis. We treated *Ascl1-luc2/DCX-DsRed* NSCs with *shMettl3*, allowed cells to recover for 48 hours, then added neurogenic media at the onset of live imaging. Indeed, we found that control NSCs show oscillations followed by sustained expression and coordinated *DCX* upregulation (Figure 4B). In contrast, loss of m⁶A caused long *Ascl1* oscillatory periods and did not lead to sustained expression nor sudden *DCX* upregulation during 20 hours of live imaging. Instead, there was a slow, linear increase in *DCX* expression over time (Figure 4C). Previous work showed that loss of m⁶A in the developing forebrain slows down the timing of neurogenesis. Therefore, we next examined whether *Mettl3*-KD NSCs would eventually upregulate *DCX* if given more time. Imaging for 35 hours showed that both *Ascl1* and *DCX* are eventually upregulated in *Mettl3*-KD NSCs, confirming the impaired timing, but not loss of competence, for neurogenesis (Figure 4D,E).

III. FUTURE WORK:

In order to isolate the importance of the period of *Ascl1* oscillation for neurogenesis, we designed experiments to optogenetically induce *Ascl1* oscillation in NSCs with an inducible knockout of endogenous *Ascl1* (*Ascl1^{fl/fl}* NSC) [178, 186]. We will virally transfect *Ascl1^{fl/fl}* NSC with Cre to induce *Ascl1* knockout (*Ascl1*-KO), then transfect constructs containing either light-inducible *Ascl1*-luc2 or control light-inducible ubiquitin-luc2 (ub-luc2) as well as shMettl3. We will induce *Ascl1* oscillations with a 3 hour period in Mettl3-KD *Ascl1*-KO NSCs to see if this can rescue the observed deficits in neural differentiation caused by Mettl3 KD. This will help to isolate the role of m⁶A on *Ascl1* from the global changes in m⁶A caused by shMettl3 treatment.

IV. DISCUSSION:

m⁶A is known to regulate neural stem cell behavior and cortical neurogenesis by promoting mRNA degradation of modified transcripts. On a global scale this has major consequences on the differentiation and proliferation capacity of NSCs, though how individual genes contribute to this phenotype is unclear. In this study we show that m⁶A-mediated mRNA processing significantly alters the expression pattern of *Ascl1* protein, which regulates neurogenesis. We find that the timing of differentiation is delayed upon loss of m⁶A, and that the delayed timing correlates with an elongated oscillatory period of *Ascl1*. This provides further insight into the previous finding that loss of m⁶A in the developing forebrain delays the timing of NSC differentiation and cortical neurogenesis. We therefore conclude that m⁶A regulates the temporal dynamics of gene expression, and that this is especially important for genes that are expressed in a non-binary pattern with tightly regulated temporal components.

Methylation of *Ascl1* mRNA may be necessary in NSCs to allow for oscillatory expression of the protein. The significant elongation of *Ascl1* mRNA half-life upon knockdown of Mettl3 confirms that *Ascl1* expression is regulated by the m⁶A system. Indeed, we found significant changes in the oscillatory period of *Ascl1* when we knocked down Mettl3, showing that m⁶A does

not only mediate mRNA abundance, but also contributes to tightly regulated temporal expression patterns at the protein level. The elongated half-life of *Ascl1* mRNA upon loss of m⁶A likely increases the availability of mRNA for translation into protein. Previous models of oscillatory gene expression consider mRNA abundance, the rate of mRNA synthesis, and the rate of mRNA translation to protein, but rarely account for the rate of mRNA degradation. While the rate of mRNA degradation contributes to total abundance, it also has a clear role in allowing for rapid, dynamic changes in protein expression, which are necessary for oscillations that occur on the timescale of a few hours.

We further confirmed that the observed change in *Ascl1* oscillatory period was due to m⁶A-mediated mRNA degradation by knocking down *YTHDF2*—the m⁶A reader protein that promotes degradation of modified transcripts. *Ythdf2* knockdown strongly recapitulated the effects of *Mettl3* knockdown on *Ascl1* oscillations, indicating that *Ascl1* is indeed regulated by the m⁶A-YTHDF2 pathway. An important caveat, however, is that m⁶A and YTHDF2 likely regulate other oscillatory transcription factors as well, including *Hes1*, which is inversely correlated with *Ascl1* oscillation. Therefore, some of the observed effects on *Ascl1* oscillatory expression patterns may be due to changes in oscillation patterns of upstream regulators like *Hes1*. We hope to address this by using optogenetic tools that will allow us to alter only *Ascl1* expression.

Finally, we chose to study the expression pattern of *Ascl1* specifically because it is a fate-determining transcription factor. It is known to regulate neurogenesis, and that oscillatory expression allows for stem cell self-renewal whereas sustained expression causes differentiation into the neurons. The fact that distinct patterns of expression have functional consequences for NSC fate spurred our interest in the regulation of its oscillatory expression pattern. We found that *Mettl3* KD and the subsequent elongation of *Ascl1*'s oscillatory period correlated with abnormal induction of *DCX* expression, indicating impairments in neurogenesis. Control cells in this study and previous studies show an abrupt, coordinated upregulation of *Ascl1* and *DCX*. This indicates there is likely a threshold of *Ascl1* expression necessary to induce *DCX* expression. In contrast,

elongated oscillations often produced a slow, linear increase in low levels of DCX expression. This linear increase may be a result of the semi-sustained *Ascl1* expression that occurs over the long oscillatory period, but does not continue to climb enough to induce truly sustained expression. Eventually, *Mettl3*-KD cells also reached sustained *Ascl1* and DCX expression indicative of differentiation, though the time to differentiation was almost double that of control cells. This reinforces in vivo findings that NSCs lacking m⁶A are competent to produce neurons, but do so much slower than wildtype NSCs [88]. While global changes in m⁶A contribute to this impairment, we hypothesize that temporal dynamics of *Ascl1* expression are especially important and that loss of m⁶A on *Ascl1* severely hinders the rate of neurogenesis. Our proposed optogenetic experiments would further confirm this hypothesis.

In conclusion, we showed that m⁶A mRNA methylation can regulate the dynamics of oscillatory gene expression in fate-determining transcription factors like *Ascl1*. This work highlights the role of m⁶A on individual gene expression patterns and its importance for temporal regulation of gene expression and NSC differentiation. It further supports the complexity of oscillatory expression systems and shows that the dynamics of mRNA processing contribute to oscillatory protein expression.

V. METHODS:

Neural stem cell (NSC) monolayer culture:

NSCs previously harvested from embryonic forebrains from transgenic mice were plated on well plates coated with Matrigel (Corning), and grown in serum-free culture medium DMEM/F12 media (Gibco) plus N2 supplement (R&D systems), 1% penicillin/streptomycin, and 10 ng/mL of FGF and EGF (Invitrogen). The media was changed every other day and cells were passaged prior to confluence.

shRNA constructs:

shRNA against Mettl3 was previously constructed and validated [88]. Briefly, short hairpin RNA against Mettl3 was cloned into a retroviral vector under control of the human U6 promoter (pUEG). shRNA against YTHDF2 was purchased (Millipore Sigma TRCN0000197932) and re-validated in NSCs by RT-qPCR.

RNA purification and quantitative RT-PCR analysis:

RNA for gene expression analysis was purified using a Dynabeads mRNA Direct purification kit (Thermo Fisher), followed by reverse transcription into cDNA using reverse transcriptase and random hexamer primers (Takara Bio). SYBR green (Sigma Aldrich) was used with cDNA and gene-specific primers for quantitative real-time PCR on a StepOnePlus qPCR Machine (Applied Biosystems). All reactions were performed in triplicate.

Half-life measurements of m⁶A-tagged mRNA:

Mouse NPCs were cultured with NSC media to 80% confluence, then treated with 5 μ M Actinomycin D (Sigma) at timepoint zero. Cells were then collected at timepoints 0, 3, and 5 hours after Actinomycin D treatment, washed in PBS, then lysed in RNA lysis buffer (Qiagen). Each sample was normalized for DNA content using a Quant-IT PicoGreen dsDNA Assay Kit (ThermoFisher) and 1 pg of control RNA (Promega) was added to each sample before RNA purification. Total RNA was then purified with an RNeasy Kit and reverse transcribed with SuperScript II First-Strand Synthesis (Thermo Fisher). RT PCR was performed as described above. Standard curves were made by plotting CT values against the known initial concentration of control RNA, then used to calculate the concentration of mRNA for each target at each time point. The natural log of mRNA concentrations at each time points were then used to calculate a linear regression as a function of time, and the slope of this line was used as the decay rate (k_{decay}). Half-life was then calculated as $t_{1/2} = \ln 2 / k_{\text{decay}}$ [176].

NSC electroporation:

Approximately 1.0×10^6 mouse NSCs were resuspended in 100 μ L Optimem media (Gibco) and up to 10 μ g total of plasmid DNA. The cells were placed in a cuvette and electroporated using a NEPA21 super-electroporator with the following conditions: (1) 5 pore-creating pulses of 175V for 2.5 ms with an interval of 50 ms and decay rate of 10%, followed by 5 transfer pulses of 20V for 50 ms at 50 ms intervals and a 40% decay rate. Cells were then re-plated with NSC media and Rock Inhibitor (Y-27632, 3 mM, Cellagentech) and imaged 48 hours later.

Bioluminescence live imaging of NSCs:

NPCs electroporated with shRNA were plated onto Matrigel-coated 35-mm glass-base dishes at 50-60% confluence at least 24 hours prior to imaging. One hour prior to imaging fresh media containing 1mM luciferin was added. Images were taken using an upright microscope (IX81; Olympus) with a 40X objective and a cooled CCD camera (iKon-M DU934P-BV, Andor). Metamorph imaging software (Universal Imaging Corp) was used to adjust filters and camera control. The luminescence channel was set to a 5 minute exposure and images were taken at a time interval of 10 minutes for 20-40 hours. Fluorescence channels were used on the same microscope and exposure times were optimized using Metamorph software.

Image analysis and quantification:

Image analysis was performed as previously described [178]. Briefly, image analysis was performed in ImageJ using custom plug-ins to remove background noise in luminescence images. Custom code is available upon request through the Kageyama Lab. First, a spike-noise filter was applied to reduce cosmic ray noise, and a temporal background reduction filter was applied to reduce CCD readout noise. Tracking individual cells and quantification of bioluminescence or fluorescent signals was conducted using the TrackMate plugin in ImageJ (<https://imagej.net/TrackMate>).

Neurogenic differentiation of NSCs:

Neuronal differentiation was induced by adding neurogenic NS-A medium (Stemcell Technologies) containing 0.5 μ M retinoic acid (Sigma), N2, and B27 supplement. Live imaging began immediately after adding neurogenic media.

FIGURES:

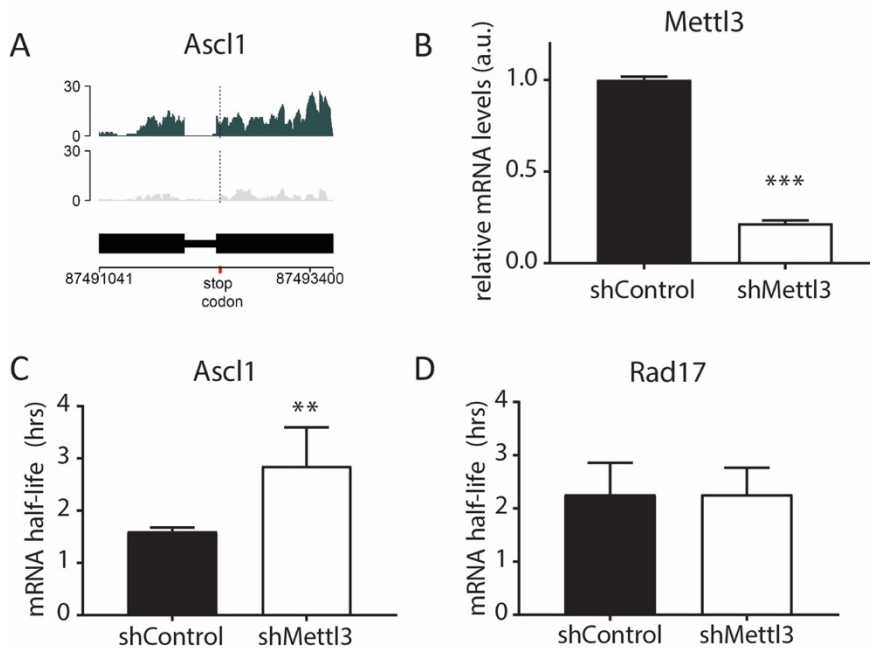


Figure 1: *Ascl1* mRNA is regulated by m^6A

(A) Coverage plot of m^6A on *Ascl1* mRNA. m^6A IP (green) shows significant enrichment over input control (gray). Gene structure is shown below **(B)** qPCR confirmation of *Mettl3* knockdown by shRNA **(C)** Half-life of *Ascl1* mRNA is significantly longer upon *Mettl3* knockdown. **(D)** Half-life of non- m^6A -modified genes like *Rad17* does not change upon *Mettl3* knockdown.

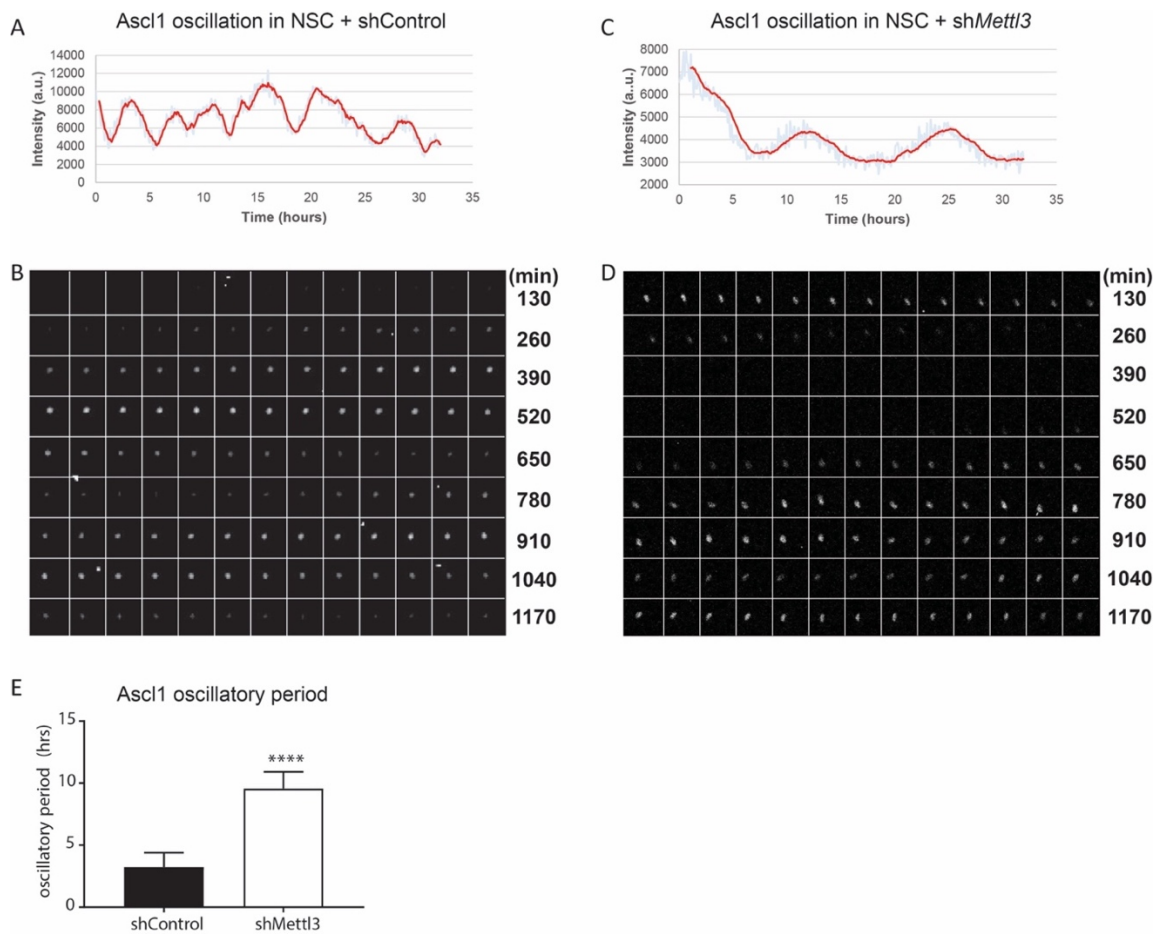


Figure 2: m⁶A regulates the oscillatory period of Ascl1 in NSCs.

(A) Trace plot of Ascl1-luc2 expression measured by luminescence live imaging in control NSCs. (B) Montage image of an individual control NSC. (C) Plot of Ascl1-luc2 expression measured by luminescence live imaging of NSCs treated with *shMettl3* shows elongation of Ascl1's oscillatory period. (D) Montage image of an individual NSC treated with *shMettl3*. (E) Quantification of the oscillatory period of Ascl1 in control and *shMettl3* treated NSCs. Blocking m6A significantly increases Ascl1's oscillatory period. n=20 per condition, ****p<0.0001.

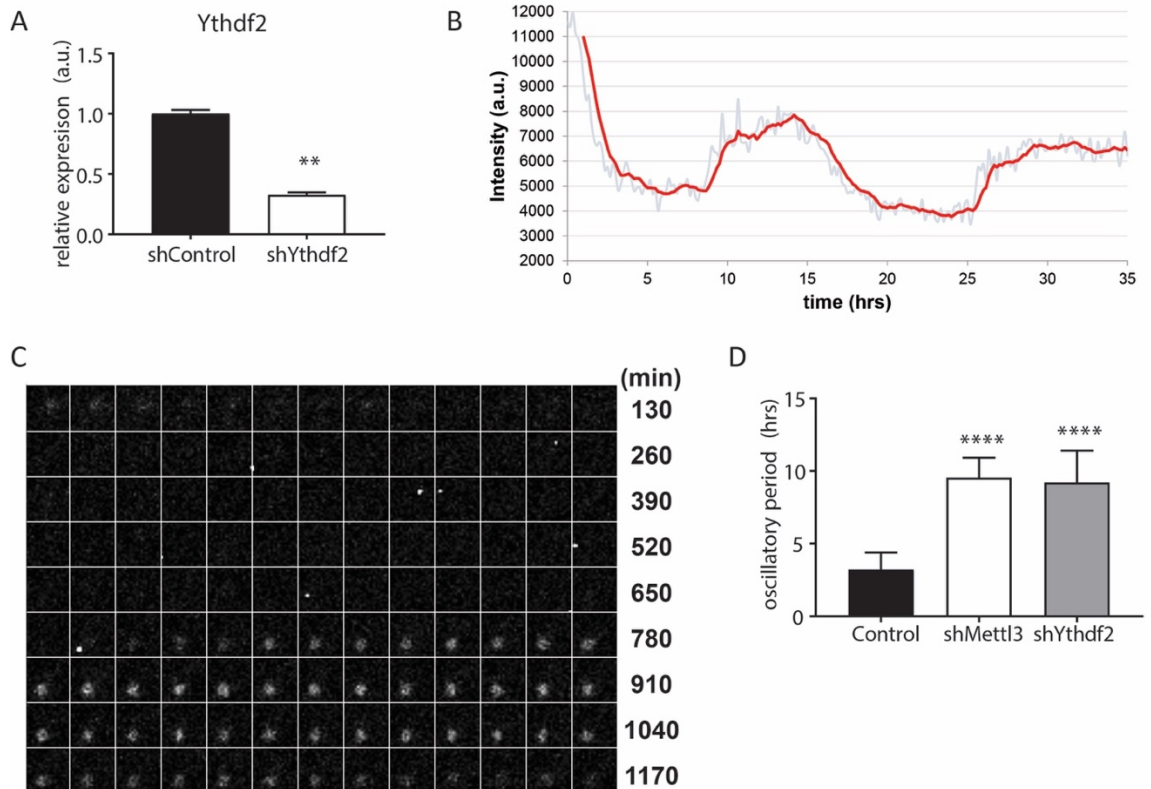


Figure 3: YTHDF2-mediated degradation of m⁶A-modified mRNA regulates Ascl1 oscillations.

(A) qPCR confirmation of *Ythdf2* shRNA knockdown. (B) Trace plot of Ascl1-luc2 expression measured by luminescence live imaging of NSCs treated with sh*Ythdf2* shows elongation of Ascl1's oscillatory period. (C) Montage image of an individual NSC treated with sh*Ythdf2*. (D) Quantification of the oscillatory period of Ascl1 in control, sh*Mettl3*, and sh*Ythdf2* treated NSCs. Blocking either m⁶A addition to mRNA or m⁶A reading by YTHDF2 significantly increases Ascl1's oscillatory period. n=20 per condition, ****p<0.0001.

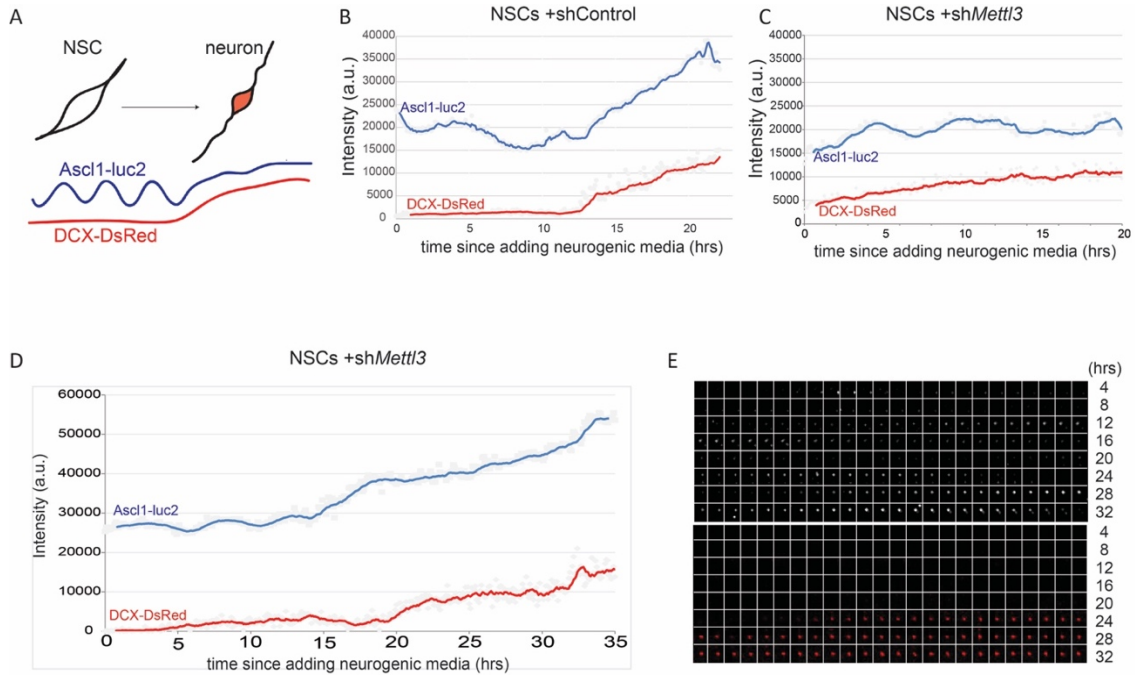


Figure 4: Elongated Ascl1 oscillation impairs the timing of neurogenesis.

(A) Model of transgenic NSC used to measure the coordination of Ascl1 oscillation and DCX as a reporter of neurogenesis. **(B)** Plot of Ascl1-luc2 expression and DCX induction for 20 hours after addition of neurogenic media in NSCs treated with control shRNA. **(C)** Plot of Ascl1-luc2 expression and abnormal DCX expression for 20 hours after addition of neurogenic media in NSCs treated with sh*Mettl3*. **(D)** Plot of Ascl1-luc2 expression and abnormal DCX expression for 35 hours after addition of neurogenic media in NSCs treated with sh*Mettl3*. **(E)** Montage image of a NSC+sh*Mettl3* expression of Ascl1-luc2 (top) and DCX-DsRed (bottom) after addition of neurogenic media.

Chapter 4

m⁶A in Neurodevelopmental Disorders: Fragile X Syndrome

Foreword:

I contributed to a study on m⁶A in Fragile X Syndrome in collaboration with Yongchao Ma's lab at Northwestern University, resulting in a second author publication in *Cell Reports*. In this chapter I will include text and figures from the published work only for parts that I contributed to and will reference the published manuscript in full for pieces that were performed solely by other authors. Therefore, this text is an adaptation of the published manuscript.

FMRP Modulates Neural Differentiation through m⁶A-Dependent mRNA Nuclear Export

Brittany M. Edens^{1,2}, Caroline Vissers³, Jing Su^{1,2}, Saravanan Arumugam^{1,2}, Zhaofa Xu^{1,2}, Han Shi^{1,2}, Nimrod Miller^{1,2}, Francisca Rojas Ringeling⁴, Guo-li Ming⁵, Chuan He⁶, Hongjun Song^{5,*}, Yongchao C. Ma^{1,2,7,*}

¹Departments of Pediatrics, Neurology, and Physiology, Northwestern University Feinberg School of Medicine, Chicago, IL 60611, USA

²Ann & Robert H. Lurie Children's Hospital of Chicago, Chicago, IL 60611, USA

³Biochemistry, Molecular and Cellular Biology Training Program, Johns Hopkins University School of Medicine, Baltimore, MD 21205, USA

⁴Gene Center, Ludwig-Maximilians-Universität München, Munich 81377, Germany

⁵Department of Neuroscience and Mahoney Institute for Neuroscience, Department of Cell and Developmental Biology, Institute for Regeneration, University of Pennsylvania, Philadelphia, PA 19104, USA

⁶Departments of Chemistry and Biochemistry and Molecular Biology, The University of Chicago, Chicago, IL 60637, USA

⁷Lead Contact

I. SUMMARY:

N⁶-methyladenosine (m⁶A) modification of mRNA is emerging as a vital mechanism regulating RNA function. Here, we show that fragile X mental retardation protein (FMRP) reads m⁶A to promote nuclear export of methylated mRNA targets during neural differentiation. Fmr1 knockout (KO) mice show delayed neural progenitor cell cycle progression and extended maintenance of proliferating neural progenitors into postnatal stages, phenocopying methyltransferase Mettl14 conditional knockout (cKO) mice that have no m⁶A modification. RNA-seq and m⁶A-seq reveal that both Mettl14 cKO and Fmr1 KO lead to nuclear retention of m⁶A-modified FMRP target mRNAs regulating neural differentiation, indicating both m⁶A and FMRP are required for the

nuclear export of methylated target mRNAs. FMRP preferentially binds m⁶A-modified RNAs to facilitate their nuclear export through CRM1. Importantly, the nuclear retention defect can be mitigated by wild-type, but not nuclear export-deficient FMRP, establishing a critical role for FMRP in mediating m⁶A-dependent mRNA nuclear export during neural differentiation.

II. INTRODUCTION:

Methylation of RNA on N⁶-adenosine (m⁶A) is emerging as a critical mechanism regulating different aspects of RNA metabolism and function, including stability (Du et al., 2016; Ke et al., 2017; Wang et al., 2014), localization (Roundtree et al., 2017), and translation (Lin et al., 2016; Meyer et al., 2015; Wang et al., 2015). In mammals, methyltransferases METTL3 (methyltransferase-like 3) and METTL14 form a complex that mediates the addition of methyl groups to adenosines in target RNAs (Liu et al., 2014). Readers such as the YTH (YT521-B homology) domain containing proteins bind and interpret m⁶A in a sequencedependent manner (Dominissini et al., 2012; Wang et al., 2014; Xu et al., 2014). The presence of m⁶A erasers has also been revealed, suggesting the complex and dynamic regulation of m⁶A (Jia et al., 2011; Wei et al., 2018). The emerging biological functions regulated by m⁶A include the proliferation and differentiation of embryonic (Batista et al., 2014; Geula et al., 2015) and neural stem cells (Wang et al., 2018; Yoon et al., 2017), as well as complex behaviors and processes such as circadian rhythms (Fustin et al., 2013), stress response (Engel et al., 2018), and learning (Koranda et al., 2018). The RNA-binding protein fragile X mental retardation protein (FMRP) is encoded by the fragile X mental retardation gene (FMR1), mutations in which result in fragile X syndrome, the leading genetic cause of intellectual disability. FMRP contains both a nuclear localization sequence (NLS) and a nuclear export sequence (NES), and it is localized in both the nucleus and the cytoplasm (Eberhart et al., 1996; Kim et al., 2009). The best-studied function of FMRP is the negative regulation of mRNA translation; thus, fragile X syndrome may result in part from the aberrant expression of FMRP target genes (Darnell et al., 2011; Richter et al., 2015). Functionally,

loss of *Fmr1* has been associated with abnormalities in cortical development and dendritic spine formation, which may contribute to aberrant learning and behavior in fragile X syndrome (Castrén et al., 2005; La Fata et al., 2014; Saffary and Xie, 2011; Shen et al., 2019; Tervonen et al., 2009). Here, we report that FMRP binds m⁶A-modified mRNAs and promotes their nuclear export to regulate neural differentiation. *Fmr1* knockout (*Fmr1*KO) mice show delayed cell cycle progression and neural differentiation, phenocopying methyltransferase *Mettl14* conditional KO (*Mettl14*cKO) mice that are devoid of m⁶A modification (Yoon et al., 2017). Both *Mettl14*cKO and *Fmr1*KO lead to the nuclear retention of m⁶A-modified FMRP target mRNAs regulating neural differentiation, including components of Notch and Hedgehog signaling pathways. FMRP preferentially binds m⁶A-modified target mRNAs and cooperates with the nuclear export protein CRM1 to facilitate nuclear export. Nuclear retention of methylated FMRP target mRNAs in *Fmr1*KO can be mitigated by wild-type *Fmr1* but not NES-lacking *Fmr1*ΔNES, suggesting that FMRP is sufficient to drive the nuclear export of m⁶A-tagged FMRP target mRNAs, and this mechanism requires the NES nuclear export. Our findings establish a role for FMRP in regulating m⁶A-dependent mRNA nuclear export during neural differentiation.

III. RESULTS:

First, Brittany Edens showed that *Fmr1* KO mice phenocopy *Mettl14* cKO mice in terms of impaired NPC proliferation in vivo (Figure 1A-D). I then performed flow cytometry analysis to show that purified *Fmr1* KO NPCs have comparable delays in cell cycle progression as *Mettl14* cKO NPCs (Figure 1E-F, Figure S1). Next, Brittany Edens showed that *Fmr1* KO mice also maintain a population of cortical NPCs into postnatal stages, as seen in *Mettl14* cKO mice.

FMRP Preferentially Binds m⁶A-Modified RNAs to Promote Their Nuclear Export during Neural Differentiation

As previous analyses have suggested that FMRP may bind to consensus RNA methylation motifs (Ascano et al., 2012; Edupuganti et al., 2017; Fu et al., 2014), we considered that FMRP could serve as an m⁶A reader to bind and interpret m⁶A to regulate RNA function. To test this possibility, Brittany Edens performed electrophoretic mobility shift assay (EMSA) and Brittany and I both performed bio-layer interferometry analysis to assess the binding affinity of purified FMRP to RNA oligos containing an endogenous m⁶A-modified sequence from mouse Dll1 mRNA or a consensus m⁶A motif. In both analyses, FMRP binding to RNA probes was significantly enhanced by m⁶A methylation, suggesting that FMRP preferentially binds to methylated RNAs compared to non-methylated RNAs (Figures 2A, 2B, S2A, and S2B). As an RNA-binding protein, FMRP localizes to both the nucleus and the cytoplasm (Eberhart et al., 1996; Kim et al., 2009). Therefore, we hypothesized that FMRP could mediate nuclear RNA export. To test this, Brittany Edens and colleagues performed RNA sequencing (RNA-seq) to compare mRNA levels in WT and Fmr1 KO NPC nuclear fractions. We found that genes involved in cell differentiation, neural development (Figure 2C), and embryonic development (Figure S2C) were enriched in Fmr1 KO nuclear fractions, suggesting nuclear retention of these mRNAs upon the loss of Fmr1. To understand how the binding of FMRP to m⁶A affects neural differentiation, I then helped compare genes that are differentially expressed in Fmr1 KO NPC nucleus to our previously published m⁶A-seq dataset of mouse embryonic neural progenitors (Figure 2D). Gene Ontology analysis revealed enrichment in processes such as neurogenesis, neural differentiation, and regulation of gene expression (Figure 2E), as well as chromatin and DNA binding (Figure S2D). Furthermore, pathway analysis yielded terms related to pluripotency and developmental signaling pathways (Figure 2F). Among the mRNAs that are both m⁶A tagged and differentially expressed in Fmr1 KO NPC nucleus, components of the Notch and Hedgehog pathways (Figures 2G and 2H) are particularly interesting, as they are involved in regulating the balance between neural stem cell maintenance and differentiation and have been genetically associated with intellectual disability (Chaudhry et al., 2015; Noor et al., 2010). We focused on six of the m⁶A modified, differentially expressed Notch-

and Hedgehog-related mRNAs (*Ptch1*, *Dll1*, *Dlg5*, *Fat4*, *Gpr161*, and *Spop*), all of which are also validated FMRP targets (Ascano et al., 2012). We quantified the levels of these six targets in WT and *Fmr1* KO NPCs by qRT-PCR. Each mRNA showed increased nuclear retention in *Fmr1* KO NPCs (Figure 2I), suggesting a critical role for FMRP in the nuclear export of these methylated target mRNAs. None of these mRNAs showed increased whole-cell levels, indicating that the increase in nuclear levels was not caused by increased general transcription (Figure S2E). We next tested the effect of the loss of m⁶A on the nuclear levels of these mRNAs in *Mettl14* cKO NPCs. The elevated nuclear retention of the FMRP target mRNAs observed in *Fmr1*KO NPCs was largely phenocopied in *Mettl14* cKO NPCs (Figure 2J), suggesting a nuclear export mechanism that requires both FMRP and m⁶A.

Finally, Edens and colleagues showed that FMRP-mediated nuclear export of m⁶A-modified targets occurs through CRM1 (Edens et al. 2019). This solidified the mechanism of FMRP-m⁶A cooperation to regulate embryonic neurogenesis.

IV. DISCUSSION:

RNA methylation on N6 -adenosine is emerging as a vital mechanism regulating RNA metabolism and function (Domissini et al., 2012; Meyer et al., 2012; Peer et al., 2017). Here, we report that FMRP regulates neural differentiation through m⁶A-dependent mRNA nuclear export. We also elucidated the underlying mechanism by which FMRP preferentially binds m⁶A-modified mRNAs and facilitates their nuclear export through CRM1 to regulate neural differentiation.

In *Fmr1*KO mice, we discovered delayed cell cycle progression and extended maintenance of proliferating neural progenitors into postnatal stages, which are also m⁶A-dependent phenotypes found in methyltransferase *Mettl14*cKO mice that have no m⁶A. These findings suggest a functional relation between FMRP and m⁶A in neural differentiation. Our RNAseq and m⁶A-seq show that both *Mettl14*cKO and *Fmr1*KO lead to nuclear retention of m⁶A-modified FMRP target mRNAs regulating neural differentiation, indicating that both m⁶A methylation and FMRP are

required for the nuclear export of target mRNAs. To establish the link between FMRP and m6A, we first tested the role of m6A in FMRP target mRNA nuclear export by CRM1 RIP in WT and *Mettl14cKO* NPCs. We found significantly reduced CRM1 binding to FMRP target mRNAs in *Mettl14cKO* NPCs that have no m6A (Figures 4G and 4H). This finding highlights the importance of m6A in CRM1-mediated nuclear export of FMRP targets. In addition, we also tested whether the reintroduction of FMRP could rescue the nuclear retention of m6A-tagged FMRP target mRNAs, including components of Notch and Hedgehog signaling pathways that have well-established roles in regulating neural proliferation and differentiation. We found that only WT FMRP, not the NES-lacking and nuclear restricted FMRP Δ NES, alleviated nuclear retention deficits in *Fmr1KO* NPCs (Figures 4I and 4J). Thus, FMRP is sufficient to drive the nuclear export of m6A-tagged FMRP target mRNAs, and this mechanism requires the NES-nuclear export. Our findings establish a critical role for FMRP in regulating m6A-dependent mRNA nuclear export during neural differentiation. Recently, in a large-scale screen to establish a global m6A interactome using mass spectrometry, FMRP was found to be one of more than 20 candidate proteins that may interact with an m6A-modified probe of 4 GGACU repeats with higher affinity in cell lines (Edupuganti et al., 2017). However, a separate study found no preferential binding of FMRP to m6A-modified RNA probes (Zhang et al., 2018), although specific enrichment of m6A in FMRP targets was discovered. The discrepancy could be due to differences in experimental conditions, design of RNA probes, or the quality of purified FMRP protein used. We used full-length FMRP iso1 purified from Sf9 cells and probe RNA sequences from mouse *Dll1* mRNA containing both consensus FMRP-binding sites and RNA methylation motifs to show that FMRP preferentially binds to methylated RNA in both EMSA and bio-layer interferometry analysis. Our data establish the role of FMRP as an m6A reader both in vivo and in vitro. The nuclear export of mRNAs related to Notch and Hedgehog signaling was found in our study to require both FMRP and m6A. Delta-like (*Dll*) binding to the Notch receptor drives the expression of *Hes1* to maintain stem cell pluripotency and suppress differentiation (Ishibashi et al., 1995). Notch has also been

shown to cross-talk with additional pathways, including Hedgehog, to regulate neural stem cell proliferation and differentiation. Hedgehog-induced maintenance of stem cell pluripotency relies in part on the activation of Notch to balance proliferation with differentiation (Dave et al., 2011; Kong et al., 2015). We found increased nuclear retention of m6A-modified FMRP targets related to Notch and Hedgehog pathways in both *Fmr1*KO and *Mettl14*cKO NPCs. Our findings suggest that a disruption in the balance between proliferation and differentiation regulated by FMRP-m⁶A-dependent nuclear export may underlie the aberrant neural differentiation phenotypes observed in *Fmr1*KO and *Mettl14*cKO mice, eventually leading to defects in neuronal function. We discovered the extended maintenance of neural progenitors into postnatal stages, accompanied by delayed cell cycle progression and neural differentiation in *Fmr1*KO mice. Cell cycle phase and duration are tightly coupled to neurogenic potential (McConnell and Kaznowski, 1991; Pilaz et al., 2016). Moreover, there is a strong association between neuronal birth-date and identity (Rakic, 1988). Therefore, the temporal aberrations in neural progenitor cell cycle and differentiation observed in *Fmr1*KO mice may influence cortical development by affecting neuron subtype specification, contributing to functional deficits in fragile X syndrome. Consistent with our observations, alterations of layer-specific neuron migration and localization have been found in *Fmr1*KO mice (La Fata et al., 2014; Tervonen et al., 2009). In addition, delayed cell cycle exit in *Fmr1*KO progenitors may deregulate the excitatory-inhibitory balance in the developing neural circuitry, as inhibitory interneuron integration into the cortex follows and depends upon pyramidal neuron differentiation and patterning (Bartolini et al., 2013). Defects in these processes in *Fmr1*KO mice could drive the altered synaptic landscape that is characteristic of fragile X syndrome. Our study elucidates a mechanism by which FMRP reads and facilitates the nuclear export of m6A-modified mRNAs to regulate neural differentiation, defects in which may contribute to functional deficits in fragile X syndrome.

V. STAR★METHODS

LEAD CONTACT AND MATERIALS AVAILABILITY: Further information and requests for resources and reagents should be directed to and will be fulfilled by the Lead Contact, Yongchao C. Ma (ma@northwestern.edu).

EXPERIMENTAL MODEL AND SUBJECT DETAILS: All animal experiments conducted within this study have been approved by the Institutional Animal Care and Use Committee (Protocol #IS6359), and performed in accordance with federal regulations governing the use of animals in laboratory research. All animals were maintained in standard housing conditions with 12-hour light/dark cycle and food and water available ad libitum. Fmr1 mice (B6.129P2-Fmr1^{tm1Cgr/J} Jackson Laboratory #003025), originally generated by the Dutch-Belgian Fragile X Consortium (1994), were obtained through Dr. Anis Contractor from Dr. David Nelson's laboratory, where the original knockout line was backcrossed onto C57/BL6 background. Heterozygous Fmr1 female mice were bred with C57/BL6 males to yield wild-type and knockout littermates for all FMRP experiments at indicated time points (E17.5, P0, P5, or P7), or utilized for generation of neural precursor cells (NPCs) at E13.5. Because Fmr1 is an X-linked gene, only males were used for knockout analysis with the mating scheme described.

METHOD DETAILS

Cell Culture—Dorsal forebrains from timed-pregnant E13.5 mouse embryos were digested with Accutase (Fisher) to yield dissociated cortical neural precursor cells (NPCs) for culture. NPCs were carried on plates coated with Matrigel (Corning) at 80 µg/ml and maintained in DMEM-F12 medium (GIBCO) supplemented with B27 (GIBCO), N2 (GIBCO), and Glutamax (GIBCO). A growth factor cocktail containing EGF (PeproTech) (20ng/ml) and basic FGF (PeproTech) (20ng/ml) in Heparin (5 µg/ml) was added to the medium fresh. Cells were carried at densities not exceeding 80%, and all experiments were performed on density- and passage-matched NPC cultures. Cells were incubated in standard conditions: 37°C with 5% CO₂. Multiple lines of NPCs were generated from independent litters of Fmr1 wild-type and knockout embryos.

Flow Cytometry—NPCs were exposed to EdU for a duration of thirty minutes, and then either fixed immediately or incubated for five hours and then fixed, and incorporation was detected with the Click-iT Plus EdU Alexa Fluor 647 Flow Cytometry Assay Kit (Invitrogen) according to manufacturer's protocol. DNA was labeled with 7-AAD (Thermo/ Fisher). Data were collected using a BD LSR II Flow cytometer (BD Biosciences). Flow cytometry data were visualized with FlowJo software.

Nuclear RNA Extraction and Quality Control—NPCs were harvested at ~80% confluency with Accutase (Fisher), and nuclear fractions were prepared as described in the NE-PER Nuclear and Cytoplasmic Extraction Kit (Thermo/Fisher) manufacturer's protocol, with minor modifications. 0.5U/ μ l of RNase inhibitor (Ambion/Fisher) was added to the CER1 reagent to prevent degradation. After separation from the cytoplasmic fraction, the nuclear pellet was washed twice with PBS (prepared in DEPC water), and resuspended in an appropriate volume of TRIzol reagent (Invitrogen). The nuclear pellet was homogenized with a Polytron PT 1200E (Kinematica). RNA was purified using the TRIzol reagent manufacturer's protocol, and quantified using the Quant-iT RNA HS Assay Kit (Invitrogen). The efficiency of separation was determined by measuring nuclear and cytoplasmic RNA fractions by qRT-PCR for the relative quantities of nuclear (U1) or cytoplasmic (beta-actin) control genes. Only nuclear RNA preparations with high U1 expression (~8-fold nuclear increase over cytoplasm) and low beta-actin expression (~7-fold cytoplasmic increase over nucleus) were utilized (Figure S4). For qPCR analysis of Leptomycin B (LMB) treated NPCs, a concentration of 20nM was used for 20 hours.

qRT-PCR—RNAs, prepared as described, were reverse-transcribed to produce cDNAs using the QuantaBio qScript cDNA SuperMix (VWR) according to manufacturer's protocol, and the QuantaBio PerfeCTa SYBR® Green SuperMix (VWR) was used for quantitative real-time PCR

(qRT-PCR). All reactions were run on the Applied Biosystems 7500 Fast Real-Time PCR System. The Delta-Delta-Ct method was used to compare relative transcript levels between groups. Unaffected control genes used for normalization are noted in the figure legends for each experiment.

RNA Sequencing and Analysis—RNAs were first subjected to Bioanalyzer analysis (Agilent) to assess RNA quality and concentration prior to sequencing. Libraries of nuclear fraction RNAs were prepared according to the TruSeq RNA-Seq Library protocol (Illumina). Sequencing was performed using the Illumina NextSeq500, 75SE High Output (100 million reads). Gene ontology analysis was performed using the TOPPFUN module of TOPPGENE (Chen et al., 2009). Pathway analysis was performed using Consensus PathDB (Herwig et al., 2016). The gene interaction network schematic was generated using GENEmania (Warde-Farley et al., 2010). Gene sets displayed in heatmaps were obtained from the GO term gene list as indicated within the figures. m6A sequencing data used to generate the list of overlapping Fmr1/m6A-tagged genes was reported previously (Yoon et al., 2017).

Electrophoretic Mobility Shift Assay (EMSA)—Full-length FMRP isoform 1 protein, tagged with six histidine on the amino-terminus, was purified from codon-optimized baculovirus-infected Sf9 cells by Dr. Yang Xiang at ABclonal. Biotinylated oligos were synthesized containing mouse Dll1 mRNA sequence,

5'- GAACACCAACAAGAAGGCGGXCUUUCACGGGGXCCAUGGAGCCGA-3' or a consensus RNA methylation sequence, 5'-CGUGGXCUGGCU-3' (X = A or m6A). In addition, oligos containing a mutated consensus sequence were synthesized 5'- GAUACXGAGAAG-3'. RNA probes were resuspended in DEPC-treated water and denatured by heating to 65°C for ten minutes. Recombinant FMRP protein was diluted in binding buffer (10mM HEPES, pH 8.0; 50mM KCl; 1mM EDTA; 0.05% Triton X-100; 5% glycerol; 10 µg/ml salmon sperm DNA; 1mM DTT;

40U/ml RNasin) to produce graded concentrations. One part RNA probe (20nM final concentration) was then mixed with one part protein (0nM, 125nM, 250nM, 500nM, and 1000nM final concentrations) and incubated at room temperature for thirty minutes. A rabbit anti-FMRP antibody (Cell Signaling Technology) or control rabbit IgG was added to binding reactions to induce supershift. The RNA probe-protein mixtures were run on a 4%–20% TBE gradient gel (Novex) and transferred onto a BioDYNE B nylon membrane (Fisher) using a Trans-Blot Turbo semi-dry transfer system (BioRad). The membrane was crosslinked using a UV Staratlinker 2400 (Stratagene) set to 180mg/cm² for 45 to 60 s. Binding was detected using the Chemiluminescent Nucleic Acid Detection Module (Fisher). Densitometry measurements of all bands were made using the measurement log feature in Adobe Photoshop to calculate the dissociation constant (K_d). Results are averaged from three independent experiments.

Bio-Layer Interferometry Analysis—Bio-layer interferometry analysis of FMRP binding to the short m⁶A-modified and non-modified RNA oligos was assessed using the BLItz system (Forte Bio). Purified His-tagged FMRP (isoform 1) was loaded onto penta-His biosensors. Binding to m⁶A-modified and non-modified RNA probes was recorded at the following RNA concentrations: 5000nM, 2500nM, 500nM, 150nM, and 0nM. Reagents were prepared in binding buffer containing 100mM KCl, 20mM HEPES, 1mM EDTA, 0.05% Triton-X, 5% glycerol, and 1mM DTT. Each reaction was performed using 30 s for all baselines, 120 s for loading, 120 s for association, and 120 s for dissociation. K_D was analyzed using MATLAB's nonlinear curve-fit function as described above, and reported data represent three replicates.

QUANTIFICATION AND STATISTICAL ANALYSIS

Statistical analysis was performed using Prism7 software (Graphpad). Non-linear curve fitting, used to determine the dissociation constant in Figure 3B, was performed using MATLAB (MathWorks). Specific details regarding the statistical test used, number of samples (n), and

number of experimental replicates are in the figure legends. All graphs present mean + SEM. For all experiments, an alpha of 0.05 was used and significance level is indicated as follows: ns $p > 0.05$, * $p \leq 0.05$, ** $p \leq 0.01$, *** $p \leq 0.001$, **** $p \leq 0.0001$. The distributions of all datasets were analyzed prior to analysis to confirm the applicability of the statistical approach (i.e., verify Normal distribution of data subjected to t test).

DATA AND CODE AVAILABILITY

Sequencing data have been deposited to the Gene Expression Database (GEO) at NCBI. Accession: GSE121809

ACKNOWLEDGMENTS

This research was supported by grants from the NIH (R01NS094564 and R21NS106307 to Y.C.M.; R37NS047344, U19MH106434, and P01NS097206 to H. Song; RM1HG008935 to C.H.; and R01MH105128, R35NS097370, and U19AI131130 to G.-l.M.); the Simons Foundation Autism Research Initiative (SAFRI) to H. Song (575050); Cure SMA and The Hartwell Foundation (to Y.C.M.); and the Chicago Biomedical Consortium (to Y.C.M. and C.H.). C.V. was partially supported by an NSF predoctoral fellowship and NIH T32GM007445. We thank Dr. Stephanie Ceman for providing WT and Δ NES Fmr1 constructs, Dr. Anis Contractor for providing Fmr1 KO mice, and Dr. Xiaoxi Zhuang for sharing Mettl14 f/f mice. We thank Dr. Tian Shao for technical assistance in validating antiFMRP antibodies. The research reported in this manuscript was made possible in part by the services of the Keck Biophysics Facility and the NUSeq Core Facility, which is supported by the Northwestern University Center for Genetic Medicine, the Feinberg School of Medicine, and the Shared and Core Facilities of Northwestern University's Office for Research. C.H. is a Howard Hughes Medical Institute Investigator. Y.C.M. is the Ann Marie and Francis Klocke M.D. Research Scholar supported by the Joseph and Bessie Feinberg Foundation.

VI. FIGURES:

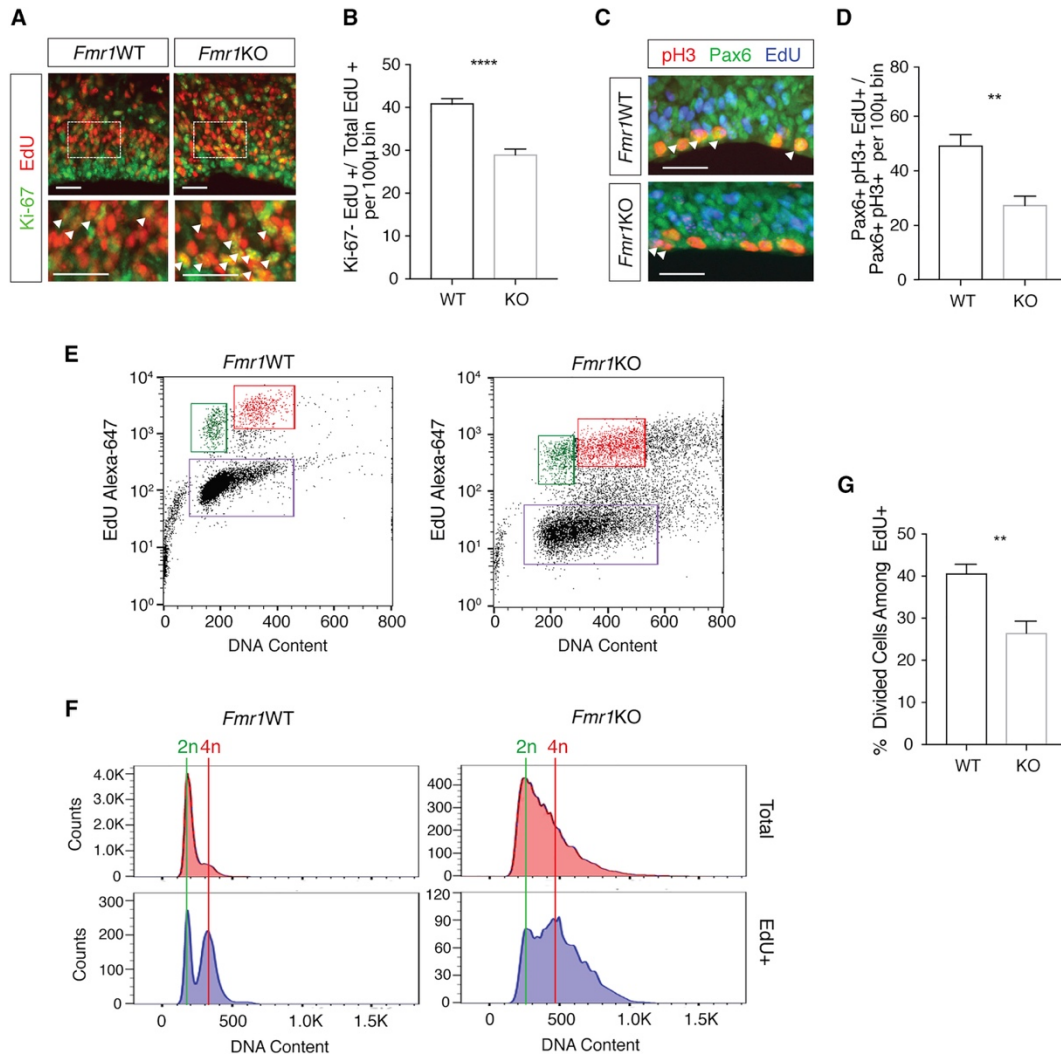


Figure 1: Genetic Knockout of *Fmr1* Leads to Delayed Neural Progenitor Cell Cycle Progression

(A) Analysis of cell cycle exit in WT and *Fmr1KO* E17.5 cortical progenitors. EdU (24 h) staining is shown in red and Ki-67 in green. Enlarged sections (bottom) highlight Ki-67⁺EdU⁺ cells (arrows). Scale bars, 25 μ m.

(B) Significantly fewer EdU⁺ cells exit the cell cycle during the 24-h EdU exposure in *Fmr1KO* cortex (**** $p \leq 0.0001$; $n = 5$ WT, 6 KO mice). Data are presented as mean + SEM.

(C) Analysis of M phase entry in WT and *Fmr1KO* cortical progenitors. pH3 staining is shown in red, Pax6 in green, and EdU in blue. Scale bar, 25 μ m.

(D) Significantly fewer EdU⁺ RGCs entered mitosis within the 2-h EdU exposure in *Fmr1KO* cortex (**p = 0.0017; n = 6 WT, 6 KO mice). Data are presented as mean + SEM.

(E) FACS analysis of cell cycle dynamics in WT and *Fmr1KO* NPCs. Cells labeled by EdU are shown in the upper quadrants. Cells that divided during the 5-h incubation are shown in green and cells remaining in G2/M are in red.

(F) Histograms comparing 2n (divided) and 4n (undivided) NPCs between WT and *Fmr1KO*.

(G) Significantly fewer *Fmr1KO* EdU⁺ NPCs completed division by the end of 5 h compared to EdU⁺ WT NPCs (**p = 0.0018; n = 6 WT, 6 KO mice). Data are presented as mean + SEM.

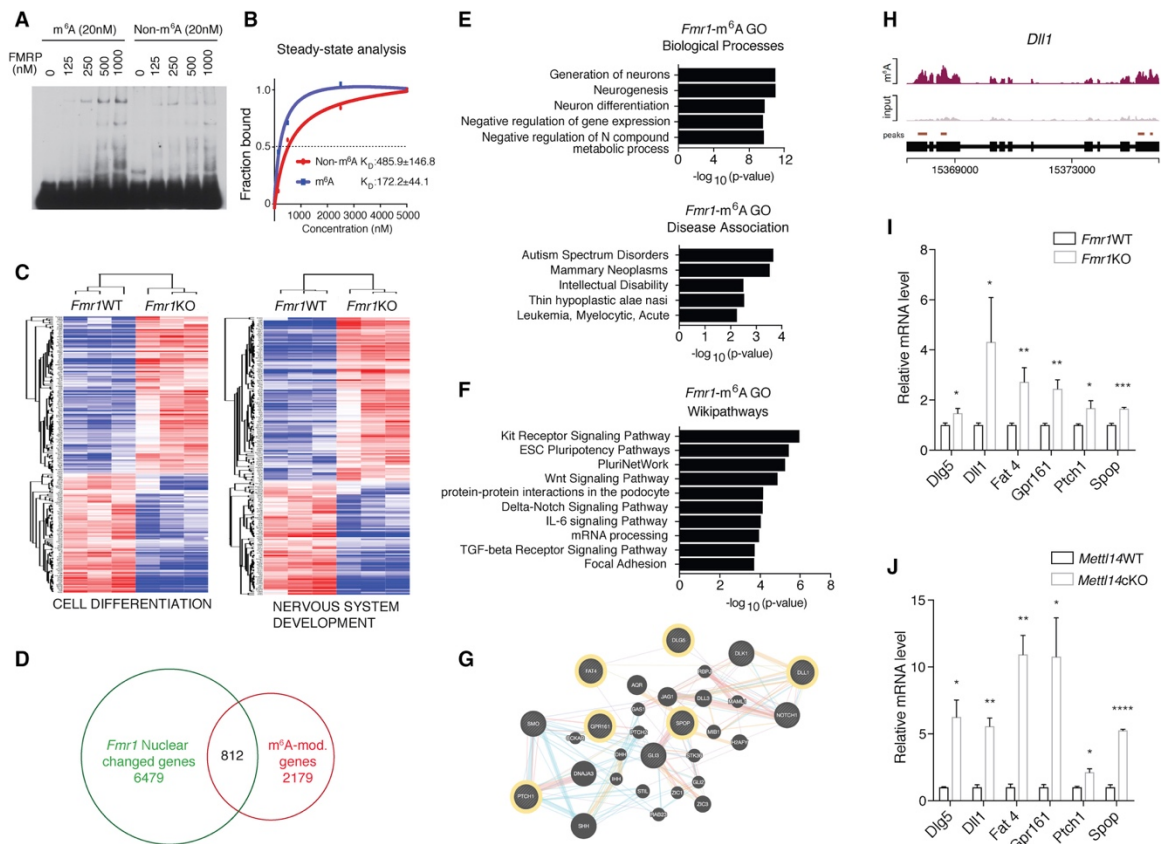


Figure 2: FMRP Preferentially Binds m⁶A-Modified RNAs to Promote Their Nuclear Export in Regulating Neural Differentiation

(A) EMSA comparing FMRP binding to non-methylated (left) or methylated (right) RNA.

(B) Steady-state analysis of FMRP binding to methylated or non-methylated RNA using bio-layer interferometry. Results are averaged from three independent experiments.

(C) Heatmaps comparing WT and *Fmr1KO* NPC nuclear expression of genes related to cell differentiation (left) and nervous system development (right).

(D) Venn diagram showing RNAs that are m⁶A modified and differentially expressed in *Fmr1KO* nucleus.

(E) Gene Ontology (GO) analysis of RNAs that are both differentially expressed in *Fmr1KO* nucleus and m⁶A modified. Biological processes (top) and disease associations (bottom) are shown.

(F) Pathway analysis of RNAs that are both differentially expressed in *Fmr1KO* nucleus and m⁶A modified.

(G) Gene interaction network of Hedgehog- and Notch-related signaling components and their cross-talk. m⁶A-tagged FMRP targets are outlined in yellow.

(H) Coverage plot of m⁶A modification of *Dlll* mRNA.

(I) RNAs of Hedgehog- and Notch-related components are retained in *Fmr1KO* nucleus quantified by qRT-PCR: *Dlg5* (*p = 0.0324), *Dlll* (*p = 0.0433), *Fat4* (**p = 0.0065), *Gpr161* (**p = 0.0020), *Ptch1* (*p = 0.0262), and *Spop* (**p = 0.0006); n = 5 WT, 3 KO biological replicates. Normalization is to *U1*. Data are presented as mean + SEM.

(J) RNAs of Hedgehog- and Notch-related components are retained in *Mettl14cKO* nucleus quantified by qRT-PCR: *Dlg5* (*p = 0.0180), *Dlll* (**p = 0.0016), *Fat4* (**p = 0.0021), *Gpr161* (*p = 0.0361), *Ptch1* (*p = 0.0164), and *Spop* (****p < 0.0001); n = 3 WT, 4 cKO biological replicates. Normalization is to *U1*. Data are presented as mean + SEM.

VII. SUPPLEMENTAL FIGURES:

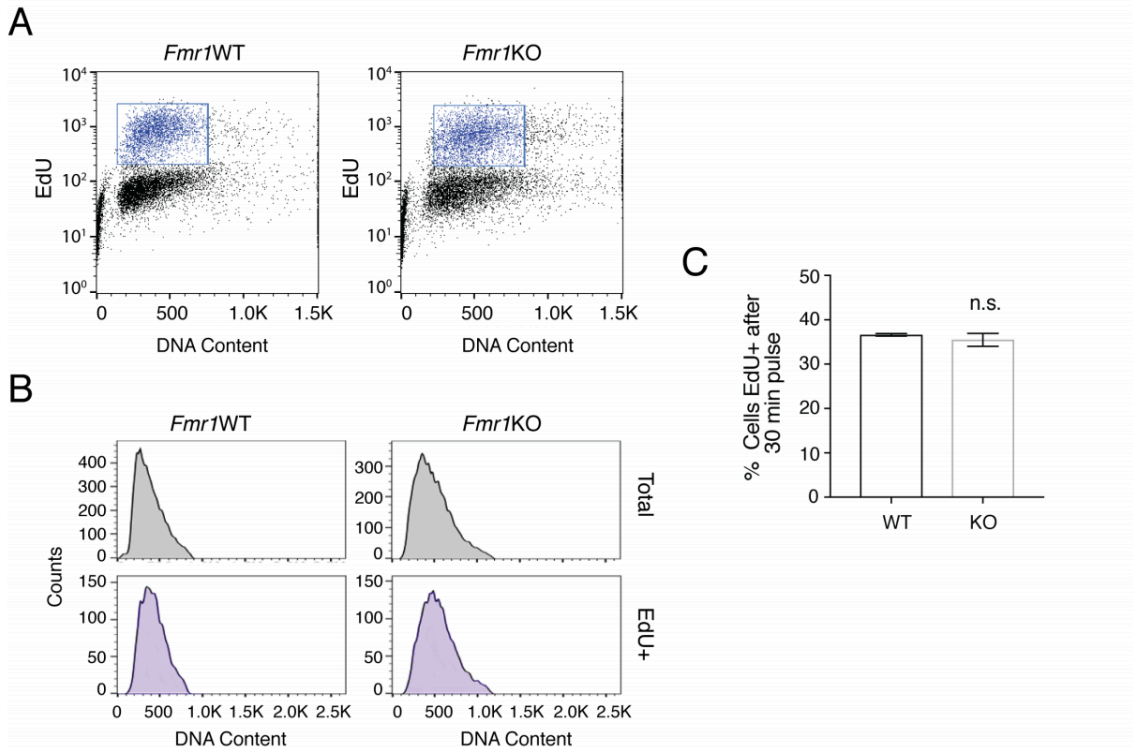


Figure S1: EdU incorporation does not differ between WT and *Fmr1*KO NPCs, Related to Figure 1.

A. FACS analysis of EdU uptake in WT and *Fmr1*KO NPCs. Cells labeled during a 30 minute EdU pulse are shown in blue. B. Histograms comparing WT and *Fmr1*KO NPCs. The number and distribution of NPCs following a 30 minute EdU pulse is similar between WT and *Fmr1*KO. C. There is no significant difference in the number of EdU+ cells following a thirty-minute pulse between WT and *Fmr1*KO NPCs ($p=0.4623$; $n=6$ WT, 6KO).

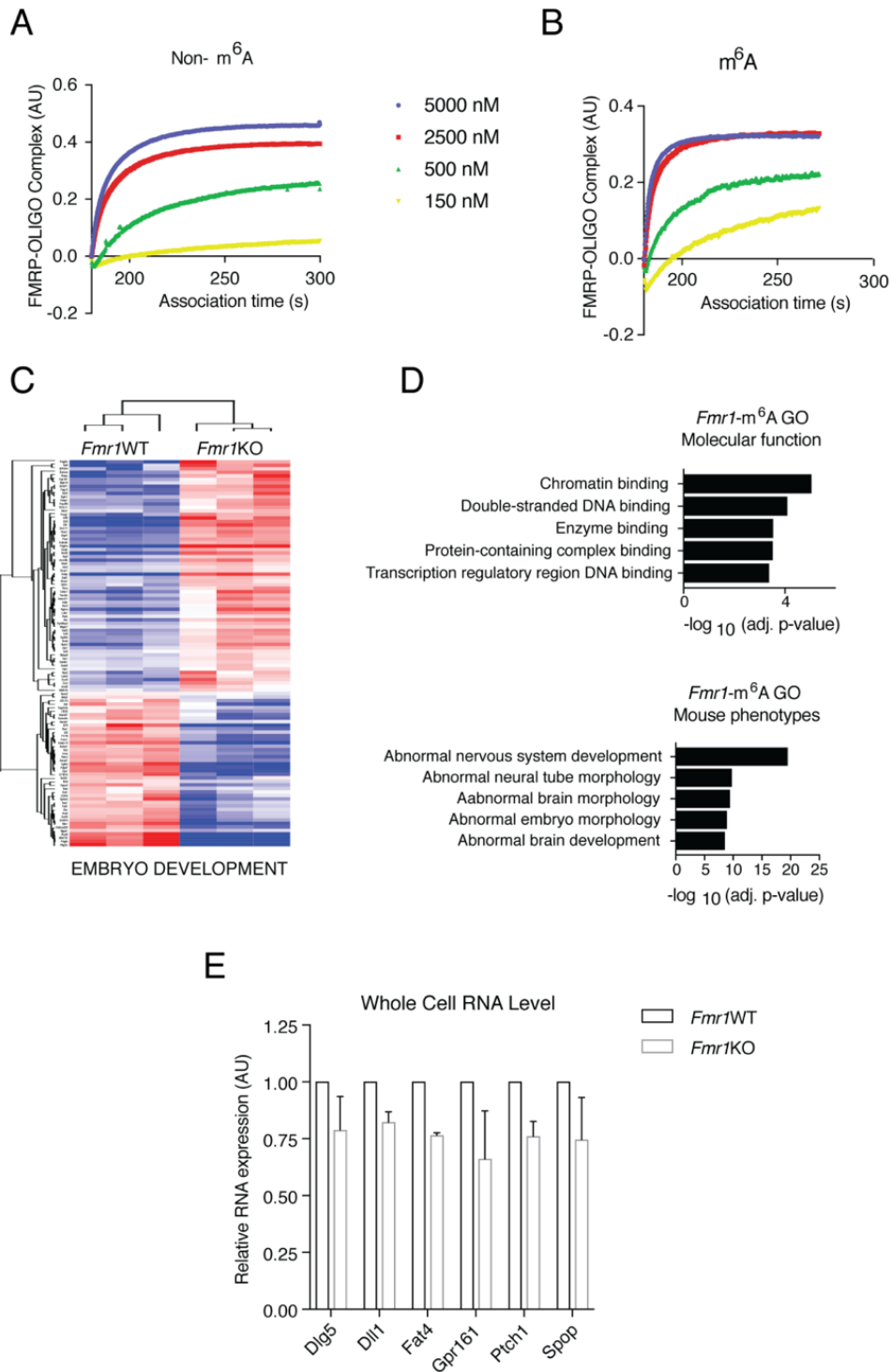


Figure S2: Binding and gene expression analysis, Related to Figure 2.

A. and B. Bio-layer interferometry kinetic association analysis of FMRP binding to methylated (A) or nonmethylated (B) RNA. Results are averaged from three independent experiments. C. Heat

map comparing WT and Fmr1KO nuclear expression of genes related to embryo development. D. Gene ontology analysis of transcripts that are both m⁶A-modified and differentially expressed in Fmr1KO nucleus. Molecular function (top) and mouse phenotypes (bottom) are shown. E. RT-qPCR analysis of m⁶A-tagged FMRP target mRNAs in whole cell WT and Fmr1KO RNAs (n=3WT, 3KO).

Chapter 5

Hypoxia-inducible factors repress translation via ALKBH5-mediated m⁶A demethylation in hypoxic breast cancer cells

Foreword: Dr. Gregg Semenza graciously accepted me into his lab for the second half of my PhD. Based on a previous study of m⁶A in the lab, I met with Dr. Semenza to propose a more in-depth analysis of the epitranscriptome and its dynamics in response to hypoxia.

Hypoxia-inducible factors repress translation via ALKBH5-mediated m⁶A demethylation in hypoxic breast cancer cells

Caroline Vissers^{a,b}, Debangshu Samanta^{b,c}, Tina Huang^{b,d}, and Gregg L. Semenza^{b,c,d,e,f,g,h}

^a Biochemistry, Cellular, and Molecular Biology Graduate Program, Johns Hopkins University School of Medicine, Baltimore, Maryland 21205, USA; ^b Institute for Cell Engineering, Johns Hopkins University School of Medicine, Baltimore, Maryland 21205, USA; ^c Department of Oncology, Johns Hopkins University School of Medicine, Baltimore, Maryland 21205, USA; ^d Department of Genetic Medicine, Johns Hopkins University School of Medicine, Baltimore, Maryland 21205, USA; ^e Department of Pediatrics, Johns Hopkins University School of Medicine, Baltimore, Maryland 21205, USA; ^f Department of Medicine, Johns Hopkins University School of Medicine, Baltimore, Maryland 21205, USA; ^g Department of Radiation Oncology, Johns Hopkins University School of Medicine, Baltimore, Maryland 21205, USA; and ^h Department of Biological Chemistry, Johns Hopkins University School of Medicine, Baltimore, Maryland 21205, USA.

Abstract

I. SUMMARY

N⁶-methyladenosine (m⁶A) is a post-transcriptional modification of mRNA that alters mRNA and protein expression with emerging roles in cancer. Intratumoral hypoxia is a driving force for cancer progression, and expression of the m⁶A demethylase ALKBH5 is strongly induced by hypoxia-inducible factors (HIFs), leading to global changes to the m⁶A landscape in hypoxic cancer cells. However, the relationship between transcriptional and post-transcriptional regulation by HIFs and ALKBH5, respectively, and downstream functional consequences of global changes in m⁶A have not been examined. We report that in hypoxic MCF7 breast cancer cells the majority of HIF-dependent genes are also ALKBH5 dependent at both the mRNA and/or protein levels. Additionally, the repression of cell cycle-promoting genes is both HIF- and ALKBH5- dependent, and knockdown of HIF-1 α /HIF-2 α or ALKBH5 causes increased levels of cancer cell proliferation in hypoxia. Loss of either HIF-1 α /HIF-2 α or ALKBH5 expression also causes increased levels of

m⁶A⁺ RNA. Through m⁶A-RNA sequencing we found that transcripts that promote translation initiation are consistently methylated in control cells, while transcripts encoding proteins mediating oxidative metabolism are dynamically demethylated in response to hypoxia. Loss of HIF-1 α /HIF-2 α or ALKBH5 broadly alters m⁶A coverage patterns on mRNA, and specifically prevents demethylation of oxidative metabolism gene transcripts, which impairs the switch from aerobic to glycolytic metabolism in hypoxia. We also found that the most highly expressed m⁶A reader protein in MCF7 cells is YTHDF1, which promotes translation of m⁶A-modified mRNA. Indeed, m⁶A⁺ mRNAs produce significantly more protein in response to hypoxia than do m⁶A⁻ mRNAs. Therefore, HIFs and ALKBH5 work in concert to limit translation, restrict cancer cell proliferation, and upregulate glycolytic metabolism in response to hypoxia.

Keywords: hypoxia-inducible factors, m⁶A, breast cancer, epitranscriptome, translation

II. INTRODUCTION:

Low intratumoral O₂ levels in breast cancer are associated with a significantly increased risk of metastasis and patient mortality [187]. Hypoxia occurs when O₂ consumption exceeds O₂ supply, due to rapid tumor growth and the formation of intratumoral blood vessels that are structurally and functionally abnormal. The mean pO₂ in advanced breast cancers is 10 mmHg (~1.5% O₂), which induces hypoxic stress in cancer cells that causes broad changes in cell motility, metabolism, and proliferation [188]. At the molecular level, cellular responses to hypoxia are mediated by hypoxia-inducible factors (HIFs), which are heterodimers consisting of an O₂-regulated HIF-1 α or HIF-2 α subunit and a constitutively expressed HIF-1 β ³. Previous studies have shown that HIF-1 and HIF-2 play central roles in cancer progression, as they regulate the transcription of genes involved in tumor growth, angiogenesis, cell metabolism, invasion, metastasis, immune evasion, and resistance to chemotherapy [187, 189-193].

In parallel with the role of hypoxia in the tumor microenvironment, changes in epigenetic regulation of gene expression play a key role in cancer progression [187]. Recently, several groups have shown an interplay between hypoxia and a new gene regulatory pathway—chemical modifications of mRNA—called epitranscriptomics [194-197]. Methylation of the N⁶ position in adenine, termed m⁶A, is the most common modification in mRNA, and is a powerful regulator of mRNA and protein expression. Hypoxia-inducible factors (HIFs) directly induce expression of the m⁶A demethylase AlkB homolog 5 (ALKBH5), causing global changes in m⁶A in human breast cancer cells exposed to hypoxia [196, 198].

m⁶A is added to mRNA by a methyltransferase complex that includes methyltransferase-like 3 (METTL3), METTL14, and Wilms tumor 1 associated protein (WTAP), whereas m⁶A is removed from mRNA by ALKBH5, making m⁶A a dynamic modification that changes according to external and internal stimuli [199]. Fat mass and obesity associated protein (FTO) may also be an m⁶A demethylase, although recent reports suggest it does not act on m⁶A in vivo [21, 200, 201]. A variety of “reader” proteins can interact with m⁶A to determine the fate of the modified RNA

transcript, which includes altered transcript half-life, alternative splicing, nuclear export, and increased translation [199, 202]. The m⁶A modification has been implicated in a variety of cancers, including glioblastoma, acute myeloid leukemia, lung cancer, and breast cancer [92, 203, 204]. The m⁶A eraser ALKBH5 is induced in breast cancer cells exposed to hypoxia. We have previously examined the role of ALKBH5 in breast cancer cells and found that HIF-dependent induction of ALKBH5 expression promoted the cancer stem cell phenotype through increased expression of pluripotency factors [196]. However, the role of ALKBH5 in modulating global gene expression to regulate breast cancer cell responses to hypoxia is unknown.

In this study, we compared MCF-7 subclones with stable expression of short hairpin RNA (shRNA) targeting HIF-1 α and HIF-2 α for double knockdown (HIF-DKD), shRNA targeting ALKBH5 for knockdown (ALK-KD), and shRNA serving as a non-targeting control (NTC). We used RNA sequencing, m⁶A⁺ RNA immunoprecipitation and sequencing, and proteomic analysis of MCF-7 breast cancer cells to identify HIF- and ALKBH5-dependent changes in mRNA and protein expression in response to hypoxia as well as changes in cell proliferation, metabolism and protein synthesis.

III. RESULTS:

HIFs and ALKBH5 coordinately regulate mRNA expression in hypoxic human breast cancer cells.

We first confirmed the knockdown of HIF-1 α in HIF-DKD cells and the knockdown of ALKBH5 in ALK-KD cells using sequence-specific short hairpin RNAs (shRNAs) (Supplementary Figure 1a-b). We used reverse transcription and quantitative real-time PCR (RT-qPCR) to investigate the HIF- and ALKBH5- dependency of genes known to be induced in response to hypoxia. Some genes, such as CA9, are HIF-dependent but not ALKBH5-dependent (Supplementary Figure 1c), whereas others, such as VEGFA, are both HIF and ALKBH5-dependent (Supplementary Figure 1d). To delineate the global regulatory roles of HIFs and ALKBH5 in breast cancer cells, we

performed RNA sequencing of HIF-DKD, ALK-KD, and NTC subclones of MCF-7 cells exposed to 20% or 1% O₂ for 24 h. We identified 1,353 mRNAs whose induction in response to hypoxia was HIF-dependent, and 1,221 mRNAs whose repression was HIF-dependent as well as 1,277 mRNAs whose induction in response to hypoxia was ALKBH5-dependent, and 1,033 mRNAs whose repression was ALKBH5-dependent (Supplementary Figures 2-4). Remarkably, 921 mRNAs lost hypoxic induction in both the HIF-DKD and ALK-KD subclones (Figure 1a), indicating coordinated regulation of mRNA expression by HIFs and ALKBH5.

Gene ontology (GO) analysis confirmed that HIF-dependent mRNAs were significantly associated with “response to oxygen levels”, “response to hypoxia”, and “glucose catabolism to pyruvate” (Supplementary Figure 5a). ALKBH5-dependent mRNAs were significantly associated with “epigenetic regulation” and “regulation of cellular differentiation” (Supplementary Figure 5b). GO analysis of mRNAs that were both HIF- and ALKBH5-dependent for induction were associated with “morphogenesis” and “organelle and vesicle fusion” (Figure 1b).

In addition to the broad induction of genes in response to hypoxia, cells repress expression of many genes, particularly those involved in cell proliferation, to conserve energy under hypoxic conditions. Again, the overlap of genes that were repressed in a HIF- and ALKBH5-dependent manner was remarkably high, with 733 genes losing repression in both groups (Figure 1c). These genes, which are repressed in response to hypoxia in NTC cells but not in HIF-DKD or ALK-KD cells, were significantly associated with cell cycle-related GO terms (Figure 1d and Supplementary Figure 5c-d).

To assess the functional relevance of impaired repression of cell cycle mRNAs, we exposed MCF-7 subclones to 20% or 1% O₂ and counted the number of live cells at 24, 48, and 72 h. Compared to NTC cells, the number of HIF-DKD, and especially ALK-KD cells, were significantly increased under hypoxic as compared to non-hypoxic conditions (Figure 1e). To determine whether these differences in cell number were attributable to differences in cell proliferation, we analyzed DNA synthesis by treating cells with 5-ethynyl-2-deoxyuridine (EdU) after 48 h of exposure to 1%

O₂. Whereas hypoxia inhibited EdU incorporation by 12% in NTC cells, this reduction in DNA synthesis was significantly impaired in HIF-DKD, and especially ALK-KD, cells (Figure 1f). These results demonstrate that HIFs and especially ALKBH5 are necessary to inhibit DNA replication and cell division under hypoxic conditions.

m⁶A levels in RNA are dynamically regulated by HIFs and ALKBH5 in response to hypoxia.

Recent reports show that FTO does not demethylate m⁶A in vivo [21, 201], suggesting that ALKBH5 is the only m⁶A demethylase, whereas the role of FTO is unclear. Nonetheless, expression of FTO is much less than ALKBH5 in MCF-7 cells and is not induced in response to hypoxia (Supplementary Figure 6). We therefore moved forward with our analysis of ALKBH5 as the major regulator of m⁶A demethylation in response to hypoxia. HIF-dependent ALKBH5 expression leads to increased demethylase activity and decreased m⁶A⁺ RNA levels (as determined by ELISA) in hypoxic NTC cells; in contrast, m⁶A levels remain static in hypoxic HIF-DKD cells, whereas in ALK-KD cells, baseline m⁶A levels are significantly increased, and rise further in response to hypoxia (Figure 2a).

We used an antibody that specifically recognizes m⁶A to perform methylated-RNA immunoprecipitation and sequencing (MeRIP-Seq) [1, 205] in order to identify mRNAs that are methylated in NTC, HIF-DKD, and ALK-KD cells exposed to 20% or 1% O₂ for 24 h. In particular, we identified mRNAs that are dynamically methylated or demethylated in response to hypoxia. The number of unique transcripts tagged with m⁶A specifically under hypoxic conditions increased from 543 in NTC to 903 in HIF-DKD and 1564 in ALK-KD cells (Figure 2b). This finding suggests that the methyltransferase complex becomes more promiscuous in response to hypoxia and that ALKBH5 normally limits this response.

GO analysis revealed that in non-hypoxic NTC cells, mRNAs modified with m⁶A were significantly associated with mRNA processing and translation (Figure 2c). m⁶A⁺ mRNAs in hypoxic NTC cells are also enriched for these same GO terms (Supplementary Figure 7). In

contrast, many more unique gene transcripts are aberrantly methylated in HIF-DKD and ALK-KD cells. 360 mRNAs were m⁶A-modified in both HIF-DKD and ALK-KD, but not in NTC, cells in response to hypoxia, indicating that these transcripts are normally demethylated by upregulated ALKBH5, and GO analysis revealed that these mRNAs were associated with chromatin and nucleosome organization (Figure 2d). Another study also found that m⁶A mRNA modification can broadly influence gene expression by modifying transcripts involved in epigenetic regulation [89].

62 mRNAs were specifically demethylated in hypoxic NTC cells, but remain methylated in hypoxic HIF-DKD cells and in both hypoxic and non-hypoxic ALK-KD cells. These mRNAs were significantly associated with mitochondrial regulation and oxidative metabolism (Figure 2e), suggesting that ALKBH5-dependent mRNA demethylation contributes to the switch from oxidative to glycolytic metabolism in hypoxic breast cancer cells. Changes in cancer cell metabolism in response to hypoxia are known to be HIF-dependent [206], but have never been studied in relation to ALKBH5. Considering the targeted, ALKBH5-dependent demethylation of oxidative metabolism genes in response to hypoxia, we tested changes in mitochondrial respiration in response to hypoxia in each subclone. We measured oxygen consumption rate (OCR) as a measure of mitochondrial respiration and extracellular acidification rate (ECAR) as a measure of glycolysis. As expected, NTC cells significantly shifted toward glycolytic metabolism (decreased OCR/ECAR ratio) after 72 h of exposure to hypoxia (Figure 2f). In contrast, both HIF-DKD and ALK-KD cells have significantly higher OCR/ECAR ratios compared to NTC cells in hypoxia. This confirms that HIF and ALKBH5 both regulate the shift toward glycolytic metabolism in hypoxic MCF-7 cancer cells.

ALKBH5 is necessary to maintain the normal distribution of m⁶A on mRNAs in hypoxic cells.

Some mRNAs, such as IFT20, are methylated in hypoxic conditions in HIF-DKD and ALK-KD, but not NTC, cells. This provides an example of transcripts that become aberrantly methylated when HIF or ALKBH5 are expression is silenced (Figure 3a). Other transcripts, such as TSMF,

are specifically demethylated in response to hypoxia in NTC cells but remain methylated in HIF-DKD and ALK-KD cells (Figure 3b).

A growing body of experimental evidence suggests that m⁶A in the 5'-untranslated region (5'-UTR), coding sequence (CDS) and 3'-UTR may be associated with distinct regulatory functions [1, 207, 208]. m⁶A coverage on introns remains fairly constant in all subclones between normoxia and hypoxia, while coverage of the UTRs and CDS is more dynamic (Figure 3c). In NTC cells, hypoxia is associated with decreased 5'-UTR methylation and increased 3'-UTR methylation, whereas in both HIF-DKD and ALKBH5-KD cells, hypoxia is associated with increased 5'-UTR methylation and decreased CDS methylation (Figure 3d). Increased 5'-UTR methylation was also observed in mouse embryo fibroblasts subjected to heat shock and was associated with increased m⁶A-mediated translation [209]. ALK-KD cells show the most dramatic changes in m⁶A coverage, with increased methylation in both the 5'-UTR and especially in the 3'-UTR in response to hypoxia. Thus, ALKBH5 appears to preferentially demethylate the UTRs of mRNAs in MCF-7 breast cancer cells.

HIFs mediate multiple aspects of post-transcriptional regulation via ALKBH5.

The fate of m⁶A-modified transcripts in a cell depends largely on the particular “reader” proteins that are expressed, which varies across cell types and developmental stages [26, 202, 210]. To address this issue, we analyzed our RNA sequencing data to determine the relative expression levels of mRNAs encoding known m⁶A readers in MCF-7 cells (Figure 4a). The most highly expressed reader was YTHDF1, which increases the translation of m⁶A-modified transcripts [202, 211]. Expression of YTHDF1 has been correlated with malignant tumor behavior and decreased patient survival in colorectal cancer [212]. YTHDC1, which was also highly expressed, regulates alternative splicing, although its function appears to vary across cell types [202, 210, 213, 214]. We found examples of hypoxia-induced alternative splicing that correlated with m⁶A status as well as alternative splicing that was independent of m⁶A status. For example, ANKZF1 mRNA is

alternatively spliced in hypoxic cells [215]. In NTC cells, ANKZF1 mRNA was not m⁶A-modified and alternative splicing was induced by hypoxia, whereas in HIF-DKD and ALK-KD cells, hypoxia induced aberrant m⁶A modification and alternative splicing of ANKZF1 mRNA was not induced (Supplementary Figure 8a). In contrast, although CYR61 mRNA was aberrantly m⁶A-modified in HIF-DKD and ALK-KD cells, hypoxia-induced alternative splicing [216] was not affected (Supplementary Figure 8b).

Expression of YTHDF2, which regulates mRNA degradation, was mildly increased in MCF-7 cells exposed to hypoxia in a HIF- and ALKBH5-independent manner (Figure 4a). Among mRNAs with hypoxia-induced expression in NTC cells, 132 mRNAs were only m⁶A-modified at 1% O₂ compared to 31 mRNAs that were only m⁶A-modified at 20% O₂, whereas among hypoxia-repressed mRNAs, 91 were m⁶A-modified only at 20% O₂ as compared to 43 that were m⁶A-modified only at 1% O₂ (Supplementary Figure 8c), suggesting that m⁶A modification is actually correlated with increased mRNA abundance ($p < 0.001$, X^2 test). This indicates that YTHDF2-mediated mRNA degradation is not the primary mechanism of m⁶A action in MCF-7 breast cancer cells. However, there is currently very little understanding of how m⁶A reader proteins selectively bind particular transcripts, and how co-expressed reader proteins might compete with one another. The expression of YTHDF2 suggests that it has specific mRNA targets in MCF-7 cells, and its specificity and competition with YTHDF1 warrants future investigation.

As described above, YTHDF1 binding to m⁶A⁺ mRNA facilitates translation of mRNA into protein. Under hypoxic conditions, many new proteins need to be synthesized, but cellular resources must also be conserved, leading to an overall decrease in mRNA and protein synthesis. This led us to examine an often-overlooked category of mRNAs: those that show no significant differential expression in NTC cells in response to hypoxia, but gain significant induction in HIF-DKD and ALK-KD cells. We found 786 HIF-regulated and 1,107 ALKBH5-regulated mRNAs that are aberrantly induced in response to hypoxia, of which 593 genes are both HIF- and ALKBH5-

dependent (Figure 4b). The top gene ontology term for these genes is “translation initiation” (Figure 4c).

Analysis of the fold-induction of mRNAs classified under the GO terms “translation initiation” (GO:0006413) and “ribosome” (GO:0005840) revealed that there was a large skew toward significant induction of translation-related genes in both HIF-DKD and ALK-KD as compared to NTC cells (Figure 4d). We next investigated the functional consequences of this induction by quantifying levels of translation initiation in response to hypoxia using L-homopropargylglycine (HPG)-Alexa Fluor 488 to label newly synthesized proteins (Supplementary Figure 8d). At 20% O₂, there was no significant difference in the levels of translation initiation between the NTC and HIF-DKD subclones, whereas translation initiation was significantly higher in the ALK-KD subclone (Figure 4e), which is consistent with the observed changes in m⁶A levels (Figure 2a). At 1% O₂, translation initiation was significantly greater in HIF-DKD and especially in ALK-KD cells (Figure 4f).

HIF and ALKBH5 regulate differential protein expression through m⁶A.

Dysregulated translation initiation in HIF-DKD and ALK-KD cells implied changes in the proteome in response to hypoxia and/or loss of HIF or ALKBH5 expression. To test this hypothesis, we performed mass spectrometry analysis of the MCF-7 subclones after incubating the cells at 20% or 1% O₂ for 48 h. Proteomic analysis revealed that 263 proteins were hypoxia-induced (Figure 5a) and 471 proteins were hypoxia-repressed (Figure 5B) in NTC cells but not in HIF-DKD or ALK-KD cells (Figure 5a-b). Many of the differentially expressed proteins were not differentially expressed at the mRNA level (Supplementary Figure 9a), which is consistent with a specific effect of m⁶A modification on mRNA translation. Several studies have previously reported a low correlation between mRNA and protein expression and identified multiple contributing factors [217, 218]. In our study, stringent selection criteria for high-confidence HIF- and ALKBH5-dependent mRNA and protein expression, the use of independently prepared samples for RNA and

protein analysis, and the number of biological replicates likely contributed to the limited overlap between differentially expressed mRNAs and proteins. Furthermore, growing awareness of the epitranscriptome is helping to explain the common discordance between mRNA and protein levels, reinforcing the necessity to look beyond only RNA sequencing results to understand which genes are being dynamically expressed in a cell [219].

GO analysis of proteins that are hypoxia-induced in a HIF- and ALKBH5-dependent manner revealed that they are significantly associated with metabolic processes and cellular respiration (Figure 5c). Proteins that are hypoxia-repressed in a HIF- and ALKBH5-dependent manner are associated with a variety of biochemical processes, including “catabolic processes”, “protein stabilization”, and “protein glycosylation” (Figure 5d). Additionally, loss of ALKBH5 reduces the number of significantly downregulated proteins to approximately half as many as in controls (Supplementary Figure 9b). Next, we quantified the \log_2 fold-change of proteins encoded by m⁶A⁺ or m⁶A⁻ mRNA. We found that proteins with corresponding m⁶A⁺ modified mRNA are induced at significantly higher levels in hypoxia than proteins made from unmethylated mRNA (Figure 5e). This supports our model that hypoxic stress causes HIF-dependent induction of ALKBH5, which demethylates many mRNAs to limit their translation (Figure 5f).

In accordance with the increase in methylated transcripts in hypoxic HIF-DKD and ALK-KD cells compared to NTC cells (Figure 2a-b) and global increases in translation (Figure 4f), some proteins become aberrantly induced in response to hypoxia in HIF-DKD and ALK-KD cells. 397 proteins in HIF-DKD and 269 proteins in ALK-KD cells are significantly ($p < 0.05$) induced in response to hypoxia that are not induced in NTC cells (Supplementary Figure 10a). These proteins fall into diverse gene ontologies including oxidative processes, mitosis, antigen presentation, and mitochondrial RNA modification (Supplementary Figure 10b-d). Furthermore, proteins that mediate translation initiation (GO:0045948) are more highly expressed in HIF-DKD and ALK-KD cells than NTC cells under hypoxic conditions (Supplementary Figure 10e), providing examples of how HIFs, through ALKBH5, can alter the proteome beyond direct transcriptional targets.

IV. DISCUSSION:

Hypoxia and HIF-dependent transcriptional activation are crucial for cancer progression [187], and are known to induce expression of the m⁶A demethylase ALKBH5 [196, 198]. However, the extent to which HIFs functions through ALKBH5 to alter gene expression in breast cancer was unknown. In the present study, we showed that the genes regulated by HIFs in response to hypoxia are largely also ALKBH5-dependent. We found that loss of HIFs or ALKBH5 causes highly overlapping changes in the response to hypoxia compared to controls, indicating that the action of HIFs extend beyond their direct DNA binding targets by inducing changes in the m⁶A system via ALKBH5. To this end, induction of ALKBH5 is necessary for global reduction of m⁶A levels in response to hypoxia. We found that MCF-7 cells most strongly express the m⁶A reader YTHDF1, which increases the translation of m⁶A⁺ mRNA [220]. In accordance with this, we showed that loss of HIF or ALKBH5 expression, and corresponding increases in m⁶A levels cause significant increases in global translation levels compared to control cells in hypoxia. This indicates, for the first time, that HIF also regulates translation via ALKBH5. Upon loss of HIF or ALKBH5, genes that mediate translation initiation are upregulated at both the mRNA and protein level in hypoxia, which may lead to global increases in translation beyond the specific m⁶A-mediated translation of individual transcripts. Though diverse categories of genes are up- and down-regulated, of particular interest are the genes that regulate mitosis. Hypoxia-induced inhibition of DNA synthesis, mediated by HIF/ALKBH5 activity, enables cancer cells to survive cytotoxic chemotherapy, which targets dividing cells.

m⁶A has recently garnered significant interest as a major regulator of gene expression, and it appears to be especially relevant in cancer [221, 222]. However, multiple distinct downstream functions of m⁶A have been shown to be at play in different types of cancers or cell lines [92, 223-225]. As we showed here, multiple reader proteins can be co-expressed within one cell type. It is

still largely unclear how m⁶A reader proteins compete with one another, though it is likely that each protein has specific target transcripts that are determined by secondary RNA structure and/or protein binding partners [226]. We have previously found that m⁶A-mediated degradation of Nanog mRNA reduces formation of breast cancer stem cells [196], and in the present study we found a correlation between m⁶A and alternative splicing of ANKZF1 RNA. Others have shown that altering methyltransferase activity can drive changes in cancer proliferation and progression [221, 227, 228]. However, the highly dynamic nature of m⁶A and limitations in detection efficiency make it difficult to attribute functional consequences to m⁶A-mediated effects on individual transcripts. Therefore, we chose to analyze broader patterns of m⁶A⁺ mRNA fate to determine HIF- and ALKBH5-dependent effects on mRNA and protein expression. To this end, we found that increases in m⁶A most strongly correspond to increases in translation in MCF-7 cells, and m⁶A⁺ transcripts have significantly higher corresponding protein abundance than m⁶A⁻ transcripts. We also found a significant correlation between m⁶A modification and increased transcript abundance, which could be due to RNA stabilization mediated by YTHDF1 binding [211].

Finally, the localization of m⁶A on mRNA has traditionally been attributed to methyltransferase activity [10]. However, we found that loss of ALKBH5 also regulates the pattern of m⁶A within transcripts, especially in response to hypoxia. In control cells, the distribution pattern of m⁶A is fairly constant between normoxia and hypoxia. Knockdown of ALKBH5 reveals that methylation patterns drastically change in response to hypoxia, and that ALKBH5 is necessary to selectively prevent increases in methylation in the 5'UTR and 3'UTR. This, along with an increase in the number of unique transcripts that are m⁶A-modified in response to hypoxia, indicates that the methyltransferase complex likely becomes more promiscuous under hypoxic stress. This finding warrants further investigation, as the specificity of how m⁶A is added onto particular mRNA transcripts is still largely unknown. Clearly, there is some balance between the action of the methyltransferase and the demethylase, but the extent to which their actions are independent from one another and how each selects its binding targets is an interesting avenue to pursue further.

Overall, studies of m⁶A in cancer have shown that it is an important regulator of gene expression. However, the notable differences in m⁶A function across cell types and physiological conditions means that the role of m⁶A will likely not be straightforward, even in a single type of cancer. Therefore, it is critical to understand that m⁶A is highly dynamic, and its function must be carefully analyzed in a case-by-case basis. In this study we show that the demethylase, ALKBH5, is especially relevant in hypoxia, and that the majority of HIF-dependent genes are also ALKBH5-dependent. Furthermore, this pathway significantly alters protein expression beyond the expected changes based on transcriptional dynamics. The coupling of HIF and ALKBH5 activity provides a mechanism to rapidly respond to hypoxia by coordinated increases in transcription, mRNA stabilization, and synthesis of proteins that mediate adaptation to reduced O₂ availability, and to downregulate the expression of mRNAs and proteins involved in cell proliferation. Inhibiting HIFs or ALKBH5 results in a remarkable degree of aberrant mRNA expression that may contribute to the effectiveness of drugs targeting this pathway as anti-cancer agents.

V. METHODS:

HIF and ALKBH5 knockdown in MCF7 cells.

Lentiviral vectors encoding shRNAs targeting HIF-1 α and HIF-2 α were previously described [229]. pLKO.1-puro lentiviral vectors encoding shRNA targeting ALKBH5 mRNA (clone ID, NM_017758.2-1625s1c1 and NM_017758.2-1176s1c1) were purchased from Sigma-Aldrich, packaged using 293T cells, then transfected into MCF-7 cells [229]. Successfully transduced cells were selected for and maintained by supplementation of the culture medium with puromycin (0.5 μ g/mL).

MCF7 cell culture.

Cells were cultured in Dulbecco's Modified Eagle Medium (Gibco) supplemented with 10% fetal bovine serum, 1% penicillin-streptomycin (Invitrogen). The medium was changed every other day, and cells were passaged prior to reaching confluence. For cell culture at 1% O₂, plates were placed in a modular incubator chamber (Billups-Rothenberg) and flushed for 2 min at 2 psi with a gas mixture containing 1% O₂, 5% CO₂, and 94% N₂.

Cell cycle analysis by cell counting and EdU pulse labeling.

Analysis of cell proliferation was performed by live cell counting over 72 h, using trypan blue to distinguish between live and dead cells. DNA synthesis analysis was performed by pulsing cultured cells with 10 μM EdU (ThermoFisher) for 45 mi. Cells were then dissociated using trypsin, washed with PBS, and fixed with 4% paraformaldehyde in PBS for 15 min on ice. Cells were permeabilized and stained with the Click-iT EdU Alexa 647 Flow Cytometry Kit (ThermoFisher) as per the kit protocol, and analyzed using a BD LSR II Flow Cytometer (BD Bioscience). EdU⁺ and EdU⁻ cells were gated and calculated as a percentage of the total cell number. Experiments were done with three replicates per experimental group.

RNA purification and RT-qPCR.

Total RNA was purified using RNA mini-prep purification columns (Zymo Research R1054), then equal quantities of purified RNA were reverse transcribed using random primers and the Invitrogen Superscript IV First-Strand Synthesis System (ThermoFisher 18091200). cDNA was measured using quantitative PCR with Fast SYBR Green Master Mix (ThermoFisher 4385610). qPCR primers used were (all listed 5' → 3'):

HIF1α_F: GAACGTCGAAAAGAAAAGTCTCG

HIF1α_R: CCTTATCAAGATGCGAACTCACA

HIF2α_F: GTGCTCCCACGGCCTGTA

HIF2 α _R: TTGTCACACCTATGGCATATCACA
ALKBH5_F: CGGCGAAGGCTACACTTACG
ALKBH5_R: CCACCAGCTTTTGGATCACCA
CA9_F: GACCTTGTTGGAATGGCTCTT
CA9_R: TGGATTCAGGTGCAAATGCAA
CYR61_exon3-4_F: GGCAGACCCTGTGAATATAA
CYR61_exon3-4_R: CAGGGTTGTCATTGGTAACT
ANKZF1_retained_intron_F: ACAATACTGTTGCGTGCTCC
ANKZF1_retained_intron_R: CGTAGGCATCTGGATTCTTC
18S_RNA_F: AACTCACTGAAGATGAGGTG
18S_RNA_R: CAGACAAGGCCTACAGACTT

m⁶A ELISA.

mRNA was purified using a Dynabeads mRNA Direct Purification Kit (ThermoFisher 61011). 100 ng of mRNA purified from each subclone cultured at 20% or 1% O₂ for 48 h was loaded onto an EpiQuik m⁶A ELISA plate (Epigentek P-9005-48) in triplicate. Signal intensity was quantified using a plate reader set to read at 450 nm. Absolute m⁶A levels were calculated based on a standard curve as per kit instructions.

Metabolic analysis by Seahorse assay.

4000 cells of each subclone type were plated on day 1. The next day the cells were incubated under 20% or 1% O₂ for 72 h, then the Agilent Seahorse assay was performed as per manufacturer's protocol.

Quantification of translation initiation.

Cells were cultured in 20% or 1% O₂ for 48 h, and protein synthesis was quantified using a Click-iT HPG Alexa Fluor 488 Protein Synthesis Assay Kit (ThermoFisher C10428) per the manufacturer's instructions. Briefly, cells were treated with HPG in L-methionine-free medium for 30 min. Hypoxic cells were exposed to 1% O₂ during treatment in a hypoxia workstation. Cells were then washed in PBS, fixed in 3.7% formaldehyde in PBS, and permeabilized using 0.5% Triton X-100. HPG was detected using the Click-iT reaction cocktail supplied in the kit along with NuclearMask Blue Stain for DNA staining. Cells were then scanned on a plate reader to measure DAPI for DNA stain detection and FITC for Alexa Fluor 488 detection. FITC levels were normalized to DAPI to quantify normalized levels of translation initiation in each cell type. Additionally, cells were grown, treated, and stained in glass slide chambers (Thermo Scientific Nunc 154526) and visualized under a confocal microscope.

RNA sequencing.

Three technical replicates of cells for each experimental group and control were collected in Trizol, from which total RNA was purified [230]. mRNA was then purified using the Dynabeads mRNA Purification Kit (Invitrogen). cDNA libraries were prepared using the Illumina NEBNext Ultra DNA Library Prep Kit, then sequenced with a 75-cycle single-end run on the Illumina Nextseq platform.

m⁶A-RNA immunoprecipitation and sequencing.

m⁶A sequencing was performed as previously described [2]. Briefly, triplicate samples of mRNA for each experimental group and controls were purified as in RNA sequencing. m⁶A pull-down was performed with a rabbit polyclonal anti-m⁶A antibody (Synaptic Systems), then mRNA was immunoprecipitated with protein G Dynabeads (ThermoFisher) using competitive elution with free N⁶-methyladenosine. The eluted samples were then used to prepare cDNA libraries for sequencing.

Bioinformatic analysis of sequencing data.

RNA and m⁶A-RNA sequencing results were processed using the FASTX toolkit (http://hannonlab.cshl.edu/fastx_toolkit/) to clip adaptors, filter out low quality reads, and collapse identical reads. Reads were mapped to the hg19 human genome using Tophat2 [166] with default settings. Differential expression analysis was performed using the DESEQ2 package in R [231]. Significance was calculated as p_{adj} , which corrects the p-value for multiple testing using the Benjamini-Hochberg correction method. Genes with significant ($p_{adj} < 0.05$) induction or repression in response to hypoxia in NTC cells were deemed “hypoxia-induced” and “hypoxia-repressed,” respectively. HIF- and ALKBH5-dependent genes were then identified as those that lose significance ($p_{adj} > 0.05$) in HIF-DKD or ALK-KD cells in hypoxic over normoxic conditions or genes that are significantly ($p_{adj} < 0.05$) higher and have $|\text{Log}_2\text{FoldChange}| > 0.5$ in hypoxic NTC cells over hypoxic HIF-DKD or hypoxic ALK-KD cells. Expression levels for individual transcripts were calculated as $\log_2(\text{transcripts per million} + 1)$, and expression heat maps were plotted using the Heatmapper online tool [232]. m⁶A peaks were identified using MACS2[167] peak calling using total RNA sequencing data as the input control. The BedTools package [168] was used to filter for high-confidence m⁶A peaks; peaks from the triplicate samples were compared in a pairwise manner to identify peaks that overlap in at least 2 out of 3 samples. Representative m⁶A coverage plots were made by converting aligned reads in bam format to bedGraph format using the BedTools package genomecov function, then plots were made in R with the GenomicRanges [233], rtracklayer [234], BSgenome.Hsapiens.UCSC.hg19, and biomaRt [235] packages. The distribution of m⁶A peaks over gene bodies was analyzed using the assignChromosomeRegion function of the ChIPpeakAnno [236] package in R. The peak distribution over mRNA plot was made using the Guitar [237] package in R.

Functional annotation and gene ontology.

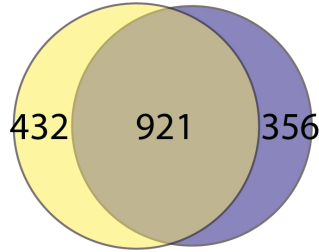
Enrichment for gene ontology terms in biological processes was tested using the ToppFunn application in the ToppGene Suite [170]. Significant enrichment was determined using a hypergeometric probability mass function and Benjamini Hochberg FDR correction with a p-value cutoff of 0.05. Redundant gene ontology terms were filtered and the parent term was kept.

Proteomic analysis by mass spectrometry.

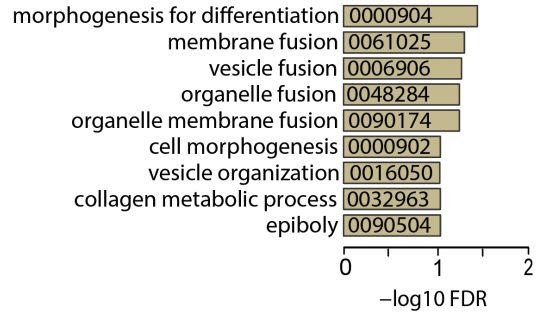
Subclones were cultured at 20% or 1% O₂ for 48 h and proteins were purified for mass spectrometry analysis. Cells were washed with ice cold PBS five times to remove serum proteins, then lysed using 0.5 mL of 2% SDS containing 1 mM EDTA and 1 mM phenylmethyl sulfonyl fluoride. Cells were sonicated on ice until the cloudy cell lysate became clear. The lysates were then centrifuged to remove any pellet and diluted. Protein content and quality were tested with a SilverQuest Silver Staining Kit (ThermoFisher LC6070) before sending samples to the Johns Hopkins Mass Spectrometry Core Facility for analysis, where a Fusion mass spectrometer was used alongside gradient fractions as previously described [238].

VI. FIGURES:

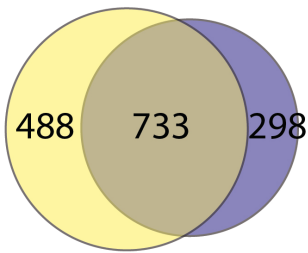
a Hypoxia-induced mRNA
HIF-dependent ALKBH5-dependent



b HIF and ALKBH5-dependent



c Hypoxia-repressed mRNA
HIF-dependent ALKBH5-dependent



d HIF and ALKBH5-dependent

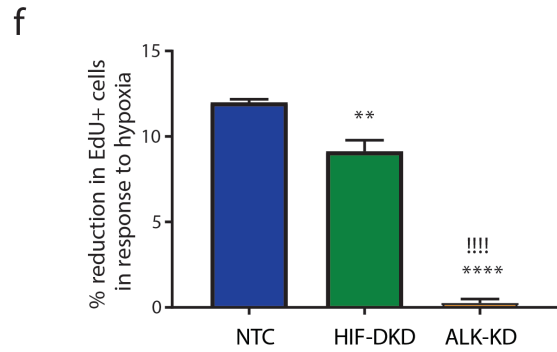
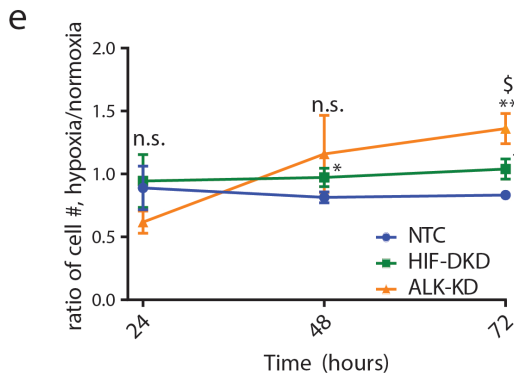
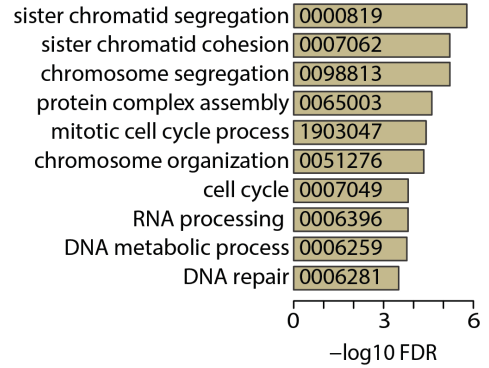


Figure 1. HIF regulation of transcriptional changes in response to hypoxia largely occurs through a shared pathway with ALKBH5.

(a) Overlap of genes that are HIF- and ALKBH5- dependent for induction in response to hypoxia. (b) Gene ontology of the 921 genes that are HIF- and ALKBH5-dependent for induction in response to hypoxia. (c) Overlap of genes that are HIF- and ALKBH5- dependent for repression in response to hypoxia. (d) Gene ontology of the 733 genes that are HIF- and ALKBH5-dependent for repression in response to hypoxia. (e) Live cell counts of NTC, HIF-DKD, and ALKBH5-KD MCF-7 cells over 72 h of hypoxia. Data are presented as the ratio of counts in live cells cultured at 1% O₂/20% O₂ (mean ± SEM, n = 3; *p < 0.05 relative to NTC, **p < 0.01 compared to NTC, ^sp < 0.05 relative to DKD). (f) Percent reduction in cells that incorporate EdU after 48 h of hypoxia in the NTC, HIF-DKD, and ALKBH5-KD subclones (mean ± SEM, n = 3; **p < 0.01 vs NTC, ****p < 0.0001 vs NTC, ^{!!!!}p < 0.0001 vs HIF-DKD).

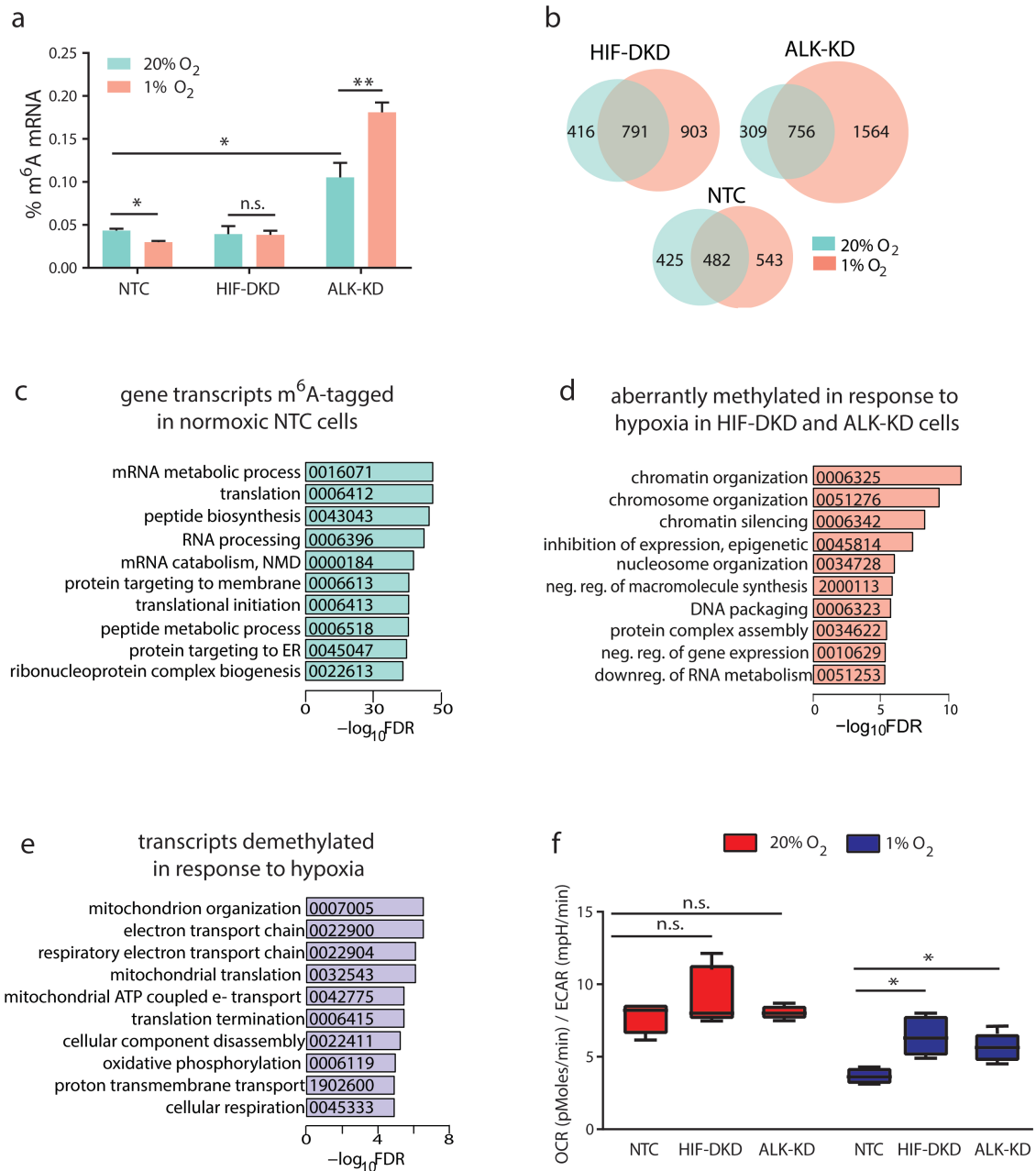


Figure 2. Dynamic changes in m⁶A transcript coverage depend on HIF and ALKBH5 expression.

(a) ELISA showing the percentage of mRNAs that are m⁶A⁺ after 24 h at 20% (teal) or 1% (peach) O₂ (mean ± SEM, n = 3; * P < 0.05, **P < 0.01; n.s., P > 0.05). (b) Venn diagrams of the number

of unique transcripts tagged with m⁶A in NTC, HIF-DKD, and ALKBH5-KD cells incubated for 48 h in 20% (teal) or 1% (peach) O₂. (c) Gene ontology of transcripts that are methylated in NTC cells at 20% O₂. (d) Gene ontology of transcripts that are not methylated in NTC cells at 20% or 1% O₂, but are methylated in HIF-DKD and ALKBH5-KD cells after exposure to 1% O₂ for 48 h. (e) Gene ontology of transcripts that are demethylated in NTC cells after exposure to 1% O₂ for 48 h, but remain methylated in hypoxic HIF-DKD and ALKBH5-KD cells. (f) Measurement of O₂ consumption rate (OCR) and extracellular acidification rate (ECAR) to analyze aerobic and glycolytic metabolism, respectively (mean ± SEM, n = 4; * p < 0.05 vs OCR of NTC at 20% O₂, **p < 0.01 vs ECAR of all other groups).

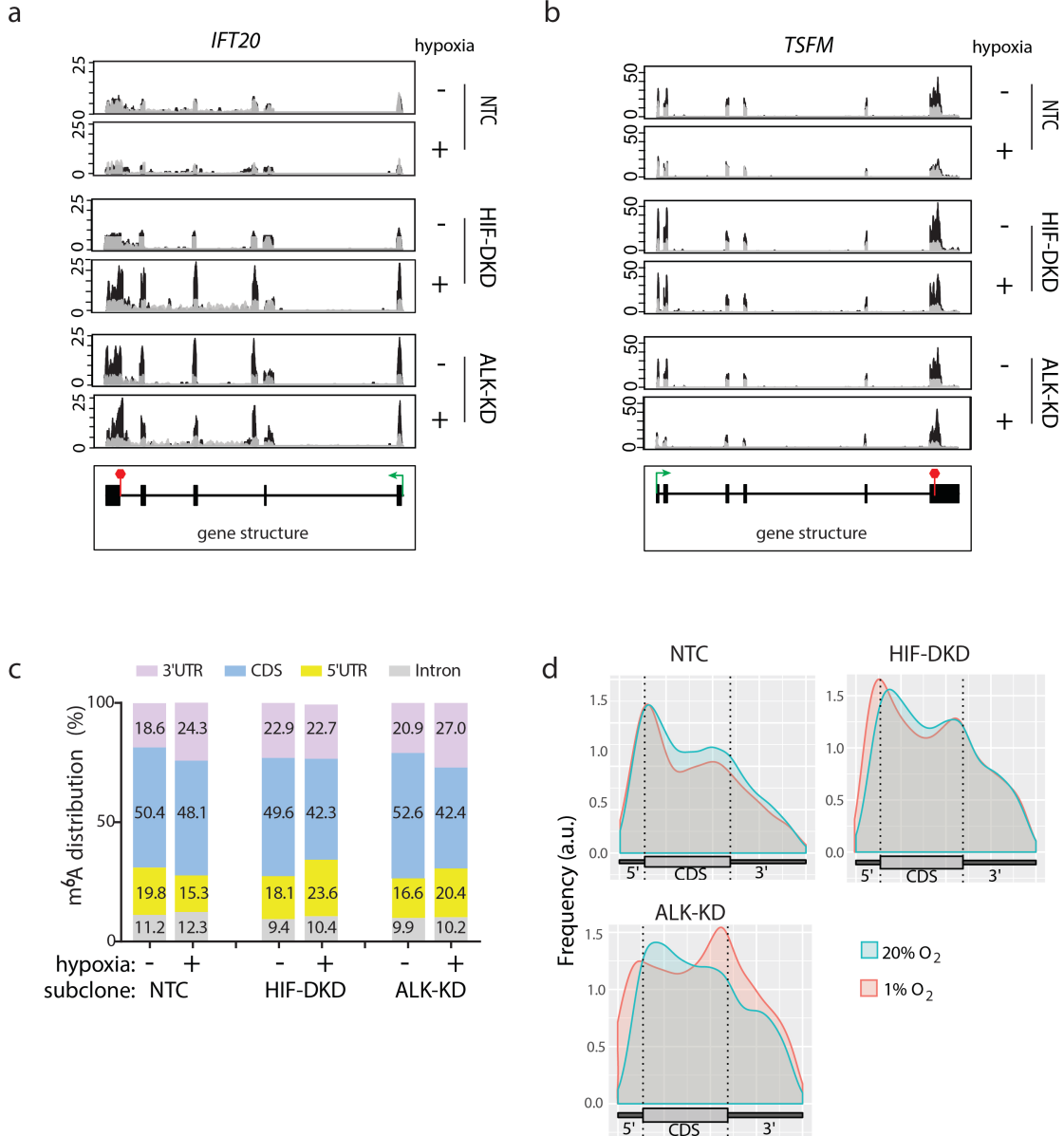


Figure 3. HIF and ALKBH5 mediate m⁶A methylation patterns across the epitranscriptome.

(a-b) Sample coverage plots showing enrichment in m⁶A⁺ RNA immunoprecipitation and sequencing (m⁶A RIP-seq; black) compared to input total RNA sequencing (gray) for IFT20 (a) and TSFM (b) RNA. The bottom panel shows the gene structure, with the position of the transcription start site shown in green, the stop codon shown in red, exons shown as large rectangles, and introns as a narrow line. mRNA was isolated from NTC, HIF-DKD, and ALKBH5-

KD cells exposed to 1% O₂ for 24 h. (c) Distribution of m⁶A peaks over 5'-UTR (yellow), CDS (blue), introns (gray) and 3'-UTR (purple) of RNA from all protein-coding genes. Percentages were calculated from peaks that occur in at least two out of three m⁶A RIP-seq replicates. (d) Gene body coverage distribution of m⁶A RIP-seq peaks in cells exposed to 20% or 1% O₂ for 24 h. Gene body is represented as the average relative length of the 5'-UTR, CDS and 3'-UTR across the genome.

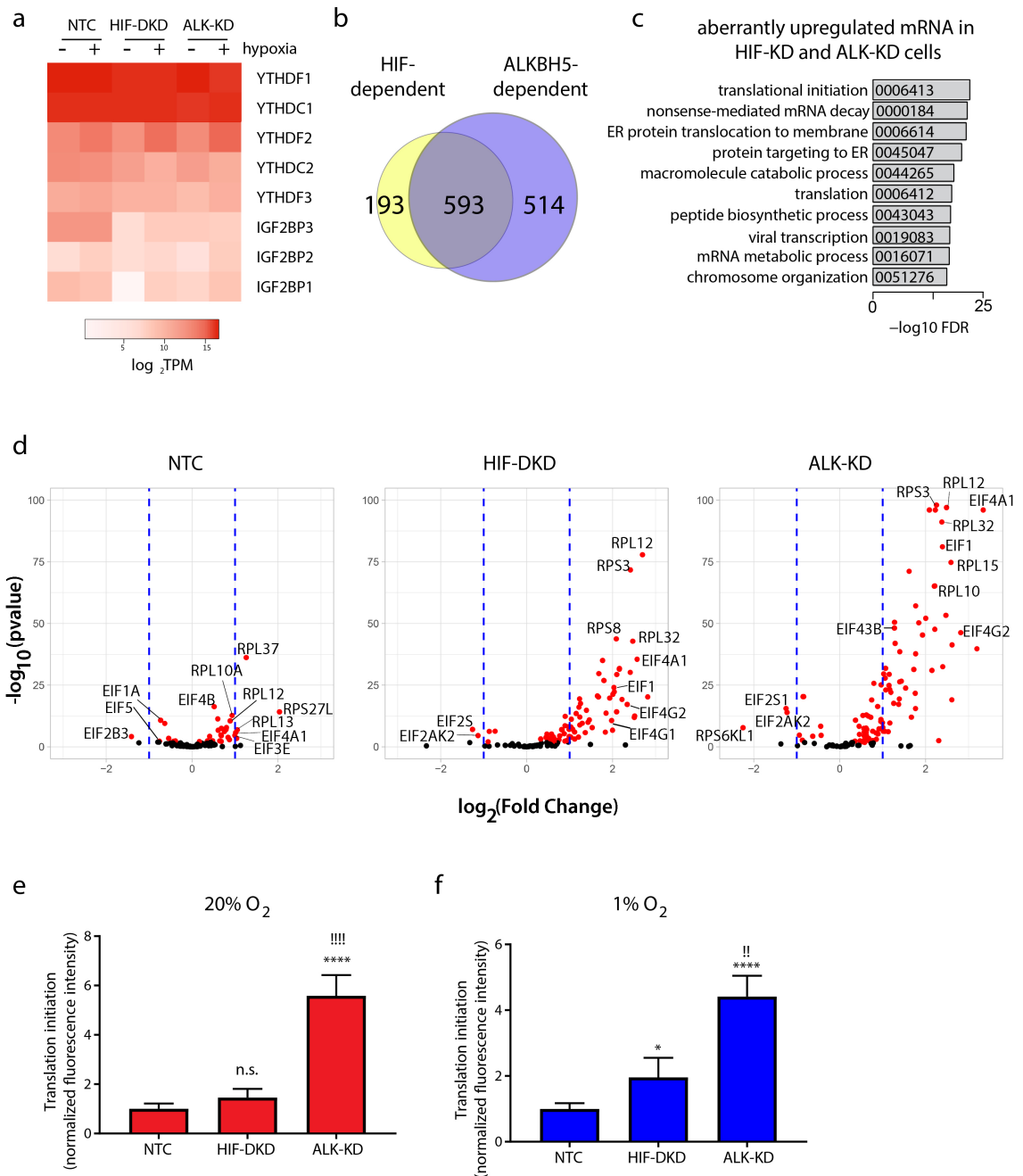


Figure 4. HIF regulates global translation via ALKBH5 and m⁶A.

(a) Heat map showing relative expression levels of mRNAs encoding known m⁶A readers in NTC, HIF-DKD, and ALKBH5-KD cells incubated at 20% or 1% O₂ for 48 h. Values are calculated as $\log_2(\text{transcripts per million [TPM]} + 1)$. (b) Venn diagram showing genes that are significantly (p_{adj}

< 0.05) induced in response to hypoxia in HIF-DKD and ALKBH5-KD cells, but not in NTC cells. (c) Gene ontology of the 593 shared significantly induced genes (from panel B) show that translation is upregulated in HIF-DKD and ALKBH5-KD cells in response to hypoxia. (d) Volcano plots showing differential expression of genes in the “translation initiation” and “ribosome” gene ontologies in NTC, HIF-DKD, and ALKBH5-KD cells incubated at 1%/20% O₂. Red dots represent genes that are significantly differentially expressed ($p_{\text{adj}} < 0.05$). Dots outside the blue dashed lines at $\text{Log}_2(\text{FoldChange}) = 1$ represent genes that are up- or down- regulated greater than 2-fold. (e) Translation initiation after incubation at 20% O₂ for 48 h, calculated by intensity of a GFP linked methionine analog (HPG) added to cells for 30 minutes before harvesting and normalized to cell number by DAPI intensity, then normalized to NTC (mean± SEM, n = 4; ****p < 0.0001 vs NTC, !!!!!p < 0.0001 vs HIF-DKD; n.s., no significance vs NTC). (f) Translation initiation levels after incubation at 1% O₂ for 48 h, calculated as in panel E (mean± SEM, n = 4; *p < 0.05 vs NTC, ****p < 0.0001 vs NTC, !! p < 0.01 vs HIF-DKD).

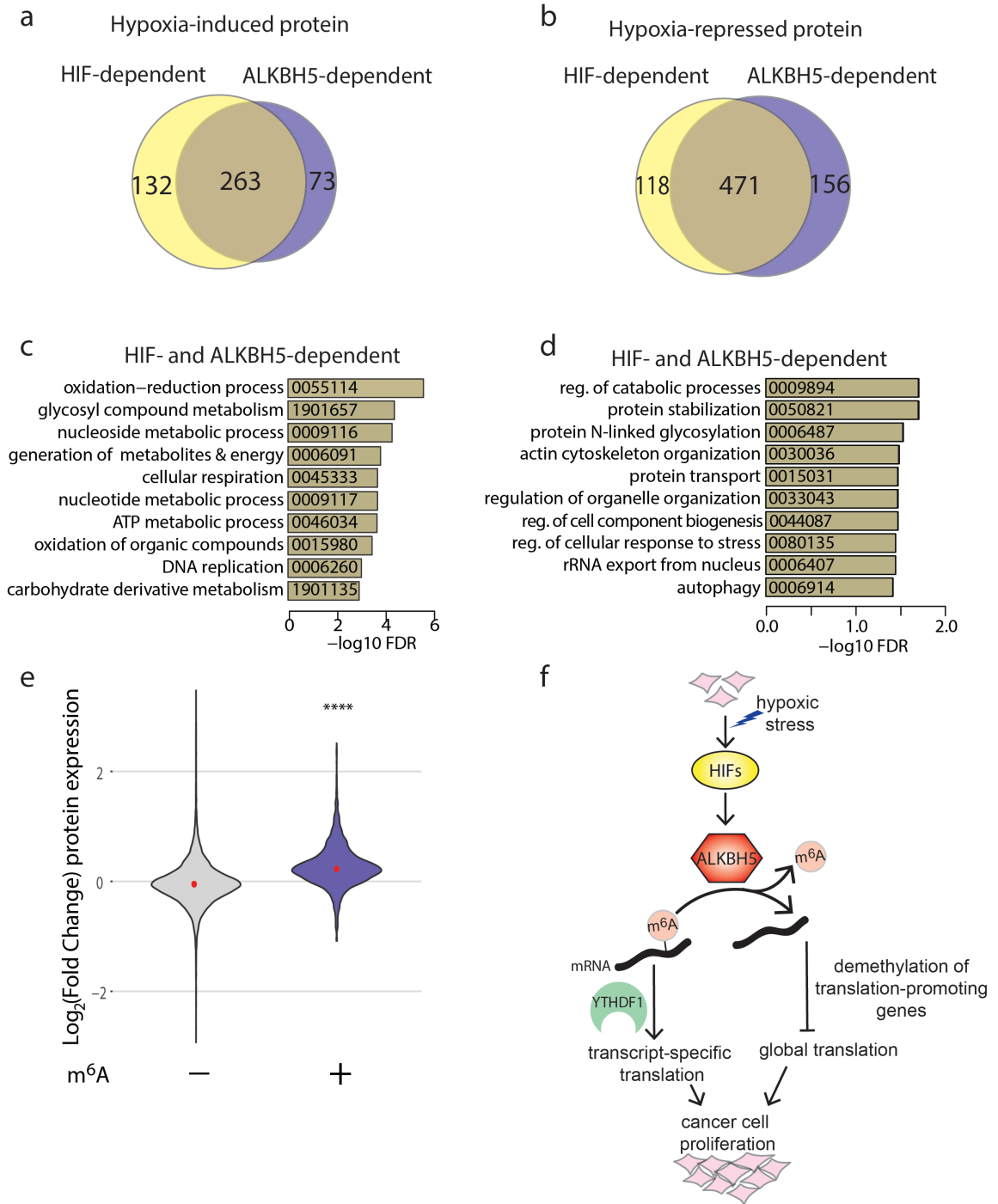
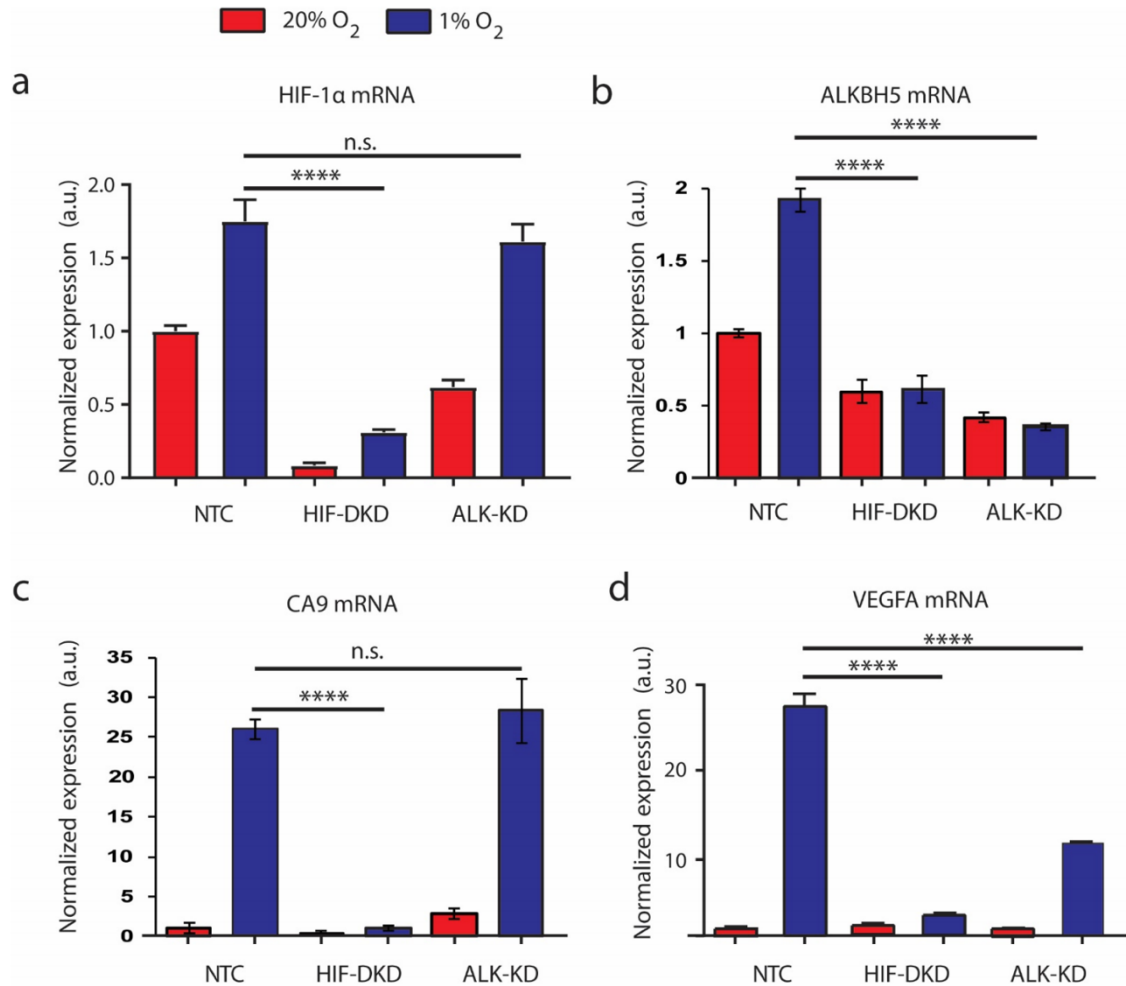


Figure 5. HIFs and ALKBH5 regulate protein expression via increased translation of m⁶A-modified mRNA.

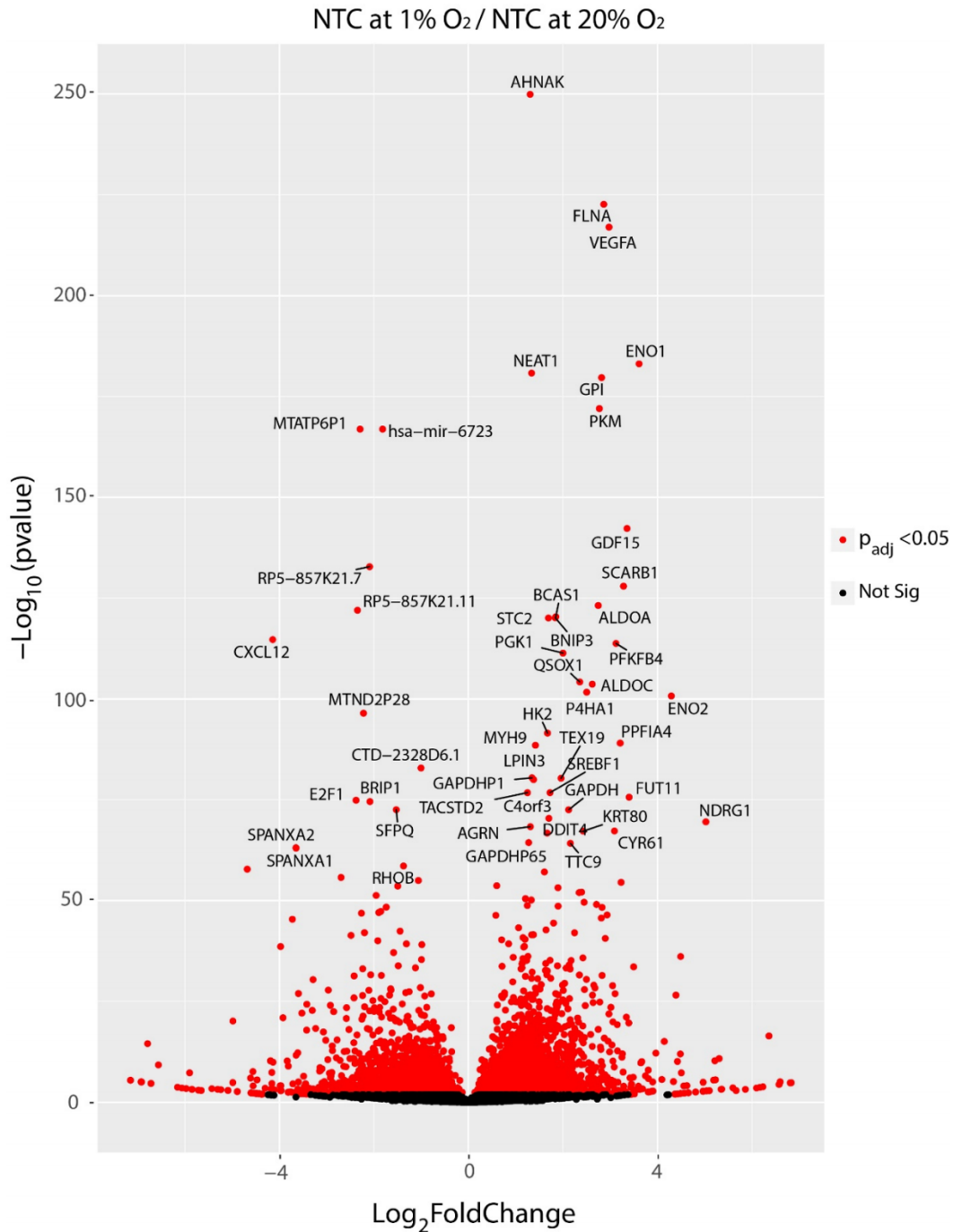
(a) Venn diagram showing overlap of proteins that are HIF- (yellow) and ALKBH5- (violet) dependent for induction in response to hypoxia. (b) Venn diagram showing overlap of proteins that

are HIF- and ALKBH5- dependent for repression in response to hypoxia. (c) Gene ontology of proteins that are HIF- and ALKBH5- dependent for induction. (d) Gene ontology of proteins that are HIF- and ALKBH5-dependent for repression. (e) Violin plot showing proteins with cognate mRNA that is m⁶A⁺ have significantly higher Log₂(Fold-Change) in expression in response to hypoxia than proteins with cognate mRNA that is m⁶A⁻. Red dots represent the mean Log₂(Fold-Change) in expression of all proteins. Height of the plot represents the total distribution of expression values, and width of the plot represents the frequency distribution of expression values (****p < 0.0001). (f) Graphic summary: hypoxic stress induces HIF-dependent induction of ALKBH5, which demethylates m⁶A from mRNA to reduce translation of modified transcripts. Many transcripts encoding proteins that promote translation are demethylated, which in turn reduces global levels of translation initiation and limits cancer cell proliferation.

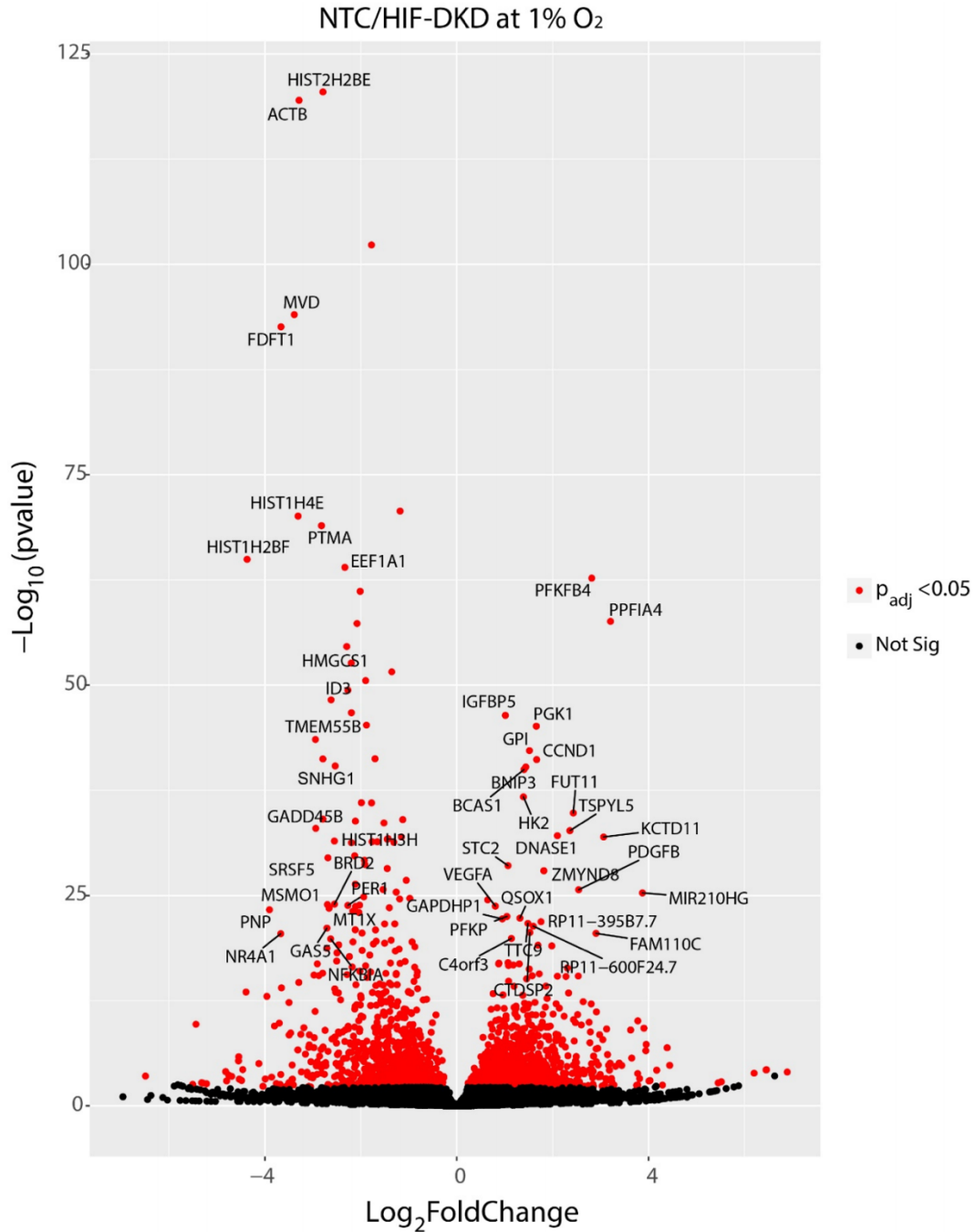
VII. SUPPLEMENTAL FIGURES:



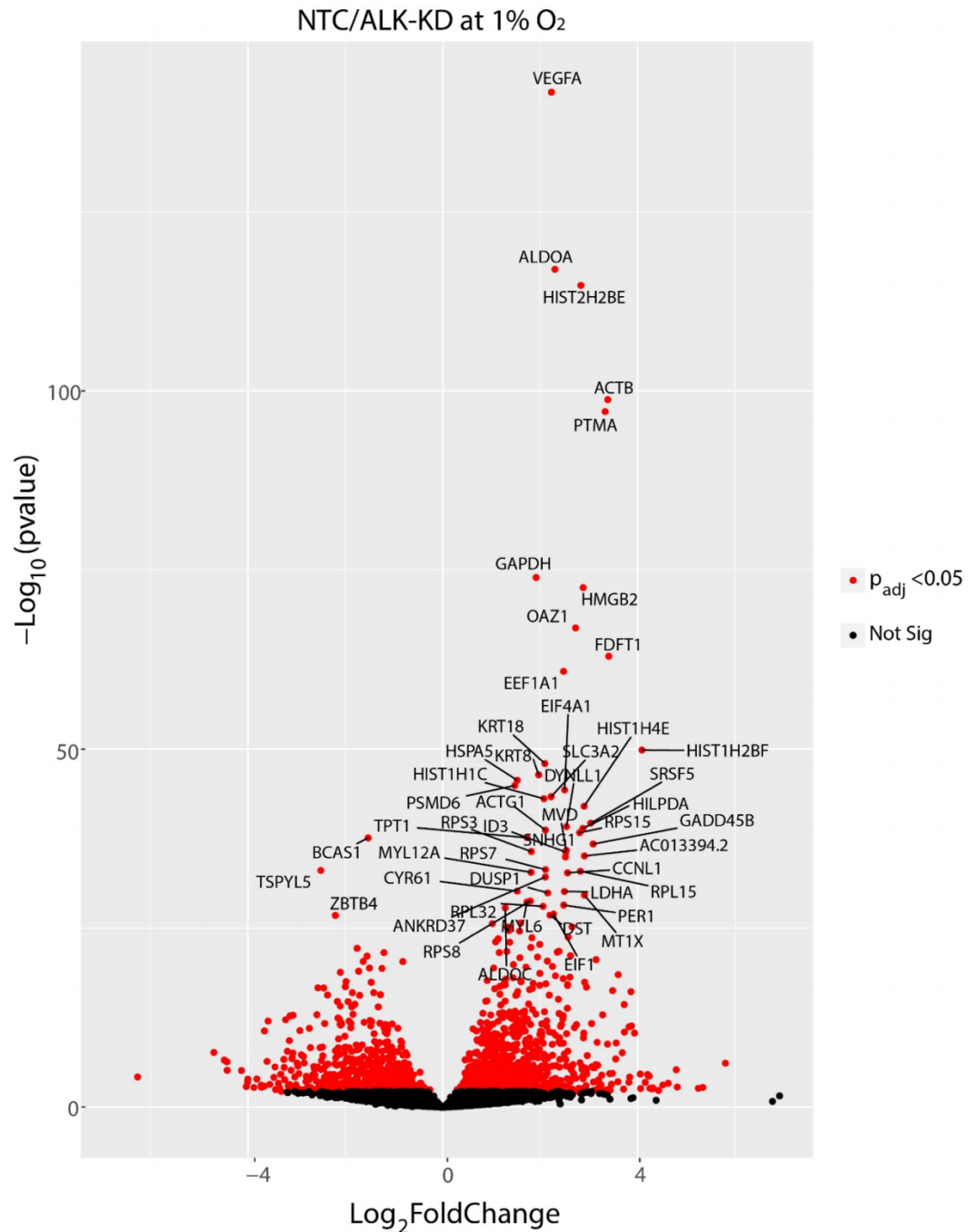
Supplementary Figure 1. Confirmation of knockdown efficiency and mRNA expression. Confirmation of HIF-1 α (a) and ALKBH5 (b) shRNA knockdown by RT-qPCR at 20% O₂ (red) and 1% O₂ (blue) (mean \pm SEM, n = 3; ****p < 0.0001; n.s., p > 0.05). (c) Analysis of HIF-dependent and ALKBH5-independent CA9 mRNA induction by RT-qPCR (mean \pm SEM, n=3; ****p < 0.0001; n.s., p > 0.05). (d) Confirmation of HIF-dependent and ALKBH5-dependent VEGFA mRNA induction by RT-qPCR (mean \pm SEM, n = 3; ****p < 0.0001; n.s., p > 0.05).



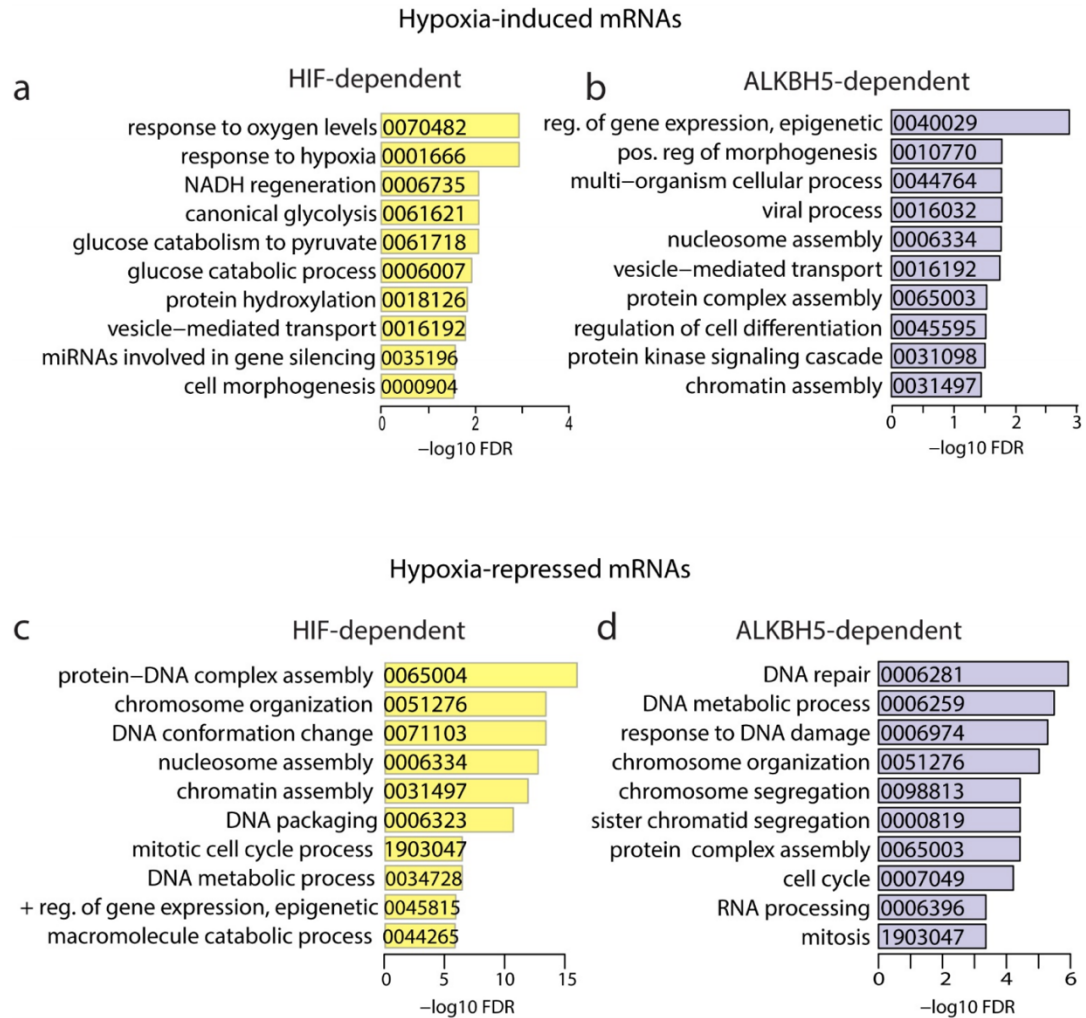
Supplementary Figure 2. Differential mRNA expression in MCF-7 NTC subclone exposed to 1% or 20% O₂ for 24 h. Log₂FoldChange of mRNA expression at 1% O₂ vs 20% O₂. Red dots represent a significant (p_{adj} < 0.05) change in gene expression. The top 50 mRNAs according to p value are labeled by name.



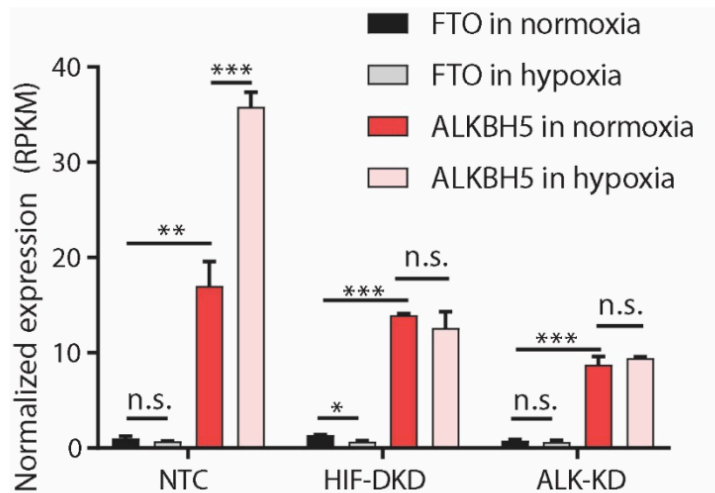
Supplementary Figure 3. Differential mRNA expression between MCF-7 NTC and HIF-DKD subclones exposed to 1% O₂ for 24 h. Log₂FoldChange of mRNA expression in NTC vs HIF-DKD subclone at 1% O₂. Red dots represent a significant (p_{adj} < 0.05) change in mRNA expression. The top 50 mRNAs according to p value are labeled by name.



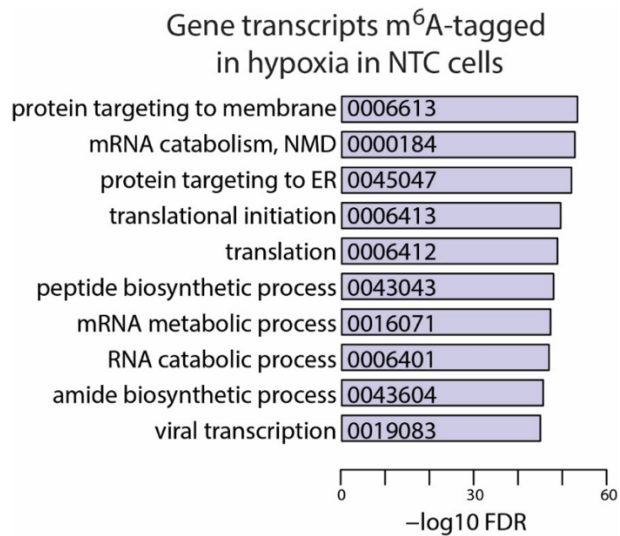
Supplementary Figure 4. Differential mRNA expression between MCF-7 NTC and ALK-KD subclones exposed to 1% O₂ for 24 h. Log₂FoldChange of mRNA expression in NTC vs ALK-KD subclone at 1% O₂. Red dots represent significant (p_{adj} < 0.05) change in mRNA expression. The top 50 mRNAs according to p value are labeled by name.



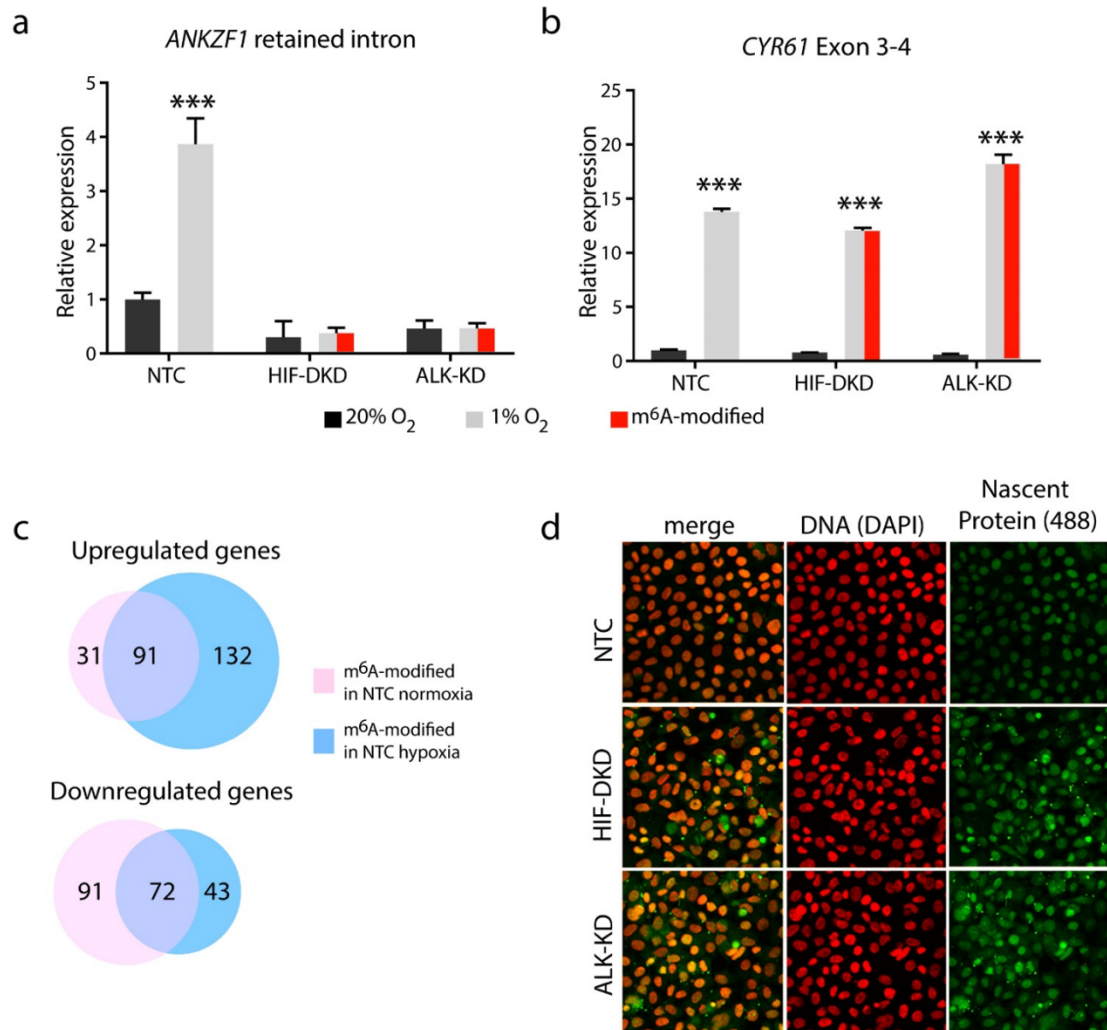
Supplementary Figure 5. Gene ontology analysis of HIF- and ALKBH5-dependent mRNAs. (a) Gene ontology of mRNAs that are HIF-dependent for induction in response to hypoxia. (b) Gene ontology of mRNAs that are ALKBH5-dependent for induction in response to hypoxia. (c) Gene ontology of mRNAs that are HIF-dependent for repression in response to hypoxia. (d) Gene ontology of mRNAs that are ALKBH5-dependent for repression in response to hypoxia.



Supplementary Figure 6. Comparison of FTO and ALKBH5 mRNA expression levels in cells exposed to 20% or 1% O₂ for 48 h. Data are RPKM (reads per kilobase of transcript, per million mapped reads) and normalized to FTO expression in normoxia (mean ± SEM, n=3; * p < 0.01 ***p < 0.001; n.s., p > 0.05).

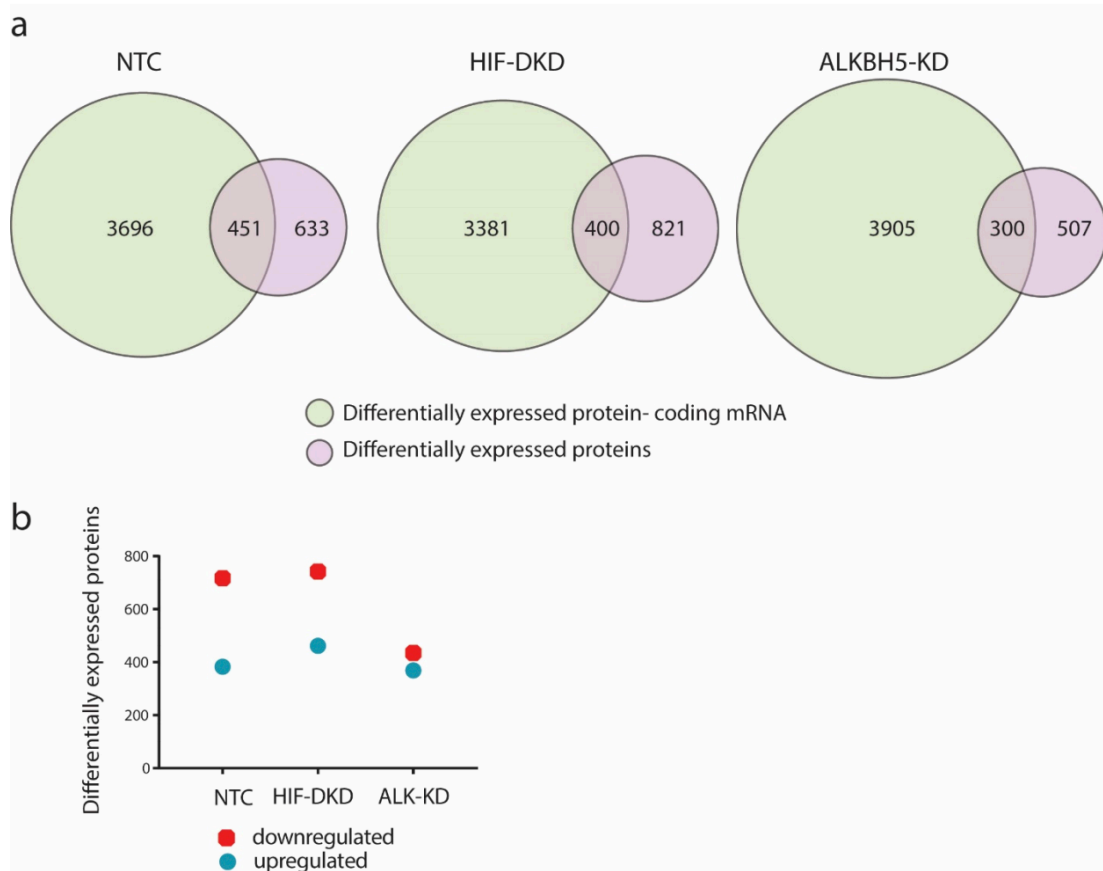


Supplementary Figure 7. Gene ontology of mRNAs that are methylated in NTC cells after exposure to 1% O₂ for 24 h.



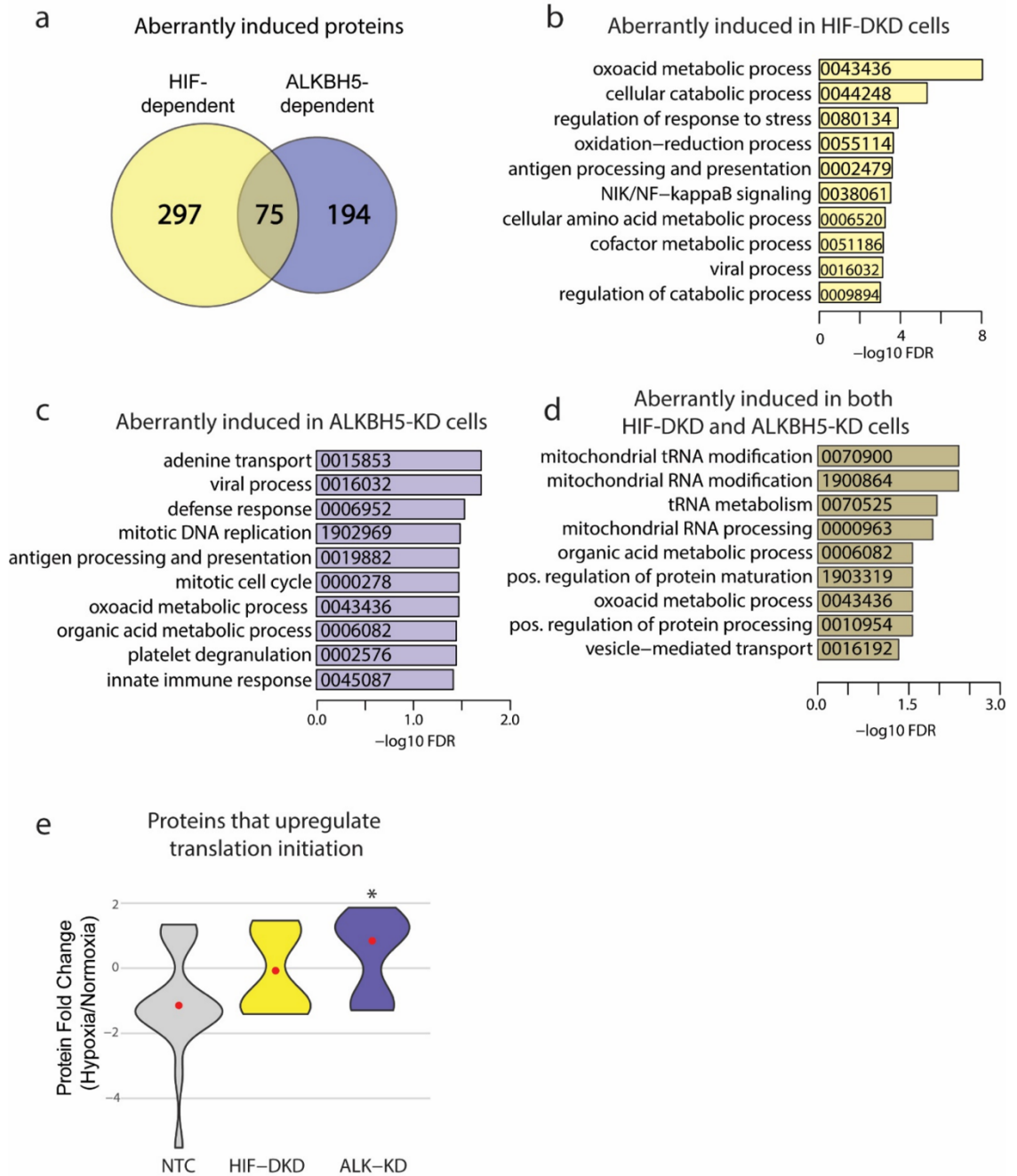
Supplementary Figure 8. Potential m⁶A functions mediated by known YTH domain-containing reader proteins. (a) Expression of alternatively spliced versions of *ANKZF1* RNA in NTC, HIFDKD, and ALKBH5-KD cells incubated at 20% or 1% O₂ for 24 h, as determined by RT-qPCR. Red bars represent gene transcripts that are m⁶A-modified in hypoxia. Alternative splicing of *ANKZF1* correlates with m⁶A status (mean± SEM, n = 3; ***p < 0.001 vs NTC at 20% O₂). (b) Expression of alternatively spliced versions of *CYR61* mRNA in NTC, HIF-DKD, and ALKBH5-KD cells incubated at 20% or 1% O₂ for 24 h as determined by RT-qPCR. Red bars represent mRNAs that are m⁶A-modified

in hypoxia. CYR61 mRNA alternative splicing does not correlate with m⁶A status (mean ± SEM, n = 3; ***p < 0.001 vs expression at 20% O₂). (c) Venn diagrams showing that more upregulated mRNAs are m⁶A-modified than not at 1% O₂, whereas fewer downregulated mRNAs are m⁶A-modified at 1% O₂. X2 analysis demonstrated significant (p < 0.001) enrichment in hypoxic cells of upregulated mRNAs that are m⁶A-modified. (d) Confirmation of translation initiation assay by confocal imaging of cells incubated at 1% O₂ for 48 h and treated with AlexaFluor488-linked methionine analog HPG for 30 min before fixation. Increased levels of nascent protein (green) are seen in the HIF-DKD and ALKBH5-KD subclones.



Supplementary Figure 9. Analysis of differentially expressed proteins in MCF-7 cells.

(a) Venn diagrams showing the overlap between differentially expressed mRNA and protein in NTC, HIFDKD and ALKBH5-KD cells exposed to 1% O₂ for 24 h (for RNA analysis) or 48 h (for protein analysis). Values determined from RNA sequencing (n = 3) and mass spectrometry (n = 4). (b) Plot of the number of proteins that are significantly (p < 0.05) upregulated (turquoise) or downregulated (violet) in NTC, HIF-DKD, and ALKBH5-KD cells incubated at 1% O₂ for 48 h.



Supplementary Figure 10. HIF and ALKBH5 prevent aberrant translation under hypoxic conditions. (a) Venn diagram of proteins that are significantly ($p < 0.05$) induced in response to hypoxia in HIF-DKD (yellow) and ALK-KD (violet), but not in NTC cells, incubated at 1% O₂ for 48 h. (b) Gene ontology of aberrantly induced proteins in HIF-

DKD cells. (c) Gene ontology of aberrantly induced proteins in ALK-KD cells. (d) Gene ontology of aberrantly induced proteins shared between HIF-DKD and ALK-KD cells. (e) Violin plot showing fold-change of expression in response to hypoxia of proteins in the “positive regulation of translation initiation” gene 4 ontology (*p < 0.05 vs NTC). Red dots represent the mean Log₂(Fold-Change) in expression of all proteins. Height of the plot represents the total distribution of expression values, and width of the plot represents the frequency distribution of expression values.

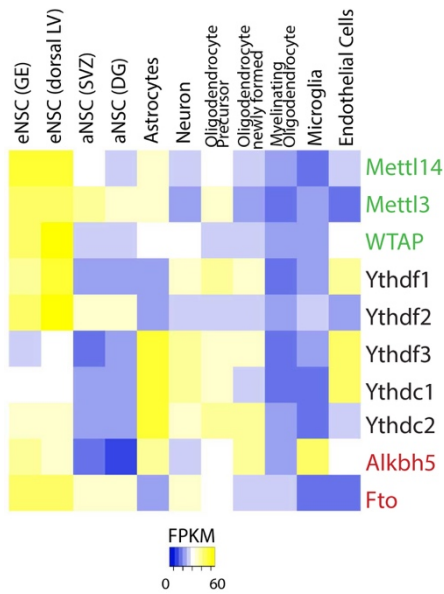
Chapter 6

Concluding Remarks

Working in different systems throughout graduate school, from neuroscience to breast cancer, highlighted the fact that m⁶A has incredibly different functions in distinct contexts. It also made it clear that m⁶A likely does not have a single function even within a singular cell type. The current state of the field is focused on identifying the central function of m⁶A in one cell type at a time. Moving forward, however, I am interested in understanding the upstream regulation of the system that allows it to be so specialized and dynamic in distinct contexts.

For example, different cell types in the nervous system express different levels of various m⁶A machinery proteins (Figure 1). Moving forward, I'm interested in understanding what regulates the expression of different m⁶A reader proteins, as well as identifying upstream regulators of methyltransferase or demethylase activity.

In addition to understanding the dynamics of m⁶A, I'm excited by the prospects of studying other epitranscriptomic marks. As detection technologies improve, other modifications will become



easier to study. For example, pseudouridine, m⁵C, and m¹A are emerging as additional important regulators of mRNA processing and require studies *in vivo*. I'm also interested in the interaction of epitranscriptomic marks on mRNA, tRNA, and rRNA that could clarify some of the uncertainties in how the epitranscriptome functions. I am honored and excited to contribute to our understanding of the epitranscriptome in the coming years.

Figure 1: Differential Expression of m⁶A Machinery

Fragments per kilobase (FPKM) as a measure of gene expression from RNA sequencing data shows highly differential expression of m⁶A methyltransferase components (green,) reader proteins (black), and demethylases (red).

BIBLIOGRAPHY

1. Meyer, K.D., et al., Comprehensive analysis of mRNA methylation reveals enrichment in 3' UTRs and near stop codons. *Cell*, 2012. 149(7): p. 1635-46.
2. Dominissini, D., et al., Topology of the human and mouse m6A RNA methylomes revealed by m6A-seq. *Nature*, 2012. 485(7397): p. 201-6.
3. Farre, D., et al., Identification of patterns in biological sequences at the ALGGEN server: PROMO and MALGEN. *Nucleic Acids Res*, 2003. 31(13): p. 3651-3.
4. Roost, C., et al., Structure and thermodynamics of N6-methyladenosine in RNA: a spring-loaded base modification. *J Am Chem Soc*, 2015. 137(5): p. 2107-15.
5. Liu, J., et al., Landscape and Regulation of m(6)A and m(6)Am Methylome across Human and Mouse Tissues. *Mol Cell*, 2019.
6. Geula, S., et al., Stem cells. m6A mRNA methylation facilitates resolution of naive pluripotency toward differentiation. *Science*, 2015. 347(6225): p. 1002-6.
7. Chang, M., et al., Region-specific RNA m(6)A methylation represents a new layer of control in the gene regulatory network in the mouse brain. *Open Biol*, 2017. 7(9).
8. Liu, J., et al., A METTL3-METTL14 complex mediates mammalian nuclear RNA N6-adenosine methylation. *Nat Chem Biol*, 2014. 10(2): p. 93-5.
9. Ping, X.L., et al., Mammalian WTAP is a regulatory subunit of the RNA N6-methyladenosine methyltransferase. *Cell Res*, 2014. 24(2): p. 177-89.
10. Schwartz, S., et al., Perturbation of m6A writers reveals two distinct classes of mRNA methylation at internal and 5' sites. *Cell Rep*, 2014. 8(1): p. 284-96.

11. Patil, D.P., et al., m(6)A RNA methylation promotes XIST-mediated transcriptional repression. *Nature*, 2016. 537(7620): p. 369-373.
12. Ke, S., et al., m(6)A mRNA modifications are deposited in nascent pre-mRNA and are not required for splicing but do specify cytoplasmic turnover. *Genes Dev*, 2017. 31(10): p. 990-1006.
13. Slobodin, B., et al., Transcription Impacts the Efficiency of mRNA Translation via Co-transcriptional N6-adenosine Methylation. *Cell*, 2017. 169(2): p. 326-337 e12.
14. Fustin, J.M., et al., RNA-methylation-dependent RNA processing controls the speed of the circadian clock. *Cell*, 2013. 155(4): p. 793-806.
15. Wang, Y., et al., N6-methyladenosine modification destabilizes developmental regulators in embryonic stem cells. *Nat Cell Biol*, 2014. 16(2): p. 191-8.
16. Batista, P.J., et al., m(6)A RNA modification controls cell fate transition in mammalian embryonic stem cells. *Cell Stem Cell*, 2014. 15(6): p. 707-19.
17. Chen, T., et al., m(6)A RNA methylation is regulated by microRNAs and promotes reprogramming to pluripotency. *Cell Stem Cell*, 2015. 16(3): p. 289-301.
18. Jia, G., et al., N6-methyladenosine in nuclear RNA is a major substrate of the obesity-associated FTO. *Nat Chem Biol*, 2011. 7(12): p. 885-7.
19. Zheng, G., et al., ALKBH5 is a mammalian RNA demethylase that impacts RNA metabolism and mouse fertility. *Mol Cell*, 2013. 49(1): p. 18-29.
20. Engel, M., et al., The Role of m(6)A/m-RNA Methylation in Stress Response Regulation. *Neuron*, 2018. 99(2): p. 389-403 e9.

21. Mauer, J., et al., Reversible methylation of m(6)Am in the 5' cap controls mRNA stability. *Nature*, 2017. 541(7637): p. 371-375.
22. Linder, B., et al., Single-nucleotide-resolution mapping of m6A and m6Am throughout the transcriptome. *Nat Methods*, 2015. 12(8): p. 767-72.
23. Cao, Y., et al., Dynamic effects of Fto in regulating the proliferation and differentiation of adult neural stem cells of mice. *Hum Mol Genet*, 2019.
24. Ma, C., et al., RNA m(6)A methylation participates in regulation of postnatal development of the mouse cerebellum. *Genome Biol*, 2018. 19(1): p. 68.
25. Roundtree, I.A., et al., Dynamic RNA Modifications in Gene Expression Regulation. *Cell*, 2017. 169(7): p. 1187-1200.
26. Patil, D.P., B.F. Pickering, and S.R. Jaffrey, Reading m(6)A in the Transcriptome: m(6)A-Binding Proteins. *Trends Cell Biol*, 2018. 28(2): p. 113-127.
27. Frye, M., et al., RNA modifications: what have we learned and where are we headed? *Nat Rev Genet*, 2016. 17(6): p. 365-72.
28. Akichika, S., et al., Cap-specific terminal N (6)-methylation of RNA by an RNA polymerase II-associated methyltransferase. *Science*, 2019. 363(6423).
29. Sun, H., et al., Cap-specific, terminal N(6)-methylation by a mammalian m(6)Am methyltransferase. *Cell Res*, 2019. 29(1): p. 80-82.
30. Boulias, K., et al., Identification of the m(6)Am Methyltransferase PCIF1 Reveals the Location and Functions of m(6)Am in the Transcriptome. *Mol Cell*, 2019. 75(3): p. 631-643 e8.
31. Sendinc, E., et al., PCIF1 Catalyzes m6Am mRNA Methylation to Regulate Gene Expression. *Mol Cell*, 2019. 75(3): p. 620-630 e9.

32. Dominissini, D., et al., The dynamic N(1)-methyladenosine methylome in eukaryotic messenger RNA. *Nature*, 2016. 530(7591): p. 441-6.
33. Li, X., et al., Transcriptome-wide mapping reveals reversible and dynamic N(1)-methyladenosine methylome. *Nat Chem Biol*, 2016. 12(5): p. 311-6.
34. Safra, M., et al., The m1A landscape on cytosolic and mitochondrial mRNA at single-base resolution. *Nature*, 2017. 551(7679): p. 251-255.
35. Schwartz, S., m(1)A within cytoplasmic mRNAs at single nucleotide resolution: a reconciled transcriptome-wide map. *RNA*, 2018. 24(11): p. 1427-1436.
36. Li, X., et al., Base-Resolution Mapping Reveals Distinct m(1)A Methylome in Nuclear- and Mitochondrial-Encoded Transcripts. *Mol Cell*, 2017. 68(5): p. 993-1005 e9.
37. Ougland, R., et al., AlkB restores the biological function of mRNA and tRNA inactivated by chemical methylation. *Mol Cell*, 2004. 16(1): p. 107-16.
38. E, A.A., C. He, and A. Klungland, ALKBHs-facilitated RNA modifications and de-modifications. *DNA Repair (Amst)*, 2016. 44: p. 87-91.
39. Aas, P.A., et al., Human and bacterial oxidative demethylases repair alkylation damage in both RNA and DNA. *Nature*, 2003. 421(6925): p. 859-63.
40. Liu, F., et al., ALKBH1-Mediated tRNA Demethylation Regulates Translation. *Cell*, 2016. 167(3): p. 816-828 e16.
41. Motorin, Y., F. Lyko, and M. Helm, 5-methylcytosine in RNA: detection, enzymatic formation and biological functions. *Nucleic Acids Res*, 2010. 38(5): p. 1415-30.

42. Li, Q., et al., NSUN2-Mediated m⁵C Methylation and METTL3/METTL14-Mediated m⁶A Methylation Cooperatively Enhance p21 Translation. *J Cell Biochem*, 2017. 118(9): p. 2587-2598.
43. Yang, X., et al., 5-methylcytosine promotes mRNA export - NSUN2 as the methyltransferase and ALYREF as an m(5)C reader. *Cell Res*, 2017. 27(5): p. 606-625.
44. Khoddami, V., et al., Transcriptome-wide profiling of multiple RNA modifications simultaneously at single-base resolution. *Proc Natl Acad Sci U S A*, 2019. 116(14): p. 6784-6789.
45. Hussain, S., et al., NSun2-mediated cytosine-5 methylation of vault noncoding RNA determines its processing into regulatory small RNAs. *Cell Rep*, 2013. 4(2): p. 255-61.
46. Ito, S., et al., Tet proteins can convert 5-methylcytosine to 5-formylcytosine and 5-carboxycytosine. *Science*, 2011. 333(6047): p. 1300-3.
47. Fu, L., et al., Tet-mediated formation of 5-hydroxymethylcytosine in RNA. *J Am Chem Soc*, 2014. 136(33): p. 11582-5.
48. Xu, Q., et al., IDH1/2 Mutants Inhibit TET-Promoted Oxidation of RNA 5mC to 5hmC. *PLoS One*, 2016. 11(8): p. e0161261.
49. Delatte, B., et al., RNA biochemistry. Transcriptome-wide distribution and function of RNA hydroxymethylcytosine. *Science*, 2016. 351(6270): p. 282-5.
50. Lin, S., et al., Mettl1/Wdr4-Mediated m(7)G tRNA Methylome Is Required for Normal mRNA Translation and Embryonic Stem Cell Self-Renewal and Differentiation. *Mol Cell*, 2018. 71(2): p. 244-255 e5.

51. Pandolfini, L., et al., METTL1 Promotes let-7 MicroRNA Processing via m7G Methylation. *Mol Cell*, 2019. 74(6): p. 1278-1290 e9.
52. Zhang, L.S., et al., Transcriptome-wide Mapping of Internal N(7)-Methylguanosine Methylome in Mammalian mRNA. *Mol Cell*, 2019. 74(6): p. 1304-1316 e8.
53. Alexandrov, A., M.R. Martzen, and E.M. Phizicky, Two proteins that form a complex are required for 7-methylguanosine modification of yeast tRNA. *RNA*, 2002. 8(10): p. 1253-66.
54. Haag, S., J. Kretschmer, and M.T. Bohnsack, WBSR22/Merm1 is required for late nuclear pre-ribosomal RNA processing and mediates N7-methylation of G1639 in human 18S rRNA. *RNA*, 2015. 21(2): p. 180-7.
55. Carlile, T.M., et al., Pseudouridine profiling reveals regulated mRNA pseudouridylation in yeast and human cells. *Nature*, 2014. 515(7525): p. 143-6.
56. Schwartz, S., et al., Transcriptome-wide mapping reveals widespread dynamic-regulated pseudouridylation of ncRNA and mRNA. *Cell*, 2014. 159(1): p. 148-162.
57. Lovejoy, A.F., D.P. Riordan, and P.O. Brown, Transcriptome-wide mapping of pseudouridines: pseudouridine synthases modify specific mRNAs in *S. cerevisiae*. *PLoS One*, 2014. 9(10): p. e110799.
58. Carlile, T.M., et al., mRNA structure determines modification by pseudouridine synthase 1. *Nat Chem Biol*, 2019. 15(10): p. 966-974.

59. Vaidyanathan, P.P., et al., Pseudouridine and N(6)-methyladenosine modifications weaken PUF protein/RNA interactions. *RNA*, 2017. 23(5): p. 611-618.
60. Davis, D.R., Stabilization of RNA stacking by pseudouridine. *Nucleic Acids Res*, 1995. 23(24): p. 5020-6.
61. Spenkuch, F., Y. Motorin, and M. Helm, Pseudouridine: still mysterious, but never a fake (uridine)! *RNA Biol*, 2014. 11(12): p. 1540-54.
62. Li, X., X. Xiong, and C. Yi, Epitranscriptome sequencing technologies: decoding RNA modifications. *Nat Methods*, 2016. 14(1): p. 23-31.
63. Garcia-Campos, M.A., et al., Deciphering the "m(6)A Code" via Antibody-Independent Quantitative Profiling. *Cell*, 2019. 178(3): p. 731-747 e16.
64. Meyer, K.D., DART-seq: an antibody-free method for global m(6)A detection. *Nat Methods*, 2019.
65. Lorenz, D.A., et al., Direct RNA sequencing enables m6A detection in endogenous transcript isoforms at base specific resolution. *RNA*, 2019.
66. Liu, H., et al., Accurate detection of m(6)A RNA modifications in native RNA sequences. *Nat Commun*, 2019. 10(1): p. 4079.
67. Grozhik, A.V. and S.R. Jaffrey, Distinguishing RNA modifications from noise in epitranscriptome maps. *Nat Chem Biol*, 2018. 14(3): p. 215-225.
68. Li, X., et al., Chemical pulldown reveals dynamic pseudouridylation of the mammalian transcriptome. *Nat Chem Biol*, 2015. 11(8): p. 592-7.

69. Hauenschild, R., et al., The reverse transcription signature of N-1-methyladenosine in RNA-Seq is sequence dependent. *Nucleic Acids Res*, 2015. 43(20): p. 9950-64.
70. Zhao, B.S. and C. He, Fate by RNA methylation: m6A steers stem cell pluripotency. *Genome Biol*, 2015. 16: p. 43.
71. Wang, X., et al., N6-methyladenosine-dependent regulation of messenger RNA stability. *Nature*, 2014. 505(7481): p. 117-20.
72. Warda, A.S., et al., Human METTL16 is a N(6)-methyladenosine (m(6)A) methyltransferase that targets pre-mRNAs and various non-coding RNAs. *EMBO Rep*, 2017. 18(11): p. 2004-2014.
73. Pendleton, K.E., et al., The U6 snRNA m(6)A Methyltransferase METTL16 Regulates SAM Synthetase Intron Retention. *Cell*, 2017. 169(5): p. 824-835 e14.
74. Mendel, M., et al., Methylation of Structured RNA by the m(6)A Writer METTL16 Is Essential for Mouse Embryonic Development. *Mol Cell*, 2018. 71(6): p. 986-1000 e11.
75. Amort, T., et al., Distinct 5-methylcytosine profiles in poly(A) RNA from mouse embryonic stem cells and brain. *Genome Biol*, 2017. 18(1): p. 1.
76. Trixl, L., et al., RNA cytosine methyltransferase Nsun3 regulates embryonic stem cell differentiation by promoting mitochondrial activity. *Cell Mol Life Sci*, 2018. 75(8): p. 1483-1497.
77. Fazi, F. and A. Fatica, Interplay Between N (6)-Methyladenosine (m(6)A) and Non-coding RNAs in Cell Development and Cancer. *Front Cell Dev Biol*, 2019. 7: p. 116.

78. Wu, R., et al., m(6)A methylation controls pluripotency of porcine induced pluripotent stem cells by targeting SOCS3/JAK2/STAT3 pathway in a YTHDF1/YTHDF2-orchestrated manner. *Cell Death Dis*, 2019. 10(3): p. 171.
79. Niwa, H., et al., Self-renewal of pluripotent embryonic stem cells is mediated via activation of STAT3. *Genes Dev*, 1998. 12(13): p. 2048-60.
80. Aguilo, F., et al., Coordination of m(6)A mRNA Methylation and Gene Transcription by ZFP217 Regulates Pluripotency and Reprogramming. *Cell Stem Cell*, 2015. 17(6): p. 689-704.
81. Wen, J., et al., Zc3h13 Regulates Nuclear RNA m(6)A Methylation and Mouse Embryonic Stem Cell Self-Renewal. *Mol Cell*, 2018. 69(6): p. 1028-1038 e6.
82. Horiuchi, K., et al., Identification of Wilms' tumor 1-associating protein complex and its role in alternative splicing and the cell cycle. *J Biol Chem*, 2013. 288(46): p. 33292-302.
83. Wan, C., et al., Panorama of ancient metazoan macromolecular complexes. *Nature*, 2015. 525(7569): p. 339-44.
84. Bertero, A., et al., The SMAD2/3 interactome reveals that TGFbeta controls m(6)A mRNA methylation in pluripotency. *Nature*, 2018. 555(7695): p. 256-259.
85. Huang, H., et al., Histone H3 trimethylation at lysine 36 guides m(6)A RNA modification co-transcriptionally. *Nature*, 2019. 567(7748): p. 414-419.
86. Malovannaya, A., et al., Analysis of the human endogenous coregulator complexome. *Cell*, 2011. 145(5): p. 787-99.
87. Lence, T., et al., m(6)A modulates neuronal functions and sex determination in *Drosophila*. *Nature*, 2016. 540(7632): p. 242-247.

88. Yoon, K.J., et al., Temporal Control of Mammalian Cortical Neurogenesis by m(6)A Methylation. *Cell*, 2017. 171(4): p. 877-889 e17.
89. Wang, Y., et al., N(6)-methyladenosine RNA modification regulates embryonic neural stem cell self-renewal through histone modifications. *Nat Neurosci*, 2018. 21(2): p. 195-206.
90. Li, M., et al., Ythdf2-mediated m(6)A mRNA clearance modulates neural development in mice. *Genome Biol*, 2018. 19(1): p. 69.
91. Wang, C.X., et al., METTL3-mediated m6A modification is required for cerebellar development. *PLoS Biol*, 2018. 16(6): p. e2004880.
92. Cui, Q., et al., m(6)A RNA Methylation Regulates the Self-Renewal and Tumorigenesis of Glioblastoma Stem Cells. *Cell Rep*, 2017. 18(11): p. 2622-2634.
93. Choudhry, Z., et al., Association between obesity-related gene FTO and ADHD. *Obesity (Silver Spring)*, 2013. 21(12): p. E738-44.
94. Hess, M.E., et al., The fat mass and obesity associated gene (Fto) regulates activity of the dopaminergic midbrain circuitry. *Nat Neurosci*, 2013. 16(8): p. 1042-8.
95. Keller, L., et al., The obesity related gene, FTO, interacts with APOE, and is associated with Alzheimer's disease risk: a prospective cohort study. *J Alzheimers Dis*, 2011. 23(3): p. 461-9.
96. Li, H., et al., FTO is involved in Alzheimer's disease by targeting TSC1-mTOR-Tau signaling. *Biochem Biophys Res Commun*, 2018. 498(1): p. 234-239.

97. Widagdo, J., et al., Experience-Dependent Accumulation of N6-Methyladenosine in the Prefrontal Cortex Is Associated with Memory Processes in Mice. *J Neurosci*, 2016. 36(25): p. 6771-7.
98. Gao, X., et al., The fat mass and obesity associated gene FTO functions in the brain to regulate postnatal growth in mice. *PLoS One*, 2010. 5(11): p. e14005.
99. Li, L., et al., Fat mass and obesity-associated (FTO) protein regulates adult neurogenesis. *Hum Mol Genet*, 2017. 26(13): p. 2398-2411.
100. Chen, J., et al., m(6)A Regulates Neurogenesis and Neuronal Development by Modulating Histone Methyltransferase Ezh2. *Genomics Proteomics Bioinformatics*, 2019. 17(2): p. 154-168.
101. Ming, G.L. and H. Song, Adult neurogenesis in the mammalian brain: significant answers and significant questions. *Neuron*, 2011. 70(4): p. 687-702.
102. Song, J., et al., Neuronal circuitry mechanism regulating adult quiescent neural stem-cell fate decision. *Nature*, 2012. 489(7414): p. 150-4.
103. Darnell, J.C., et al., FMRP stalls ribosomal translocation on mRNAs linked to synaptic function and autism. *Cell*, 2011. 146(2): p. 247-61.
104. Richter, J.D., G.J. Bassell, and E. Klann, Dysregulation and restoration of translational homeostasis in fragile X syndrome. *Nat Rev Neurosci*, 2015. 16(10): p. 595-605.
105. De Diego Otero, Y., et al., Transport of fragile X mental retardation protein via granules in neurites of PC12 cells. *Mol Cell Biol*, 2002. 22(23): p. 8332-41.

106. Arguello, A.E., A.N. DeLiberto, and R.E. Kleiner, RNA Chemical Proteomics Reveals the N(6)-Methyladenosine (m(6)A)-Regulated Protein-RNA Interactome. *J Am Chem Soc*, 2017. 139(48): p. 17249-17252.
107. Zhang, F., et al., Fragile X mental retardation protein modulates the stability of its m6A-marked messenger RNA targets. *Hum Mol Genet*, 2018. 27(22): p. 3936-3950.
108. Edens, B.M., et al., FMRP Modulates Neural Differentiation through m(6)A-Dependent mRNA Nuclear Export. *Cell Rep*, 2019. 28(4): p. 845-854 e5.
109. Hsu, P.J., et al., The RNA-binding protein FMRP facilitates the nuclear export of N (6)-methyladenosine-containing mRNAs. *J Biol Chem*, 2019.
110. Shaheen, R., et al., A homozygous truncating mutation in PUS3 expands the role of tRNA modification in normal cognition. *Hum Genet*, 2016. 135(7): p. 707-13.
111. de Brouwer, A.P.M., et al., Variants in PUS7 Cause Intellectual Disability with Speech Delay, Microcephaly, Short Stature, and Aggressive Behavior. *Am J Hum Genet*, 2018. 103(6): p. 1045-1052.
112. Shaheen, R., et al., PUS7 mutations impair pseudouridylation in humans and cause intellectual disability and microcephaly. *Hum Genet*, 2019. 138(3): p. 231-239.
113. van Tran, N., et al., The human 18S rRNA m6A methyltransferase METTL5 is stabilized by TRMT112. *Nucleic Acids Res*, 2019. 47(15): p. 7719-7733.
114. Richard, E.M., et al., Bi-allelic Variants in METTL5 Cause Autosomal-Recessive Intellectual Disability and Microcephaly. *Am J Hum Genet*, 2019. 105(4): p. 869-878.

115. Jamuar, S.S. and C.A. Walsh, Genomic variants and variations in malformations of cortical development. *Pediatr Clin North Am*, 2015. 62(3): p. 571-85.
116. Taverna, E., M. Gotz, and W.B. Huttner, The cell biology of neurogenesis: toward an understanding of the development and evolution of the neocortex. *Annu Rev Cell Dev Biol*, 2014. 30: p. 465-502.
117. Gage, F.H. and S. Temple, Neural stem cells: generating and regenerating the brain. *Neuron*, 2013. 80(3): p. 588-601.
118. Kriegstein, A. and A. Alvarez-Buylla, The glial nature of embryonic and adult neural stem cells. *Annu Rev Neurosci*, 2009. 32: p. 149-84.
119. Okano, H. and S. Temple, Cell types to order: temporal specification of CNS stem cells. *Curr Opin Neurobiol*, 2009. 19(2): p. 112-9.
120. Shibata, M., F.O. Gulden, and N. Sestan, From trans to cis: transcriptional regulatory networks in neocortical development. *Trends Genet*, 2015. 31(2): p. 77-87.
121. Martynoga, B., D. Drechsel, and F. Guillemot, Molecular control of neurogenesis: a view from the mammalian cerebral cortex. *Cold Spring Harb Perspect Biol*, 2012. 4(10).
122. Nord, A.S., et al., Genomic perspectives of transcriptional regulation in forebrain development. *Neuron*, 2015. 85(1): p. 27-47.
123. Miller, J.A., et al., Transcriptional landscape of the prenatal human brain. *Nature*, 2014. 508(7495): p. 199-206.
124. Greig, L.C., et al., Molecular logic of neocortical projection neuron specification, development and diversity. *Nat Rev Neurosci*, 2013. 14(11): p. 755-69.

125. Rubenstein, J.L. and P. Rakic, Patterning and Cell Type Specification in the Developing CNS and PNS. 2013: Elsevier.
126. Guillemot, F., et al., Molecular mechanisms of cortical differentiation. *Eur J Neurosci*, 2006. 23(4): p. 857-68.
127. Telley, L., et al., Sequential transcriptional waves direct the differentiation of newborn neurons in the mouse neocortex. *Science*, 2016. 351(6280): p. 1443-6.
128. Dezi, V., et al., Nucleotide modifications in messenger RNA and their role in development and disease. *Biochem Soc Trans*, 2016. 44(5): p. 1385-1393.
129. Zhao, B.S., I.A. Roundtree, and C. He, Post-transcriptional gene regulation by mRNA modifications. *Nat Rev Mol Cell Biol*, 2017. 18(1): p. 31-42.
130. Desrosiers, R.C., K.H. Friderici, and F.M. Rottman, Characterization of Novikoff hepatoma mRNA methylation and heterogeneity in the methylated 5' terminus. *Biochemistry*, 1975. 14(20): p. 4367-74.
131. Meyer, K.D. and S.R. Jaffrey, The dynamic epitranscriptome: N6-methyladenosine and gene expression control. *Nat Rev Mol Cell Biol*, 2014. 15(5): p. 313-26.
132. Ke, S., et al., A majority of m6A residues are in the last exons, allowing the potential for 3' UTR regulation. *Genes Dev*, 2015. 29(19): p. 2037-53.
133. Meyer, K.D. and S.R. Jaffrey, Rethinking m6A Readers, Writers, and Erasers. *Annu Rev Cell Dev Biol*, 2017.
134. Haussmann, I.U., et al., m6A potentiates Sxl alternative pre-mRNA splicing for robust *Drosophila* sex determination. *Nature*, 2016. 540(7632): p. 301-304.

135. Lence, T., et al., m6A modulates neuronal functions and sex determination in *Drosophila*. *Nature*, 2016. 540(7632): p. 242-247.
136. Zhao, B.S., et al., m6A-dependent maternal mRNA clearance facilitates zebrafish maternal-to-zygotic transition. *Nature*, 2017. 542(7642): p. 475-478.
137. Dwyer, N.D., et al., Neural Stem Cells to Cerebral Cortex: Emerging Mechanisms Regulating Progenitor Behavior and Productivity. *J Neurosci*, 2016. 36(45): p. 11394-11401.
138. Englund, C., et al., Pax6, Tbr2, and Tbr1 are expressed sequentially by radial glia, intermediate progenitor cells, and postmitotic neurons in developing neocortex. *J Neurosci*, 2005. 25(1): p. 247-51.
139. Guerrier, S. and F. Polleux, The ups and downs of neural progenitors: Cep120 and TACCs control interkinetic nuclear migration. *Neuron*, 2007. 56(1): p. 1-3.
140. Spencer, S.L., et al., The proliferation-quiescence decision is controlled by a bifurcation in CDK2 activity at mitotic exit. *Cell*, 2013. 155(2): p. 369-83.
141. Wang, X., et al., Human m6A writers: Two subunits, two roles. *RNA Biol*, 2017. 14(3): p. 300-304.
142. Hevner, R.F., et al., Transcription factors in glutamatergic neurogenesis: conserved programs in neocortex, cerebellum, and adult hippocampus. *Neurosci Res*, 2006. 55(3): p. 223-33.
143. Duffy, E.E., et al., Tracking Distinct RNA Populations Using Efficient and Reversible Covalent Chemistry. *Mol Cell*, 2015. 59(5): p. 858-66.

144. Radle, B., et al., Metabolic labeling of newly transcribed RNA for high resolution gene expression profiling of RNA synthesis, processing and decay in cell culture. *J Vis Exp*, 2013(78).
145. Schoenberg, D.R. and L.E. Maquat, Regulation of cytoplasmic mRNA decay. *Nat Rev Genet*, 2012. 13(4): p. 246-59.
146. Du, H., et al., YTHDF2 destabilizes m(6)A-containing RNA through direct recruitment of the CCR4-NOT deadenylase complex. *Nat Commun*, 2016. 7: p. 12626.
147. Yoon, K.J., et al., Modeling a genetic risk for schizophrenia in iPSCs and mice reveals neural stem cell deficits associated with adherens junctions and polarity. *Cell Stem Cell*, 2014. 15(1): p. 79-91.
148. Qian, X., et al., Brain-Region-Specific Organoids Using Mini-bioreactors for Modeling ZIKV Exposure. *Cell*, 2016. 165(5): p. 1238-54.
149. Tebbenkamp, A.T., et al., The developmental transcriptome of the human brain: implications for neurodevelopmental disorders. *Curr Opin Neurol*, 2014. 27(2): p. 149-56.
150. Ohi, K., et al., Specific gene expression patterns of 108 schizophrenia-associated loci in cortex. *Schizophr Res*, 2016. 174(1-3): p. 35-8.
151. Schizophrenia Working Group of the Psychiatric Genomics, C., Biological insights from 108 schizophrenia-associated genetic loci. *Nature*, 2014. 511(7510): p. 421-7.
152. Kohwi, M. and C.Q. Doe, Temporal fate specification and neural progenitor competence during development. *Nat Rev Neurosci*, 2013. 14(12): p. 823-38.

153. Xu, C.R., et al., Chromatin "prepattern" and histone modifiers in a fate choice for liver and pancreas. *Science*, 2011. 332(6032): p. 963-6.
154. Chen, T. and S.Y. Dent, Chromatin modifiers and remodellers: regulators of cellular differentiation. *Nat Rev Genet*, 2014. 15(2): p. 93-106.
155. Sansom, S.N., et al., The level of the transcription factor Pax6 is essential for controlling the balance between neural stem cell self-renewal and neurogenesis. *PLoS Genet*, 2009. 5(6): p. e1000511.
156. Yao, B., et al., Epigenetic mechanisms in neurogenesis. *Nat Rev Neurosci*, 2016. 17: p. 537-49.
157. Hirabayashi, Y. and Y. Gotoh, Epigenetic control of neural precursor cell fate during development. *Nat Rev Neurosci*, 2010. 11(6): p. 377-88.
158. Du, T., et al., An association study of the m6A genes with major depressive disorder in Chinese Han population. *J Affect Disord*, 2015. 183: p. 279-86.
159. Daoud, H., et al., Identification of a pathogenic FTO mutation by next-generation sequencing in a newborn with growth retardation and developmental delay. *J Med Genet*, 2016. 53(3): p. 200-7.
160. Boissel, S., et al., Loss-of-function mutation in the dioxygenase-encoding FTO gene causes severe growth retardation and multiple malformations. *Am J Hum Genet*, 2009. 85(1): p. 106-11.
161. Tronche, F., et al., Disruption of the glucocorticoid receptor gene in the nervous system results in reduced anxiety. *Nat Genet*, 1999. 23(1): p. 99-103.
162. Wen, Z., et al., Synaptic dysregulation in a human iPS cell model of mental disorders. *Nature*, 2014. 515(7527): p. 414-8.

163. Ge, S., et al., GABA regulates synaptic integration of newly generated neurons in the adult brain. *Nature*, 2006. 439(7076): p. 589-93.
164. Wang, Z., et al., Cyclin B1/Cdk1 coordinates mitochondrial respiration for cell-cycle G2/M progression. *Dev Cell*, 2014. 29(2): p. 217-32.
165. Terry, N.H. and R.A. White, Flow cytometry after bromodeoxyuridine labeling to measure S and G2+M phase durations plus doubling times in vitro and in vivo. *Nature Protocols*, 2006. 1(2): p. 859-869.
166. Kim, D., et al., TopHat2: accurate alignment of transcriptomes in the presence of insertions, deletions and gene fusions. *Genome Biol*, 2013. 14(4): p. R36.
167. Zhang, Y., et al., Model-based analysis of ChIP-Seq (MACS). *Genome Biol*, 2008. 9(9): p. R137.
168. Quinlan, A.R. and I.M. Hall, BEDTools: a flexible suite of utilities for comparing genomic features. *Bioinformatics*, 2010. 26(6): p. 841-2.
169. Anders, S., P.T. Pyl, and W. Huber, HTSeq--a Python framework to work with high-throughput sequencing data. *Bioinformatics*, 2015. 31(2): p. 166-9.
170. Chen, J., et al., ToppGene Suite for gene list enrichment analysis and candidate gene prioritization. *Nucleic Acids Res*, 2009. 37(Web Server issue): p. W305-11.
171. Zhang, B., S. Kirov, and J. Snoddy, WebGestalt: an integrated system for exploring gene sets in various biological contexts. *Nucleic Acids Res*, 2005. 33(Web Server issue): p. W741-8.
172. Shannon, P., et al., Cytoscape: a software environment for integrated models of biomolecular interaction networks. *Genome Res*, 2003. 13(11): p. 2498-504.

173. Li, B. and C.N. Dewey, RSEM: accurate transcript quantification from RNA-Seq data with or without a reference genome. *BMC Bioinformatics*, 2011. 12: p. 323.
174. Langmead, B. and S.L. Salzberg, Fast gapped-read alignment with Bowtie 2. *Nat Methods*, 2012. 9(4): p. 357-9.
175. Leng, N., et al., EBSeq: an empirical Bayes hierarchical model for inference in RNA-seq experiments. *Bioinformatics*, 2013. 29(8): p. 1035-43.
176. Chen, C.Y., N. Ezzeddine, and A.B. Shyu, Messenger RNA half-life measurements in mammalian cells. *Methods Enzymol*, 2008. 448: p. 335-57.
177. Lee, C., H. Shin, and J. Kimble, Dynamics of Notch-Dependent Transcriptional Bursting in Its Native Context. *Dev Cell*, 2019. 50(4): p. 426-435 e4.
178. Imayoshi, I., et al., Oscillatory control of factors determining multipotency and fate in mouse neural progenitors. *Science*, 2013. 342(6163): p. 1203-8.
179. Imayoshi, I. and R. Kageyama, Oscillatory control of bHLH factors in neural progenitors. *Trends Neurosci*, 2014. 37(10): p. 531-8.
180. Kageyama, R., H. Shimojo, and A. Isomura, Oscillatory Control of Notch Signaling in Development. *Adv Exp Med Biol*, 2018. 1066: p. 265-277.
181. Nolte, C. and D. Staiger, RNA around the clock - regulation at the RNA level in biological timing. *Front Plant Sci*, 2015. 6: p. 311.
182. Bessho, Y., et al., Hes7: a bHLH-type repressor gene regulated by Notch and expressed in the presomitic mesoderm. *Genes Cells*, 2001. 6(2): p. 175-85.
183. Shimojo, H. and R. Kageyama, Oscillatory control of Delta-like1 in somitogenesis and neurogenesis: A unified model for different oscillatory dynamics. *Semin Cell Dev Biol*, 2016. 49: p. 76-82.

184. Imayoshi, I., et al., Genetic visualization of notch signaling in mammalian neurogenesis. *Cell Mol Life Sci*, 2013. 70(12): p. 2045-57.
185. Sueda, R., et al., High Hes1 expression and resultant Ascl1 suppression regulate quiescent vs. active neural stem cells in the adult mouse brain. *Genes Dev*, 2019. 33(9-10): p. 511-523.
186. Isomura, A., et al., Optogenetic perturbation and bioluminescence imaging to analyze cell-to-cell transfer of oscillatory information. *Genes Dev*, 2017. 31(5): p. 524-535.
187. Semenza, G.L., The hypoxic tumor microenvironment: A driving force for breast cancer progression. *Biochim Biophys Acta*, 2016. 1863(3): p. 382-391.
188. Muz, B., et al., The role of hypoxia in cancer progression, angiogenesis, metastasis, and resistance to therapy. *Hypoxia (Auckl)*, 2015. 3: p. 83-92.
189. Semenza, G.L., Oxygen sensing, hypoxia-inducible factors, and disease pathophysiology. *Annu Rev Pathol*, 2014. 9: p. 47-71.
190. Axelson, H., et al., Hypoxia-induced dedifferentiation of tumor cells--a mechanism behind heterogeneity and aggressiveness of solid tumors. *Semin Cell Dev Biol*, 2005. 16(4-5): p. 554-63.
191. Vaupel, P., M. Hockel, and A. Mayer, Detection and characterization of tumor hypoxia using pO₂ histography. *Antioxid Redox Signal*, 2007. 9(8): p. 1221-35.
192. Schito, L. and G.L. Semenza, Hypoxia-Inducible Factors: Master Regulators of Cancer Progression. *Trends Cancer*, 2016. 2(12): p. 758-770.

193. Mimeault, M. and S.K. Batra, Hypoxia-inducing factors as master regulators of stemness properties and altered metabolism of cancer- and metastasis-initiating cells. *J Cell Mol Med*, 2013. 17(1): p. 30-54.
194. Fry, N.J., et al., N(6)-methyladenosine contributes to cellular phenotype in a genetically-defined model of breast cancer progression. *Oncotarget*, 2018. 9(58): p. 31231-31243.
195. Fry, N.J., et al., N(6)-methyladenosine is required for the hypoxic stabilization of specific mRNAs. *RNA*, 2017. 23(9): p. 1444-1455.
196. Zhang, C., et al., Hypoxia induces the breast cancer stem cell phenotype by HIF-dependent and ALKBH5-mediated m(6)A-demethylation of NANOG mRNA. *Proc Natl Acad Sci U S A*, 2016. 113(14): p. E2047-56.
197. Zhang, C., et al., Hypoxia-inducible factors regulate pluripotency factor expression by ZNF217- and ALKBH5-mediated modulation of RNA methylation in breast cancer cells. *Oncotarget*, 2016. 7(40): p. 64527-64542.
198. Thalhammer, A., et al., Human AlkB homologue 5 is a nuclear 2-oxoglutarate dependent oxygenase and a direct target of hypoxia-inducible factor 1alpha (HIF-1alpha). *PLoS One*, 2011. 6(1): p. e16210.
199. Yoon, K.J., et al., Epigenetics and epitranscriptomics in temporal patterning of cortical neural progenitor competence. *J Cell Biol*, 2018. 217(6): p. 1901-1914.
200. Meyer, K.D. and S.R. Jaffrey, Rethinking m(6)A Readers, Writers, and Erasers. *Annu Rev Cell Dev Biol*, 2017. 33: p. 319-342.
201. Mauer, J. and S.R. Jaffrey, FTO, m(6) Am , and the hypothesis of reversible epitranscriptomic mRNA modifications. *FEBS Lett*, 2018. 592(12): p. 2012-2022.

202. Liao, S., H. Sun, and C. Xu, YTH Domain: A Family of N(6)-methyladenosine (m(6)A) Readers. *Genomics Proteomics Bioinformatics*, 2018. 16(2): p. 99-107.
203. He, L., et al., The dual role of N6-methyladenosine modification of RNAs is involved in human cancers. *J Cell Mol Med*, 2018.
204. Liu, J., et al., m(6)A demethylase FTO facilitates tumor progression in lung squamous cell carcinoma by regulating MZF1 expression. *Biochem Biophys Res Commun*, 2018. 502(4): p. 456-464.
205. Dominissini, D., et al., Transcriptome-wide mapping of N(6)-methyladenosine by m(6)A-seq based on immunocapturing and massively parallel sequencing. *Nat Protoc*, 2013. 8(1): p. 176-89.
206. Semenza, G.L., HIF-1 mediates metabolic responses to intratumoral hypoxia and oncogenic mutations. *J Clin Invest*, 2013. 123(9): p. 3664-71.
207. Meyer, K.D., et al., 5' UTR m(6)A Promotes Cap-Independent Translation. *Cell*, 2015. 163(4): p. 999-1010.
208. Xiao, W., et al., Nuclear m(6)A Reader YTHDC1 Regulates mRNA Splicing. *Mol Cell*, 2016. 61(4): p. 507-519.
209. Zhou, J., et al., Dynamic m(6)A mRNA methylation directs translational control of heat shock response. *Nature*, 2015. 526(7574): p. 591-4.
210. Kasowitz, S.D., et al., Nuclear m6A reader YTHDC1 regulates alternative polyadenylation and splicing during mouse oocyte development. *PLoS Genet*, 2018. 14(5): p. e1007412.
211. Wang, X., et al., N(6)-methyladenosine Modulates Messenger RNA Translation Efficiency. *Cell*, 2015. 161(6): p. 1388-99.

212. Nishizawa, Y., et al., Oncogene c-Myc promotes epitranscriptome m(6)A reader YTHDF1 expression in colorectal cancer. *Oncotarget*, 2018. 9(7): p. 7476-7486.
213. Roundtree, I.A., et al., YTHDC1 mediates nuclear export of N(6)-methyladenosine methylated mRNAs. *Elife*, 2017. 6.
214. Shima, H., et al., S-Adenosylmethionine Synthesis Is Regulated by Selective N(6)-Adenosine Methylation and mRNA Degradation Involving METTL16 and YTHDC1. *Cell Rep*, 2017. 21(12): p. 3354-3363.
215. Brady, L.K., et al., Transcriptome analysis of hypoxic cancer cells uncovers intron retention in EIF2B5 as a mechanism to inhibit translation. *PLoS Biol*, 2017. 15(9): p. e2002623.
216. Hirschfeld, M., et al., Alternative splicing of Cyr61 is regulated by hypoxia and significantly changed in breast cancer. *Cancer Res*, 2009. 69(5): p. 2082-90.
217. Haider, S. and R. Pal, Integrated analysis of transcriptomic and proteomic data. *Curr Genomics*, 2013. 14(2): p. 91-110.
218. Maier, T., M. Guell, and L. Serrano, Correlation of mRNA and protein in complex biological samples. *FEBS Lett*, 2009. 583(24): p. 3966-73.
219. Noack, F. and F. Calegari, Epitranscriptomics: A New Regulatory Mechanism of Brain Development and Function. *Front Neurosci*, 2018. 12: p. 85.
220. Berlivet, S., et al., Readers of the m(6)A epitranscriptomic code. *Biochim Biophys Acta Gene Regul Mech*, 2019.
221. Luo, J., et al., Aberrant Regulation of mRNA m(6)A Modification in Cancer Development. *Int J Mol Sci*, 2018. 19(9).

222. Pan, Y., et al., Multiple functions of m(6)A RNA methylation in cancer. *J Hematol Oncol*, 2018. 11(1): p. 48.
223. Vu, L.P., et al., The N(6)-methyladenosine (m(6)A)-forming enzyme METTL3 controls myeloid differentiation of normal hematopoietic and leukemia cells. *Nat Med*, 2017. 23(11): p. 1369-1376.
224. Ma, J.Z., et al., METTL14 suppresses the metastatic potential of hepatocellular carcinoma by modulating N(6) -methyladenosine-dependent primary MicroRNA processing. *Hepatology*, 2017. 65(2): p. 529-543.
225. Bai, Y., et al., YTHDF1 Regulates Tumorigenicity and Cancer Stem Cell-Like Activity in Human Colorectal Carcinoma. *Front Oncol*, 2019. 9: p. 332.
226. Xu, C., et al., Structural Basis for the Discriminative Recognition of N6-Methyladenosine RNA by the Human YT521-B Homology Domain Family of Proteins. *J Biol Chem*, 2015. 290(41): p. 24902-13.
227. Visvanathan, A., et al., Essential role of METTL3-mediated m(6)A modification in glioma stem-like cells maintenance and radioresistance. *Oncogene*, 2018. 37(4): p. 522-533.
228. Weng, H., et al., METTL14 Inhibits Hematopoietic Stem/Progenitor Differentiation and Promotes Leukemogenesis via mRNA m(6)A Modification. *Cell Stem Cell*, 2018. 22(2): p. 191-205 e9.
229. Zhang, H., et al., HIF-1-dependent expression of angiopoietin-like 4 and L1CAM mediates vascular metastasis of hypoxic breast cancer cells to the lungs. *Oncogene*, 2012. 31(14): p. 1757-70.

230. Rio, D.C., et al., Purification of RNA using TRIzol (TRI reagent). Cold Spring Harb Protoc, 2010. 2010(6): p. pdb prot5439.
231. Love, M.I., W. Huber, and S. Anders, Moderated estimation of fold change and dispersion for RNA-seq data with DESeq2. Genome Biol, 2014. 15(12): p. 550.
232. Babicki, S., et al., Heatmapper: web-enabled heat mapping for all. Nucleic Acids Res, 2016. 44(W1): p. W147-53.
233. Lawrence, M., et al., Software for computing and annotating genomic ranges. PLoS Comput Biol, 2013. 9(8): p. e1003118.
234. Lawrence, M., R. Gentleman, and V. Carey, rtracklayer: an R package for interfacing with genome browsers. Bioinformatics, 2009. 25(14): p. 1841-2.
235. Durinck, S., et al., Mapping identifiers for the integration of genomic datasets with the R/Bioconductor package biomaRt. Nat Protoc, 2009. 4(8): p. 1184-91.
236. Zhu, L.J., et al., ChIPpeakAnno: a Bioconductor package to annotate ChIP-seq and ChIP-chip data. BMC Bioinformatics, 2010. 11: p. 237.
237. Cui, X., et al., Guitar: An R/Bioconductor Package for Gene Annotation Guided Transcriptomic Analysis of RNA-Related Genomic Features. Biomed Res Int, 2016. 2016: p. 8367534.
238. Wang, Y., et al., Reversed-phase chromatography with multiple fraction concatenation strategy for proteome profiling of human MCF10A cells. Proteomics, 2011. 11(10): p. 2019-26.

CURRICULUM VITAE

Education:

Johns Hopkins School of Medicine

2015-2019

Ph.D. in Biochemistry, Cellular, and Molecular Biology; Department of Neuroscience

Thesis: “m⁶A mRNA modification is a key regulator of stem cell behavior in health and disease”

Training in the labs of Hongjun Song and Gregg Semenza

Year-long collaboration in Dr. Ryoichiro Kageyama’s lab at **Kyoto University** (09/2018-08/2019)

University of California, Davis

2010-2014

Graduated *summa cum laude* with a B.S. in animal science and focus in genetics. Cumulative GPA: 3.92

Publications:

1. Edens B, **Vissers C**, Su J, Arumugam S, Shi H, Miller N, Rojas-Ringeling F, Ming GL, He C, Song H, Ma Y. FMRP modulates neural differentiation through m⁶A-dependent mRNA nuclear export. *Cell Reports*. 2019 Jul; 28(4):845-854.e5. PMID: PMC6687293
2. **Vissers C**, Ming GL, Song H. Nanoparticle technology and stem cell therapy team up against neurodegenerative disorders. *Advanced Drug Delivery Reviews*. 2019 Aug; 148:239-251 PMID: PMC6703981
3. Yoon KJ., **Vissers C**, Ming GL, Song H. Epigenetics and epitranscriptomics in temporal patterning of cortical neural progenitor competence. *J Cell Biology*. 2018 Jun; 217(6):1901-1914. PMID: PMC5987727
4. Weng Y, Wang, X., An R, Cassin J, **Vissers C**, Xu T, Wang X, Wong Z, Joseph J, Dong Q, Zheng W, Jin P, Wu H, Zhuang X, He C, Song H, Ming GL. Epitranscriptomic m⁶A regulation of axon regeneration in the adult mammalian nervous system. *Neuron*. 2018 Jan; 97(2):313-325. PMID: PMC5777326
5. Yoon KJ*, Rojas-Ringeling F*, **Vissers C***, Jacob F, Pokrass M, Jimenez-Cyrus D, Su Y, Kim N, Zhu Y, Zheng L, Kim S, Wang X, Hyde T, Weinberger D, Jin P, Zhuang X, Regot S, Canzar S, He C, Ming GL, Song H. Temporal control of mammalian cortical neurogenesis by m⁶A mRNA methylation. *Cell*. 2017 Nov; 171, 1–13. PMID: PMC5679435
***co-first authors**
6. Yoon KJ., Song, G., Qian, X., Pan, J., Xu, D., Rho, HS., Kim, NS., Habela, C., Zheng, L., Jacob, F., Zhang, F., Lee, EM., Huang, WK., Ringeling, FR., **Vissers, C.**, Li, C., Yuan, L., Kang, K., Kim, S., Yeo, J., Cheng, Y., Liu, S., Wen, Z., Qin, CF., Wu, Q., Christian, KM., Tang, H., Jin, P., Xu, Z., Qian, J., Zhu, H., Song and H., Ming, GL. Zika-Virus-Encoded NS2A Disrupts Mammalian Cortical Neurogenesis by Degrading Adherens Junction Proteins. *Cell Stem Cell*. 2017 Aug; 7;21(3):349-358. PMID: PMC5600197
7. **Vissers C**, Harvestine JN, Leach JK. Pore size regulates mesenchymal stem cell response to bioglass-loaded composite scaffolds. *J. Mater. Chem. B*. 2015 Sep; 44(3) 8650-8658. DOI: 10.1039/c5tb00947b

8. Ho S, Murphy KC, Binder B, **Vissers C**, Leach JK. Increased Survival and Function of Mesenchymal Stem Cell Spheroids Entrapped in Instructive Alginate Hydrogels. *Stem Cell Trans. Med.* 2016 Jun; 5(6):773-81. DOI: 10.5966/sctm.2015-0211
9. Murphy KC, Hughbanks ML, Binder BY, **Vissers C**, Leach JK. Engineered Fibrin Gels for Parallel Stimulation of Mesenchymal Stem Cell Proangiogenic and Osteogenic Potential. *Ann Biomed Eng.* 2015 Aug; 43(8):2010-21. PMID: PMC4878334
10. **Vissers C**, Kageyama R. Highlight: Bursting the Notch Bubble: New Insights into In Vivo Transcriptional Dynamics. *Developmental Cell.* 2019 Aug; 50(4):393-394. DOI: 10.1016/j.devcel.2019.07.028
11. **Vissers C**, Ming GL, Song H. Highlight: Stem Cells Take the Stairs. *Journal of Biological Chemistry.* 2017 Dec; 292: 19605-19606. DOI: 10.1074/jbc.H117.796383

Submitted/ In preparation:

12. **Vissers C**, Samanta D, Huang T, Semenza GL. Hypoxia Inducible Factor (HIF) regulates translation via ALKBH5 induction in breast cancer cells. *Submitted*

Awards and Recognitions:

Fellowships:

- Sandler Faculty Fellowship, UCSF 2020-2025
- Grass Fellowship to perform entirely independent research for 14 weeks 2018
- NSF Graduate Fellow 2016-current
 - NSF Graduate Opportunities Worldwide (GROW) additional funding 2018-2019
- Arnold and Mabel Beckman Foundation Scholar 2013-2014

Awards:

- Johns Hopkins Fall Consulting Case Competition: 1st place 2019
- Lasker Foundation Essay Contest: 3rd Place 2018
 - Title: “Diversity at the Top of the Social Media Signaling Cascade”
- Johns Hopkins 3 Minute Thesis: 1st place and People’s Choice Award 2018
- Best Talk, Kyoto International Student Seminar 2018
- Kelly Award: merit award for excellence in graduate school 2016
- Hopkins Research Scholar: opportunity to design independent coursework after testing out of two core courses 2016
- Rhodes Scholar Finalist 2014
- Chancellor’s Award for Excellence in Undergraduate Research: for the top scientific research at my university 2014
- Citation Award, Department of Animal Science for true distinction in service to the department. 2014
- Best Delegate at Rome, Italy Model United Nations for my representation of China in the discussion of labor laws through the ILO-WTO Council 2012
- Best Delegate at Stockholm, Sweden Model United Nations for my representation of Senegal in the discussion of the Millennium Goals through the Economic and Social Council 2012

Scholarships:

- UC Davis Gretta Breedlove Ross Award 2013
- UC Davis Laben Award for academic excellence and leaderships skills 2013
- UC Davis Student Alumni Association Leadership Scholarship 2010
- UC Davis Jastro Scholarship for academic and extracurricular achievement 2010-2014

Selected Presentations:

Oral:

- Invited Seminar (1 hour): Kyoto University; Department of Cell, Developmental, and Systems Biology. “Molecular regulation of stem cells by m⁶A mRNA methylation.” Kyoto, Japan. November 2018
- Grass Fellowship Symposium. “m⁶A as a regulator of transcription factor oscillatory expression in neural stem cells.” Woods Hole, MA. August 2018
- Kyoto University International Seminar. “Regulation of neurogenesis by m⁶A mRNA methylation.” March 2018
- Center for Excellence in Genomic Science Annual Meeting. “Temporal control of mammalian cortical neurogenesis by m⁶A mRNA methylation” Seattle, WA. October 2017
- Biochemistry, Cellular and Molecular Biology Graduate Program Annual Retreat. “Temporal control of mammalian cortical neurogenesis by m⁶A mRNA methylation” Cambridge, MD. October 2017
- Epigenetics, Metabolism & Nutrition Seminar. “Temporal control of mammalian cortical neurogenesis by m⁶A mRNA methylation.” Gustave Roussy Intitute, Villejuif, France. March 2017
- UC Davis Undergraduate Research Conference. “Engineering Composite Scaffolds.” Davis, CA. June 2014

Posters:

- Neuroepigenetics and Neuroepitranscriptomics Meeting. “RNA Modifications regulate neural differentiation.” Cancun, Mexico. February 2018
- Center for Excellence in Genomic Science Annual Meeting. “mRNA Methylation in Neurogenesis” Seattle, WA. October 2017
- ISSCR National Conference. “Temporal Control of Mammalian Cortical Neurogenesis by m⁶A mRNA Methylation.” Boston, MA. June 2017
- Center for Excellence in Genomic Science Annual Meeting. “The role of m⁶A RNA modification in neurogenesis” Palo Alto, CA. October 2016
- Beckman Scholar Symposium. “Role of Pore Size in Composite Scaffolds for Bone Regeneration.” Irvine, CA. Aug 2014

- IEEE Annual Conference of Engineering in Medicine and Biology. “Effects of Pore Size in Composite Scaffolds for Bone Regeneration.” Chicago, IL. Aug 2014
- Biomedical Engineering Society Annual Conference. “Effects of Pore Size in Composite Scaffolds for Bone Regeneration.” San Antonio, TX. Oct 2014

Academic Teaching Experience:

- **mentored** one rotation student, two undergraduates, and a high school student in Hongjun Song’s Lab. Also taught multiple postdocs about RNA sequencing and bioinformatics in Dr. Gregg Semenza’s lab. Institute for Cell Engineering, Johns Hopkins School of Medicine 2016-2018
- Developed self-guided presentations to replace traditional lectures in the Scientific Foundations of Medicine Course for medical students. **I designed 10 “biodes”** on a variety of subjects that are used to teach several hundred students each year about basic science as it relates to human medicine. Johns Hopkins School of Medicine 2017
- **Guest Lecturer** for upper level developmental biology course. Department of Biology, Loyola University 2017
- **Graduate Teaching Assistant** for the Scientific Foundations of Medicine course for first-year medical students. I led a daily discussion group of about 30 students and provided guidance to approximately 200 students in the course. School of Medicine, Johns Hopkins School of Medicine 2016
- **Undergraduate Teaching Assistant** for Introductory Animal Science. Led a lab section and worked with numerous students on writing skills for their final papers. Department of Animal Science, University of California, Davis 2013